GROWTH OF QUANTUM MATERIALS AND PHOSPHORUS-DOPED DIAMOND, AND THEIR CHARACTERIZATION BY TRANSPORT MEASUREMENTS

By

Milos Sretenovic

A DISSERTATION

Submitted to
Michigan State University
in partial fulfillment of the requirements
for the degree of

Physics—Doctor of Philosophy
Electrical Engineering—Dual Major

2025

ABSTRACT

The advancement of technology requires pushing the boundaries of materials, whether searching for new ones with unique properties or identifying well-known ones with untapped potential. This work makes progress in both of those directions, first looking to quantum materials then to semiconducting diamond. Understanding these materials primarily relies on electrical and thermal transport measurements which give insights into their fundamental properties.

Single crystals of the kagome lattice compounds $Tb_xY_{1-x}Mn_6Sn_6$ were grown and characterized by transport measurements and neutron scattering. We assemble a phase diagram of magnetic structure across stoichiometry and temperature. We see how Tb substitution systematically alters the magnetic transitions, challenging earlier claims of an easy-cone phase and instead showing only an in-plane to out-of-plane ferrimagnetic transition. Increasing Tb generally raises T_N, though with some lower values that suggest complex competing interactions between Mn and Tb. We also see transient incommensurate phases that appear within narrow temperature ranges, highlighting the need for further neutron scattering studies.

Single crystals of hexagonal van der Waals compounds were also grown and characterized by thermal transport measurements and neutron scattering. In our study of VCl_3 we resolve the nature of its structural transition, which goes from the space group $R\bar{3}$ to $P\bar{1}$ at low temperature with slight V–V dimerization. Despite clear magnetic ordering, no magnetic Bragg peaks are observed by neutron scattering implying an unusually small magnetic moment. Our observations of the family of compounds $V_xCr_{1-x}I_3$ identify modified exchange interactions, with mixed V and Cr compositions producing more complex magnetic structures than either parent compound. Their thermal Hall responses show magnon-phonon coupling and a temperature-driven sign inversion that may indicate a topological transition, though the absence of crystal structure data prevents us from determining if the effects arise from true mixing or coexisting end member components.

A method of preparing phosphorus-doped diamond for electronic transport was developed. To reduce the formation of a large edge bead during spin coating, a series of tests was carried out by varying photoresist application methods, dilution levels, rotation rates, developing times, exposure

times, and substrates, among others. The most successful strategy was to spin the substrate away from the center of rotation which almost completely eliminates the edge bead. The requirement of a heavily P-doped layer beneath metal contacts led to the creation of a procedure for selective diamond growth using patterned and annealed SiO_2 that is able to withstand etching by the reactor plasma for a certain time. The reactor ramp-up sequence was also optimized for SiO_2 longevity.

Finally, a P-doped diamond sample was successfully prepared for electrical transport measurements. Though we can demonstrate ohmic contacts, the transport data suggest that the selectively grown diamond regions are not of sufficient quality, either due to inadequate P-doping or high defect or impurity content. We proceed to grow a series of samples in an attempt to find growth conditions that lead to high quality heavily P-doped diamond. Though the ideal conditions have not been found, directions for progress in future attempts are identified.

In this work we characterize materials of several different classes using a common measurement technique, namely electrical and thermal transport, which provides fundamental insight into material properties. We investigate magnetic systems with topological behaviors and quasiparticle interactions that may one day lead to new kinds of technologies, and we lay the groundwork for future studies of *n*-type diamond which has major potential advantages not yet achieved by other semiconductors.

To Adam

ACKNOWLEDGEMENTS

Thanks to all the members of my committee as well as Remco Zegers for helping me though a difficult transition. I would not have finished this Ph.D. without their support and the confidence of Shannon and Jonas. Special thanks to Luke Suter and Aaron Hardy for donating so much of their time, effort, and occasionally diamonds to my research project. Shout out to Sarah and Loomis who have been the best lab mates (and also Ian, Logan, Kai, and Theresa, they're cool too).

I will fondly remember Tibor Nagy who had some hilarious jokes and always brought pie for his TAs on the last meeting of the semester.

TABLE OF CONTENTS

LIST OF TABLES

LIST OF FIGURES

LIST OF ABBREVIATIONS

AFM Atomic Force Microscopy

AntiFM Antiferromagnet *or* Antiferromagnetic

BDD Boron-Doped Diamond

BZ Brillouin Zone

CVD Chemical Vapor Deposition

CVT Chemical Vapor Transport

DFM Dynamic Force Microscope

DMI Dzyaloshinskii–Moriya Interaction

DS5 Diamond System 5

FC Field-Cooled

FCC Face-Centered Cubic

FiM Ferrimagnet *or* Ferrimagnetic

FM Ferromagnet *or* Ferromagnetic

FTIR Fourier-Transform Infrared

GKA Goodenough-Kanamori-Anderson

HFIR High Flux Isotope Reactor

HPHT High Temperature, High Pressure

IC Incommensurate

MFC Mass Flow Controller

MSU Michigan State University

NV Nitrogen-Vacancy

NPD Neutron Powder Diffraction

ORNL Oak Ridge National Laboratory

PDD Phosphorus-Doped Diamond

PECVD Plasma-Enhanced Chemical Vapor Deposition

PGMEA Propylene Glycol Methyl Ether Acetate

PM Paramagnetism *or* Paramagnetic

PPMS Physical Property Measurement System

PV Phosphorus-Vacancy

r.l.u. Reciprocal Lattice Unit

SCD Single-Crystal Diamond

SNS Spallation Neutron Source

SOC Spin-Orbit Coupling

SQUID Superconducting Quantum Interference Device

TOF Time Of Flight

UV-vis Ultraviolet-visible

XRD X-Ray Diffraction

ZFC Zero-Field-Cooled

CHAPTER 1

INTRODUCTION

1.1 Motivation

Though semiconductor technology has achieved major success with silicon, candidate materials continue to be tested and refined to push the boundaries of the field. The advancement of this field requires growth and characterization of novel materials.

The promise of materials with nontrivial topology is in the potential to access states that are robust against perturbations from impurities, defects, and noise. [1, 2] Macroscopically, these states could lead to devices that can tolerate the non-ideal conditions. MoS_2 is a topological insulator that was recently used to fabricate a microprocessor containing 5,900 transistors. [3]

Magnetic materials with nontrivial topology could push the envelope even further by replacing electrical currents with spin currents. [4, 5, 6, 7] In spintronic devices, spin currents are used to transmit signals by replacing the transmission of charge carriers (electrons) with transmission of spin carriers. Future technologies may use spintronics to replace conventional electronics that are prone to Joule heating which is wasted thermal energy that results from electric currents. [8, 9, 10]

Resistance against noise would also be a great benefit for quantum computing, where the current barriers to practical quantum computers are the difficulty in increasing scalability and eliminating noise-induced decoherence. [11, 12] Increasing the noise and fault tolerance of qubits would reduce their susceptibility to external disturbances making them less prone to errors and better at correcting errors that do occur. [13] Qubits based on topological materials, such as those involving Majorana fermions, are fault-tolerant and reduce the need for error correction protocols. [14, 15] These kinds of qubits have yet to be realized, but the materials discussed in this thesis have provided a sandbox for researchers to develop rudimentary devices that motivate more sophisticated ideas. [16, 17, 18]

Currently, the leading qubit for quantum sensing applications is the diamond NV center, illustrated in figure 1.1a, because it has a long coherence time and it can be initialized and read out optically at room temperature. Yet one challenge of using NV centers is the need to keep them in the negatively charged NV^- state which is higher in energy relative to the NV^0. Typically, a green

laser is used to excite the NV^0 state, and electron capture then leads to the NV^- state. [19] The drawback of this method is slower performance and reduced optical control [20, 21]. An alternative method of stabilizing the NV^- state is by surrounding it in a donor environment. By implanting NV centers in phosphorus-doped diamond, more than 99% were kept in the negative charge state [20, 22, 23, 24]. NV centers have also been implanted within the intrinsic layer of diamond *pin* diodes with doped phosphorus in the *n*-type layer, as illustrated in Fig. 1.1b. These diodes work as single photon emitters when electron-hole recombination at the NV center is triggered. [25]

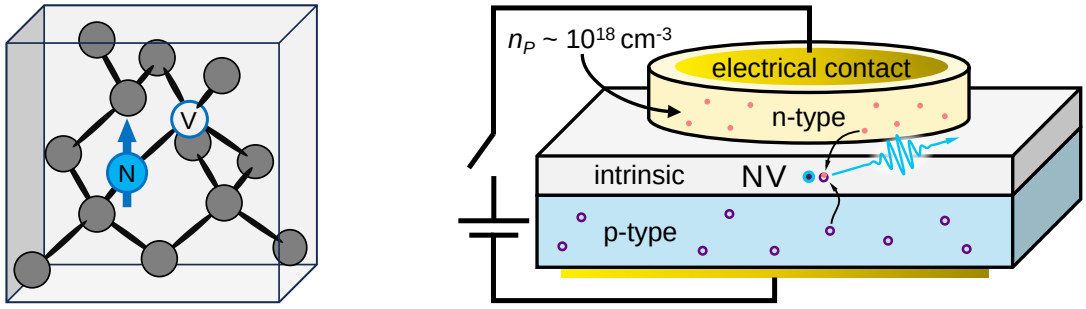

(a) (b)

Figure 1.1 (a) Structure of the nitrogen-vacancy center. (b) A *pin* junction that works as a single-photon emitter.

As a semiconductor, diamond has a uniquely high thermal conductivity and high breakdown voltage that make it the first choice for high-temperature and high-frequency applications where Si and SiC fail to perform adequately [26, 27]. The pursuit of diamond electronics began a long search for effective *p*- and *n*-type doping of single-crystal diamond and so far a wide variety of diodes and transistors have been fabricated. [28, 29, 30] But a persistent bottleneck has been the reduced effectiveness of *n*-type doping compared to *p*-type.

The success of *p*-type single-crystal diamond has outpaced *n*-type thanks to boron which can be doped in concentration ranges of 10^{12} to 10^{22} atoms/cm^3 with low acceptor compensation. [31, 32] Heavily B-doped samples can be metallic and even superconducting. [33, 34, 35] The best *n*-type dopant is currently phosphorus, but P incorporation has been successful in a more narrow range, topping out at 10^{20} atoms/cm^3 with higher donor compensation. Growth of high-quality single-crystal P-doped samples has so far succeeded in a smaller window of conditions that has

limited the variety of these samples. For example, only growth on the (111) lattice plane can achieve high P incorporation, but this surface is difficult to polish mechanically and tends to result in more defects compared to growth on (100) substrates. As is discussed further in this chapter, P-doping relies on striking a balance between lattice quality and donor incorporation which are influenced by the applied growth conditions in unintuitive ways. The aim of studying the effects of growth conditions on P-doped diamond is to produce a more symmetric understanding of *p*- and *n*-type semiconducting diamond.

1.2 Structures

1.2.1 Crystal Structures

A crystal is a periodic structure of atoms that can be constructed from a repeating unit cell. Crystals are sorted into Bravais lattices according to their translational symmetries. Point groups describe a single unit cell's symmetries, which include reflection, rotation, and inversion. Glide planes and screw axes introduce more symmetries. Considering all possible symmetry combinations allows us to classify every crystal structure into one of 230 space groups. [36] X-ray diffraction is the standard technique for crystal structure characterization and it is described in Section 2.2.1.

1.2.2 Magnetic Structures

Some atoms possess magnetic moments which may also form periodic structures. A ferromagnetic (FM) structure, for example, has moments of equal magnitude all aligned in the same direction. A ferrimagnetic (FiM) structure has at least two kinds of antiparallel moments that result in a nonzero net magnetization. An antiferromagnetic (AntiFM) structure has its individual moments arranged such that there is no overall magnetic moment. Some basic examples are illustrated in Fig. 1.2. For many magnetic structures such as MnO, adjacent crystal unit cells possess different arrangements of magnetic moments, meaning the crystal unit cell is no longer the fundamental repeating unit. Instead, we must define a larger magnetic unit cell that is the repeating unit of the atoms and their moments.

When the magnetic unit cell contains an integer number of atomic unit cells, the magnetic structure is said to be commensurate. Otherwise, the magnetic structure is incommensurate. The

propagation vector (denoted k) relates the periodicity of the two unit cells by defining the magnetic structure in reciprocal lattice units (nml). For commensurate structures n, m, and l are rational fractions. When the crystal and magnetic unit cells are identical $k = (0\ 0\ 0)$. In the case of MnO, an antiferromagnetic material whose magnetic cell is double the crystal cell in every dimension, $k = (\frac{1}{2}\ \frac{1}{2}\ \frac{1}{2})$.

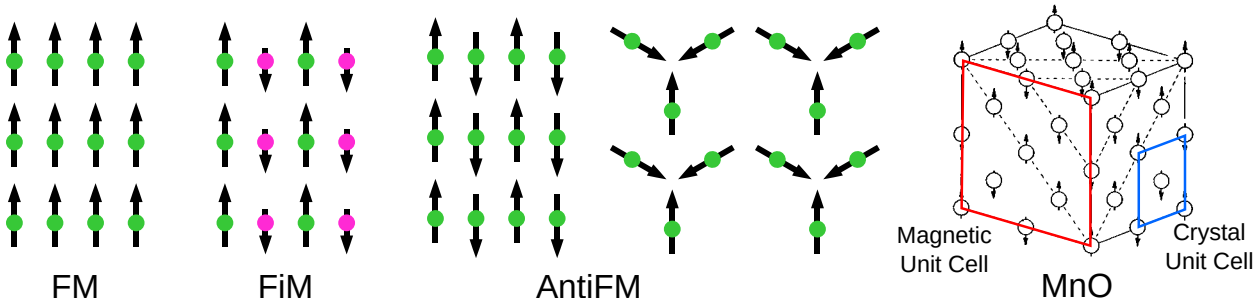

Figure 1.2 The moments in a ferromagnetic (FM) structure are all equal and parallel. A ferrimagnetic (FiM) structure consists of two FM sublattices whose moments are unequal and opposite. Antiferromagnetic (AntiFM) structures have no net moment. MnO has a commensurate antiferromagnetic structure. [37]

Magnetism introduces more ways of breaking symmetries and allows us to categorize crystals into magnetic space groups (also called Shubnikov groups). Typically, magnetic space groups are categorized into irreducible representations labeled Γ_n and their basis vectors $\vec{\Psi}_m(\Gamma_n)$. Neutron scattering is necessary to fully characterize a material's magnetic structure. This is described in Section 2.2.2.

1.2.3 Sources of Magnetic Order

Magnetic structures arise from interactions on the microscopic level. In the Ising model, spins are treated as vectors of fixed magnitude pointing either up or down. Each spin $\vec{S}_i$ experiences an exchange interaction with its nearest neighbors that compels it to reduce its energy by pointing in the same direction. By convention, the sign of the interaction J_{ij} is positive. Thus the Ising Hamiltonian only includes nearest-neighbor interactions and an applied B-field that must be coaxial to the spin vectors. [38]

$$H = -\sum_{\langle ij \rangle} J_{ij} S_i S_j - \mu_B \sum_i S_i B \tag{1.1}$$

The notation $\langle ij \rangle$ indicates a sum over nearest neighbors and μ_B is the Bohr magneton. At sufficiently high temperature, the energy barrier of the interaction is exceeded and the spins fluctuate freely resulting in paramagnetism, i.e., no magnetic order.

In the Heisenberg model, the moments are free to point in any direction and interactions can be positive or negative. [38, 39] The previous Hamiltonian can be rewritten as

$$H = -\sum_{\langle ij \rangle} J_{ij} \vec{S}_i \cdot \vec{S}_j - \mu_B \sum_i \vec{S}_i \cdot \vec{B}. \tag{1.2}$$

Depending on the sign of J_{ij}, the exchange will favor parallel (positive J_{ij}) or antiparallel (negative J_{ij}) spin configurations.

The Heisenberg Hamiltonian also allows for more freedom to include interactions beyond nearest neighbors, as well as anisotropies, spin-orbit-coupling (SOC), Zeeman effects, and more. It can also include moments of different magnitudes corresponding to different elements. The full Hamiltonian can produce a complex phase diagram with many magnetic structures over a range of temperature and field, making the Heisenberg model much more versatile and useful than the Ising model.

The temperature at which ferromagnetism occurs is called the Curie temperature, T_C. The temperature at which antiferromagnetism occurs is called the Néel temperature, T_N. At high temperature (above T_C or T_N), the susceptibility can be fit to the Curie-Weiss equation

$$\chi = \frac{C}{T - T_C} \tag{1.3}$$

in order to determine the Curie constant C and Curie Temperature T_C. The Curie constant can be used to calculate the effective magnetic moment (in cgs units). [40]

$$\mu_{\text{eff}} = \sqrt{8C}\mu_B \tag{1.4}$$

1.2.4 Exchange Mechanisms

At the root of any Hamiltonian is the mechanism of interaction itself. How do magnetic moments influence each other? One possible explanation is the dipole-dipole interaction. While such a term may be present in the full Hamiltonian, it is not often very important since a dipole field

falls off according to distance cubed. The main way moments interact in crystals is by exchanging electrons. The exact mechanism depends on the elements involved and their configurations.

Coulomb exchange results from the combined effects of Coulomb repulsion and the antisymmetric properties of electrons. Qualitatively, Hund's rules tell us that electrons reduce their energy by aligning their spins, so ferromagnetism should be preferred. However, from a statistical perspective, electrons cannot hop between orbitals when they have the same spin. That would violate the Pauli exclusion principle. Direct exchange, resulting from electron hopping, therefore, favors antiparallel spin configurations and antiferromagnetism. [41] The electrons' movements are shown in Fig. 1.3.

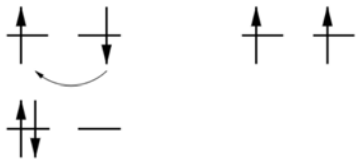

Figure 1.3 Direct exchange favors antiparallel spin configurations. [41]

These exchange mechanisms, however, play a minor role when magnetic atoms are separated by nonmagnetic elements such as oxygen. In transition-metal oxides, direct exchange must bridge across the oxygen's *p*-orbitals in a mechanism called superexchange. Now we must consider the hopping possibilities between two *d*-orbitals separated by a *p*-orbital in a linear configuration so as to create maximal orbital overlap. Fig. 1.4 illustrates why antiferromagnetism is preferred in systems where superexchange is likely.[1] But, when the bond angle is 90°, the orbitals do not overlap. Nevertheless, exchange is still available by combining Coulomb exchange with electron hopping. The resultant double exchange favors parallel spins, as illustrated in Fig. 1.5. For bonds between 90° and 180°, we assume that superexchange and double exchange compete.

More complex exchange mechanisms exist that allow for exchange beyond nearest neighbors. However, the greater the distance the electrons must hop, the weaker the exchange is. The Goodenough-Kanamori-Anderson (GKA) rules summarized here serve as a guide to predict the magnetic properties of transition metal compounds. [42, 43, 44, 45]

[1] MnO (Fig. 1.2) is an example of antiferromagnetism caused by superexchange domination. [38]

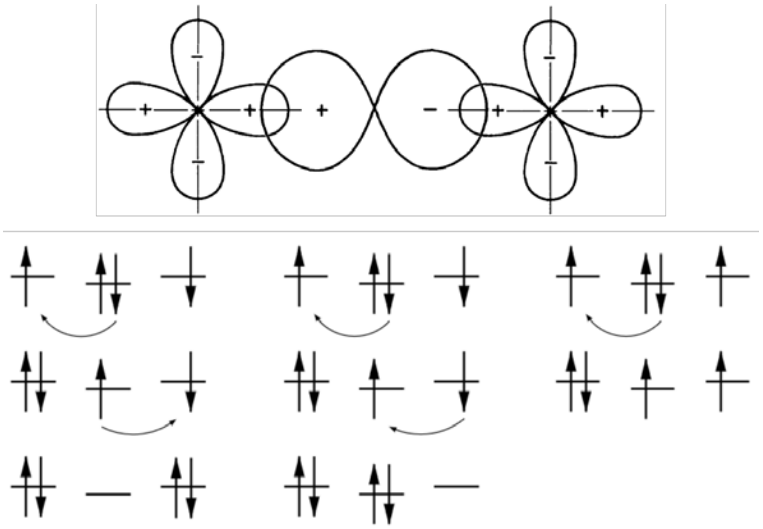

Figure 1.4 Superexchange results in antiferromagnetism.[41]

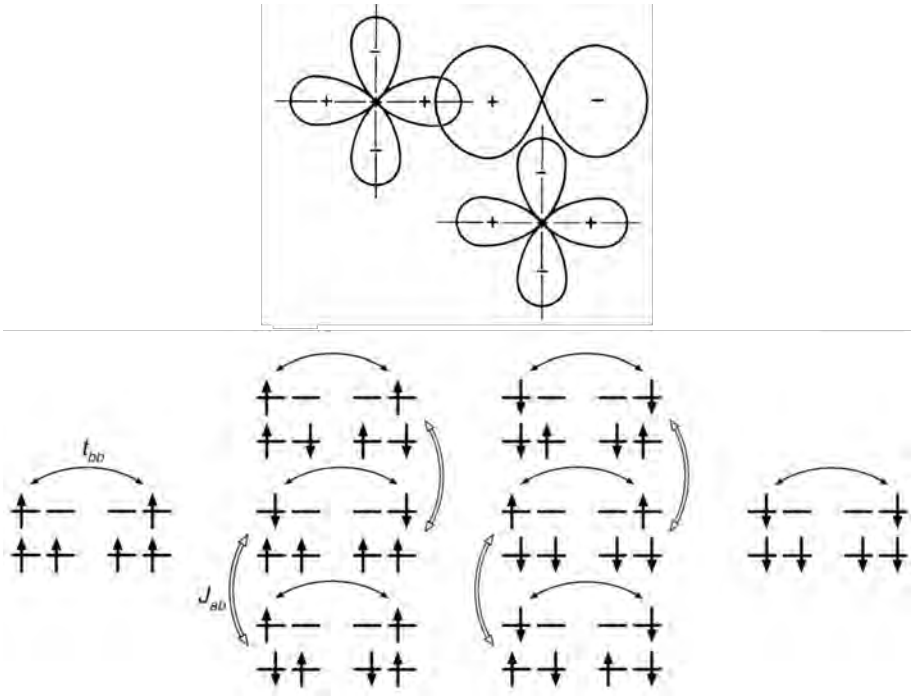

Figure 1.5 Double exchange results in ferromagnetism. [41]

The magnetic susceptibility χ describes how a material's magnetization $\vec{M}$ responds to an applied magnetic field $\vec{H}$. [38]

$$\vec{M} = \chi \vec{H} \tag{1.5}$$

In general, the susceptibility is a tensor that can have complex behavior that may be used to infer something about a material's magnetic structure. For example, a very basic model of magnetism predicts that the susceptibility of a ferromagnet will show hysteresis as an external field is varied cyclically and that the susceptibility of an antiferromagnet will not.

The susceptibility is also temperature dependent and it can be used to identify phase transitions. It is common to measure the susceptibility as a function of temperature under two kinds of conditions. In a field-cooled (FC) measurement, a field is applied (often 0.1 to 1 T) as the sample is cooled and the susceptibility is measured as the temperature is raised. In a zero-field-cooled (ZFC) measurement, no field is applied as the sample is cooled, then the field is turned on at low temperature (again 0.1 to 1 T) and the susceptibility is measured upon warming. Sharp changes in the derivative (such as kinks and steps) are strongly suggestive of phase transitions.

1.3 Carriers

The preceding sections provide a static description of structure. Each atom and electron in the crystal lattice has a fixed position and moment with no reason to wiggle. But above absolute zero, thermal energy allows for some deviation from the ideal structure. Atoms can jostle their neighbors, electrons can travel across bonds, and moments can precess, flip, and disturb each other. In reality, energy and momentum are transported through a structure by carriers, and transport describes how a system responds macroscopically to an imbalance in potential. If an appropriate carrier exits, it will flow from high to low potential in an attempt to return to balance.

1.3.1 Bands

In crystal lattices, periodic boundary conditions restrict the permissible momentum and energy states of carriers and the dispersion relation in free space $E = \frac{\hbar^2 \vec{k}^2}{2m}$ no longer applies. Instead, a plot of carrier dispersion $E(\vec{k})$ reveals bands across the Brillouin zone that determine many of the behaviors of individual carriers as well as macroscopic properties of the material as a whole.

The band structure is effectively a fingerprint that is unique to a given material, but certain patterns carry universal significance. The energy states of electrons fill up from low to high energy because of the Pauli exclusion principle. If a gap separates the highest occupied level of the valence band from the lowest unoccupied level of the conduction band, electrons in the valence band cannot overcome a large energy barrier to reach the conduction band and the material will be insulating. If no gap is present, electrons can travel within a single band and the material will be metallic. Semimetals are also conducting due to small overlap between two bands, where the lower band will be conductive due to holes and the upper band will be conductive due to electrons. A semiconductor has a band much like an insulator, and it will be insulating at low temperature, but will become conductive at higher temperature either due to a sufficiently small band gap or due to dopants that populate one of the bands with electrons or holes. [46]

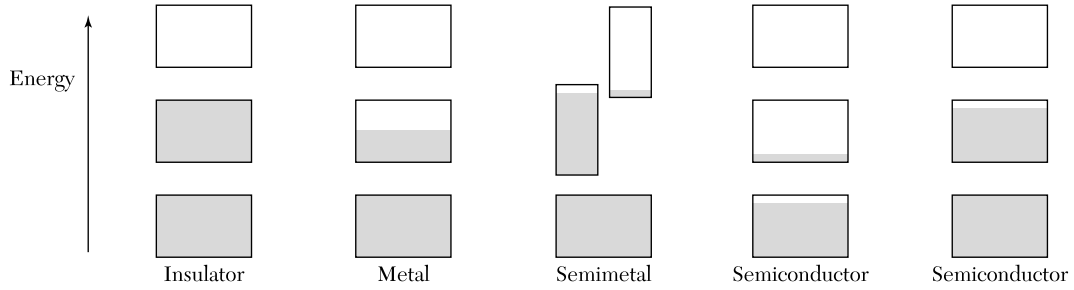

Figure 1.6 Some generalized band structures. Boxed areas represent simplified bands across momentum and energy. Filled electron states are indicated by the gray areas.

Holes are vacancies in filled bands. They can be treated as positively charged electrons that occupy the valence band and react to applied electric and magnetic fields like ordinary particles. Because a carrier's behavior is partly determined by the curvature of the band it occupies, and electrons and holes exist in separate bands, their behavior is not identical but they are always described by the same equations of motion.

Bands can also be calculated for quasiparticles of collective excitations such as phonons and magnons.

1.3.2 Electrons and Holes

1.3.2.1 Ohm's Law

Electrons are fundamental particles with spin 1/2 (in units of $\hbar$), making them fermions. Therefore, they must obey the Pauli exclusion principle and a gas of non-interacting electrons will be described by the Fermi-Dirac distribution function

$$f(\varepsilon, \mu, T) = \frac{1}{e^{(\varepsilon-\mu)/k_B T} + 1} \tag{1.6}$$

where ε is the energy, μ is the chemical potential, and k_B is the Boltzmann constant.

In the Drude model, electrons in a solid are thought of as a classical gas of free, negatively charged particles moving through a stationary lattice of heavy, positively charged ions. When an electric field is applied to the electron gas, a current arises and the electrons begin to accelerate.

$$\vec{F} = -e\vec{E} = m_e \frac{d\vec{v}}{dt} \tag{1.7}$$

Due to this force, electrons gain some velocity v between collision intervals of time τ, which is a characteristic of the lattice,

$$v = -\frac{eE\tau}{m_e} \tag{1.8}$$

but lose the momentum that they acquired whenever they collide with the ions in the lattice. Additionally, their mass m_e is under the influence of the local band curvature, making it an effective mass.

$$\frac{1}{m_e} = \frac{1}{\hbar^2}\frac{d^2\varepsilon}{dk^2} \tag{1.9}$$

When the total charge density is $-ne$, we can define a charge current

$$J = -nev = \frac{ne^2 E\tau}{m_e}\,, \tag{1.10}$$

electrical conductivity

$$\sigma = \frac{J}{E} = \frac{ne^2\tau}{m_e}\,, \tag{1.11}$$

and electrical resistivity

$$\rho = \sigma^{-1}\,. \tag{1.12}$$

The behavior of holes mirrors the behavior of electrons, so the real conductivity will include the contributions of both,

$$\sigma = \sigma_e + \sigma_h = \frac{ne^2\tau_e}{m_e} + \frac{pe^2\tau_h}{m_h} \tag{1.13}$$

where σ_e and σ_p are the contributions of electrons and holes, respectively. Thus, electrons and holes are charge carriers and the conductivity and resistivity are electrical transport properties of a given material.

1.3.2.2 The Hall Effect

In 1879, Edwin Hall observed that applying a current and perpendicular magnetic field resulted in a voltage perpendicular to both. [47] Until then, electricity was thought of as a fluid and it was not clear how this transverse voltage could arise. Now this phenomenon, known as the Hall effect, is understood as the result of the Lorentz force

$$\vec{F} = -e\left(\vec{E} + \vec{v} \times \vec{B}\right) \tag{1.14}$$

acting on subatomic particles. In a bar-shaped sample of dimensions $w \times t \times l$ where the current flows through the length, the Lorentz force curves the motion of electrons and holes and pins them to the sides of the sample. The system comes to a steady state when the Lorentz force is opposed by the electric field of the pinned charges. We can define a transverse resistivity if we measure the transverse voltage V_H.

$$\rho_{xy} = \frac{E_y}{J_x} = \frac{V_H/w}{I/wt} = \frac{V_H}{It} \tag{1.15}$$

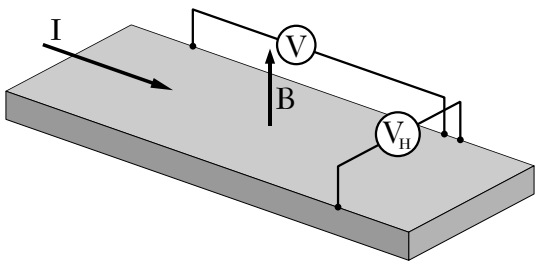

Figure 1.7 Measurement of the resistivity and Hall effect.

Varying the magnetic field reveals that ρ_{xy} is related by a proportionality constant R_H, known as the Hall coefficient.

$$\rho_{xy} = R_H B \tag{1.16}$$

This coefficient contains information about the carriers. For a metal

$$R_H = -\frac{1}{en}\,, \tag{1.17}$$

and for a semiconductor that has significant numbers of both electrons and holes

$$R_H = \frac{p\mu_h^2 - n\mu_e^2}{e\left(p\mu_h - n\mu_e\right)^2}. \tag{1.18}$$

Here e is the (positive) elementary charge, n is the free electron density, p is the free hole density, μ_e is the electron mobility, and μ_h is the hole mobility.

For samples that cannot be shaped into a bar, placing electrical connections along the perimeter of the sample in the van der Pauw configuration can be used to measure the Hall effect and carrier densities as long as the sample is of uniform thickness and is free of cracks and voids. The sample can be any shape, but to most effectively remove the effects of contact resistance the cloverleaf shape is preferable. [48]

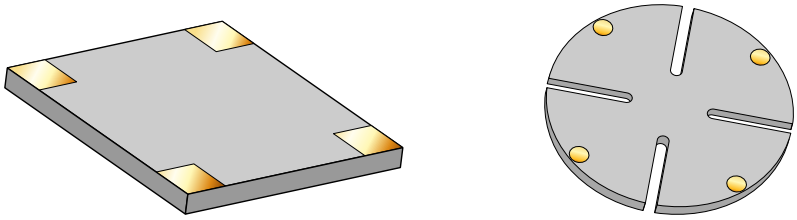

(a) Square plate sample (b) Cloverleaf sample

Figure 1.8 Measuring the Hall effect with the van der Pauw configuration. Four electrical connections are made to the contact pads drawn in gold.

Because four contacts allow the current to pass through one pair while independently measuring the voltage across the other pair, it is possible to separate the longitudinal and transverse components. This geometry eliminates lead and contact resistances, allowing the intrinsic transport properties of the sample to be extracted. For a sample with contacts labeled as shown in Fig. 1.9, we use the notation $V_{12,34}$ to refer to the potential difference $V_3 - V_4$ measured when contact 1 serves as the positive current terminal and contact 2 as the negative current terminal. The resistance is calculated in two orthogonal orientations and averaged.

$$\rho_a = \frac{\pi f_a t}{4\ln(2) I}\left(V_{21,34} - V_{12,34} + V_{32,41} - V_{23,41}\right) \tag{1.19}$$

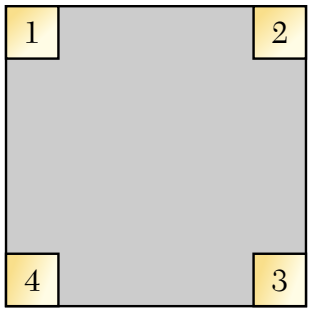

Figure 1.9 Contact labels of the van der Pauw configuration.

$$\rho_b = \frac{\pi f_b t}{4\ln(2) I}\left(V_{43,12} - V_{34,12} + V_{14,23} - V_{41,23}\right) \tag{1.20}$$

$$\rho = \frac{1}{2}\left(\rho_a + \rho_b\right) \tag{1.21}$$

Here t is the sample thickness, and f_a and f_b are geometric factors which account for the size and placement of the contacts. Because diamond samples are grown on a substrate of insulating intrinsic diamond, the thickness of the grown layer is used. This calculations stem from the fundamental relationship between ρ, ρ_a, and ρ_b

$$e^{\frac{-\pi R_1}{R_S}} + e^{\frac{-\pi R_2}{R_S}} = 1 \tag{1.22}$$

where

$$R_1 = \frac{V_{21,34} - V_{12,34} + V_{32,41} - V_{23,41}}{4I} \tag{1.23}$$

$$R_2 = \frac{V_{43,12} - V_{34,12} + V_{14,23} - V_{41,23}}{4I} \tag{1.24}$$

and R_S is the sheet resistance. [49] Eq. 1.22 can be used to solve for R_S numerically, and the geometric factors follow from there.

$$f_a = \frac{R_S \ln(2)}{\pi R_1} \tag{1.25}$$

$$f_b = \frac{R_S \ln(2)}{\pi R_2} \tag{1.26}$$

The additional relation

$$\rho = R_S t \tag{1.27}$$

can be used to verify Eq. 1.21.

The Hall coefficient requires applying a magnetic field B perpendicular to the sample's top surface. It is also calculated in two orthogonal orientations and averaged.

$$R_a = \frac{t}{4BI}\left[V_{31,42}(B) - V_{13,42}(B) + V_{13,42}(-B) - V_{31,42}(-B)\right] \tag{1.28}$$

$$R_b = \frac{t}{4BI}\left[V_{42,13}(B) - V_{24,13}(B) + V_{24,13}(-B) - V_{42,13}(-B)\right] \tag{1.29}$$

$$R_H = \frac{1}{2}\left(R_a + R_b\right) \tag{1.30}$$

The mobility and carrier concentration, respectively, are

$$\mu = \frac{|R_H|}{\rho} = |R_H|\,\sigma \tag{1.31}$$

$$n = \frac{1}{eR_H}\ . \tag{1.32}$$

1.3.2.3 Thermoelectric Transport

Joule heating is the common experience of electrical currents producing heat in materials of finite resistance.

$$P = I^2R \tag{1.33}$$

On a microscopic scale, it is the result of electrons dumping energy into the lattice by scattering off of the ions. However, electrons can act as heat carriers even when no electric current is applied. The Wiedemann-Franz law relates the electrical conductivity σ and the thermal conductivity κ of a metal by a proportionality constant called the Lorenz number L.

$$\frac{\kappa}{\sigma} = LT \tag{1.34}$$

Using the Drude model, the Lorenz number is expected to be equal for all conductors.

$$L = \frac{\pi^2}{3}\left(\frac{k_B}{e}\right)^2 = 2.45 \times 10^{-8}\,\mathrm{W\Omega/K^2} \tag{1.35}$$

Experimental values of L are in very good agreement, indicating that electrons are by far the primary heat carriers in metals. For this reason, thermal conductivity mirrors the electrical conductivity of metals, and it was not deemed a useful transport property of metallic samples in this work. Thermal conductivities are only reported for insulating samples.

However, for reasons explained in Section 1.4, the thermoelectric tensor **S** can contain information about nontrivial topology. This tensor relates a transverse and longitudinal electrical potential under an applied thermal current and magnetic field.

$$\mathbf{S} = \begin{bmatrix} S_{xx} & S_{xy} \\ -S_{xy} & S_{xx} \end{bmatrix} \tag{1.36}$$

The diagonal terms are known as the Seebeck coefficient and the off-diagonal terms are known as the Nernst coefficient.

$$S_{xx} = \frac{V_x}{\Delta T} \tag{1.37}$$

$$S_{xy} = \frac{V_y/w}{\Delta T/l} \tag{1.38}$$

Here, the longitudinal voltage V_x and temperature gradient ΔT are measured across a length l, and the transverse voltage V_y is measured across the sample width w. The contact configuration is shown in Fig. 1.10.

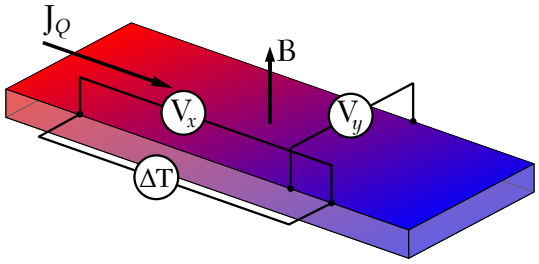

Figure 1.10 Measurement of the Seebeck and Nernst coefficients.

1.3.3 Phonons

A phonon is a collective excitation of atoms in a lattice. Phonons are quasiparticles because they are quantized and have a well-defined momentum, and they are bosons because they follow the Bose-Einstein distribution for their occupation number

$$f(\omega, T) = \frac{1}{e^{\hbar\omega/k_B T} - 1}\,. \tag{1.39}$$

Because boson number is not a conserved quantity, light and heat can generate phonons within a material as long as energy and momentum are conserved. Light absorption leading to a phonon lattice excitation must also obey certain selection rules determined by the lattice symmetry.

In solids, thermal energy is stored in lattice vibrations which makes phonons heat carriers. In insulators, they are the most significant heat carriers. As quasiparticles, they can scatter off of impurities, defects, and each other. Like electrons, phonon dispersion forms bands across the Brillouin zone.

1.3.4 Magnons

A magnon is a collective excitation of magnetic moments in a lattice. Like phonons, magnons are bosonic quasiparticles that transport thermal energy. But uniquely, magnons are also spin carriers. In a magnetically ordered material, spins are aligned due to exchange interactions. If one spin deviates from its aligned state, the disturbance will propagate through the system as a wave. The energy of a magnon is proportional to its momentum and is related to the strength of the magnetic exchange interaction, and collectively magnon dispersion forms band structures.

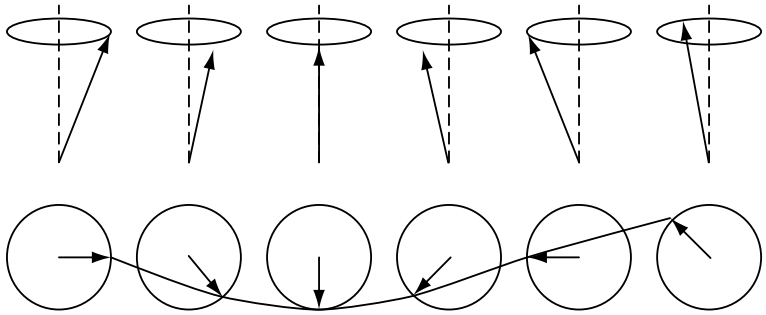

Figure 1.11 A chain of aligned moments allowed to process around their equilibrium positions can form a propagating spin wave.

To illustrate magnons' quasiparticle nature, we can use a 1D ferromagnet chain. Fig. 1.11 shows how the procession of individual moments creates a collective spin wave. Considering only nearest-neighbor interactions, the energy the exchange energy of the nth spin is

$$E_n = -2J\vec{S}_n \cdot \left(\vec{S}_{n-1} + \vec{S}_{n+1}\right) \tag{1.40}$$

where J is the nearest neighbor exchange interaction. Using the spin's magnetic moment

$$\vec{\mu}_n = -g\mu_B\vec{S}_n \tag{1.41}$$

where μ_B is the Bohr magneton, and replacing the energy with

$$E_n = \vec{\mu}_n \cdot \vec{B}_n \ , \tag{1.42}$$

Eq. 1.40 can be rewritten as

$$\vec{B}_n = -\frac{2J}{g\mu_B}\left(\vec{S}_{n-1} + \vec{S}_{n+1}\right). \tag{1.43}$$

To further approximate, we will only look for low-energy solutions such that there are only small deviations $\vec{\sigma}_n$ from $\vec{S}_n$.

$$\vec{S}_n = -S\hat{z} + \vec{\sigma}_n \tag{1.44}$$

This is a useful approximation since magnetic order is destroyed at high temperatures. The dispersion of these waves will obey the equation

$$\hbar\omega = 4JS\,(1 - \cos ka) \tag{1.45}$$

where a is the lattice spacing. The magnon energy near $k = 0$ is approximately

$$\varepsilon = \hbar\omega \approx 2JSa^2k^2 \tag{1.46}$$

which suggests that these low energy magnons have an effective mass equal to

$$\mu_{eff} = \frac{\hbar^2}{4JSa^2}\,. \tag{1.47}$$

Using the approximate form of the energy in equation 1.46 and the Bose-Einstein distribution function, the energy of these magnons is

$$E = E_0 + \frac{V}{4\pi^2\hbar}\left(\frac{1}{2JSa^2}\right)^{3/2}(k_BT)^{5/2}\int_0^\infty \frac{x^{3/2}}{e^x - 1}dx \tag{1.48}$$

and the heat capacity is

$$C = \frac{dE}{dT} \propto \frac{1}{\hbar}\left(\frac{1}{JS\pi a^2}\right)^{3/2} k_B^{5/2}\,T^{3/2}\,. \tag{1.49}$$

The magnon heat capacity varies as $T^{3/2}$ at low temperature. [50, 51]

The exact nature of the phonon dispersion and heat capacity depend on the spin structure. Though in this example the dispersion was quadratic for low k, in an antiferromagnetic 1D spin chain the dispersion would be linear. Fig. 1.12 illustrates that antiparallel moments can also form a propagating spin wave.

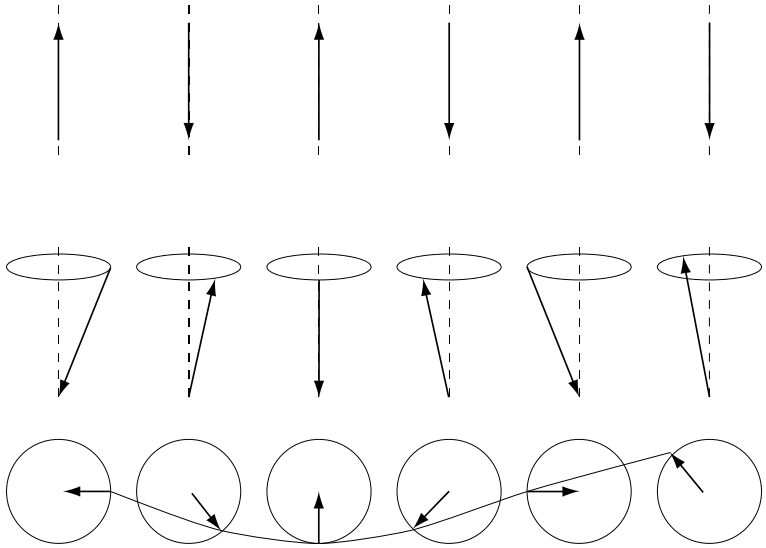

Figure 1.12 A chain of antiparallel moments can also form a propagating spin wave.

1.3.5 Thermal Conductivity

Thermal conductivity is the analog of electrical conductivity. If a thermal current J_Q flows across a bar-shaped sample of dimensions l, w, and t, as shown in Fig. 1.13, a temperature difference ΔT will arise. We define a thermal resistivity analogous to the electrical resistivity.

$$W = \frac{\Delta T\, w\, t}{J_Q\, l} \tag{1.50}$$

However, the conductivity κ is usually preferable.

$$\kappa = W^{-1} \tag{1.51}$$

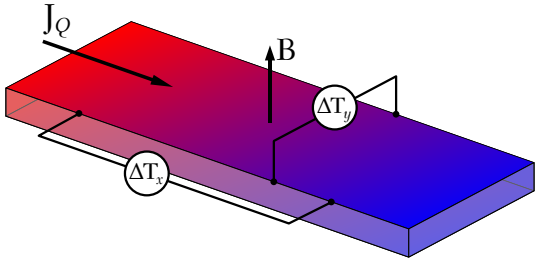

Figure 1.13 Measurement of the longitudinal and transverse thermal conductivity.

1.3.6 The Thermal Hall Effect

In many samples, application of a magnetic field will generate a transverse temperature gradient completely analogous to the electrical Hall effect, even in insulating samples whose only thermal

carriers are magnons and phonons. As before we can define a transverse thermal conductivity

$$W_{xy} = \frac{\Delta T_y}{J_Q\, t} \tag{1.52}$$

where ΔT_y is the transverse temperature gradient and J_Q is the thermal current. The full thermal resistivity must be though of as a rank two tensor.

$$\mathbf{W} = \begin{bmatrix} W_{xx} & W_{xy} \\ -W_{xy} & W_{xx} \end{bmatrix} \tag{1.53}$$

For the samples studied in this work which have layered structures, it is safe to assume that the in-plane conductivities of all transport quantities are isotropic (i.e., $W_{xx} = W_{yy} = W$)

Inverting gives the thermal conductivity tensor.

$$\boldsymbol{\kappa} = \mathbf{W}^{-1} = \frac{1}{W_{xx}^2 + W_{xy}^2} \begin{bmatrix} W_{xx} & -W_{xy} \\ W_{xy} & W_{xx} \end{bmatrix} = \begin{bmatrix} \kappa_{xx} & \kappa_{xy} \\ -\kappa_{xy} & \kappa_{xx} \end{bmatrix} \tag{1.54}$$

$$\kappa_{xx} = \frac{W_{xx}}{W_{xx}^2 + W_{xy}^2} \tag{1.55}$$

$$\kappa_{xy} = -\frac{W_{xy}}{W_{xx}^2 + W_{xy}^2} \tag{1.56}$$

Since W_{xx} is much larger than W_{xy}, we can reduce the longitudinal thermal conductivity to the standard form.

$$\kappa_{xx} \approx W_{xx}^{-1} \quad \Rightarrow \quad \kappa = W^{-1} \tag{1.57}$$

The thermal Hall effect (also called the Righi–Leduc effect) is the result of nontrivial topology. It is not common to all magnetic samples. This is discussed further in Section 1.4.

1.3.7 Coupling

Phonons and magnons are both heat carriers. Magnons are also spin carriers. Measurements of thermal transport reveal their dynamics within a lattice, with the specific goal of observing their interactions. As quasiparticles, they can scatter off each other. The nature of this scattering can give insight into the nontrivial topology of the material being studied but to do this we must observe how thermal transport is affected by a magnetic field.

Will the thermal conductivity change when a magnetic field is applied? If phonons are the only heat carriers present, we anticipate no B-field dependence because there is no mechanism for lattice vibrations to interact with magnetic fields. However, if magnons are also present, an applied B-field should have a noticeable effect. Under a magnetic field, deviation from the field orientation becomes energetically costly and more thermal energy is required to create the collective excitation of magnetic moments that creates a magnon. Thus, a magnetic field suppresses the magnon population. This reduces the number of magnons that are available to transport heat and should reduce the macroscopic thermal conductivity.

However, a second phenomenon becomes important when a B-field is applied. When magnons and phonons are both present, they scatter each other and reduce each other's transport length. By reducing the magnon population with an applied field, scattering events become more infrequent. Phonons, which are unaffected by the B-field, are therefore able to travel farther down the temperature gradient and transport heat more effectively than before, leading us to conclude that the macroscopic conductivity should be enhanced by an applied field.

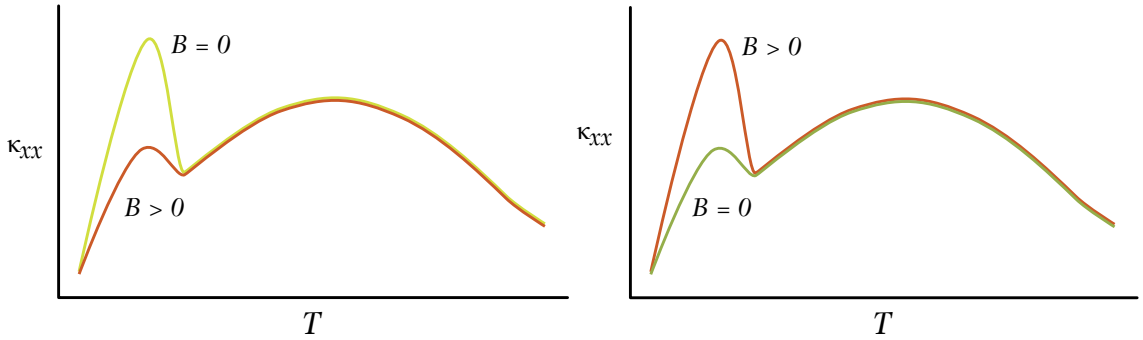

Figure 1.14 (a) A system with weak magnon-phonon coupling will show reduction of the heat conductivity at low temperature as the magnon population is suppressed. (b) A system with strong magnon-phonon coupling will show higher heat conductivity at low temperature because phonons can propagate further with fewer magnons present.

Which is correct? Is the conductivity reduced or enhanced by a B-field? The answer will depend on the strength of the magnon-phonon coupling. In samples that show reduced conductivity under the applied field, the magnon-phonon coupling is weak and the reduction in magnon population reduces the conductivity more than the greater travel time of the phonons increases it. In samples

that show an increase in conductivity, the magnon-phonon coupling is strong and phonons can act as carriers more effectively once magnons are suppressed. Fig. 1.14 illustrates this point.

1.4 Topology

The simple explanation of the Hall effect fails to explain the electrical properties of some common metals such as iron and nickel, which possess a transverse resistivity when no magnetic field is applied. This anomalous Hall resistivity was identified early on to be common to ferromagnetic materials, and its magnitude was proportional to the internal magnetization of the metal. Ultimately, the cause was found to be SOC in systems where symmetry is broken by ferromagnetism. [52] In fact, SOC can give rise to the anomalous Hall effect (AHE) in antiferromagnets as well, but the explanation is more subtle.

The Berry phase is a geometric phase acquired by a wavefunction when it is varied adiabatically along a closed loop. In periodic potentials, where wavefunctions are described by Bloch states $|n\rangle$, the Berry phase arises as the integral of the Berry connection over a closed path in the Brillouin zone.

$$\Omega^n_{\mu\nu} = i \sum_{n' \neq n} \frac{\left\langle n \left| \frac{\partial H}{\partial R^\mu} \right| n' \right\rangle \left\langle n' \left| \frac{\partial H}{\partial R^\nu} \right| n \right\rangle - \left\langle n \left| \frac{\partial H}{\partial R^\nu} \right| n' \right\rangle \left\langle n' \left| \frac{\partial H}{\partial R^\nu} \right| n \right\rangle}{\left(\varepsilon_n - \varepsilon_{n'}\right)^2} \tag{1.58}$$

The matrix elements such as $\left\langle n \left| \frac{\partial H}{\partial R^\mu} \right| n' \right\rangle$ represent the coupling between the Bloch states. This geometric phase reflects the underlying topology of the electronic wavefunctions. Integrating the Berry curvature over the first Billouin zone gives the Chern number.

$$C_n = \frac{i}{2\pi} \int_{\mathrm{BZ}} \Omega_n(\vec{k}) d^2k \tag{1.59}$$

For the structures studied in this work, we conclude they have trivial topology when the Chern number integrates to zero, and nontrivial topology when it integrates to ± 1. There are different kinds of invariants for other kinds of structures. Theoretical calculations are necessary to determine the value of the invariant for a given system.

Anomalous transport results from the effect of the Berry curvature, which acts as a magnetic field, combined with the applied electric field, which drives the current on the electron distribution

function. An anomalous velocity arises according to

$$\vec{v}^A = -\frac{e}{\hbar}\vec{\Omega}(\vec{k}) \times \vec{E} \ . \tag{1.60}$$

The transverse current arises from the anomalous velocity induced by the Berry curvature. For the systems discussed in this work, the anomalous transport coefficients due to electron transport can be summarized by the following equations

$$\sigma_{xy}^A = \frac{e^2}{\hbar} \int d\varepsilon \int_{\mathrm{BZ}} \frac{d^2k}{(2\pi)^2} f_{FD} \left(\frac{\partial f_{FD}}{\partial \varepsilon} \right) \Omega \tag{1.61}$$

$$\kappa_{xy}^A = \frac{k_B^2 T}{\hbar} \int d\varepsilon \left(\frac{\varepsilon - \mu}{k_B T} \right)^2 \int_{\mathrm{BZ}} \frac{d^2k}{(2\pi)^2} f_{FD} \left(\frac{\partial f_{FD}}{\partial \varepsilon} \right) \Omega \tag{1.62}$$

$$\alpha_{xy}^A = \frac{k_B e}{\hbar} \int d\varepsilon \left(\frac{\varepsilon - \mu}{k_B T} \right) \int_{\mathrm{BZ}} \frac{d^2k}{(2\pi)^2} f_{FD} \left(\frac{\partial f_{FD}}{\partial \varepsilon} \right) \Omega \tag{1.63}$$

$$\boldsymbol{\sigma}\mathbf{S} = \boldsymbol{\alpha} \tag{1.64}$$

where the Fermi-Dirac distribution function f_{FD} and Berry Curvature Ω are integrated over energy ε and the two-dimensional subspace of the Brillouin Zone (BZ) corresponding to the planar lattice.

In insulating systems, electronic transport does not occur, but the AHE is present in magnetic systems when magnon bands posses analogous topological properties. The Dzyaloshinskii-Moriya (DM) interaction can play a twofold role towards anomalous transport. This is an antisymmetric exchange interaction between two moments that can be written as

$$H = \vec{D}_{ij} \cdot \left(\vec{S}_i \times \vec{S}_j \right) \tag{1.65}$$

where the vector $\vec{D}_i$ expresses the strength of the interaction. [53] Generally, the strength of DM interaction is enhanced in systems with large SOC. The nature of the cross product means that magnetic moments with a strong DM interaction become canted and a spin chirality χ_{ijk} develops [54], which can be defined by the geometry of three neighboring spins as

$$\chi_{ijk} = \vec{S}_i \cdot \left(\vec{S}_j \times \vec{S}_k \right) . \tag{1.66}$$

This quantity is nonzero for non-collinear antiferromagnets, and it results in symmetry breaking and acts like an effective magnetic field, deflecting electrons much like the Lorentz force. The antisymmetric nature of the DM interaction limits it to bonds that are do not have inversion symmetry, as will be explained for the systems studied in this work. The second role of the DM interaction in anomalous transport is in its ability to open gaps in otherwise ungapped magnonic bands which modifies the Berry curvature in a way that is analogous to electronic bands with nontrivival topology. [53] Together, spin chirality generates real-space Berry curvature, while spin-orbit coupling generates momentum-space Berry curvature. Both contribute to the AHE through their respective Lorentz-like forces on the magnetic transport. Therefore, the anomalous transport can be considered the sum of all these effects.

$$\rho_{xy} = R_H B + \underbrace{R_S M + \rho_\Omega + \rho_\chi}_{\rho^A_{xy}} \tag{1.67}$$

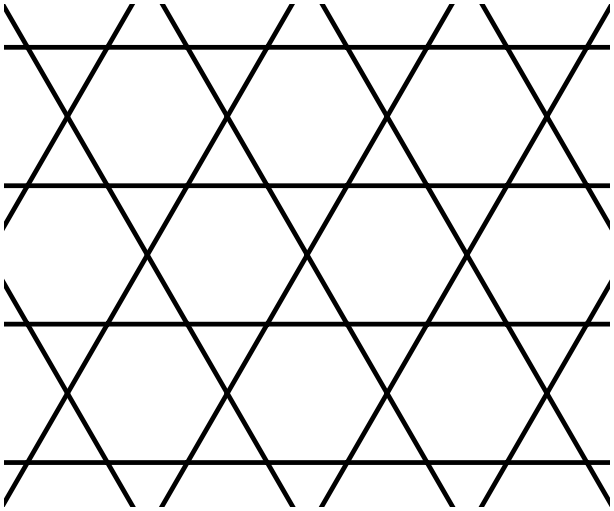

Figure 1.15 A kagome lattice.

1.5 R166 Kagome Metals

A kagome lattice is a two-dimensional network of corner-sharing triangles that forms a hexagonal pattern as shown in Fig. 1.15. This kind of lattice has drawn much attention due to its unique symmetry that results in a distinctive band structure featuring a perfectly flat band arising from destructive interference and linearly dispersing Dirac-like crossings at the Brillouin zone corners.

Materials with kagome lattices have shown novel physical properties such as magnetic frustration, superconductivity, charge density waves, and anomalous transport. [55] Kagome metals have provided opportunities to study the interplay among frustrated magnetism, electronic correlation, and topological electronic structure induced by SOC. [56] The R166 family of compounds, which have the formula RMn_6Sn_6 where R = Y or rare earth element, posses stacked layers of magnetic Mn atoms in kagome-lattice planes. They order at high temperatures because of strong ferromagnetic Mn-Mn exchange. [57] However, these materials posses complex structures due to competing Mn and R magnetic interactions and competing interlayer magnetic interactions. [58] For magnetic R elements, the strong Mn-R interaction makes R and Mn moments collinear and ferrimagnetic at all temperatures, but with a variety of canting angles. [57] $TbMn_6Sn_6$ is unique in this family for its out-of-plane spin alignment, which creates a gap in the Dirac crossings and generates nontrivial topology in the electronic band structure. [59] Nontrivial topology in the magnon band structure has also been proposed. [58] YMn_6Sn_6, where Y is a non-magnetic atom, expresses the competing exchange interactions between Mn kagome layers. The intralayer Mn-Mn interactions are strongly ferromagnetic but interactions between layers involve both FM and AntiFM components that lead to frustration. [60] The magnetic structure of YMn_6Sn_6 has Mn moments collinear in the kagome planes with an incommensurate spiral structure along the *c*-direction. This material is topologically nontrivial in both its electronic and magnon band structures. [56] Topological magnons are made possible by the DM interaction that opens a gap in the band structure. [61]

1.6 Honeycomb Lattice van der Waals Magnets

van der Waals (vdW) compounds are constructed of two-dimensional layers with internal covalent or ionic bonds, that are held together in the third dimension by the weak intermolecular van der Waals attraction. [62, 63] The weak interlayer bonds have drawn comparison to graphene which hosts nontrivial topology, but with the possibility of bringing topology to magnetic systems. One of the most studied vdW materials is CrI_3, which is comprised of stacked layers of Cr atoms arranged in honeycomb lattices, an example of which is shown in Fig. 1.16. As a monolayer, the Cr atoms order ferromagnetically. As a bilayer, the ordering is antiferromagentic. And for three

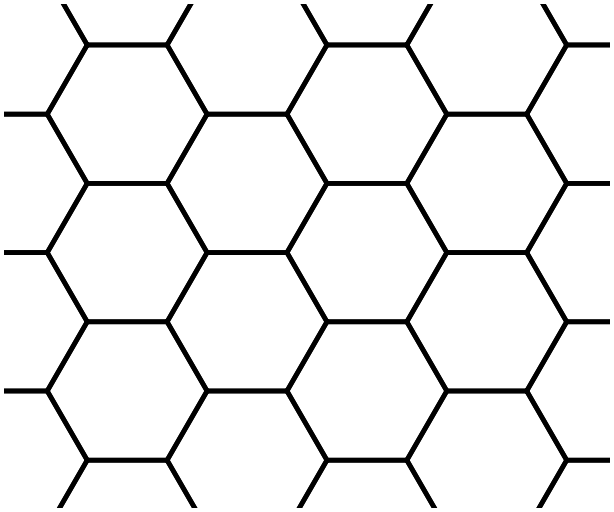

Figure 1.16 A hexagonal or honeycomb lattice.

layers and as a bulk material, it reverts back to FM order. [64, 65] The magnon bands in CrI_3 are gapped by the Dzyaloshinskii-Moriya interaction along next-nearest-neighbor bonds, which makes this material topologically nontrivial and leads to observations of the thermal Hall effect. [66, 67, 68, 69] Its relatives $CrBr_3$ and VI_3 are also a stacked honeycomb ferromagnets that are topologically nontrivial due to the DM interaction. [70, 71, 72, 73] However, VI_3 is unique in that its THE is driven by topological magnons at higher temperature and by magnon-phonon coupling at lower temperature. [74] In contrast, magnon-phonon coupling has not been observed in CrI_3.

1.7 Diamond

Diamond possesses unique properties that make it stand out as a material. Its large band gap (5.5 eV) translates to an ability to withstand high voltage without electrical failure and low leakage current that is essential for efficient power electronics. [75, 76] It has the highest thermal conductivity of any known material and high carrier mobility, specifically for holes. [77, 75] A rich menagerie of point defects and high optical transparency also make it a leading material for building qubits. [78]

The crystal structure of diamond consists of two interpenetrating face-centered cubic (FCC) lattices of carbon atoms, where each atom is tetrahedrally coordinated to four neighbors. The cubic unit cell has an edge length of 3.567 Å and belongs to the space group $Fd\bar{3}m$.

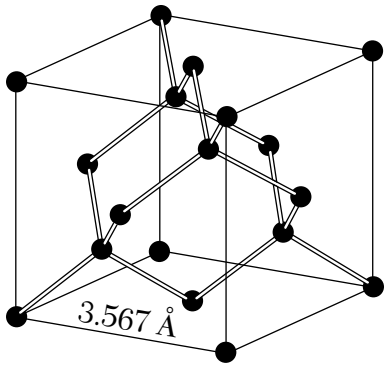

Figure 1.17 The unit cell of diamond.

1.7.1 Growing Diamond

Growing diamond is challenging primarily because it is metastable at atmospheric pressure. The phase diagram of carbon, displayed in Fig. 1.18, shows that graphite is the stable allotrope of carbon under typical crystal growth conditions. Fortunately, diamond can exist outside of high-pressure environments because the strong bonds between carbon atoms create a high energy barrier for the interconversion to graphite.

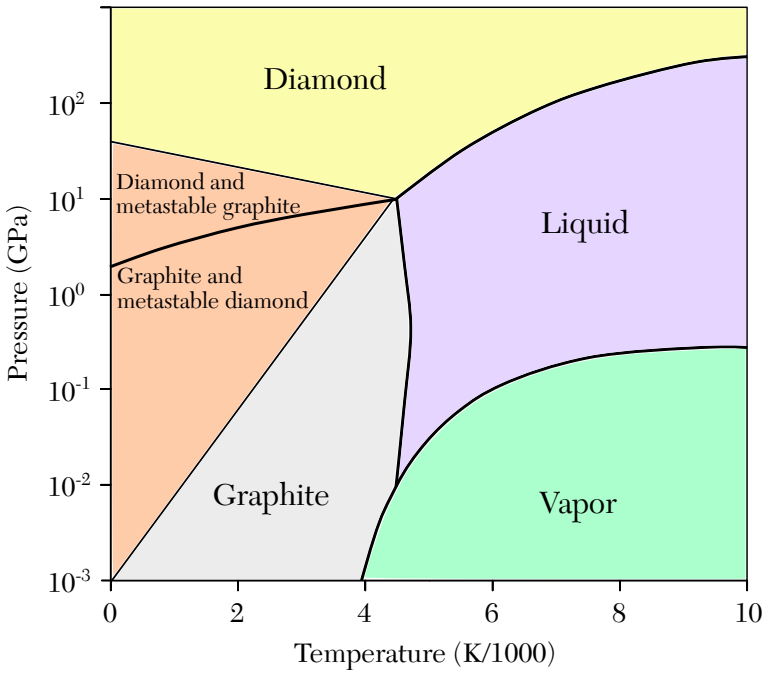

Figure 1.18 The phase diagram of carbon. [79]

High-pressure, high-temperature (HPHT) reactors convert graphite into diamond by mimicking the natural conditions of diamond formation deep within the earth. These reactors can quickly

produce large diamonds but have low control over impurity incorporation. Impurities are introduced by the metal catalysts needed to spur the reaction as well as the atmosphere which introduces nitrogen. In the standard convention of diamond classification by impurity content, HPHT diamonds are Type Ib, making them unsuitable for certain kinds of electronic applications. Table 1.1 describes the criteria for this classification and others, which were founded on spectroscopy measurements of natural diamonds. [80] Chemical vapor deposition (CVD) growth contrasts HPHT growth in its ability to dope diamonds more precisely with better control of impurities. This makes CVD grown diamonds a better choice for semiconductor applications where precise doping is needed. However the drawback of CVD is slow growth rate in a single direction, which makes CVD unable to produce large wafer-like substrates. CVD diamond is also prone to incorporating certain impurities such as Si and H. [81, 82, 83]

There are many kinds of CVD reactors, but they all manage to grow diamond at temperatures and pressures much lower than HPHT reactors by using a two-fold reaction mechanism. A plasma excites a carbon-containing gas in the presence of a diamond substrate to grow the crystal lattice atom by atom, while hydrogen etches off any graphite accumulation by disrupting the weaker graphitic sp^2 carbon-carbon bonds without significantly destroying the strong sp^3 carbon-carbon bonds of the diamond lattice. [84] Thus, CVD growth skirts the limits of thermodynamics that make diamond growth unfavorable.

Diamond Type	**Criteria**
Type Ia	Aggregated nitrogen impurities.
Type Ib	Single substitutional nitrogen impurities.
Type IIa	Nearly free of nitrogen impurities.
Type IIb	Contains boron impurities.

Table 1.1 Criteria defining the main diamond types. [80]

1.7.2 Substrate Orientation

CVD growth requires a substrate with a defined growth surface. The substrate orientation has effects on both rate and quality of the grown layer so the crystal plane is an important choice. The low-index planes (100), (110), and (111) are most often chosen. Figure 1.19 illustrates how the

unit cell is cut to expose these planes.

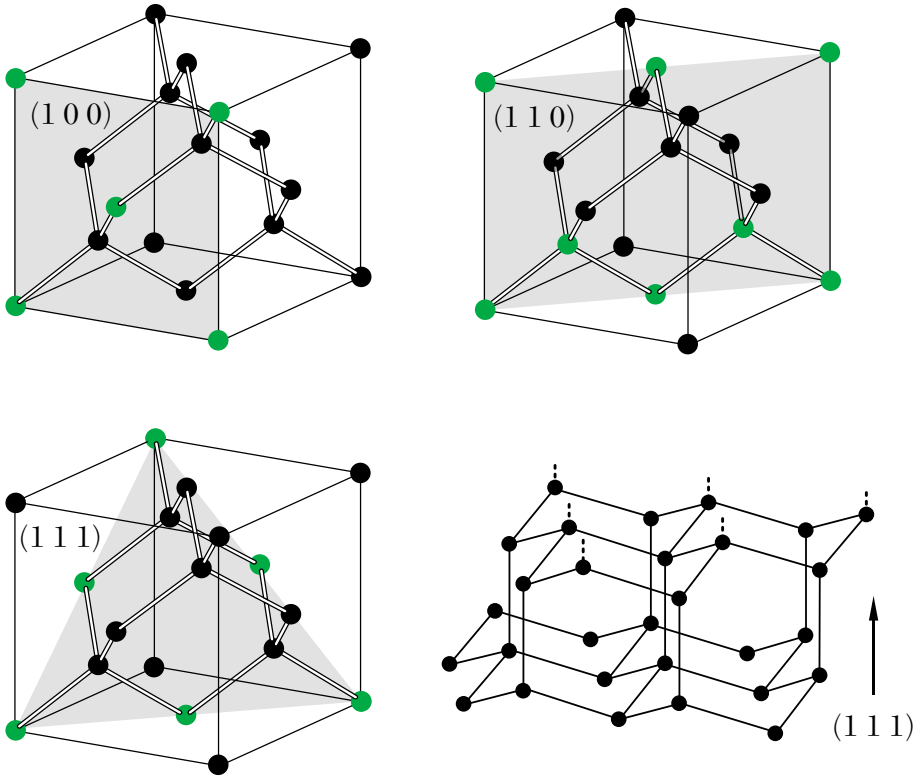

Figure 1.19 Cutting through the unit cell along a crystal plane reveals how to expose (a) the (1 0 0) plane, (b) the (1 1 0) plane, and (c) the (1 1 1) plane. In (d) the (1 1 1) plane is exposed on the top surface to show the bond geometry.

1.7.3 Crystal Defects

No crystal is a perfect lattice. Real crystals contain irregularities, called defects. A point defect can be a vacancy, an atom in the wrong spot in the lattice, or an atom of another element in the lattice, among others. The diamond NV center is an example of a point defect. [36]

A line defect can be identified by a chain of broken bonds. A missing half-plane of atoms will form an edge dislocation. A helical shift in the lattice will form a screw dislocation. [36]

Planar defects occur when bonds are mismatched along a plane. Stacking faults, for example, exists when the stacking pattern is disrupted either by omission or intrusion of a plane. Twinning can be considered a planar defect where the stacking pattern reverses. [36]

1.7.4 Diamond Defects

To understand the cause of growth defects, we must consider what happens on an atomic scale. We shall first assume that the surface of the diamond is perfectly smooth. When a carbon atom from the plasma approaches the surface, it will encounter a dangling bond and form a covalent bond. This reaction is energetically favorable, but the atom lacks the same stability it would have inside the lattice if it were surrounded by atoms on all sides. As a result, this atom is likely to be etched off the surface. However, if the atom attaches at a step, it will be more stabilized and less likely to get etched. As a result, lattice growth is much faster along steps and this mechanism is called step flow growth. [85, 86] In reality, the hydrogen plasma in a CVD reactor will terminate the dangling bonds with hydrogen atoms which must be displaced before a carbon can attach to the lattice. First principles calculations of the (100) surface suggest that hydrogen desorption is preferable at a step edge compared to a surface, further corroborating the step-flow growth model. [87] It is possible to use step flow growth to improve the rate of deposition by polishing the diamond surface with a greater angle to the lattice plane, called a miscut or offcut angle, so that more steps are available for growth.

A screw dislocation creates a step-like local environment. As growth progresses, the step is continuously grown over and rebuilt, and the dislocation axis extends parallel to the direction of growth. Though the screw dislocation may promote growth, the bonds along the axis are strained. In general, line defects can begin on the surface of the substrate, or they may form during growth and propagate as shown in Fig. 1.20(e).

Twinning is a common defect in diamond that results in a mirrored region of the lattice and it is especially common during growth on the (111) surface. This surface's faster growth rate tends to result in more defective growth because atoms have less time to move into the correct position and because the high bond symmetry allows for mirrored nucleation structures. Fig. 1.21 illustrates how twin formation begins on the atomic scale and it is easy to imagine how step-flow growth could result in a twinned layer separated by a grain boundary. In general, grain boundaries reduce the electrical and thermal transport properties of diamond, and are undesirable for electronic

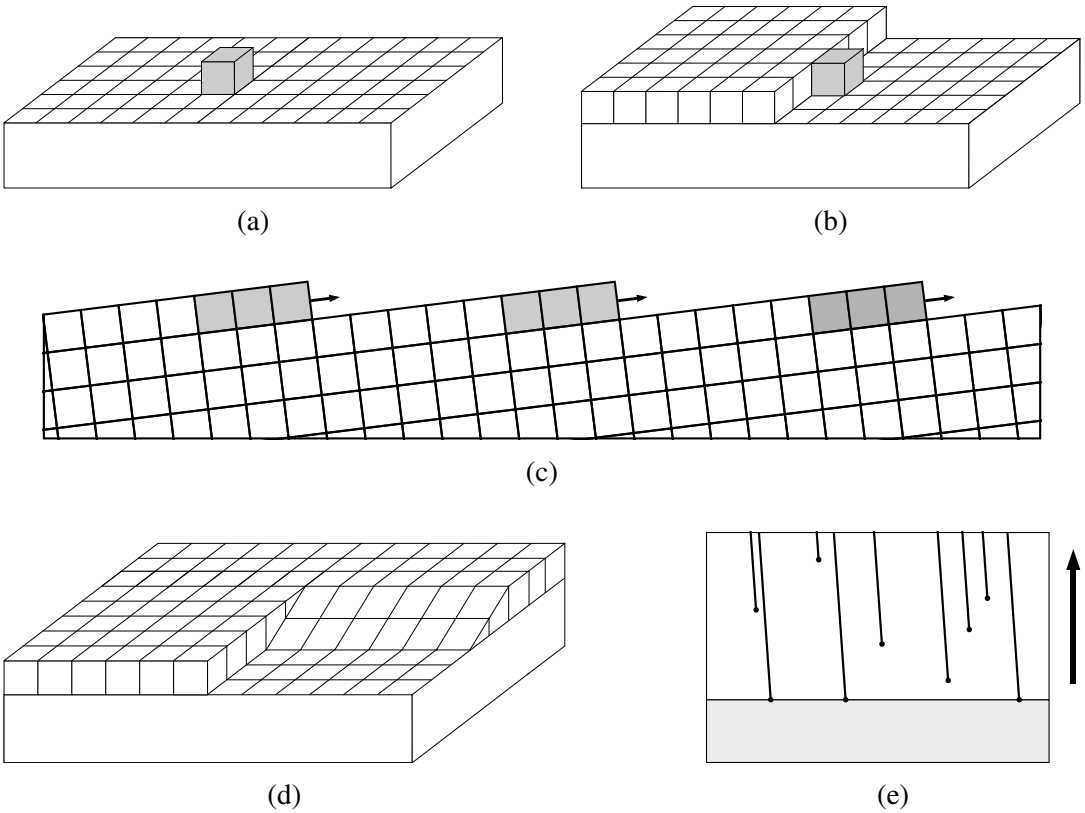

Figure 1.20 (a) A generalized unit of growth (shaded box, not a unit cell) has attached to the crystal surface. (b) The unit of growth is better stabilized when it attaches along a step. (c) When a series of steps are present, growth can occur in a step-flow mechanism. (d) The geometry of a screw dislocation offers a preferable location for attachment that extends though the lattice like a spiral staircase. (e) A cross-sectional view of a CVD-grown diamond. Screw dislocations and other line dislocations will originate on the substrate (shaded region) or nucleate during growth and follow the growth direction (upward). Some figures adapted from ref. [36]

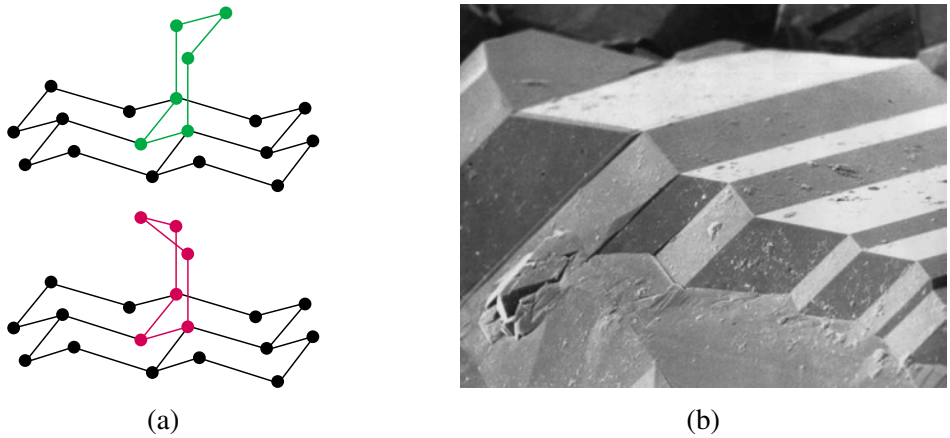

Figure 1.21 (a) Comparisons of diamond growth. The upper bond configuration will result in the correct stacking arrangement, while the lower configuration will result in a twin. (b) A diamond grain from a polycrystalline film showing a series of twins. [88]

applications.

Graphitic inclusion is the last defect to consider. Because the (111) surface is a corrugated hexagonal lattice, bond misalignment between adjacent layers can lead to flattening of the hexagonal lattice, as in the crystal structure of graphite.

1.7.5 Optical Properties

Optical studies of diamond can reveal information about electronic and structural properties. In the ultraviolet range, photons of wavelength 225 nm are energetic enough to excite an electron into the conduction band, making diamond strongly absorbing below the absorption edge of 225 nm. [89] In the infrared range, light absorption to phonon modes is possible, but only for certain symmetry conditions. The octahedral symmetry of the diamond bonds does not support an electric moment and one-phonon absorption is forbidden. Two- and three-phonon absorption is observed for wavenumbers between 1500 and 4000 cm^{-1}. [90, 91] However, the presence of impurities and defects can break symmetry locally, allowing one-phonon absorption to be observed for some samples. [92]

Intrinsic diamond is transparent in the visible range, which is key to the use of color centers as qubits.

1.7.6 Semiconductor Basics

For an intrinsic semiconductor, the number of carrier electrons is given by the number of states N and the Fermi-Dirac distribution function f.

$$n = \int_{E_C}^{\infty} N\left(E\right) f\left(E\right) dE \tag{1.68}$$

For practical temperature ranges, this can be approximated as follows

$$n = N_C \, e^{-\frac{E_C - E_F}{k_B T}} \tag{1.69}$$

where N_C is the effective density of states in the conduction band.

$$N_C = 2M_C \left(\frac{2\pi m_{dos} k_B T}{h^2}\right)^{\frac{3}{2}} \tag{1.70}$$

M_C is the number of equivalent minima in conduction band equal to 6 for diamond. m_{dos} is density-of-state effective mass of electrons, given by

$$m_{dos} = \left(m_l m_t^2\right)^{1/3} \tag{1.71}$$

where m_l and m_t are the longitudinal and transverse effective masses, respectively, which are determined empirically.

When an electron donor is doped into the semiconductor, the ratio of neutral donors N_{D^0} and ionized donors N_{D^+} follows a similar form to Eq. 1.69

$$\frac{N_{D^0}}{N_{D^+}} = g_D \, e^{-\frac{E_C - E_F}{k_B T}} \tag{1.72}$$

but here g_D is the donor level degeneracy, equal to 2 for diamond. Combining Eqs. 1.69 and 1.72, and defining the donor level E_D below the bottom of the conduction band, we can obtain the equation

$$\frac{N_{D^0}}{n N_{D^+}} = \frac{g_D}{N_C} \, e^{-\frac{E_D}{k_B T}}. \tag{1.73}$$

The neutral donor number can be eliminated by substitution.

$$N_{D^0} = N_D - N_{D^+} \tag{1.74}$$

For a slightly compensated n-type semiconductor, charge neutrality requires that

$$p + N_{D^+} = n + N_{A^-} = n + N_A - N_{A^0} \tag{1.75}$$

but holes and neutral acceptors are vastly outnumbered by electrons and donors so we can approximate that

$$N_{D^+} \approx n + N_A. \tag{1.76}$$

Therefore, we obtain the useful equation of carriers, donors, and acceptors for a slightly compensated n-type semiconductor. [93, 94]

$$\frac{n\,(n + N_A)}{N_D - N_A - n} = \frac{N_C}{g_D} e^{-\frac{E_D}{k_B T}} \tag{1.77}$$

It is useful to define a compensation ratio η

$$\eta = \frac{N_A}{N_D} \tag{1.78}$$

and an active donor ratio r_D

$$r_D = \frac{N_D - N_A}{[\mathrm{P}]} \tag{1.79}$$

where [P] it the density of all P atoms in the diamond lattice. The incorporation ratio r_{inc} provides a way to gauge how effectively phosphorus enters the lattice by comparing its concentration in the diamond to the input gases.

$$r_{inc} = \frac{[\mathrm{P}]_{latt}/[\mathrm{C}]_{latt}}{[\mathrm{PH_3}]_{gas}/[\mathrm{CH_4}]_{gas}} \tag{1.80}$$

1.7.7 Doping Diamond

Though diamond's large band gap is advantageous for high-power electronics, it results in insulating behavior at room temperature. If diamond is to be made into a semiconductor, it must be doped. Achieving *p*-type conductivity has been successful using boron, whose addition into the lattice creates an acceptor level approximately 0.37 eV above the valence band. Boron atoms are of similar size to carbon atoms, so their incorporation into the lattice is favorable and CVD growth of B-doped diamond (BDD) is well understood. Boron doping can achieve concentrations of 10^{12} to 10^{22} atoms/cm^3, [31, 32] and acceptor compensation as low as 0.4%. [95] High incorporation efficiency can be achieved under similar growth conditions for all substrate orientations, reaching up to 1000% for some reported samples. [96] Hole mobility has been reported up to 2200 cm^2/V·s at room temperature with a maximum of 3370 cm^2/V·s. [97, 98] BDD can be metallic and superconducting. [33, 34, 35] Boron is also easily added to CVD growth though several precursors, with the most common being diborane. There is no doubt that boron is an excellent choice for *p*-type semiconducting diamond.

Achieving *n*-type diamond has been much more difficult. The most logical choice of dopant is nitrogen due to its similar atomic radius to carbon. Indeed, nitrogen adsorption onto the growth surface is energetically favorable and the atom readily incorporates into the lattice during CVD growth [99] but its deep donor level of 1.7 eV effectively renders N-doped diamond an insulator

at room temperature. [100] The Pauli exclusion principle creates a repulsion between nitrogen's lone pair and the dangling bond of a neighboring carbon atom which pushes the two atoms apart and breaks the local bond symmetry. [101, 102] The donor electron is extremely localized because its wavefunction has significant antibonding character and its entry into the lattice is suppressed. [103, 99]

Currently the most promising donor element is phosphorus. Though still relatively deep, phosphorus's donor level of 0.6 eV is a significant improvement over nitrogen [104]. Like nitrogen, phosphorus breaks the local symmetry and this contributes 10% of the donor depth. [105, 106] The most widely accepted bond configuration corresponds to the point group C_{3v} [107, 108, 109, 110, 111] although a D_{2d} symmetry has been proposed as well and there may be a transition to this symmetry at low temperature. [112, 105] The electronic structure of substitutional phosphorus has also been studied. [113, 114, 115, 60]

In contrast to boron and nitrogen, phosphorus has a large atomic radius and its incorporation into the diamond lattice is reduced. As a result, progress on *n*-type diamond still lags behind *p*-type.

The earliest reported phosphorus-doped diamonds (PDD) grown by CVD were polycrystalline samples grown using one of diphosphorus pentaoxide (P_2O_5) or trimethyl phosphite ($P(CH_3O)_3$) precursors. [116, 117] When phosphine (PH_3) was used, it was estimated that P incorporates 3000 times less readily than B incorporates from diborane (B_2H_6). [118]

Koizumi *et al.* reported the first SCD samples with confirmed *n*-type conductivity. [119] They achieved successful growth with higher temperature and lower methane concentration than previous attempts and characterized their sample with Hall effect measurements. Their growth conditions only worked with (111)-oriented substrates and failed to incorporate phosphorus when (100)-oriented substrates were used. Their sample had a phosphorus concentration of 2.5×10^{19} cm^{-3}, an activation energy of 0.43 eV, and low mobility of only 23 $cm^2/V{\cdot}s$. At the time, they believed that the low mobility was due to silicon contamination from within their reactor and later growths on a metal-chamber type reactor did result in an improvement of the mobility to 240 $cm^2/V{\cdot}s$ and revised the activation energy to 0.6 eV. [120] However, their first study marked the

beginning of a continuously growing field of research into PDD.

Early *ab initio* calculations had predicted a phosphorus donor level ranging from 0.2 eV [121] up to as much as 1.09 eV [122] but the currently accepted value has settled on 0.6 eV, with some variation downwards due to compensating impurities. [123] For some time, only growth on (111) substrates proved to be successful, and currently the highest reported values of phosphorus incorporation ($\sim 10^{20}$ cm^{-3}) have been achieved on (111) substrates. [124, 125, 126] Growth of (100) diamonds is typically preferred for electronic applications because this surface is easier to polish mechanically with low surface roughness, and it has better metal/diamond junction properties. [127, 128] Early PDD growths on (1 0 0) substrates required higher methane and phosphine gas flow and initially suffered from very low incorporation efficiency (100 times lower than (111) growth) and donor compensation as high as 90%. [129, 130] However, advancements in growth on (100) surfaces allow for reasonably high doping concentrations up to $\sim 10^{19}$ cm^{-3} [131, 132] but compensation is still high in these samples, the lowest reported donor compensation value being 30% [31], compared to (111) samples which can have even smaller compensation ratios with the lowest being 5.5%. [133, 134, 135] PDD growth on (110) and (113) surfaces has also been successfully demonstrated, with P concentrations reaching 10^{16} cm^{-3} and 10^{19} cm^{-3}, respectively. [136, 137, 138] Curiously, growth on the (110) surface was reported to proceed at a very high rate of 33 μm/hr. [136] So far, the highest mobilities have been achieved on lightly-doped (100) samples, equal to 1060 cm^2/V·s at room temperature, with a maximum of 1500 cm^2/V·s [31], although this is primarily a consequence of low doping concentration since incorporated P increases electron scattering. The highest active donor fraction is observed in (111) samples, which can reach upwards of 80% [133, 139], although (100) samples have been reported with values not far lower. [140, 31]

Despite nearly 30 years of progress since the growth of the first single-crystal samples, phosphorus doping still lags behind boron doping in achieving lower doping concentrations, higher compensation, and unequal quality among the different surface orientations. While atomic radius is the major difference between P and B and N, to understand PDD more deeply, it is necessary to consider the dynamics of growth beyond numerical properties.

When it comes to understanding P incorporation, the journey from plasma to lattice must be considered step by step. The first step is adsorption of a phosphorus radical onto the growth surface. This occurs because the radical reduces its energy and becomes stabilized upon adsorption. However, *ab initio* calculations suggest that this stabilization is reduced for larger elements. [99] The stabilization energy is smaller for phosphorus than nitrogen, which introduces one factor that contributes to reduced phosphorus incorporation. Moreover, the calculations also show that the stabilization energy on the (111) surface is greater than for the (100) surface, partly explaining the disparity in growth success of these two substrate orientations. [99]

Next, when phosphorus adsorbs onto the surface of the diamond there is no guarantee that it will enter the lattice. Phosphorus has a surface adsorption time of approximately 0.4 s, which is several times shorter than boron (equal to 2.1 s). [131] To maximize the number of incorporated phosphorus atoms, it may be best to increase the growth rate, which could be done by growing on substrates with a large offcut angle (the density of step edges is high) or by growing at hotter temperature and higher pressure. However, while adsorbed onto the substrate surface, P has a long average migration distance, eight times longer than adsorbed carbon. [141] This suggests that it is possible to give P an advantage over C by spreading out the step edges, i.e., by growing on surfaces with a low offcut angle. It is not immediately clear which of these factors is more consequential.

Once a P atom is incorporated into the diamond lattice, its large size creates strain among the surrounding environment. While the atom is still in the subsurface, the region of the lattice near the surface, the tendency for the atoms to reduce strain will lead to P getting pushed back onto the surface of the diamond, thereby thwarting P incorporation. *Ab inito* calculations reveal that the energetic cost of this local strain is 2.6 eV for (1 1 1) substrates, and 4 eV for (1 0 0) substrates. [142] This further contributes to P incorporation on (1 1 1) surfaces being more successful. To reduce the effect of this strain expulsion tendency, it is necessary to outcompete it by growing faster than the velocity of P migration back to the surface. Once the atoms are deep in the bulk, they become stabilized. Fast growth may be achieved by a larger offcut angle (more step edges) or higher pressure (more radicals in the plasma), although it is not a straightforward matter.

Increasing the number of phosphorus atoms is important, but arguably it is more important to prevent them from becoming compensated. A theoretical study calculated electron concentration at 300 K over a range of compensation ratios and found that above $\eta = 10^{-4}$ it is insensitive to N_D, meaning there is practically no benefit to a higher donor concentration if compensation also remains large. [143] Currently, no published study has reported compensation of less than 5%.

Naturally, it is important to avoid contamination by elements from the environment such as boron, but with good sample and reactor hygiene they are not major concerns. Nitrogen should also be avoided since, although it is a donor atom, its incorporation tends to result in some number of NV centers which can act as acceptors. The presence of hydrogen is unavoidable but it has been shown that hydrogen can passivate P. [144] CVD diamond tends to have a large concentration of incorporated hydrogen [131, 125, 136], yet it does not completely kill the donor activity. The reality is that most of the incorporated hydrogen is likely segregated along dislocations and grain boundaries where there are many dangling bonds. [145, 146] Since hydrogen promotes diamond growth by etching defective growth, it is suggested that hydrogen-rich growth conditions will reduce P passivation by hydrogen. [83] Hydrogen has also been seen to cluster in and around non-epitaxial crystallites. [146] It has been observed that increased lateral growth which can result from a larger offcut angle (more step edges) suppresses growth of hillocks by covering nucleation points before a hillock can grow. [147] This provides another strategy for reducing H incorporation.

Paradoxically, the most potent compensator may involve phosphorus itself. The formation of a phosphorus-vacancy (PV) complex creates a twofold problem. In this complex, P is stabilized by splitting the vacancy in half which reduces some of the strain associated with its large size. Then it has the option of bonding with six neighboring carbon atoms. Since P is pentavalent, forming the sixth bond requires an electron from a donor P atom. In this process, two P atoms are eliminated as donors making the PV complex extremely undesirable. [128, 148]

With all these considerations, diamond growers have tried to understand the pitfalls of PDD growth though experimental analysis as well. If P is incorporated into the lattice but not electrically active, it may not be in substitutional positions. Interstitial phosphorus appears to be extremely

unlikely due to its large atomic size and associated energy of formation of 22 eV. [149] An experimental study placed an upper bound of 10% P atoms being in interstitial positions. [150] However, in defective diamond, phosphorus may become trapped in defects that reduce its availability as a donor. Pinault-Theury *et al.* found that for (100) substrates, phosphorus incorporation was improved by a large offcut and rough surface that supported a macrostep morphology, shown in Fig. 1.22. The macrostep has a terrace and riser geometry, where the riser is a high-index plane with a tendency to grow much faster than the low-index (100) plane, and the phosphorus was most effectively incorporated into the riser rather than the terrace. [151, 152, 153] However, their samples were fully compensated due to defect formation which was also increased by the growth morphology. [154] Later they found nearly 100% donor activity when they grew on surfaces with low roughness. [155] This sample was a (100)-oriented diamond, and as discussed above, growth tends to be more defective on (111) surfaces than (100) surfaces. Although low roughness leading to higher P incorporation was corroborated on (111)-oriented samples as well. [156]

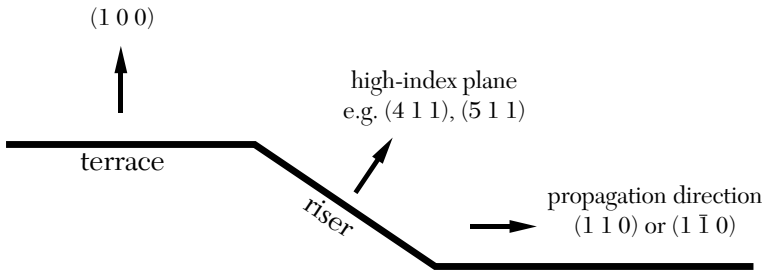

Figure 1.22 Geometry of the macrostep morphology observed by [151, 152].

Katagiri *et al.* grew lightly doped diamond samples with measurable electrical activity when the phosphorus concentration was as low as 7×10^{16} cm^{-3}. [133] But when the phosphorus concentration was below 10^{16} cm^{-3}, the donors were fully compensated indicating that their diamonds had a background of compensating defects on the order of 10^{15} cm^{-3}. It may be the case the phosphorus itself introduces or requires compensating defects since faulty growth can allow for the reduction of stress that comes from phosphorus's large atomic radius. [157] Indeed, it was noticed early on that high P concentration corresponds to poor crystal quality. [104] Kato *et al.* found in one growth series that the compensation ratio was constant regardless of P concentration

and concluded that P doping introduces acceptors. [130] In further studies, Kato *et al.* attempted to pinpoint the identity of these compensators by fabricating diamond diodes to determine the energies of the acceptor states. [158, 159, 160] Unfortunately, the energy they calculated did not convincingly correspond to a known defect, but they suspected that hydrogen complexes or carbon vacancies could be responsible.

Hydrogen has been called an "electron killer" and CVD diamonds are typically rich in hydrogen, sometimes containing more hydrogen atoms than phosphorus. [125, 131, 144, 159] Yet high hydrogen content is not enough to completely kill donor activity. This is likely because hydrogen clusters in non-epitaxial crystallites and places with high concentrations of dangling bonds such as grain boundaries. [145, 146] It has also been predicted that hydrogen complexes such as the H-P complex can passivate donors. [128, 161] With this in mind, diamond growers have considered ways of reducing hydrogen incorporation.

A study of intrinsic diamond growths on (1 1 1)-oriented substrates by Sakaguchi *et al.* revealed some patterns in H incorporation. [83] They found that more H is incorporated under higher temperatures and lower microwave power, and increased pressure reduces H incorporation up to a point where no more change occurs. The most important conclusion they came to was that a H-rich plasma actually results in abstraction of H from the growth surface and reduced H incorporation into the lattice. They saw that high power produces more H radicals that also lead to surface abstraction of H. Their observations were in agreement with Goodwin's law, which roughly describes the relation between defect concentration X (in this case hydrogen), growth rate G, and atomic H concentration. [162, 163, 164]

$$X \propto \frac{G}{[H]^n} \tag{1.81}$$

It was later realized that at high pressure, H radicals increase faster than CH_3 radicals. [165, 166] Therefore, high pressure may promote less defective growth. High pressure can also increase growth rate and plasma discharge power density. [167] Even if the discharge core is small compared to the substrate area, a high density of reactive radicals extends beyond it so that temperature and growth rate remain uniform across the substrate. [168, 169]

Increasing methane content increases growth rate as well [170, 171], but high methane content results in more defects and soot formation can occur. [172]

When it comes to phosphorus doping, the source of the phosphorus precursor was also considered. PH_3 has been the most typical choice because it is readily available due its usefulness in the semiconductor industry. However, PH_3 has three P-H bonds. Organophosphorus precursors such as *tert*-butylphosphine ($H_2P(C(CH_3)_3)$) and trimethylphosphine ($P(CH_3)_3$) instead have one or three P-C bonds, respectively. They are also less toxic and liquids at room temperature which makes them safer, though more challenging to use for CVD growth. [134] Perhaps these organophosphorus compounds could reduce compensation by H. Unfortunately, CVD growth using these precursors did not materialize any significant improvement. All three P precursors become fully radicalized at the high temperature of the plasma. [123, 126, 128, 135, 173] There is likely no affect on the P atom as it incorporates into the lattice, whichever precursor is used.

In summary, incorporating phosphorus while reducing compensation involves several factors that have contrary effects. Phosphorus has a short desorption time on the growth surface which implies that a larger offcut angle (more step edges where P is likeliest to enter the lattice) is preferable. But its longer migration length compared to carbon implies that high incorporation will be achieved with a smaller offcut (fewer step edges). The effect of strain pushing P out of the subsurface means that a high growth rate is necessary, especially with (1 0 0) substrates, which could be achieved with higher pressure. However, fast growth may promote defect formation since atoms have less time to find the correct lattice positions. A hydrogen rich plasma may be beneficial in reducing defects because it etches them away, which would be a benefit since defects reduce mobility by scattering electrons. This could also possibly reduce PV complexes which are doubly compensating. Also, a hydrogen rich plasma could reduce hydrogen incorporation which is desirable since it can also compensate P. If defects are a major concern, (111)-oriented substrates should be avoided for being prone to defective growth (such as twin formation). Yet, the effect of strain pushing P out of the lattice is reduced for (111) surfaces and P incorporation is highest for this surface. However, P incorporation itself seems to benefit from defective growth in order to

reduce the strain associated with phosphorus's large atomic radius.

With all this to consider, the path to producing high quality single-crystal PDD samples is not straightforward. The diamond grower must consider a wide variety of factors which work in competing ways to influence the dynamics of growth and shape the final product.

1.7.8 Ohmic Contacts

To accurately measure the electronic properties a semiconductor, it is necessary to form ohmic contacts on the surface, which have a low specific resistance and a linear current-voltage relationship. The presence of a Schottky barrier at the metal-semiconductor interface prevents charge from flowing continuously, but charge can cross the barrier by two primary methods. Thermionic emission is the process of charge flow by carriers with enough thermal energy to overcome the energy barrier. Field emission is the process of charge flow by tunneling. [93] A hybrid process can also occur when the width of the barrier is not uniform. Thermionic field emission occurs when thermal energy facilitates tunneling. [174]

Methods of forming ohmic contacts on a P-doped diamond surface are limited because the Schottky barrier height is pinned at 4 eV due to diamond's large band gap. This is largely independent of the choice of metal, including metals with low work functions. Using a carbide-forming metal such as Ti will also form rectifying contacts. [175] Forming defects at the metal-diamond interface by ion-beam irradiation can successfully create ohmic contacts, but introduces damages to the lattice. [176] The best way of forming ohmic contacts on PDD is to create a heavily doped region that will allow for a tunneling current, and to choose metals with low resistivities. [177, 174] Successful transport measurements on PDD have been reported using a heavily doped layer with a P concentration of at least 10^{20} cm^{-3} and a thickness of at least 400 nm. [31]

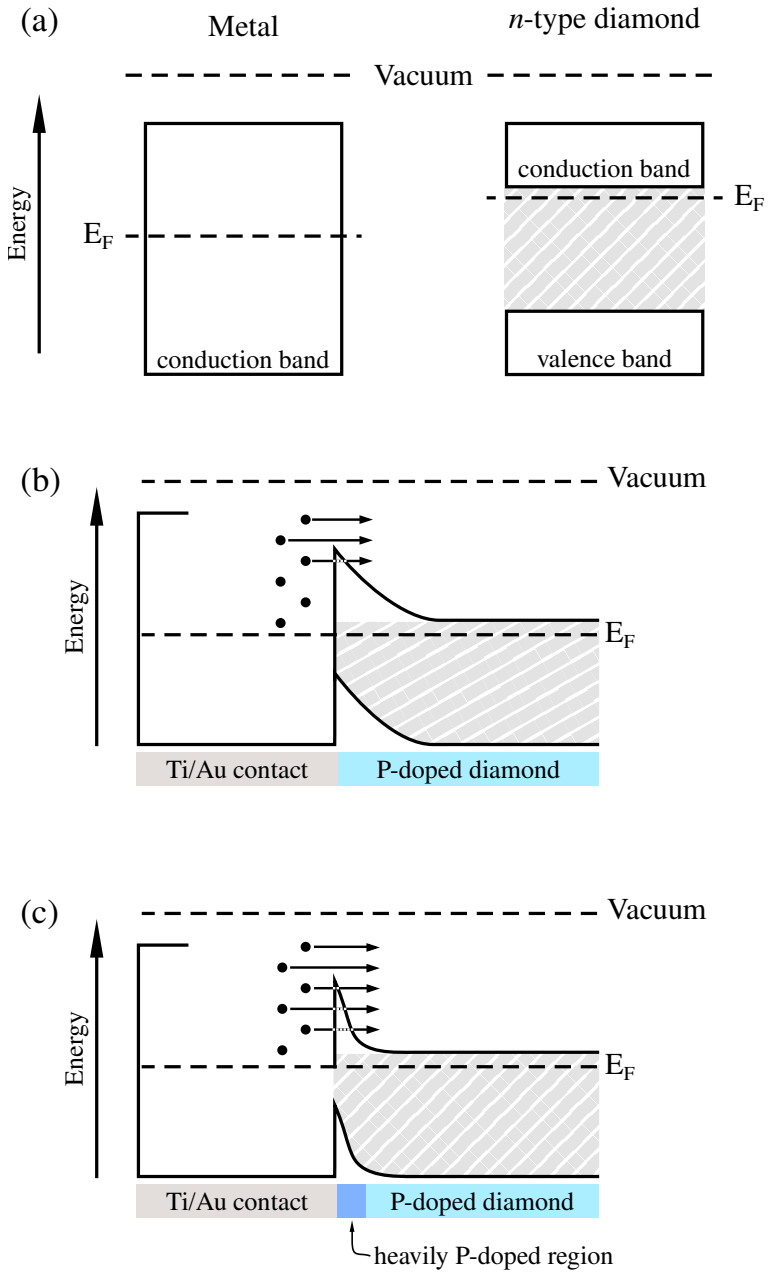

Figure 1.23 (a) A metal and *n*-type diamond have different energy band structures when isolated. (b) Depositing metal contacts onto the diamond surface creates a Schottky barrier that prevents electron transport. Only electrons with high thermal energy can cross the interface. (c) A layer of heavily P-doped diamond does not change the energy to overcome the barrier but changes the width of the barrier to allow low-energy electrons to tunnel through.

CHAPTER 2

METHODS

2.1 Transport Measurements

2.1.1 The Electrical Hall Effect

Electrical Hall effect measurements were carried out using two separate methods on different instruments, depending on the material. The Hall bar method was used to study topological metals and the van der Pauw configuration was used to study P-doped diamond.

2.1.1.1 The Hall Bar Method

Hall effect measurements of metallic samples were carried out on a commercial Physical Property Measurement System (PPMS) from Quantum Design, with some additions which have been described elsewhere. [178] The samples were cut and polished into thin prisms and mounted to a measurement puck in thermal contact with the PPMS chamber. The electrical contacts were made by connecting the sample to the puck with gold wires and silver paste. Each Hall bar was formed with the crystal *ab*-plane (i.e., the Kagome lattice plane) parallel to the puck surface and perpendicular to the applied magnetic fields. The correct orientation is clear from the crystal habit, as shown in Fig. 2.1.

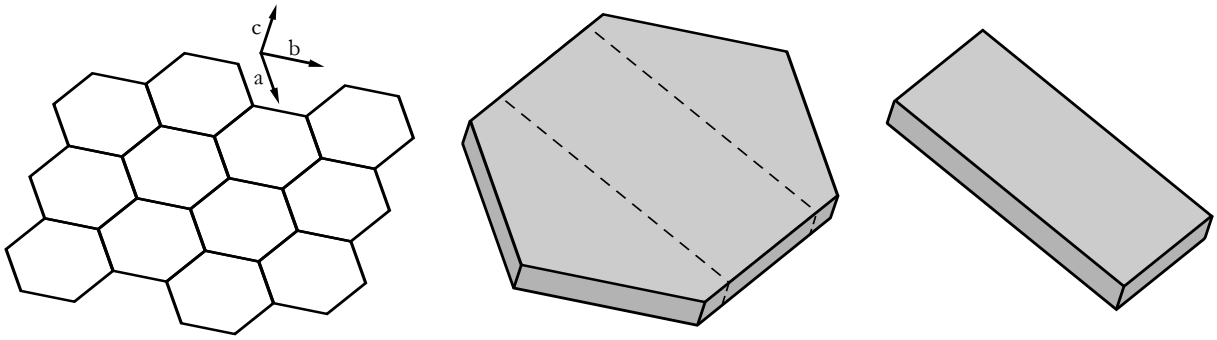

Figure 2.1 Preparing the Hall bar. The lattice symmetry has a distinct effect on the habit of the macroscopic crystal and it is clear which orientation of the sample corresponds to the *ab*-plane. The Hall bar is formed by cutting or grinding away the excess material.

The contact configuration to measure voltages V_1, V_2, and V_3 and their separation l and w is shown in Fig. 2.2 following a specific sign convention. I is the applied current and t is the sample

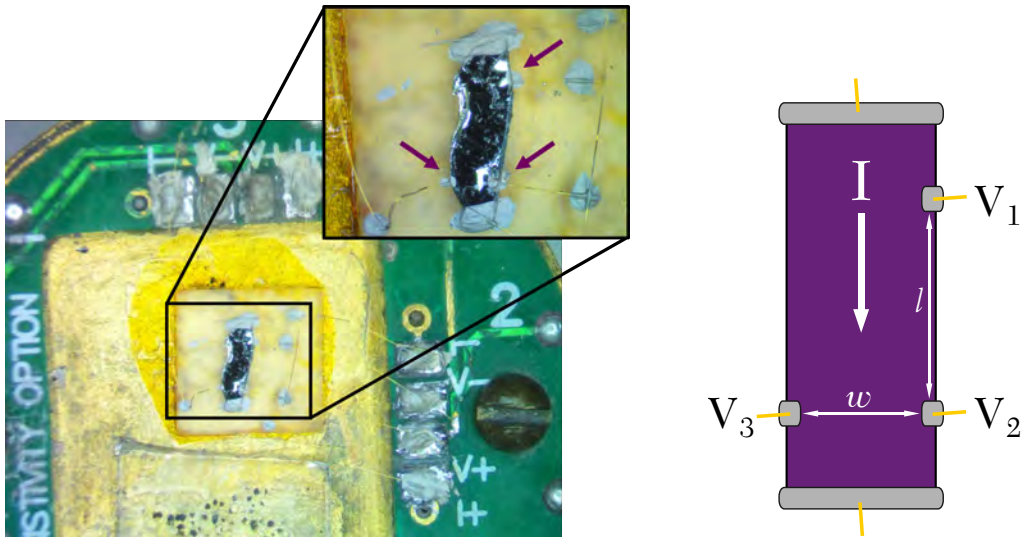

(a) (b)

Figure 2.2 Mounting the Hall bar to the measurement puck with the electrical connections. (a) A sample mounted onto the measurement puck. (b) Contact placement.

thickness. We make the following definitions for the longitudinal and Hall resistivities.

$$\Delta V_x = V_2 - V_1 \tag{2.1}$$

The longitudinal resistance is

$$R_{xx} = \frac{\Delta V_x}{I} \tag{2.2}$$

and the longitudinal resistivity is

$$\rho_{xx} = R_{xx}\frac{wt}{l} = \rho_{yy} \tag{2.3}$$

which is assumed to be even and isotropic in the plane.

$$\Delta V_y = V_2 - V_3 \tag{2.4}$$

The transverse resistance is

$$R_{xy} = \frac{\Delta V_y}{I} \tag{2.5}$$

and the transverse resistivity is

$$\rho_{xy} = \frac{R_{xy}}{t} = -\rho_{yx} \tag{2.6}$$

which must both be odd under parity because the resistivity tensor is antisymmetric. We can use these properties to account for small misalignment in the contact placement when we analyze the

data.

$$f_{\text{even}}(B) = \frac{1}{2}\left[f\left(B\right) + f\left(-B\right)\right] \tag{2.7}$$

$$f_{\text{odd}}(B) = \frac{1}{2}\left[f\left(B\right) - f\left(-B\right)\right] \tag{2.8}$$

However this is complicated by hysteresis. To correctly retrieve the transverse component, we must sweep the field in both directions and symmetrize the data of each sweep with respect to its counterpart.

$$f^{+\rightarrow-}_{\text{antisym}}(B) = \frac{1}{2}\left[f^{+\rightarrow-}\left(B\right) - f^{-\rightarrow+}\left(-B\right)\right] \tag{2.9}$$

$$f^{-\rightarrow+}_{\text{antisym}}(B) = \frac{1}{2}\left[f^{-\rightarrow+}\left(B\right) - f^{+\rightarrow-}\left(-B\right)\right] \tag{2.10}$$

For example, $f^{+\rightarrow-}\left(B\right)$ could be ρ_{xy} from positive to negative B-field, and $f^{-\rightarrow+}\left(B\right)$ could be ρ_{xy} from negative to positive B-field. This data processing step is absolutely necessary to reliably retrieve the transverse component, which is much weaker than the longitudinal component. A relatively small presence of the longitudinal component can obscure the transverse signal. The final step necessary to retrieve the anomalous component ρ^{A}_{xy} is to fit a smooth portion of the curve to a line and subtract the linear term.

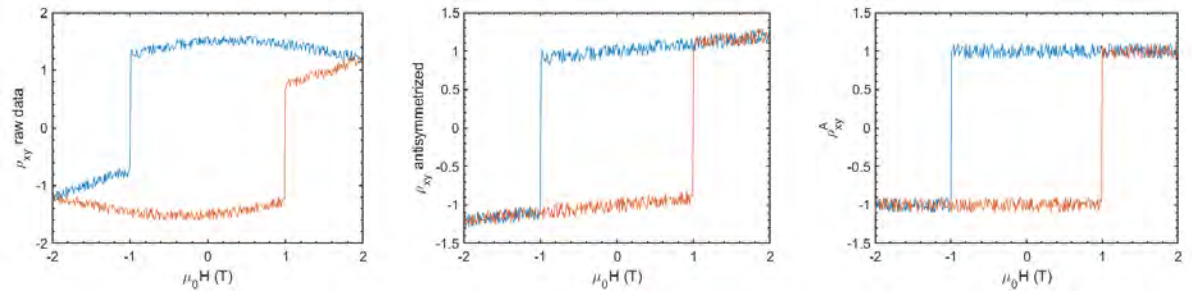

(a) (b) (c)

Figure 2.3 The process of antisymmetrizing data with hysteresis. The $+ \rightarrow -$ sweep is in blue and the $- \rightarrow +$ is in orange. (a) This plot shows a contribution from the longitudinal resistivity due to misalignment of the contacts. (b) In this plot, the odd part has been isolated. (c) The anomalous resistivity can be calculated by subtracting the linear components of the curves.

2.1.2 The van der Pauw Method

For diamond samples, the van der Pauw configuration was used to measure the Hall effect. Preparing a sample for this measurement involves a lengthy process.

First SiO_2 is deposited onto the diamond to a thickness of 6 μm. Using a plasma-enhanced chemical vapor deposition system (PECVD) with the sample stage set to 300°C, the deposition occurs over 80 minutes with 710 sccm of N_2O and 170 sscm of 5% SiH_4 in N_2 feed gasses at 1 torr pressure and 20 W input power.

Then the sample is attached to the edge of a plastic disk (such as a petri dish lid) using double-sided tape. Two Si wafers of similar thickness are placed along opposite sides of the diamond as shown in Fig. 2.4. S1813 photoresist is spread over the diamond with a very narrow pipette tip. The plastic disk is spun in a spin-coater at 6000 rpm for 60 seconds. The diamond is baked at 115°C for 60 seconds and exposed with the inverse van der Pauw pattern under a mercury short arc lamp with peak intensity at 365 nm for 90 seconds on a Karl Suss MJB3 mask aligner. The photoresist is then dipped in Microposit MF-319 developer solution for 60 seconds, washed with deionized water, air dried, and baked again at 115°C for 60 seconds. The sample is dipped in a buffered HF solution [179] for 15 minutes, which is enough to etch the SiO_2 completely in the four contact areas. Then, the sample is annealed in a furnace at 900°C for four hours.

The annealed SiO_2 can withstand the conditions of diamond growth for at least 15 minutes, which is enough to grow about 0.5 μm of diamond in the reactor under the conditions listed in Table 2.1.

Next the sample is dipped in the buffered HF for at least an hour to completed etch the annealed SiO_2. To eliminate the possibility that diamond from the second growth step has formed a ring around the edge of the original substrate, a laser is used to cut off a very small margin from each edge, followed by an acid clean procedure described in Section 2.8 to remove any graphite that may form along the cuts.

The spin-coating and exposure are repeated as before but without the second baking step. Ti/Au contacts are deposited with thickness of 30 nm and 70 nm, repectively, using an Edwards Auto 306 Turbo thermal evaporator. The sample is dipped in Microposit Remover 1165 for at least 24 hours before the excess metals can be lifted off with very short sonication. This long lift-off process is needed because the sample gets hot in the thermal evaporator and the photoresist becomes very

polymerized.

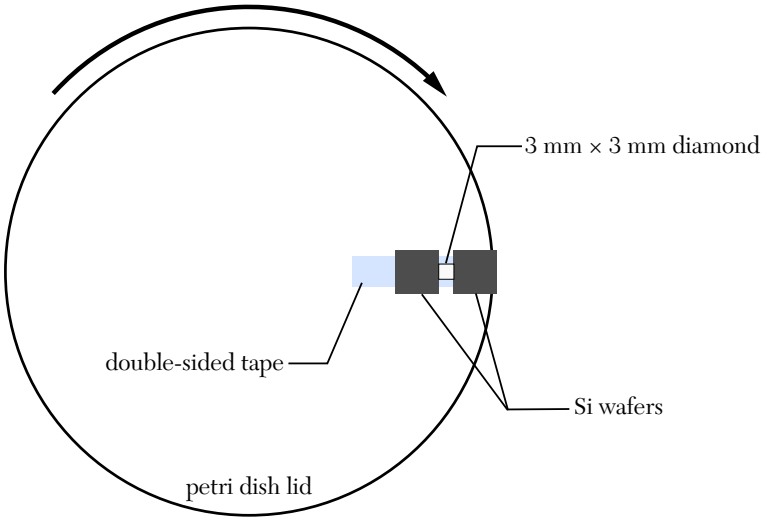

Figure 2.4 Mounting the diamond on a 90 mm (3.5 inch) diameter petri dish lid for spin-coating. The diamond is placed approximately 40 mm away from the center. (Figure not to scale.)

Pressure	240 torr
MW Power	2050 ± 50 W
Temperature	980°C
[H_2]	280 sccm
[CH_4]	12 sccm
[PH_3]	56 sccm
Time	15 min

Table 2.1 Growth conditions for the selectively grown regions. The PH_3 is diluted to 0.1% in hydrogen.

The sample is mounted to an electrically insulated stage and electrical connections were made to the Ti/Au pads using gold wire and silver paste. Hall effect measurements were taken up to 700 K on a homemade apparatus described in detail elsewhere. [180] The measurement begins at 700 K and proceeds to lower temperatures in order to anneal the contacts, forming the TiC interface, and reduce the contact resistivity.

2.1.3 Thermal Hall Effect

The thermal Hall effect (also known as the Righi–Leduc effect) is the heat analog of the electrical Hall effect and the experimental setup reflects this. A sample must be shaped into a thin prism and mounted onto a puck at only one end to ensure thermal isolation. Again, the Hall bar is formed

with the crystal *ab*-plane perpendicular to the direction of the field. A small 1 kΩ resistor which will act as a heater is connected with a very short gold wire (a lower gauge is preferred for better heat transfer) and silver paste. Three Cernox thermometers (commercially available from Lake Shore Cryotronics) are attached in the same confirmation as the electrical Hall measurement, also with gold wire and silver paste. The Cernoxes are electrically connected to the PPMS measurement puck with manganin wire, which is a very poor thermal conductor, to encourage as much thermal energy as possible to pass through the crystal. The sample preparation is shown in Fig. 2.5. The placement of contacts to measure temperatures T_1, T_2, and T_3 and their separation l and w are defined in Fig. 2.5(b) following a specific sign convention. J_Q is the applied thermal current and t is the sample thickness.

The longitudinal and transverse thermal conductivities are defined as follows.

$$\Delta T_x = T_2 - T_1 \tag{2.11}$$

$$W_{xx} = \frac{\Delta T_x w t}{I_Q l} = W_{yy} \tag{2.12}$$

$$\Delta T_y = T_2 - T_3 \tag{2.13}$$

$$W_{xy} = \frac{\Delta T_y}{I_Q t} = -W_{yx} \tag{2.14}$$

The longitudinal thermal resistivity is

$$\kappa_{xx} = \frac{W_{xx}}{W_{xx}^2 + W_{xy}^2} \approx \frac{1}{W_{xx}} \tag{2.15}$$

and it is assumed to be isotropic in the plane just as Eq. 2.3. The transverse thermal conductivity is

$$\kappa_{xy} = -\frac{W_{xy}}{W_{xx}^2 + W_{xy}^2} = -\kappa_{yx} \tag{2.16}$$

and it must be odd under parity like Eq. 2.6.

The same symmetrization and antisymmetrization considerations as for the Hall effect (Section 2.1.1.1) must be made to get correct data.

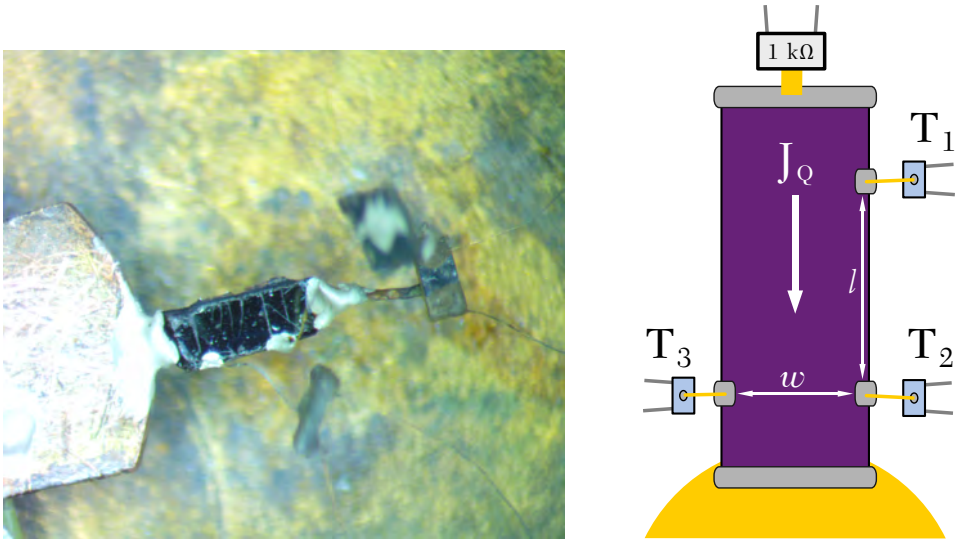

(a) (b)

Figure 2.5 Connections for thermal conductivity measurements. (a) The photo shows a sample set up to measure longitudinal conductivity only. The heat flows from the resistor (top rectangle) to the sink (copper base). (b) A diagram of connections for both longitudinal and transverse thermal conductivity measurements.

2.1.4 Seebeck and Nernst Coefficients

The Seebeck and Nernst coefficients belong to a third tensor where the diagonal terms are equal to the Seebeck coefficient S_{xx} and the antisymmetric off-diagonal terms are equal (in magnitude) to the Nernst coefficient S_{xy}. The measurement is done just like for the thermal Hall effect but with additional measurement of the longitudinal and transverse voltages. The placement of contacts to measure voltages V_1, V_2, and V_3 and their separations l_1, l_2, and w are defined in Fig. 2.6 following a specific sign convention. J_Q is the applied thermal current.

$$S_{xx} = \frac{(V_2 - V_1)/l_1}{(T_2 - T_1)/l_2} \tag{2.17}$$

$$S_{xy} = \frac{(V_1 - V_2)/w}{(T_2 - T_1)/l} \tag{2.18}$$

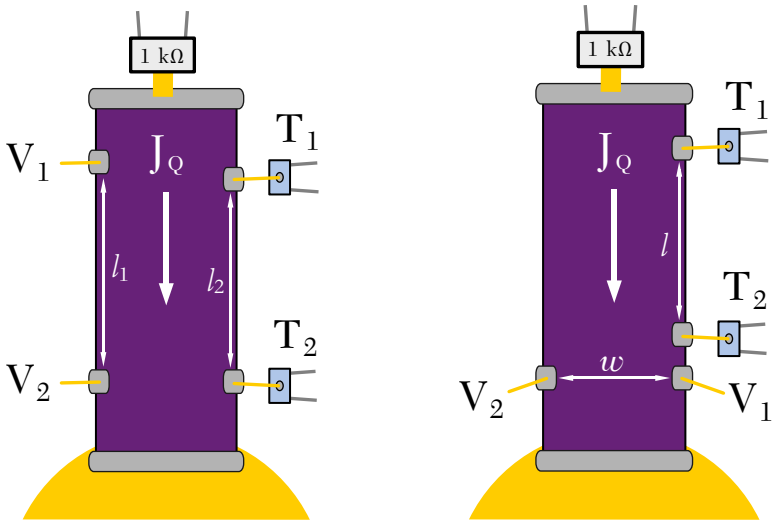

Figure 2.6 Connections for (a) the Seebeck coefficient and (b) the Nernst coefficient. Heat flows form the resistor (top rectangle) to the heat sink (copper base).

2.2 Scattering Methods

2.2.1 X-Ray Diffraction

Scattering is one of the most illuminating techniques for structure characterization. The interaction of waves with the atoms in a crystal lattice produces a diffraction pattern that can be used to infer the crystal's structure. X-rays in particular are useful for probing crystals because of the similarity in sizes of their wavelengths with typical atomic spacings (1 to 100 Å).

At the foundation of x-ray diffraction (XRD) is Bragg's condition, which is met when waves with a certain wavelength scatter off a periodic structure constructively, illustrated in Fig. 2.7. Mathematically, this can be written as

$$n\lambda = 2d\sin(\theta) \tag{2.19}$$

where λ is the beam wavelength, d is the atomic distance, θ is the scattering angle, and n is the diffraction order. [181]

Scattering off a single crystal orientations produces a three-dimensional diffraction pattern of sharp peaks that acts as a fingerprint for that structure. By using a powder sample, however, the structural information is averaged over all directions and all peaks are observed as a function of

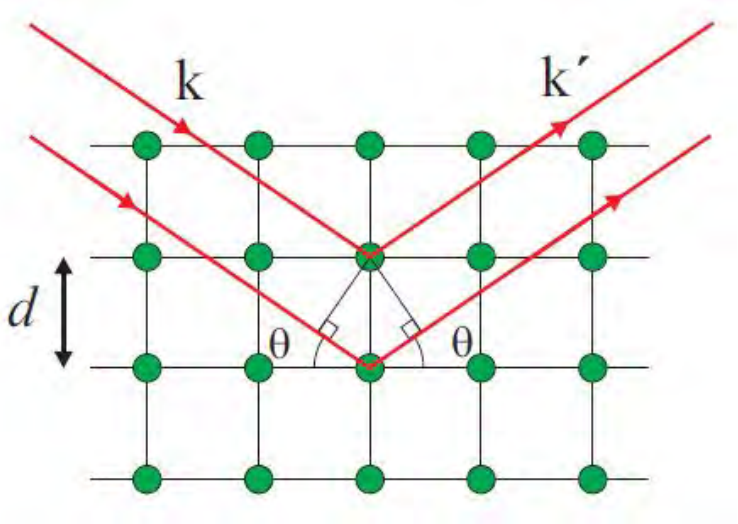

Figure 2.7 Two beams scattering off atoms in a crystal. Constructive interference occurs when the Bragg condition is met. [181]

incident angle. Nonetheless, powder XRD is very useful in refining the structure of a given sample from a reference.

The crystal structure of γ-Fe_2WO_6 was examined using a Bruker Davinci x-ray diffractometer. The powder was packed tightly into the commercial sample holder and placed in the beam path. The diffraction pattern was fit using the Bruker software to confirm the identity of the substance.

To measure the offcut angle of diamond substrates, a Rigaku SmartLab x-ray diffractometer was used to observe the position of the (111) peak relative to the substrate top surface.

2.2.2 Neutron Scattering

Neutrons, though normally thought of as particles, can scatter as waves like x-rays with some key differences. Neutrons interact with nuclei, unlike x-rays which interact with electrons. As a result, scattering lengths of the elements vary chaotically so neutrons can distinguish between adjacent elements on the periodic table and different isotopes more easily than x-rays, which scatter off electron clouds. [182, 183] The large differences in scattering behavior is shown in Fig. 2.8. Since adjacent elements have similar number of electrons, it is usually hard to distinguish them using XRD but not with neutrons.

Because neutrons of a given wavelength have much lower energies than x-rays of equal wavelength, they can penetrate much deeper into the bulk without causing damage, making it possible

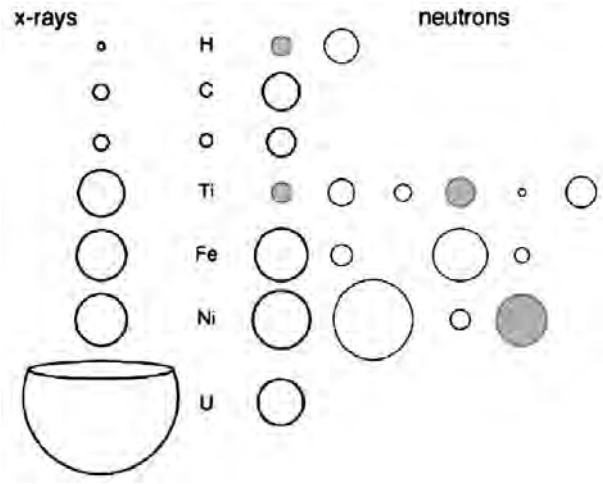

Figure 2.8 Comparison of scattering cross sections of x-rays and neutrons for some elements and their isotopes. (Shading indicates large incoherent scattering.) [183]

to investigate the dynamics of crystal systems using inelastic scattering techniques. [183]

Unlike x-rays, neutrons possess a magnetic moment that couples to moments in the crystal structure. Even though electrons do not interact with neutrons via nuclear forces, neutrons are sensitive to their spins which allows neutron diffraction to carry information about magnetic order within the crystal.

In elastic scattering, the incident neutron with wave vector $\vec{k}$ scatters to a wave vector of equal magnitude but different direction $\vec{k}'$. The difference gives us the scattering vector $\vec{Q}$.

$$\vec{Q} = \vec{k} - \vec{k}' \tag{2.20}$$

Its magnitude is related to the scattering angle θ according to

$$Q = \frac{4\pi}{\lambda}\sin\theta \ . \tag{2.21}$$

The form factor $F(Q)$ relates the scattering intensity to the scattering angle. For neutrons, the form factor falls off quickly for increasing Q, hence magnetic Bragg peaks can only be observed for small values of Q and θ. [183]

Clearly neutron scattering has significant advantages over XRD. Unfortunately, neutron beams are much less safe and accessible than x-ray beams.

2.2.3 Neutron Spectrometers

HB2A is a powder neutron diffraction at the High Flux Isotope Reactor at Oak Ridge National Laboratory (ORNL). Neutrons are generated continuously by the reactor and the beam is passed through a monochromator to select an incident beam of a desired wavelength. The beam is diffracted by the sample and a detector bank counts diffracted neutrons over a range of angles. [184] This is reported as intensity as a function of θ or Q.

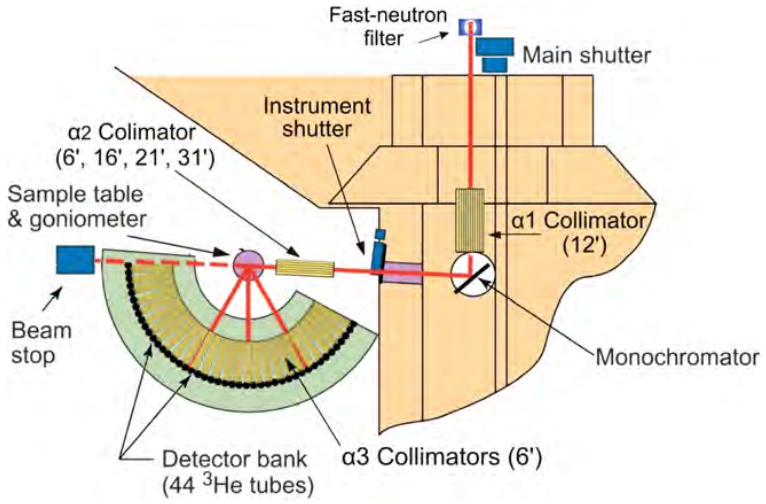

Figure 2.9 Schematic of HB2A. [184]

POWGEN is a time-of-flight (TOF) spectrometer at the Spallation Neutron Source at ORNL, where neutrons are generated in 60 Hz pulses. To select an incident wavelength, the neutrons pass through a 60 m guide and a series of synchronized choppers that block neutrons of undesired energies from reaching the sample. A bank of detectors counts the scattered neutrons to record a diffraction pattern. [185, 186]

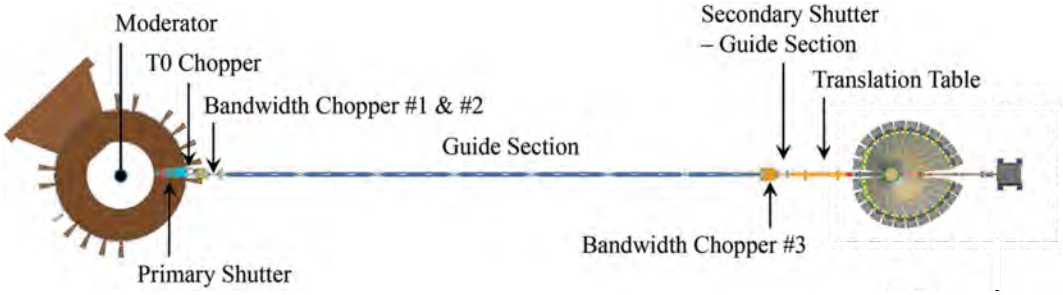

Figure 2.10 Schematic of POWGEN. [185]

Neutron powder diffraction measurements on $\sim$ 4 g of γ-Fe_2WO_6 were performed using the neutron powder diffractometers HB2A and POWGEN at ORNL.

2.2.4 Structure Refinement

Once a diffraction pattern is recorded, it must be refined to obtain a structure. FullProf is a software package that is widely used for the analysis of powder diffraction data. [187] Starting with a reference structure and information about the instrument used to collect the data, FullProf shifts atom positions to find the structure that best fits the given diffraction pattern. If the structure is magnetic, the user can label the magnetic Bragg peaks and use FullProf to generate a few possible k vectors.

Using the crystal symmetry and k vector, the program SARAh can generate the possible magnetic symmetry groups and their basis vectors. [188] The most likely magnetic structure is found by fitting all the possible basis vectors to the diffraction pattern using FullProf. Fig. 2.11 illustrates the structure refinement progression in FullProf.

2.3 Magnetic Susceptibility

The instrument used to measure magnetic susceptibility is a magnetometer, such as a Superconducting QUantum Interference Device (SQUID). In a SQUID, current is passed though a superconducting loop of two Josephson junctions in parallel, as shown in Fig. 2.12. A Josephson junction is a device formed by two superconductors separated by a thin insulating barrier. When there is a magnetic field within the loop, the current though the two halves of the loop acquire a measurable phase difference which can be used to determine the strength magnetic field to a high precision.

2.4 Atomic Force Microscopy

Sample roughness was measured using a Hitachi model AFM5100N atomic force microscope. The microscope was used in dynamic force microscope (DFM) mode where the tip oscillates as it moves so that it taps the sample surface rather than dragging across it. The position of the tip is monitored by a laser that reflects off the tip onto the optical detector.

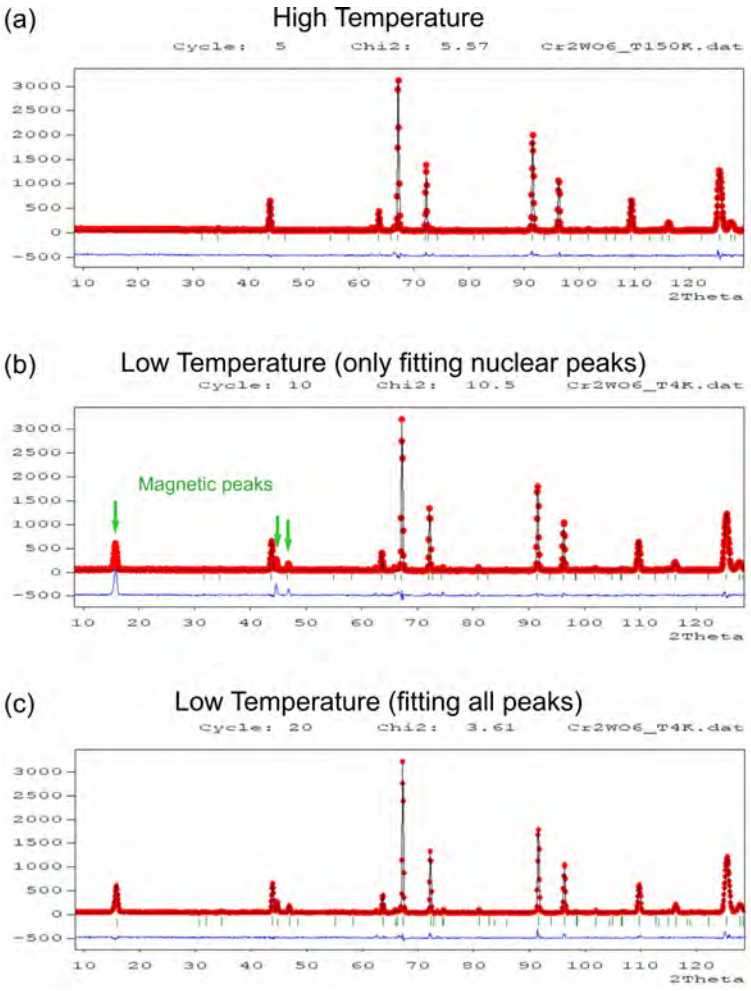

Figure 2.11 The process of fitting a magnetic structure in FullProf. (a) Fitting nuclear peaks at high temperature. (b) Fitting nuclear peaks at low temperature while ignoring magnetic peaks (green arrows). (c) Fitting both nuclear and magnetic peaks at low temperature.

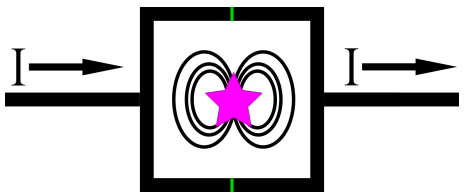

Figure 2.12 A basic schematic of a SQUID. The sample (pink star) creates a magnetic field that the SQUID can measure. Thin barriers in the superconducting material (green) form the Josephson junctions.

The average linear roughness for a length L is calculated according to the equation

$$R_a = \frac{1}{L}\int_0^L |z(x)|\, dx \tag{2.22}$$

where $z(x)$ is the height of the surface.

The average surface roughness over a rectangular area $L_x \times L_y$ is calculated according to the equation

$$S_a = \frac{1}{L_x L_y}\int_0^{L_x}\int_0^{L_y} |z(x,y)|\, dx\, dy\ . \tag{2.23}$$

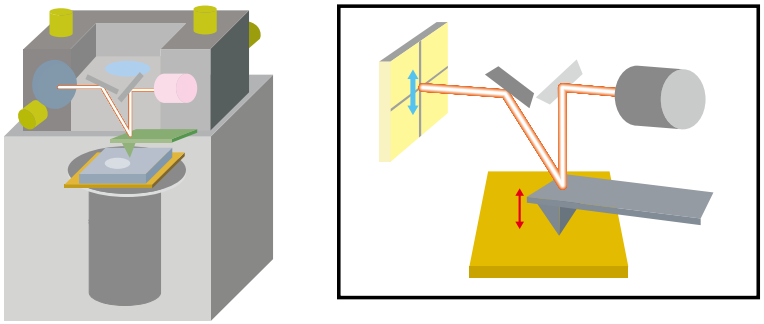

(a) (b)

Figure 2.13 A simple schematic of the Hitachi model AFM5100N atomic force microscope. (a) A view of the sample on the movable stage during measurement. (b) A close up view of the beam path as the tip moves vertically.

2.5 Thickness Measurements

The thickness of diamond samples was measured using a Mitutoyo EH-10P linear encoder. Five measurements were taken near each of the four corners and ten measurements were taken in the center. The average is reported for the overall sample thickness.

2.6 Profilometry Measurements

A stylus profilometer measures surface topography by dragging a diamond-tipped stylus across a sample while monitoring its vertical position. As the stylus moves across the surface, it rises and falls with the surface features and the instrument records the height along a linear path. Profilometry measurements were taken on a Bruker DektakXT stylus profilometer.

2.7 Crystal Growth

The crystalline materials studied in the work were all grown from chemical precursors, however, different methods of growth had to be employed depending on the possible growth mechanism of each material. There is no universal method to grow a crystalline material.

2.7.1 Furnace Growth

A furnace is a temperature-controlled environment in which a heating element heats the interior of the furnace to a specified temperature that is monitored by a thermocouple, and a digital component allows a sequence of temperatures to be programmed over the desired lengths of time. The furnace is not completely closed to the environment and has no input for process gasses, but the reaction mixture can be isolated from the environment within a sealed ampoule. An open quartz tube is closed on one end using a blow torch. The reactive species are placed inside and the tube is connected to a vacuum pump. While the pump pulls a vacuum, we use the blow torch to separate the lower portion of the tube to form a sealed ampoule containing the reactants under vacuum. Then the ampoule can be placed in the furnace for crystal growth. The quartz tube limits the furnace temperature to about 1500°C, which is when the quartz begins to soften. Rupturing the ampoule is not desirable.

2.7.1.1 Solid-State Reaction

A solid-state reaction is the simplest example of furnace growth. The reactants in powder form are thoroughly mixed together using a morter and pestle in the stoichiometric ratio of the final product. Then the powder is sealed in the ampoule and heated in the furnace. The result is always a polycrystalline product. This method is commonly used for oxide materials such as perovskites, spinels, and high-T_C superconductors which require precise stoichiometric control and high temperatures for the reactants to diffuse and react. Examples of other furnace grown polycrystalline materials can be found in [103, 189, 190].

2.7.1.2 Flux Growth

When discussing crystal growth, a molten mixture of metals is called flux. Therefore, in flux growth, metallic elements are sealed in a quartz ampoule and heated in a furnace to produce a melt.

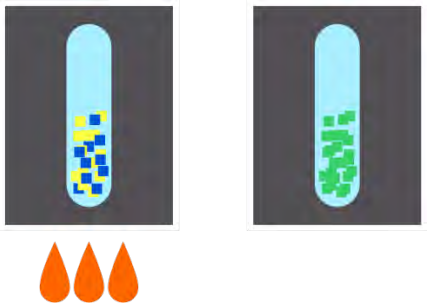

Figure 2.14 Solid state reaction.

However, this type of growth differs from the solid-state growth in several important ways. First, the reactants are not mixed in the stoichiometric ratio of the desired product. One metal, chosen for its low melting point, often tin or germanium, is added in significant excess. Second, a sieve such as quartz wool (which is chemically inert and does not melt) is placed on top of the metals within the ampoule. And third, the temperature sequence must allow for the metals to melt completely before cooling the mixture gradually to begin crystallization. While the flux is still molten, the ampoule is taken from the furnace, inverted, and centrifuged. The sieve catches the crystals and separates them from the excess flux, allowing them to be retrieved once the ampoule is broken open. This method can produce very large metallic crystals if enough time is allowed for crystallization, but only works if one of the reactants can be used as the flux. Examples of flux growth can be found in [60, 191, 192].

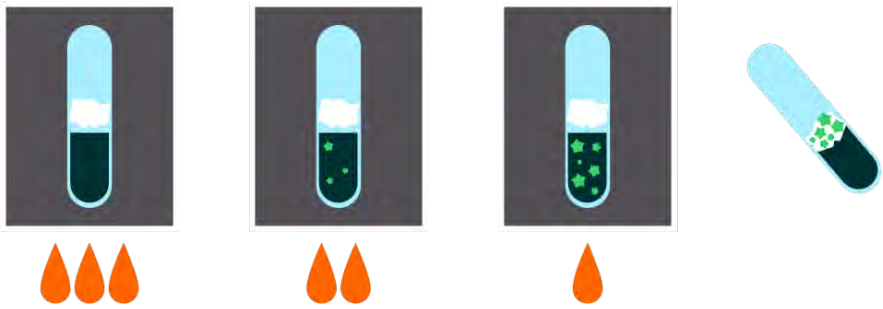

Figure 2.15 Flux growth.

2.7.1.3 Chemical Vapor Transport

A two-zone furnace contains two independently controlled temperature zones. The reactant species are sealed in a quartz ampoule and placed horizontally in the furnace with the reactants in

the hot zone and the empty side of the ampoule in the cold zone. The reaction occurs thanks to a transport agent, usually a halogen, that vaporizes in the hot zone, picks up some atoms of the other elements, and takes them to the cold zone where they crystallize. This method can produce large crystals with the right temperature difference and enough time. However, a good transport agent is required for the reaction to succeed. Examples of CVT growth can be found in [193, 194, 195].

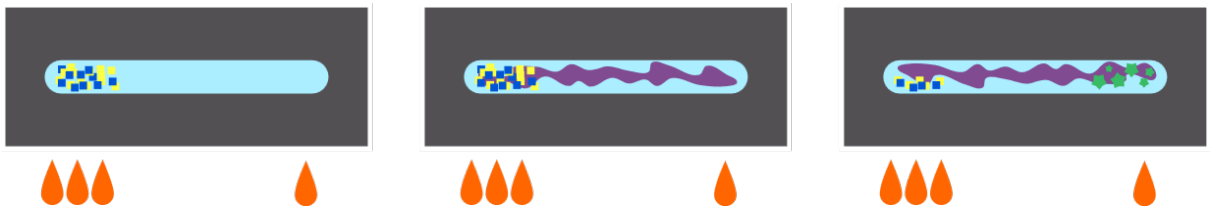

Figure 2.16 Chemical vapor transport growth.

2.7.2 Microwave-Plasma Assisted Chemical Vapor Deposition

The diamond samples studied in this work were grown on Diamond System 5 (DS5), a home-made diamond reactor located on the campus of Michigan State University (MSU). The main body of this reactor is a metal cylinder that works as a resonant cavity for electromagnetic fields. A 2.45 GHz microwave generator sends electromagnetic waves along a rectangular waveguide and an antenna redirects the waves downward into the resonant cavity. The primary excitation mode is the TM_{013} mode. The water-cooled stage with a molybdenum sample holder sits in the lower portion of the cavity beneath a quartz dome that is sealed off from the atmosphere. Process gases flow within the dome during growth, otherwise vacuum is pulled when the reactor is not being loaded. The height of the cavity can be tuned by a sliding short to achieve optimal coupling efficiency and minimize reflected power. All diamond growths in this work were carried out with a fixed chamber height. The pressure is controlled by the balance of gas flowing into the chamber which is set by the mass flow controllers (MFCs) and the position of the butterfly valve that leads to the vacuum pump. The microwave power can range from 300 W to 3000 W, although 2700 W is the recommended limit for the longevity of the power supply. The gases hydrogen, methane, and phosphine can be flowed into the reactor, with the phosphine being diluted to 1000 ppm in hydrogen. The MFCs for the gas flow can reach 500 sccm for hydrogen, 50 sccm for methane, and 500 sccm for the diluted

phosphine, with the minimum recommended flow being 10% of the maximum. A quartz window in the reactor wall lets the temperature of the sample be read by an optical pyrometer. Fig. 2.17 shows an illustration of the reactor.

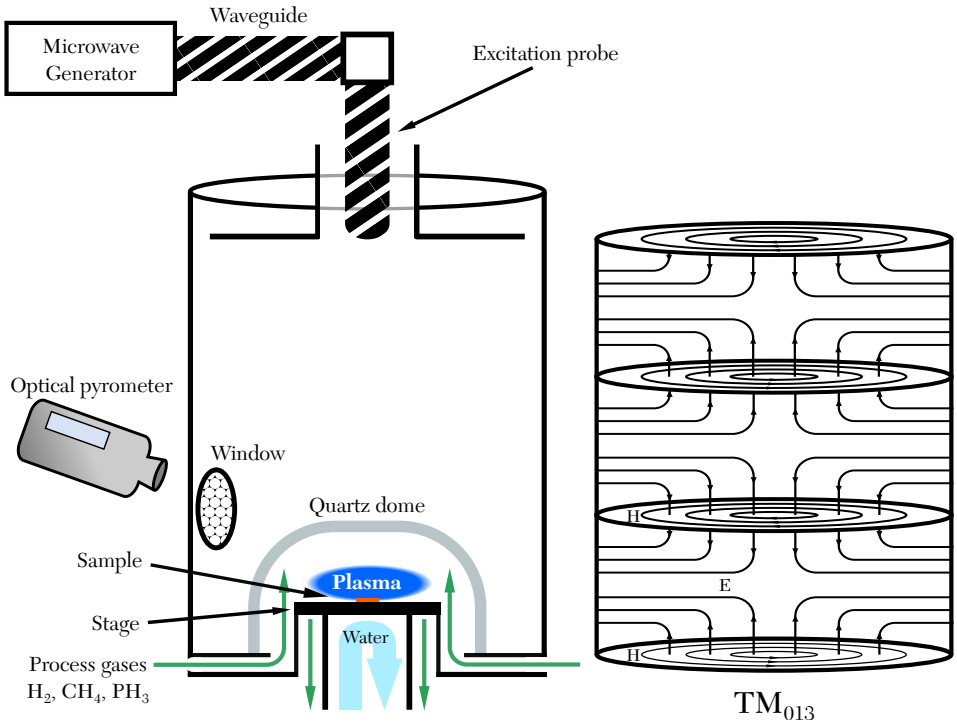

Figure 2.17 Schematic illustration of the reactor chamber and EM fields within it.

2.8 Acid Cleaning Procedure

Before diamond growth, it is necessary to clean the substrate according to the following procedure to reduce the presence of surface contaminants as much a possible. First the diamond is boiled for at least 20 minutes in a 1:1 bath of concentrated H_2SO_4 and HNO_3. This eliminates solvent and grease residues. Then the diamond is boiled for at least 20 minutes in concentrated HCl to eliminate metal ions. Finally the diamond is sonicated in acetone for 5 minutes, followed by sonication in methanol for 5 minutes, and blown dry with nitrogen.

CHAPTER 3

$\gamma - Fe_2WO_6$

3.1 Previous Studies

First described in 1957 [196], Fe_2WO_6 is now known to occur in three polymorphs, α, β, and γ-Fe_2WO_6, which are synthesized under different growth conditions [197]. Crystalizing with space group *Pbcn*, γ-Fe_2WO_6 forms zig-zag chains of MO_6 (M = Fe or W) octahedra along the *c*-axis which share edges with adjacent octahedra of the same chain and corners with octahedra of neighboring chains as illustrated in Fig. 3.1(a,b). Two types of chains are present: those with only iron octahedra and those with alternating iron and tungsten octahedra [198]. The Fe^{3+} ions are expected to be in the high-spin S = 5/2 state [199].

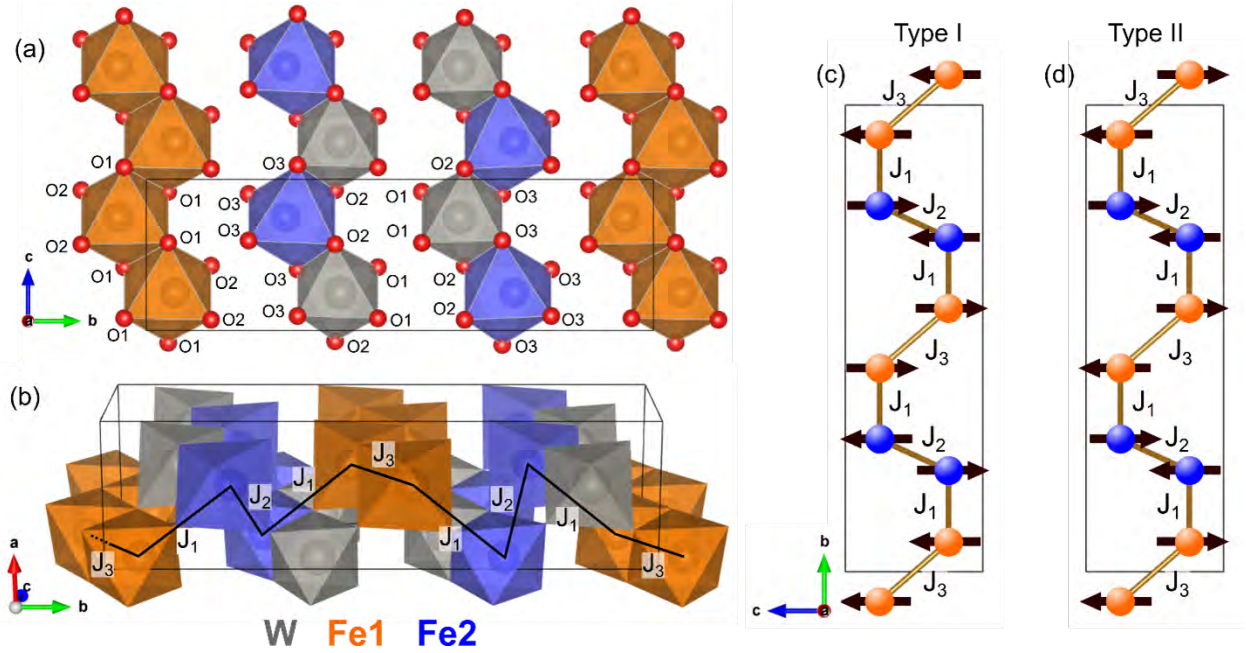

Figure 3.1 Schematics of crystal and magnetic structures of γ-Fe_2WO_6. (a) Crystal structure projected along [100] showing a single layer ($x \approx 0$). (b) Crystal structure with labeled Fe-Fe couplings. (c,d) Magnetic structures used for the DFT calculation: (c) structure reported by Pinto *et al.* [200] equivalent to $\Psi_4(\Gamma_3)$, (d) the $\Psi_6(\Gamma_4)$ component of our refinement.

Since its discovery, several studies have attempted to probe the magnetic properties of γ-Fe_2WO_6 using a variety of techniques [201, 202, 203, 204, 205, 200, 206]. Neutron powder diffraction (NPD) measurements indicate that it is antiferromagnetic (AntiFM) with propagation

vector k = (000) [200, 206]. The ground-state spin structure proposed by Pinto *et al.* [200], which belongs to the magnetic space group *Pbc'n'*, is illustrated in Fig. 3.1(c) and denoted as Type I. Weitzel arrived at a structure belonging to the space group *Pn'c*2' which is similar but has the moments canted in the *ac*-plane [206]. Measurements of magnetic susceptibility, specific heat, dielectric constant, and Bragg reflection ordering parameters tend to suggest the existence of at least two transitions. One transition in a temperature range from 240 to 285 K has been commonly attributed to the AntiFM ordering transition, while a second transition of unclear origin has been observed between 150 K and 230 K [201, 205, 200]. Pinto *et al.* attributed the low-temperature transition to a crystallographic change [200]. Panja *et al.* observed a third feature in the magnetic susceptibility data at $\sim$ 22 K, below which a magnetic glass-like state was proposed [205]. The variety in transition temperatures and refined spin structures suggests that the magnetic properties of γ-Fe_2WO_6 are sample specific. The goal of this study was to sharpen the picture of γ-Fe_2WO_6 and deepen the understanding of this material though new experimental and theoretical techniques.

3.2 Sample Growth

Polycrystalline samples of γ-Fe_2WO_6 were synthesized through a solid-state reaction. An equimolar mixture of the raw materials Fe_2O_3 (Sigma Aldrich, 99%) and WO_3 (Sigma Aldrich, 99.9%) was ground uniformly by mortar and pestle before being put in an alumina crucible. The mixture was then heated up to 950°C in a box furnace for 96 hours in order to achieve a single-form sample of γ-Fe_2WO_6.

3.3 Density Functional Theory

DFT calculations of γ-Fe_2WO_6 were done using the Vienna *ab initio* simulation package (VASP) [207] with the projector augmented wave method [208] and the generalized gradient approximation in the parametrization of Perdew, Burke, and Enzerhof [209] for exchange-correlation. For Fe and O, standard potentials were used (Fe and O in the VASP distribution), and for W a potential in which *s* states are treated as valence states is used (W_{sv} in the VASP distribution). We chose 500 eV as an energy cutoff and used 8 × 2 × 8 *k*-point grid. To account for correlation effects, the local U is included on the Fe *d*-orbital states [210]. In the presented results, we consider U_{eff} = 4.0 eV

[211]. The spin-orbit coupling is turned on. The c2x tool uses DFT to generate Fermi surfaces, which can be visualized by the program FermiSurfer. [212]

3.4 Results

Fig. 3.2(a) presents the magnetic susceptibility $\chi(T)$ measured upon warming after the sample was field-cooled (FC) and zero-field-cooled (ZFC). One can see that the sample exhibits a magnetic phase transition at $T_N = 235$ K. Slightly below T_N, a bifurcation between FC and ZFC curves is clearly observed. However, no hysteresis loop is convincingly observed down to 10 K, which excludes the possibility of a spin-glass-like ground state. This is supported by the sharp magnetic Bragg peaks revealed in NPD measurements which will be discussed later. Instead, the bifurcation feature can be attributed to the formation of magnetic domains during the ZFC process. This may also account for the broad peak around 13 K observed in the ZFC data. In addition to the feature in $\chi(T)$ observed at T_N, one also sees a small feature at about 285 K, which is consistent with the findings by Panja *et al.* [205] However, as is supported by NPD and will be discussed later, this feature actually belongs to α-Fe_2O_3. [213, 214] By performing the Curie-Weiss fit to the magnetic susceptibility in the high temperature region (290 K – 340 K), we obtain the Curie-Weiss temperature $T_C = -174(2)$ K and an effective magnetic moment $P_{eff} = 4.93(1)\ \mu_B$/Fe. Here P_{eff} is close to the predicted moment of Fe^{3+} in the high-spin state, S = 5/2. This is in sharp contrast to an early report by Panja *et al.* who found P_{eff} equal to 1.22(6) μ_B/Fe, which was attributed to the low spin state of Fe^{3+}. [205] Potential oxygen non-stoichiometry of the compound was discussed in Refs. [199, 205].

NPD POWGEN data measured at T = 10, 150, 190 and 300 K are shown in Fig. 3.3(a) and Fig. 3.3(b). Due to the rapid decrease in magnetic form factor as a function of Q, there is little magnetic scattering intensity contribution at large Q values. Thus, by comparing the diffraction data with large Q values measured at various temperatures, we can conclude that there is no structural phase transition observed down to 10 K within the instrumental resolution. On the other hand, enhanced Bragg peak intensity is observed at small Q regions when decreasing the measurement temperature, such as at the (110), (021), and (040) Bragg reflections shown in Fig. 3.3(b).

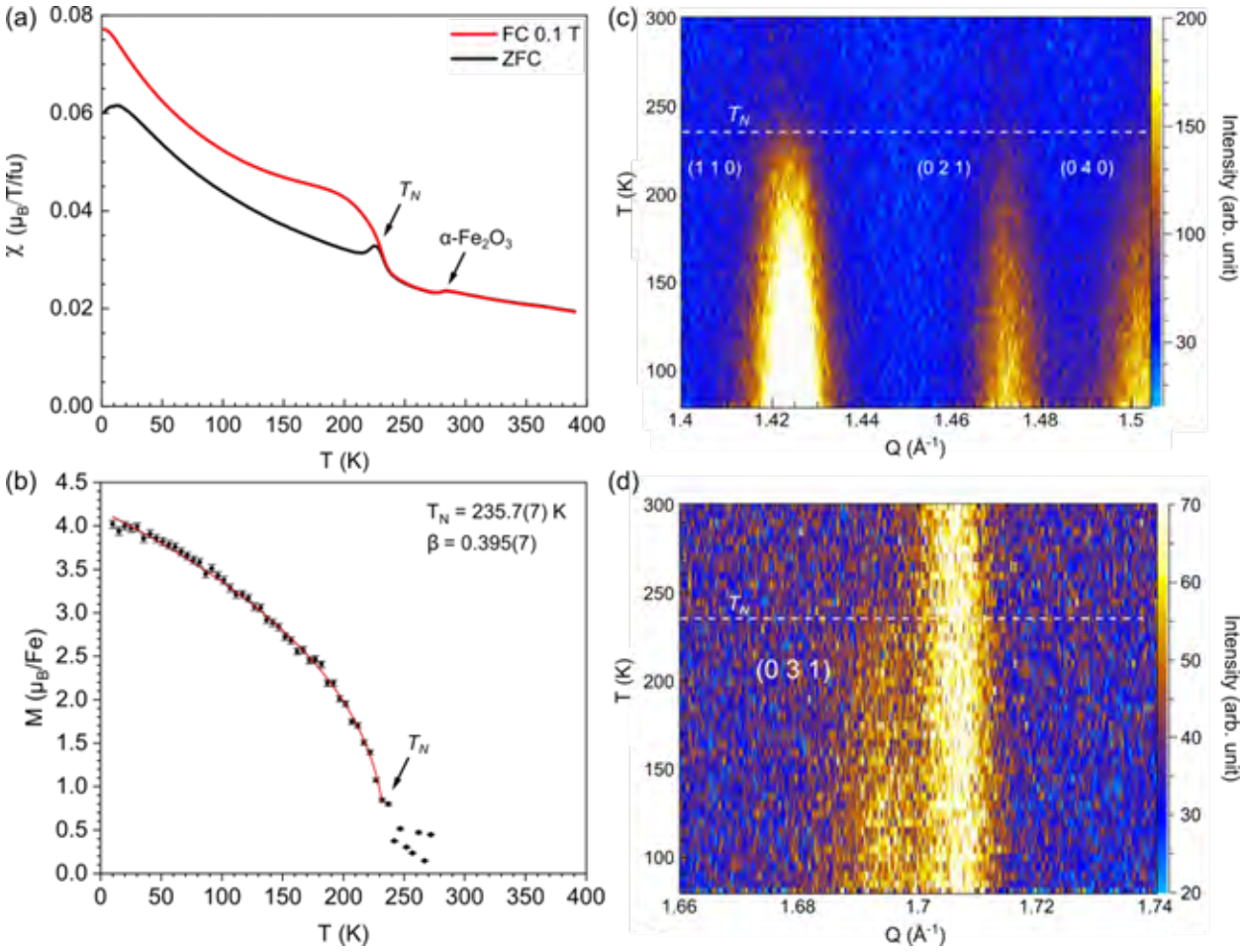

Figure 3.2 (a) Magnetic susceptibility as a function of temperature measured with an applied field of 0.1 T. (b) Fe magnetic moment as a function of temperature calculated from the NPD intensity of the (110) Bragg peak measured on HB2A. (c,d) Contour plots of selected Bragg reflections over a temperature range of 70 to 300 K measured on POWGEN.

These peaks, therefore, indicate overlapping nuclear and magnetic Bragg reflections, suggesting a propagation vector of $k = (000)$. We note that the intensity of the peak at 1.37 Å^{-1} decreases at low temperature. Order parameter measurements (not shown) reveal that it drops in intensity at 285 K, consistent with the feature in the magnetic susceptibility (Fig. 3.2(a)). As will be discussed later, this peak can be fit to the magnetic phase of α-Fe_2O_3. In fact, previous studies have shown that an α-Fe_2O_3 impurity is inevitable in stoichiometric mixtures of Fe_2WO_6. [215] Thus, it seems likely that the magnetic transition at higher temperature in previous studies of γ-Fe_2WO_6 may stem from the α-Fe_2O_3 impurity instead of being intrinsic to γ-Fe_2WO_6. Note that this magnetic impurity Bragg peak is near the (100) peak of γ-Fe_2WO_6 phase that has much smaller intensity, as seen in

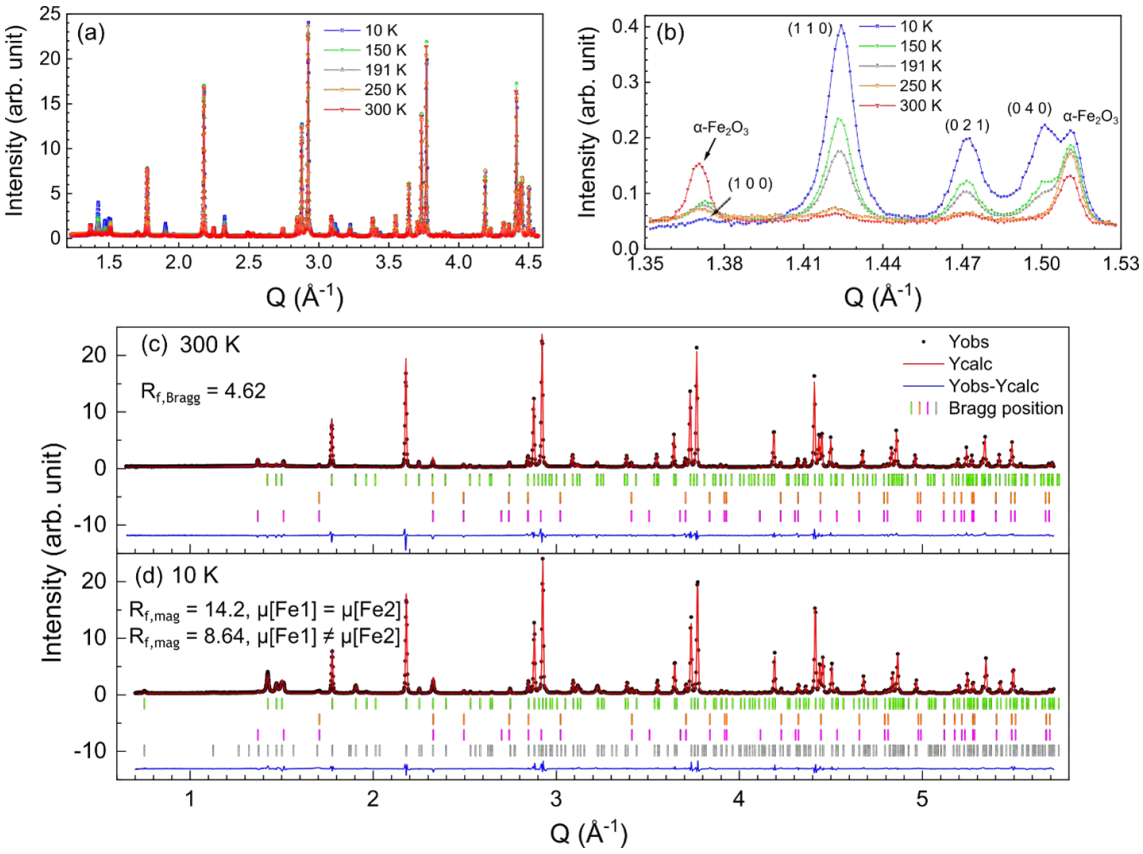

Figure 3.3 NPD POWGEN data collected at different temperatures. (a) Overlaid diffraction patterns from Q = 1.2 to 4.6 Å^{-1}. (b) Overlaid diffraction patterns from Q = 1.35 to 1.53 Å^{-1}. (c,d) Diffraction patterns and the refinements at 300 K and 10 K, respectively. Black points represent experimental data. Red lines show Rietveld fitting. Vertical strokes label Bragg peak positions. The topmost row of strokes (green) labels γ-Fe_2WO_6 nuclear peaks. The second row (orange) labels α-Fe_2O_3 nuclear peaks. The third row (pink) labels α-Fe_2O_3 magnetic peaks. The bottom row (grey) labels γ-Fe_2WO_6 magnetic peaks. The bottom blue curve is the residual of the fit.

Fig. 3.3(b).

Rietveld refinements of the neutron diffraction data measured at T = 300 K and 10 K are shown in Figs. 3.3(c) and (d), respectively. The data at high Q region (for nuclear structure refinement) is well fitted with the space group *Pbcn*. The refined atomic positions are listed in Table 3.1. The crystallographic space group *Pbcn* paired with the propagation vector k = (000) allows for eight irreducible representations, represented by Γ_{mag} (Fe) = $1\Gamma_1 + 1\Gamma_2 + 2\Gamma_3 + 2\Gamma_4 + 1\Gamma_5 + 1\Gamma_6 + 2\Gamma_7 + 2\Gamma_8$, following the labeling scheme used by Kovalev. [216] The magnetic moments along the crystallographic a, b, and c-axis are described by $\Psi_3(\Gamma_3)$, $\Psi_5(\Gamma_4)$, $\Psi_8(\Gamma_7)$, $\Psi_{11}(\Gamma_8)$ basis vectors, $\Psi_1(\Gamma_{14})$, $\Psi_2(\Gamma_2)$, $\Psi_7(\Gamma_5)$, $\Psi_8(\Gamma_6)$ basis vectors, and $\Psi_4(\Gamma_3)$, $\Psi_6(\Gamma_4)$, $\Psi_{10}(\Gamma_7)$, $\Psi_{12}(\Gamma_8)$ basis

	300 K			4 K		
atom	x	y	z	x	y	z
Fe1	0	0.0565(2)	0.25	0	0.0572(7)	0.25
Fe2	0	0.7247(1)	0.25	0	0.7257(7)	0.25
W	0	0.3882(2)	0.25	0	0.3871(8)	0.25
O1	0.2366(4)	0.0407(2)	0.5922(7)	0.250(1)	0.0418(7)	0.581(2)
O2	0.2766(5)	0.1266(2)	0.0713(4)	0.270(2)	0.1281(8)	0.068(1)
O3	0.2703(5)	0.2029(2)	0.5818(7)	0.285(1)	0.2057(4)	0.594(2)

Table 3.1 Atomic positions of γ-Fe_2WO_6 at 300 and 4 K, obtained from Rietveld refinement of NPD data.

vectors, respectively. There are two unique Fe atoms, designated as Fe1 and Fe2.

The NPD spectrum measured at 300 K was refined with the crystallographic phase of γ-Fe_2WO_6 and the crystallographic and magnetic phases of α-Fe_2O_3. The α-Fe_2O_3 impurity phase is found to be about 5.2 mol% (0.22 wt%). The 10 K data was best fit by including a magnetic phase of γ-Fe_2WO_6 consisting of $\Psi_4(\Gamma_3)$ and $\Psi_6(\Gamma_4)$. $\Psi_3(\Gamma_3)$ and $\Psi_5(\Gamma_4)$, which would drive the canted moment in the *ac*-plane, were not included because they resulted in divergence of the fit. The corresponding magnetic space group is $P2_12'_12'$. The magnetic phases both appear at $\sim$ 235 K. This can be seen in the contour plots of Fig. 3.2(c) and (d). By fitting the temperature dependence of magnetic momentum size shown in Fig. 3.2(b), which is extracted from NPD ordering parameter measurements, to the function $M(T) = A(1 - T/T_N)^{-\beta}$, we obtain a T_N of 235.7(7) K and β of 0.395(7). $\Psi_6(\Gamma_4)$ is responsible for the (100), (021), and (040) peaks (Fig. 3.2(c)), while $\Psi_4(\Gamma_3)$ produces the (031) peak (Fig. 3.2(d)). The refinement was carried out with and without constraining the magnetic moments of Fe1 and Fe2 to be the same for each basis vector individually. The refined moment size with this constraint is 4.02(4) μ_B, and the proportion of $\Psi_4(\Gamma_3)$ and $\Psi_6(\Gamma_4)$ is about 23% and 77%, respectively. Without the constraint, the moment of Fe1 is 3.6(1) μ_B and the moment of Fe2 is 4.5(1) μ_B, and the proportions of $\Psi_4(\Gamma_3)$ and $\Psi_6(\Gamma_4)$ are found to be about 24% and 76%, respectively. The magnitudes of these moments are consistent with the effective magnetic moment extracted from the Curie-Weiss fit to the magnetic susceptibility data as discussed above. They are larger than the moments observed by Pinto *et al.* who found moments of 2.48(7) μ_B with the constraint, and 2.55(7) μ_B for Fe1 and 2.15(15) μ_B for Fe2 without the constraint. [200] As will

be discussed later, such a difference may be associated with the difference of the electronic state of the samples studied.

Interestingly, $\Psi_4(\Gamma_3)$ is the same structure arrived at by Pinto *et al.* [12]. Weitzel's structure also consists of this basis vector with $\Psi_{11}(\Gamma_8)$ [206], but this did not give a good fit with our sample. Qualitatively, the coupling between nearest neighbors is the same for $\Psi_4(\Gamma_3)$ and $\Psi_6(\Gamma_4)$ with the exception of the Fe1-Fe1 coupling, which is ferromagnetic in $\Psi_4(\Gamma_3)$ and antiferromagnetic in $\Psi_6(\Gamma_4)$. Therefore, $\Psi_4(\Gamma_3)$ is denoted as a Type I magnetic structure while $\Psi_6(\Gamma_4)$ is equivalent to a Type II magnetic structure. We note that the presence of these two magnetic phases does not imply the presence of two distinct crystal structures because diffraction patterns could be fitted using only one crystal structure for γ-Fe_2WO_6. Had our sample contained 24% of the structure observed by Pinto et al., due to the large difference in bond angles which would lead to large difference in the diffraction intensity of some nuclear Bragg reflections, the diffraction patterns would have been noticeably different and a second structure would have needed to be included in the refinement. Thus, we conclude that γ-Fe_2WO_6 in our sample contains only one crystal phase that is pure or nearly pure, and that these two magnetic phases coexist in competition with each other in the sample.

To better understand the origin of the phase competition and the difference between the magnetic structure obtained in this study and that reported in the literature [200], we have performed first-principles DFT calculations. To the best of our knowledge, thus far no inelastic neutron scattering measurements on this system have been reported and the exact magnetic interactions and Hamiltonian remain unknown. The calculations were carried out using our refined nuclear structure (lattice parameters and atomic positions) at low temperature and the one reported by Pinto *et al.* [200] listed in Table 3.2. For each nuclear structure, the calculations were done for four different spin structures in order to extract the exchange interactions J_1, J_2, and J_3 illustrated in Fig. 3.1. The obtained energies for Type I and Type II structures and the extracted exchange parameters are listed in Table 3.3 (the energies calculated for the other two types of spin structures are not shown here). One can see that indeed Type II spin structure is the most energetically favorable for the calculation

	This work (4 K)	Pinto *et al.* [200]
Fe1–O1–Fe1 angle	98.5(4)°	106.4°
Fe1–Fe1 distance	3.115(13) Å	3.282 Å
Fe1–O2–Fe2 angle	125.5(5)°	141.1°
Fe1–Fe2 distance	3.598(11) Å	3.425 Å
Fe2–O3–Fe2 angle	127.6(6)°	140.2°
Fe2–Fe2 distance	3.484(6) Å	3.564 Å
a (Å)	4.562(1)	4.576
b (Å)	16.699(1)	16.766
c (Å)	4.953(1)	4.967

Table 3.2 Sample-dependent crystallographic properties of γ-Fe_2WO_6.

using our refined crystal structure. For Type II spin structure, J_1, J_2, and J_3, which represent the exchange interactions of Fe1-Fe2, Fe2-Fe2, and Fe1-Fe respectively, are all antiferromagnetic and the strength of J_3 is the smallest. Interestingly, the calculations done using the crystal structure obtained by Pinto *et al.* reveals a magnetic ground state exhibiting Type I spin structure that is consistent with the magnetic structure they reported based on their NPD data. [200] While J_1 and J_2 are also positive indicating antiferromagnetic coupling, J_2 is negative corresponding to ferromagnetic spin alignment between two adjacent Fe1 ions.

In order to understand different signs of J_3 for Type II and Type I spin structures, we have also calculated the electronic structures corresponding to these two different types of spin structures. Fig. 3.4(a,b) present the calculated density of states (DOS) of both magnetic phases where one can see a striking contrast. Type II magnetic structure corresponds to an insulating electronic phase with a band gap of $\sim$ 1 eV, which is slightly smaller than in previous reports, 1.5 and 1.7 eV. [217, 218, 219] Intriguingly, the DOS associated with the Type I magnetic structure shows metallic behavior as shown in Fig. 3.4(b). To gain further insight of the correlation between magnetic structure and electronic properties, in Fig. 3.4(c,d) we present the corresponding electronic band dispersions. For the insulating phase, the highest occupied states are mainly from oxygen (note that the line width corresponds to the sum of Fe1, Fe2 and W contributions) and the lowest unoccupied states are from Fe1 (red), while W (blue) contributes to energies slightly above Fe1. Thus, J_1, J_2, and J_3 are predominantly antiferromagnetic super-exchange interactions, leading to Type II spin

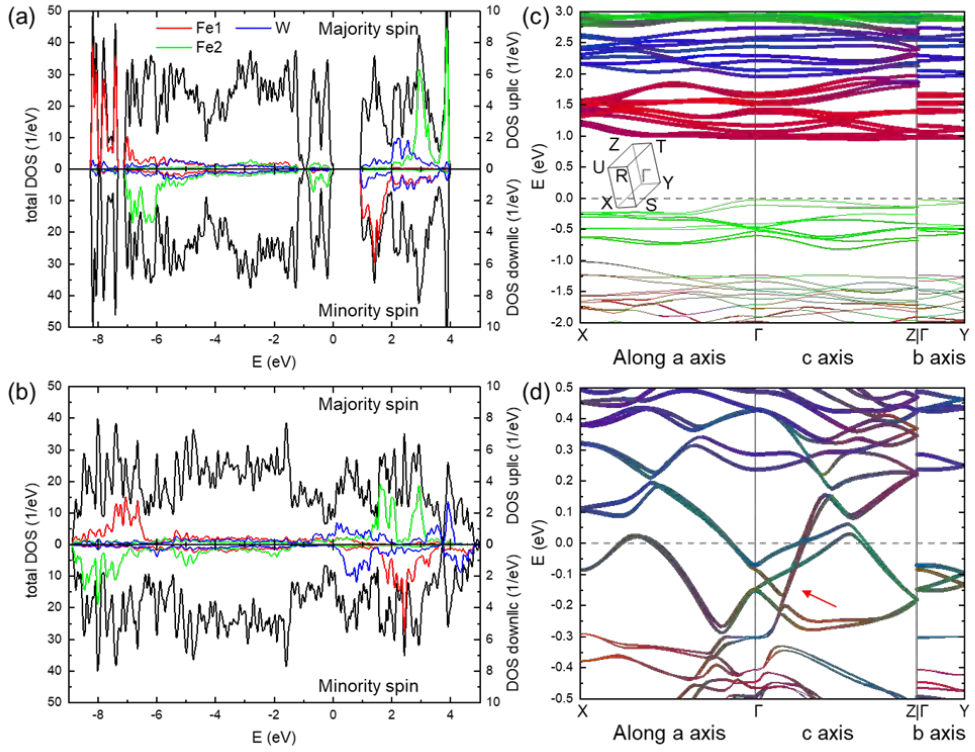

Figure 3.4 DFT results. DOS of Type II (a) and Type I (b) crystal structures projected on Fe1, Fe2 and W sites located on the top right corner of the unit cell shown in Fig. 3.1(a). Red curves are the contributions from Fe1, green curves are from Fe2, blue curves are from W, and black curves are total DOS. Spin axis is taken along the *c*-axis. Band structure of the Type II (c) and Type I (d) crystal structures. The color scheme is the same as in (a,b), and the line width is proportional to the sum of the weight of Fe1, Fe2, and W. The red arrow in (d) indicates bands with the mixed character of W and Fe1, which may be responsible for FM coupling on J_3 bonds. Energy is measured from the Fermi level. The inset of (c) shows the first octant of the first Brillouin zone.

structure. In contrast, for the metallic phase, oxygen dominates the DOS near the Fermi level with some contributions from Fe1, Fe2, and W. Interestingly, there are strongly dispersive bands crossing the Fermi level along the Γ-Z direction, as indicated by the red arrow in Fig. 3.4(d). These dispersive bands have mixed character of W and Fe1 and, therefore, are expected to be responsible for the ferromagnetic coupling (J_3) of Fe1-Fe1 bonds along the *c*-axis via the double-exchange-type mechanism which dominates over the antiferromagnetic superexchange interaction, thus giving rise to Type I spin structure. Note that it is likely that the itinerant electronic state obtained based on the crystal structure reported by Pinto *et al.* is associated with the smaller magnetic moment reported in Ref. [200], which is in contrast to the insulating state of our sample (we found its resistance to

	E (eV) Type I (4 K)	E (eV) Type II (4 K)	J_1 (meV)	J_2 (meV)	J_3 (meV)	M_{Fe1} (μ_B)	M_{Fe1} (μ_B)
Nuclear structure reported by Pinto *et al.* [200]	-254.7817	**-254.6142**	24.6	2.97	6.84	3.5	3.9
Nuclear structure obtained in this work	**-282.2317**	-282.2939	3.0313	7.97	1.763	4.2	4.1

Table 3.3 Calculated energies for Type I and Type II spin structures, exchange interactions, and size of ordered spin moment based on the nuclear structure reported by Pinto and the nuclear structure obtained in this work. The ground state energy for each structure is shown in bold.

very large, beyond our measurement capability).

The source of the difference between the two magnetic/electronic phases lies in structural distortion of the materials introduced during the synthesis process. Detailed information of the crystalline structure of the samples studied in this work and the ones reported in the literature [200] is listed in Table 3.2. Overall, the bond angles and bond lengths differ significantly between samples in these two studies. For instance, the larger Fe1-O-Fe2 bond angle and the shortened Fe1-Fe2 bond length in Pinto's sample are expected to contribute to the enhanced antiferromagnetic coupling J_1, as confirmed by the DFT calculation results listed in Table 3.3. On the other hand, while the Fe1-O-Fe1 bond angle is larger for the sample of Pinto *et al.*, the resultant enhanced antiferromagnetic superexchange interaction still yields to the ferromagnetic double-exchange interaction for the J_3 bond.

3.5 Conclusion

In summary, using magnetic susceptibility, neutron powder diffraction measurements, and first-principles calculations, we find that γ-Fe_2WO_6 possesses two competing magnetic phases with significantly different electronic properties which are closely tied to different local structural distortions that can be introduced during the material synthesis process but without invoking a change of crystalline space group. This study demonstrates that γ-Fe_2WO_6 is an excellent example of correlated material where spin, charge, and lattice degrees of freedom are strongly coupled to each other

CHAPTER 4

TOPOLOGICAL KAGOME METAL FAMILY $Tb_xY_{1-x}Mn_6Sn_6$

4.1 Growth

Single crystals of $Tb_xY_{1-x}Mn_6Sn_6$ were grown using the flux method. The elements Tb, Y, Mn, and Sn were sealed in a quartz ampoule in the ratio $x : 1-x : 6 : 20$, respectively, heated to 1000°C for 10 hours, then allowed to cool to 600°C at a rate of 8°C/hour. At 600°C, the quartz ampoules were centrifuged and the crystals were collected. Samples were grown for $x = 0.1$, 0.175, 0.25, 0.35, and 0.5, where x is the nominal stoichiometry. The true stoichiometry has not been verified.

4.2 Discussion

4.2.1 $x = 0.5$

Fig. 4.1(a) shows the magnetic susceptibility of $Tb_{0.5}Y_{0.5}Mn_6Sn_6$ as a function of temperature under ZFC and FC conditions, and indicates that this material mirrors the pure-Tb parent compound. Magnetic order sets in below 400 K followed by magnetic transition at 280 K. The increase in χ_c below 280 K suggests that the structure goes from an in-plane alignment to an out-of-plane alignment at lower temperature. This is confirmed by the M(H) curves plotted in Fig. 4.1(b) and the transport functions in Fig. 4.2 which show that hysteresis occurs only at lower temperatures when the field is perpendicular to the kagome planes. No additional transitions are suggested by the susceptibility.

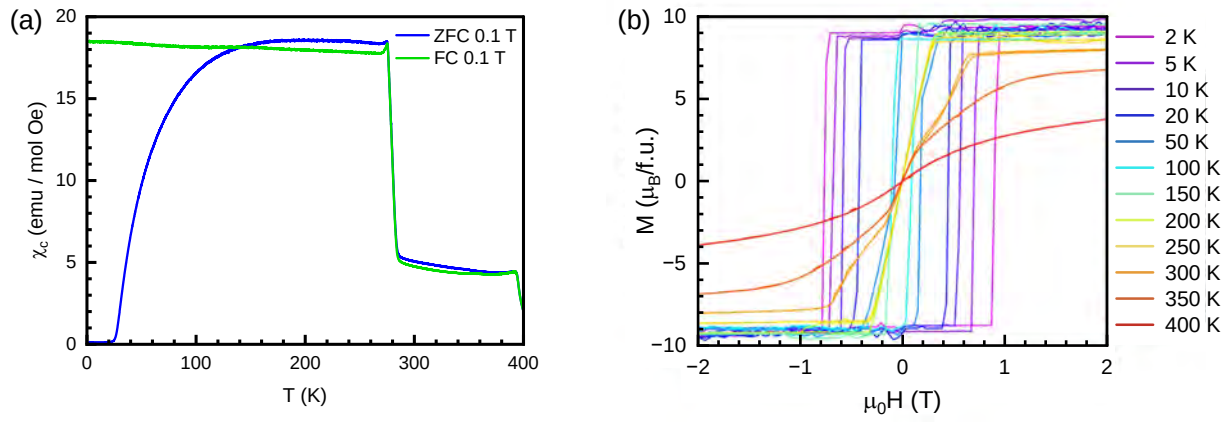

Figure 4.1 Magnetic properties of $Tb_{0.5}Y_{0.5}Mn_6Sn_6$.

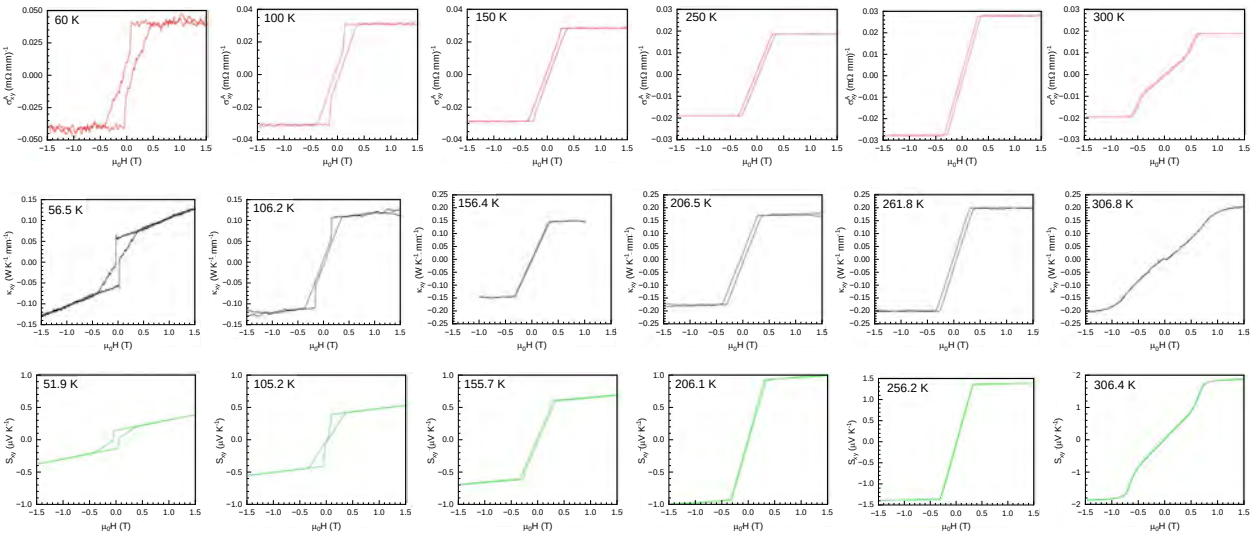

Figure 4.2 Transverse transport properties of $Tb_{0.5}Y_{0.5}Mn_6Sn_6$ under varied field and temperature.

Neutron scattering data shown in Fig. 4.3 confirm the existence of a spin reorientation transition around 280 K with the (0 0 1) magnetic peak being most informative. The magnetic structure form factor $\vec{F}(\vec{Q})$ is the Fourier transform of the spatial distribution of magnetic moments in a crystal, describing how the scattering intensity varies with momentum transfer $\vec{Q}$, and it can be expressed as a sum over the magnetic atoms in the unit cell, where $\vec{S}_n$ denotes the effective magnetic moment of the n^{th} atom located at position $\vec{r}_n$

$$\vec{F}(\vec{Q}) = \sum_n \vec{S}_n e^{i\vec{Q}\cdot\vec{r}_n} \ . \tag{4.1}$$

However, an incident neutron only scatters when its moment is perpendicular to its momentum so the intensity of Bragg peaks is proportional to the component of $\vec{F}$ that is perpendicular to $\vec{Q}$.

$$I(\vec{Q}) \propto \left|\vec{F}_\perp(\vec{Q})\right|^2 \tag{4.2}$$

$$\vec{F}_\perp(\vec{Q}) = \vec{F}(\vec{Q}) - \hat{Q}\cdot\vec{F}(\vec{Q}) \tag{4.3}$$

The intensity of the (0 0 1) peak, shown in Figs. 4.3(a) and (d), is therefore the clearest sign of the reorientation transition. Its intensity begins to rise below 400 K and drops sharply to the background level at 280 K, signaling that the magnetic structure possesses an in-plane component until 280 K when it turns fully out of the plane. The (0 0 2) magnetic peak shows a similar pattern for the same reason, and the (1 0 0) peak shows the opposite behavior because its scattering vector

is perpendicular to the (0 0 1) and (0 0 2) peaks. Below the spin-reorientation temperature, the (0 0 2) and (1 0 0) peaks continue to show temperature dependence that is most likely a result of independent contributions to the form factor from the different magnetic species. Lattice symmetry creates addition and cancellation of magnetic moments that have unique temperature dependence and it results in overall temperature dependence of the observed intensity. As a whole, these data convincingly show an in-plane to out-of-plane transition below 280 K.

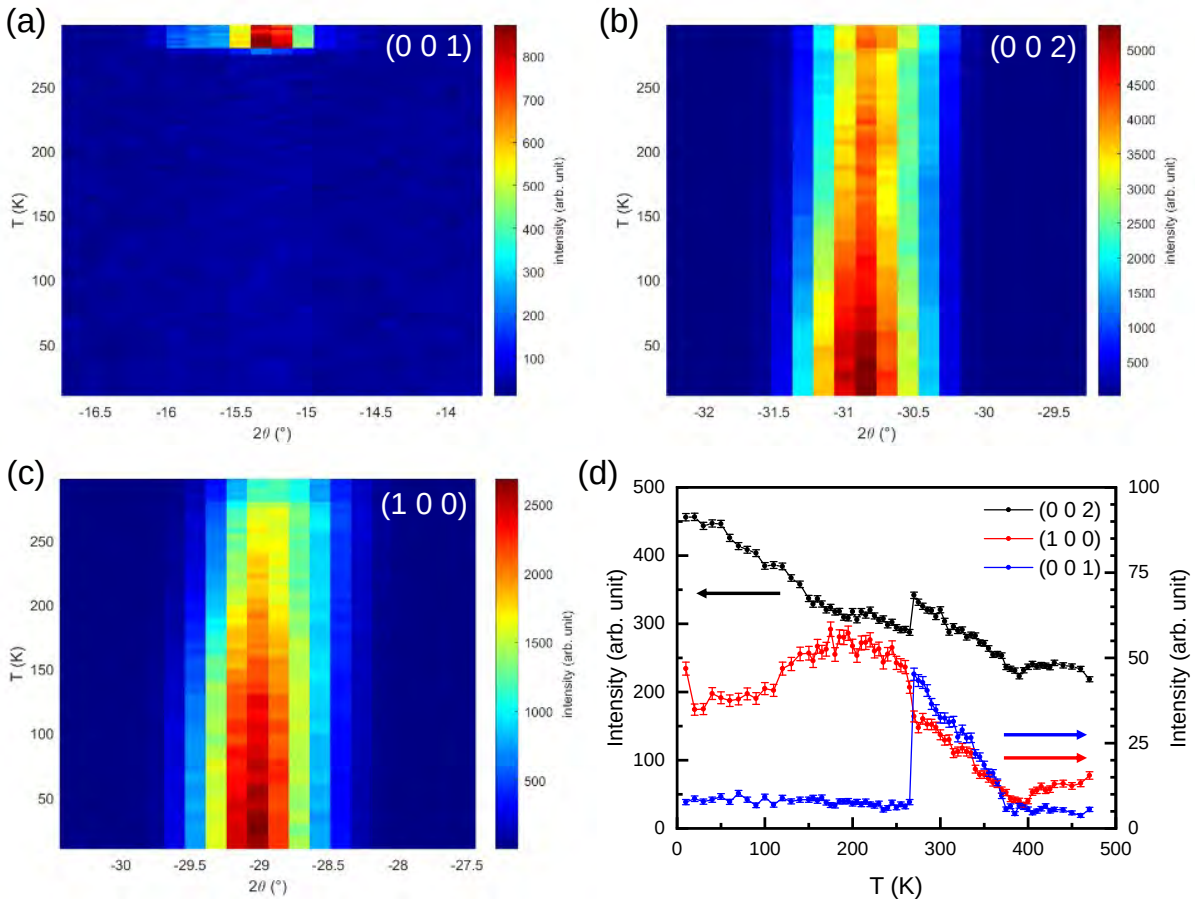

Figure 4.3 Temperature dependence of magnetic Bragg peaks of $Tb_{0.5}Y_{0.5}Mn_6Sn_6$.

4.2.2 $x = 0.35$

The magnetic susceptibility and transport curves for $Tb_{0.35}Y_{0.65}Mn_6Sn_6$, shown in Figs. 4.4 and 4.5, respectively, reveal similar behavior as $Tb_{0.5}Y_{0.5}Mn_6Sn_6$, with the change that transitions are observed at 390 K and 260 K.

Neutron scattering of $Tb_{0.35}Y_{0.65}Mn_6Sn_6$, shown in Fig. 4.6 reveals that this compound also

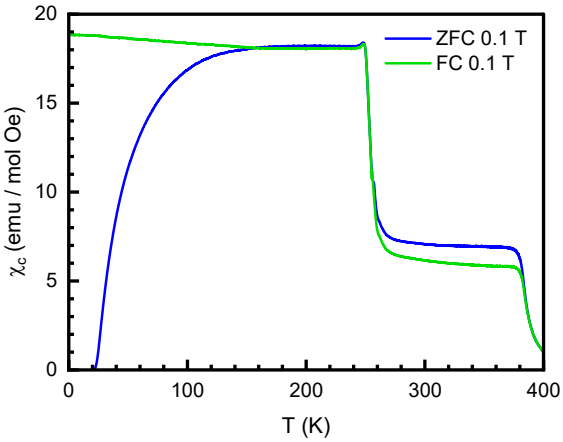

Figure 4.4 Temperature-dependent susceptibility of $Tb_{0.35}Y_{0.65}Mn_6Sn_6$.

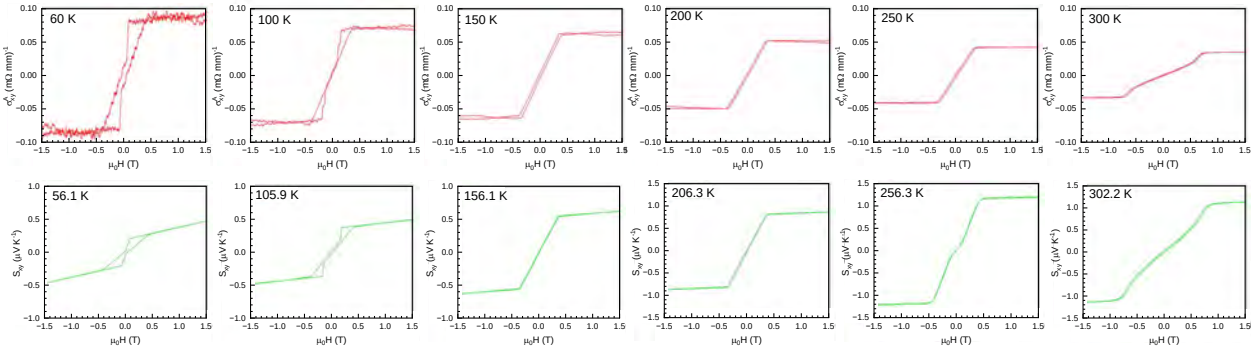

Figure 4.5 Transverse transport properties of $Tb_{0.35}Y_{0.65}Mn_6Sn_6$ under varied field and temperature.

undergoes a spin reorientation from in-plane to out-of-plane directions near 260 K. During data collection, the sample briefly fell out of alignment resulting some incorrect data points which are indicated by arrows in Fig. 4.6.

4.2.3 $x = 0.25$

The susceptibility of $Tb_{0.25}Y_{0.75}Mn_6Sn_6$, plotted in Fig. 4.7 under ZFC and FC conditions, shows the existence of three phase transitions at approximately 360 K, 270 K, and 210 K. Transport properties of this material shown in Fig. 4.8 do not give any new insight into the nature of these phases.

Neutron scattering data of $Tb_{0.25}Y_{0.75}Mn_6Sn_6$, shown in Fig. 4.9, reveals more information of these transitions. Again, there is evidence of a spin reorientation transition from in-plane to out-of-plane directions at 260 K. The (0 0 1) peak increases below 360 K until it falls sharply

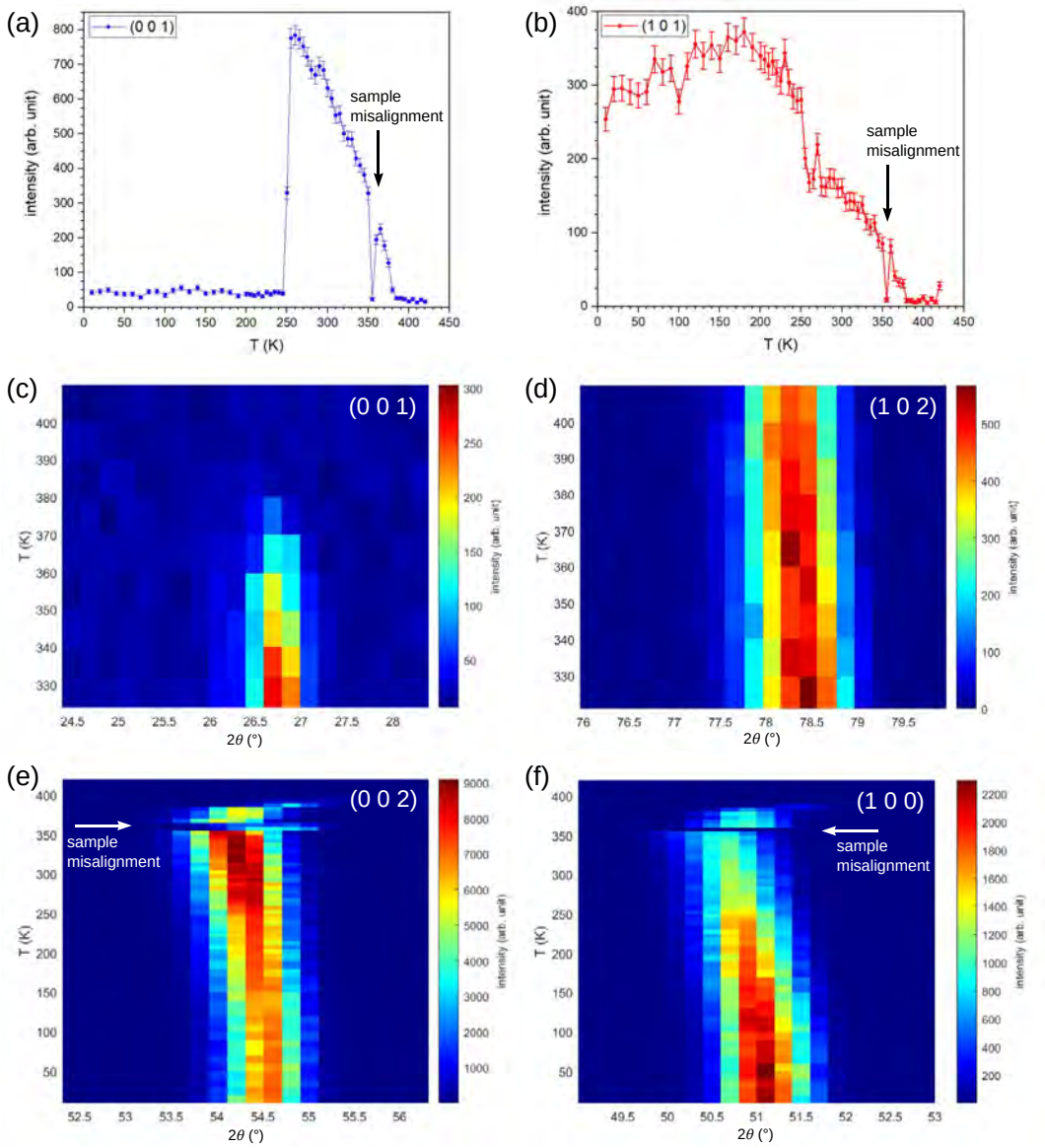

Figure 4.6 Temperature dependence of magnetic Bragg peaks of $Tb_{0.35}Y_{0.65}Mn_6Sn_6$. Some sample misalignment occurred during the measurement and affected data points are indicated by arrows.

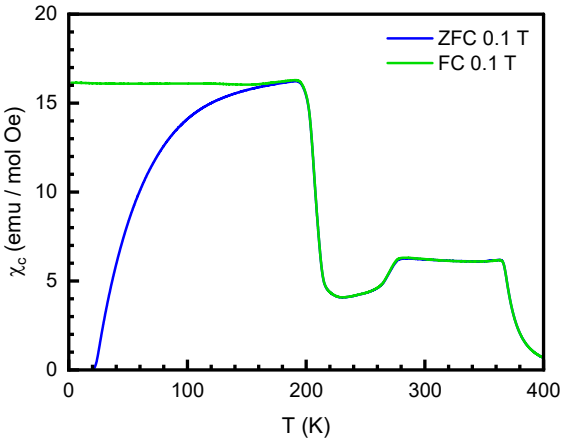

Figure 4.7 Temperature-dependent magnetic susceptibility of $Tb_{0.25}Y_{0.75}Mn_6Sn_6$.

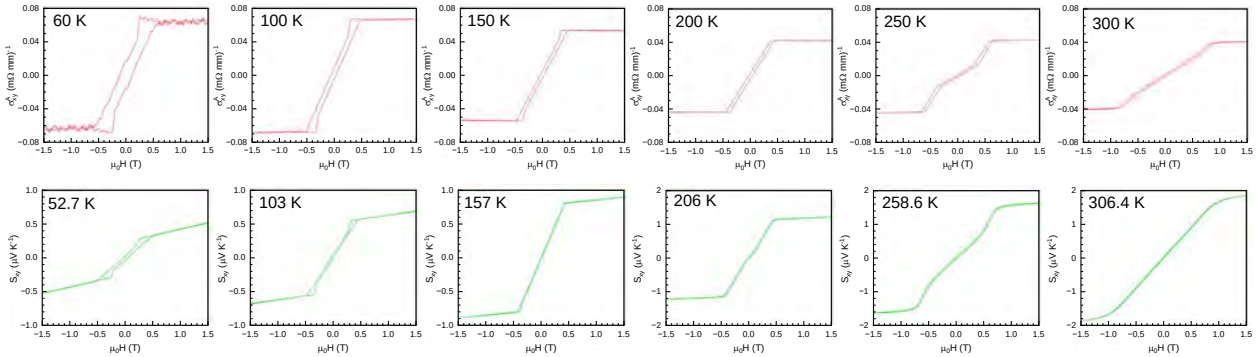

Figure 4.8 Transverse transport properties of $Tb_{0.25}Y_{0.75}Mn_6Sn_6$ under varied field and temperature.

near 270 K. However, a contour plot of the (0 0 2) peak reveals two symmetric satellite peaks at $L = 2 \pm \delta$. The value of δ reaches up to ~ 0.1 reciprocal lattice units (r.l.u) until the satellite peaks completely vanish at 210 K. These satellite peaks indicate the presence of an incommensurate (IC) magnetic phase. The modulation wavelength $\lambda^c_{\text{mod}} = \frac{c}{\delta}$ is temperature dependent. Just above the temperature that the IC phase vanishes, $\delta \sim 0.1$ r.l.u. so λ^c_{mod} begins very large until it falls to a length of roughly 10 unit cells.

The remaining peaks show the same transitions at 350 and 330 K. The falling value of the susceptibility below 350 K suggests that this structure is AntiFM. Below 330 K the IC phase vanishes and the saturated intensity of the (1 0 0) peak plus the near-zero intensity of the (0 0 1) peak tells us that the moments are fully oriented out of the kagome plane. It is not possible to characterize the IC phase further from this data. Future neutron diffraction measurements of a

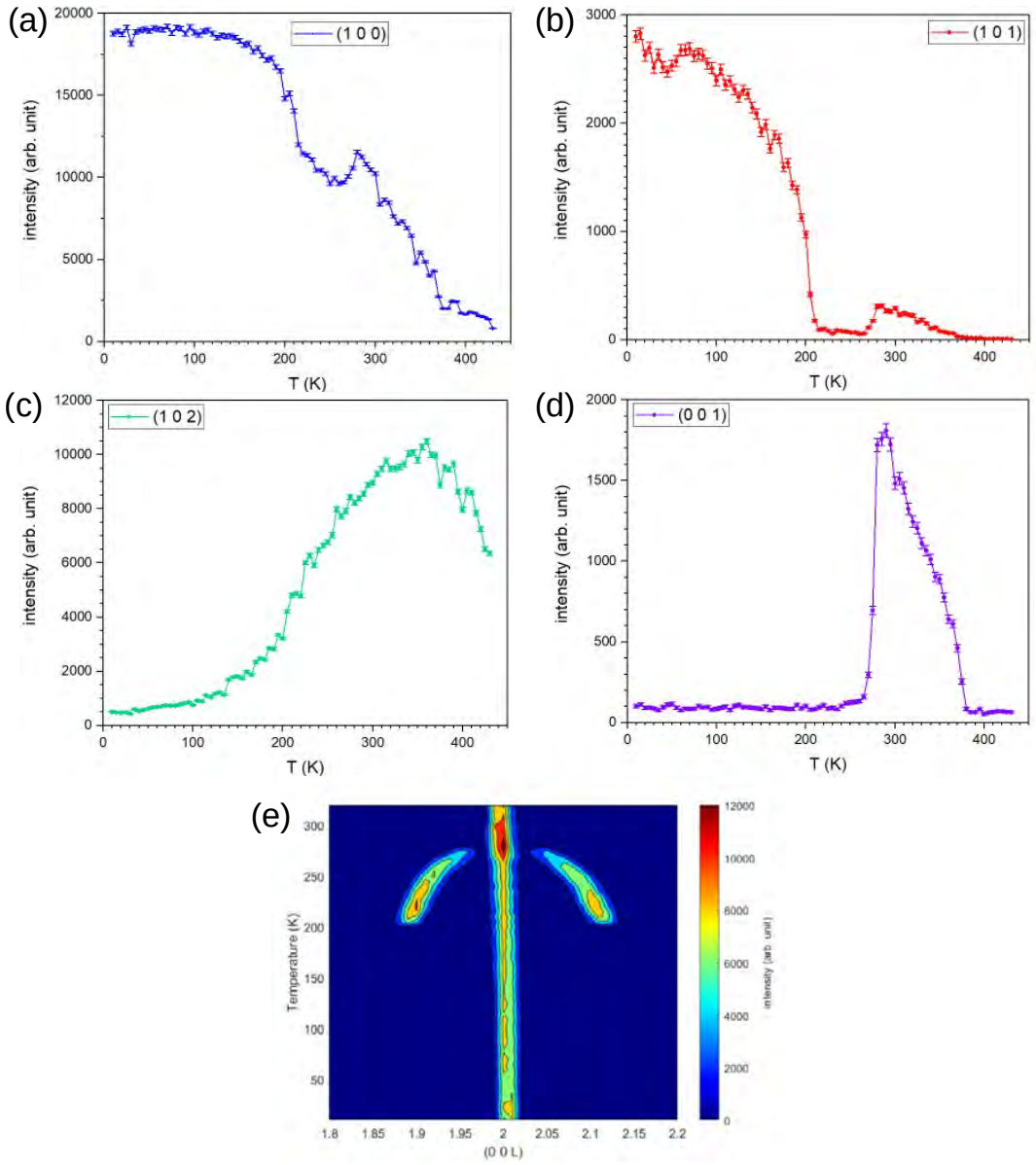

Figure 4.9 Temperature dependence of magnetic Bragg peaks of $Tb_{0.25}Y_{0.75}Mn_6Sn_6$.

powder sample could allow us to resolve the magnetic structure fully.

4.2.4 $x = 0.175$

Magnetic susceptibility of $Tb_{0.175}Y_{0.825}Mn_6Sn_6$ is shown in Fig. 4.11. It shows transitions at approximately 350 K, 330 K, 75 K. Transport coefficients are shown in Fig. 4.11.

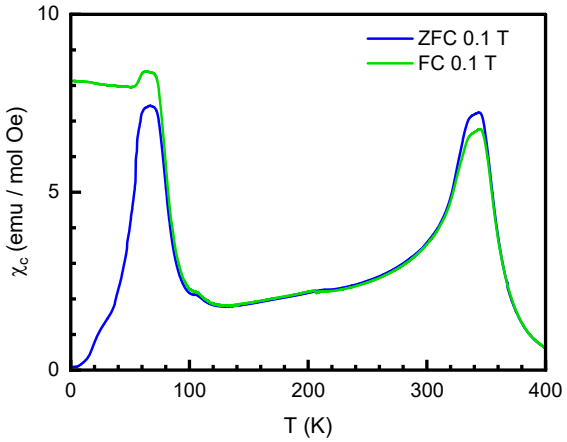

Figure 4.10 Temperature-dependent susceptibility of $Tb_{0.175}Y_{0.825}Mn_6Sn_6$.

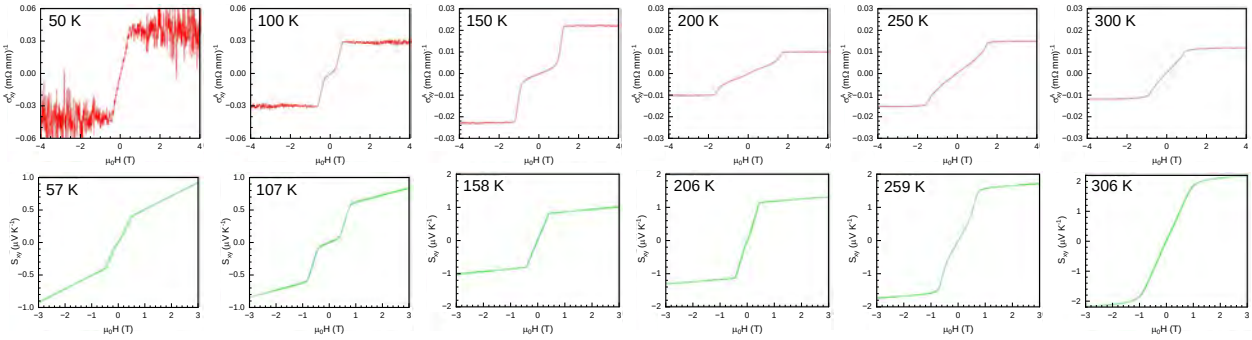

Figure 4.11 Transverse transport properties of $Tb_{0.175}Y_{0.825}Mn_6Sn_6$.

Neutron scattering data for this compound illuminates the nature of these transitions. The Bragg peak intensity contour plot in Fig. 4.12 contains some artifacts due to faulty sample misalignment, but the general picture is still clear. At 350 K, two satellite peaks adjacent to the magnetic (0 0 2) peak appear with a temperature dependent δ that begins close to zero and increases to a stable value near 330 K. Then around 75 K, the satellite peaks shift to a slightly lower δ but remain stable upon further cooling.

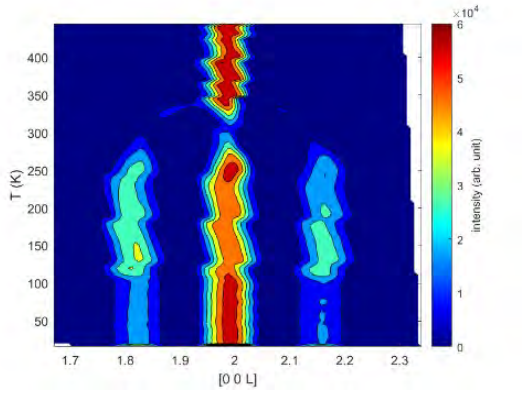

Figure 4.12 Temperature dependence of magnetic Bragg peaks of $Tb_{0.175}Y_{0.825}Mn_6Sn_6$. Some artifacts are present in the data due to sample alignment issues.

4.2.5 $x = 0.1$

Magnetic susceptibility of $Tb_{0.1}Y_{0.9}Mn_6Sn_6$ is shown in Fig. 4.13. It shows transitions at approximately 340 K and 85 K. The declining value of χ_c at low temperatures strongly suggests that the material is antiferromagentic below 340 K. Transport coefficients are shown in Fig. 4.14.

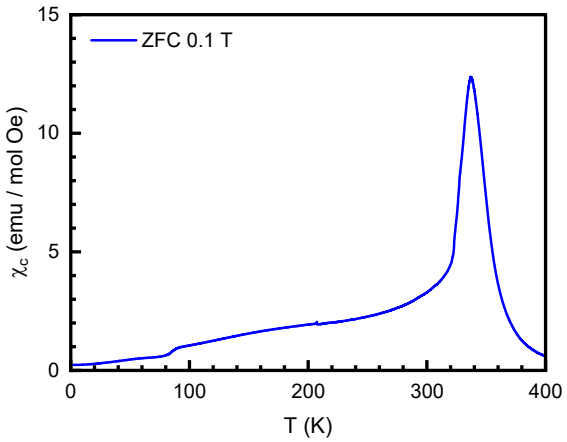

Figure 4.13 Temperature-dependent magnetic susceptibility of $Tb_{0.1}Y_{0.9}Mn_6Sn_6$.

A contour plot around the (0 0 L) magnetic peak reveals the presence of an IC phase throughout the range below 340 K that undergoes a transition at 85 K. The decrease in δ below 85 K tells us that the modulation wavelength λ^c_{mod} increases slightly at lower temperature.

4.2.6 Phase diagram of $Tb_xY_{1-x}Mn_6Sn_6$

To illustrate the differences in magnetic properties of the measured $Tb_xY_{1-x}Mn_6Sn_6$ compounds, the ZFC susceptibilities have been plotted together in Fig. 4.16. By following the

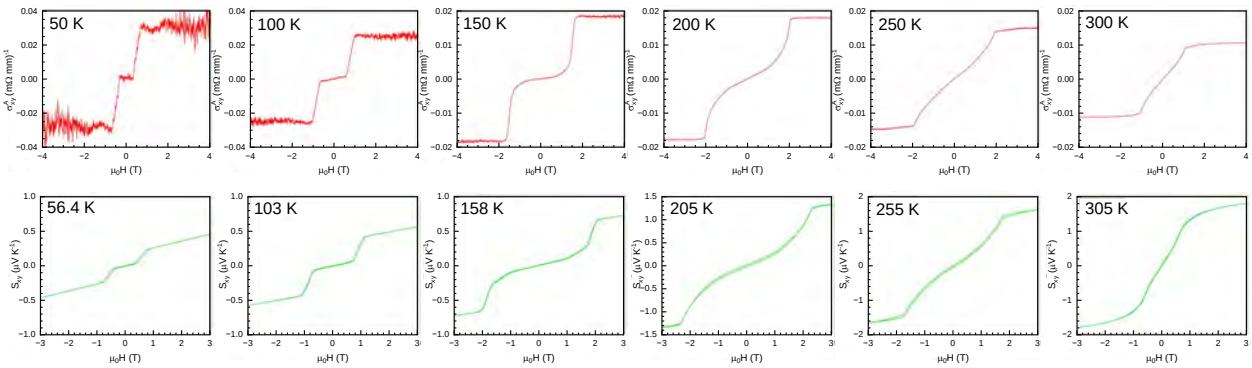

Figure 4.14 Transverse transport properties of $Tb_{0.1}Y_{0.9}Mn_6Sn_6$.

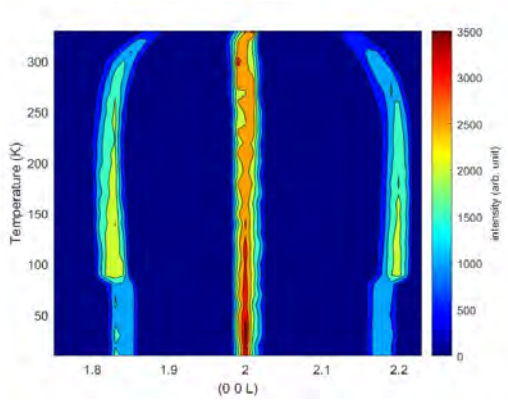

Figure 4.15 Contour plot of the (0 0 2) peak of $Tb_{0.1}Y_{0.9}Mn_6Sn_6$ plotted over temperature.

progression of transition temperatures across the range of samples paired with the neutron scattering data that tells us about the nature of the magnetic structures, we can create a phase diagram of this family of compounds across the full range of x which is shown in Fig. 4.17.

First we note that there is no evidence to support an easy cone phase for any sample as was suggested by previous studies. [220, 221] Instead, samples in the range $x \geq 0.35$ have only one transition from in-plane to out-of-plane FiM phases which is in agreement with more recent studies. [222, 223, 224]

The phase diagram also shows that the gradual replacement of Y with Tb leads to a few trends. To begin with, T_N generally increases with larger Tb fraction. Since paramagnetism (PM) occurs when sufficient thermal energy is available to overcome the energetic barriers in the magnetic Hamiltonian, it is expected that adding more magnetic interactions would raise the energy needed to reach the PM state. However, our $x = 0.35$ sample had a lower T_N than either end member

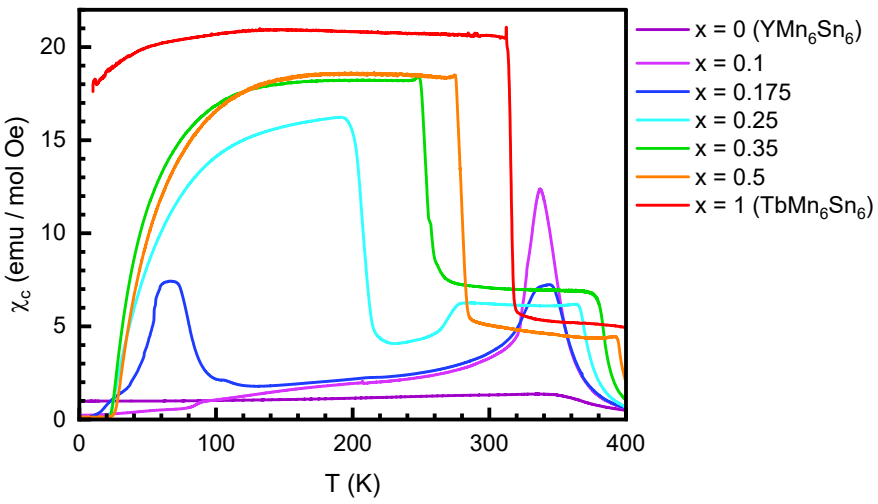

Figure 4.16 Susceptibilities of all measured $Tb_xY_{1-x}Mn_6Sn_6$ samples. Going from one parent compound to the other reveals a rich variation in magnetic properties.

indicating that the magnetic Hamiltonian is affected more subtly than simply including additional exchange interactions. For example, studies of the end members include crystal anisotropy terms in the Hamiltonian and it has been reported that the Mn ions favor an easy axis anisotropy while the Tb ions favor an easy plane anisotropy. [225, 58] The partial contribution of Tb to the Hamiltonian is currently speculative and understanding the cause of lowered T_N warrants future measurements of inelastic neutron scattering.

Comparison of the parent compounds shows that both have in-plane phases, and though they are different in their arrangement of moments, together they form a continuous area within the phase diagram. While we cannot make specific inferences about the nature of the IC phases observed in our samples, it is reasonable to conjecture that low x samples would reflect the magnetic interactions of Mn ions more strongly than those of Tb ions. Studies of the parent compounds have shown that Mn ions favor an easy plane anisotropy while Tb ions favor an easy axis anisotropy. Therefore, addition of Tb has the double affect of stabilizing the competing interactions between Mn atoms that lead to IC phases resulting in a fully commensurate in-plane phase, as well as rotating the whole spin structure to the out-of-plane direction at certain temperatures. It it intriguing that the out-of-plane structure arises at relatively low values of x given that Tb is outnumbered by Mn six to one.

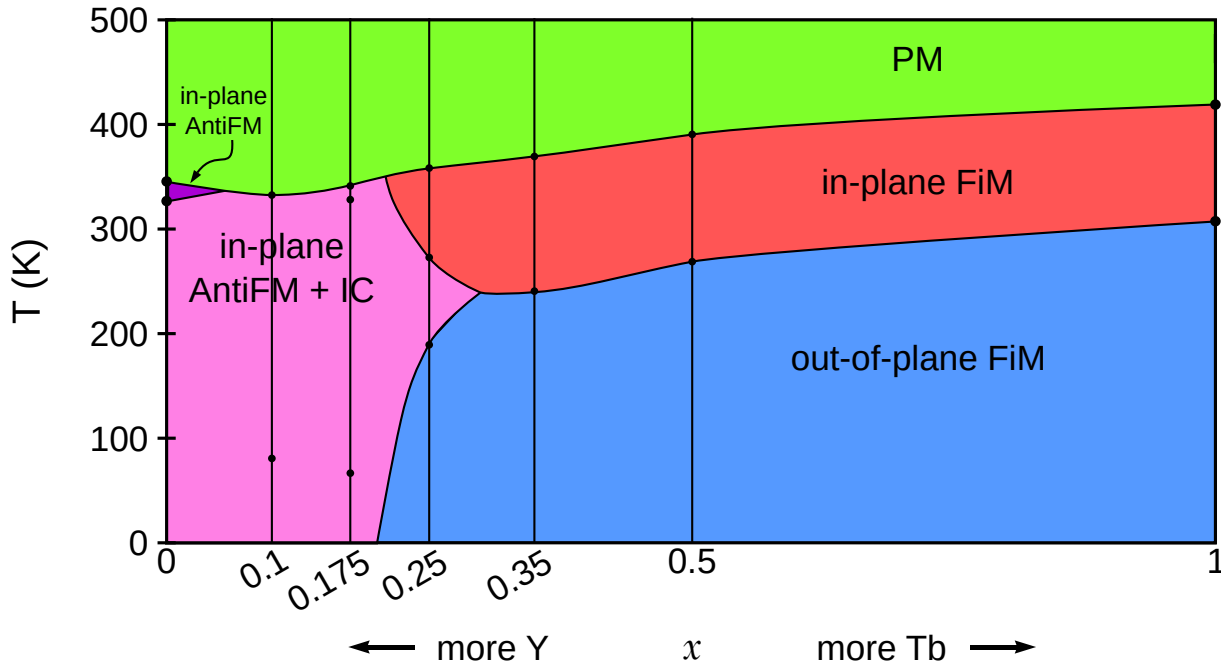

Figure 4.17 Phase diagram of the $Tb_xY_{1-x}Mn_6Sn_6$ group of compounds. Points represent observed transitions or transitions reported elsewhere. Connecting lines are speculative. Vertical lines represent temperature-dependent measurements of the values of x observed in this work.

One arguably unlikely cause to any trends seen in the phase diagram is the change in the crystal unit cell. Since it is impossible to add Tb without changing the crystal structure itself, it is conceivable that some variations of the magnetic structure would reflect changes to the spacing of Mn atoms which would in turn have an affect of their exchange interactions. However, the unit cells of the two end members are almost identical. Comparison of the parent compounds revels that the a and c lattice dimensions vary from 5.54 Åand 9.019 Å, respectively, to 5.53 Åand 9.023 Å, going from $x = 0$ to $x = 1$. [58, 61] Atomic positions within the two unit cells are also nearly unchanged. It is therefore unlikely that trends in the phase diagram can be strongly attributed to physical changes of the unit cell.

Our most novel observation in this study has been the transient nature of the magnetic IC phases. Previous studies of mixed Y-Tb compounds reported samples that were either purely commensurate or observed incommensurate phases at all temperatures below T_N. In contrast, our $x = 0.25$ sample shows an IC phase within a narrow temperature range bounded between two purely commensurate phases of different natures.

We also see that our IC phases exhibit additional transitions of a scattered nature. Our $x = 0.175$ sample appears to show three distinct IC phases and our $x = 0.1$ sample shows two distinct IC phases. Unfortunately it is not possible to describe these IC phases further without additional neutron scattering data. Additional focus on the $x < 0.35$ range of compounds is needed to fully characterize the nuances of this fascinating family of materials.

4.3 Conclusion

In this chapter, we have studied the $Tb_xY_{1-x}Mn_6Sn_6$ family of compounds and observed a rich variety of magnetic phases. By growing a series of samples with varying values of x and characterizing them from measurements of magnetism, transport properties, and neutron scattering, we have developed a magnetic phase diagram across the range $0 \leq x \leq 1$. This phase diagram sheds light on some of the conflicting data in the study of these materials and supports previously reported results while pointing to novel observations that merit further investigation. Our phase diagram reveals more complexity in the low-Tb end of the spectrum than was previously known, seen from the presence of novel incommensurate phases and multiple transitions within individual samples. We have not been able to characterize these IC phases at this time, but anticipate that interesting new physics may be found stemming from nontrivial topology or complex spin textures.

CHAPTER 5

VAN DER WAALS MATERIALS: METAL TRIHALIDES

5.1 Magnetism and Crystal Structure of VCl_3

5.1.1 Measurements

VCl_3 single crystals were grown by CVT. Vanadium granules (Alpha Aesar, 99.7%) and TeCl4 powder (Acros Organics, 99%) were mixed in a molar ratio of 2:3 and sealed in an evacuated quartz tube which was loaded into a two-zone furnace heated to 700°C at the hot end and 600°C at the cold end. After a reaction period of 10 days, the ampoule was cooled to room temperature and millimeter-size plate-like crystals such as the one shown in Fig. 1(a) were collected. The crystals are moisture sensitive and they degrade within minutes in air.

Heat capacity measurements were conducted according to the method described in Section 2.1. Magnetic susceptibility was measured with a commercial SQUID magnetometer as described in Section 2.3. Neutron powder diffraction measurements using POWGEN at ORNL, as described in Section 2.2.3. The neutron diffraction data were refined using the Fullprof suite to obtain the crystal structure as described in Section 2.2.4. [187]

5.1.2 Discussion

To determine the magnetism of VCl_3, we measured the temperature dependence of magnetic susceptibility with an applied field of 0.1 T along the c axis under ZFC conditions, as shown in Fig. 5.1(b). As the temperature decreases from 200 K, the susceptibility increases and then undergoes an AntiFM transition. The Néel temperature T_N, which is defined as the maximum of the derivative $\frac{d\chi}{dT}$, is found to be 21.7 K. In the inset of Fig. 5.1(b) a subtle kink is present at T_S = 104 K, which can be attributed to the structural phase transition revealed in the NPD data. Above 150 K, the susceptibility follows the Curie-Weiss law

$$\chi = \frac{C}{T - T_C} + \chi_0 \tag{5.1}$$

where χ_0 is an additional term to Eq. 1.3 for a temperature-independent paramagnetic susceptibility, C is the Curie constant and T_C is the Curie-Weiss temperature. In Fig. 5.1(c), we plot the temperature

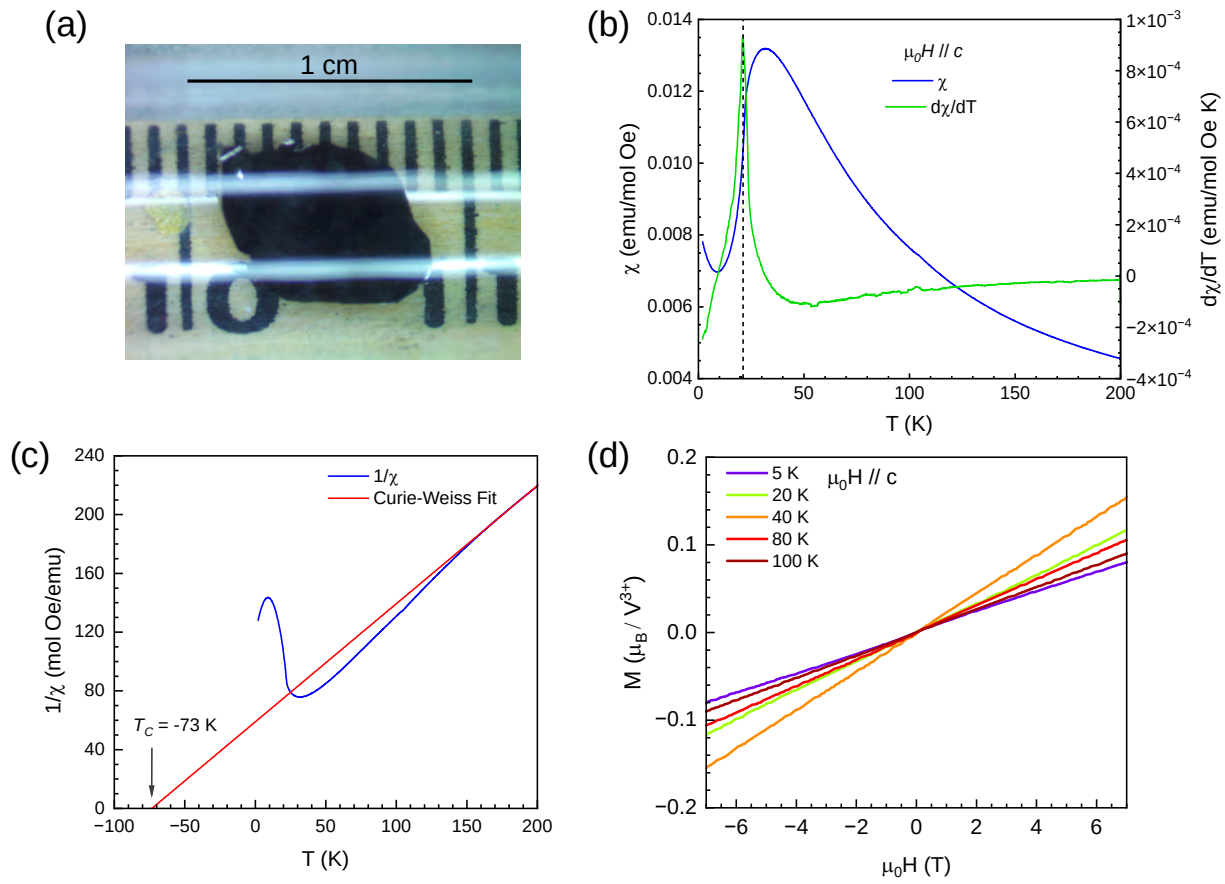

Figure 5.1 (a) An optical image of an as-grown VCl_3 single crystal sealed inside a quartz tube. (b) Temperature dependence of the magnetic susceptibility χ_c and its temperature derivative. The inset shows an expanded view near the structural phase transition T_S. (c) The temperature dependence of inverse magnetic susceptibility and the Curie-Weiss fit. (d) Isothermal magnetization measured at various temperatures.

dependence of $1/\chi$ together with the Curie-Weiss fit. It yields $T_C = -75$ K and the slope $1/C = 0.80$ mol Oe/emu K. The negative value of T_C indicates that antiferromagnetic interactions dominate the magnetic behavior. The effective magnetic moment μ_{eff} can be calculated from the Curie constant using

$$\mu_{eff}^2 = \frac{3k_B C}{\mu_B^2 N_A} \tag{5.2}$$

where the k_B is Boltzmann's constant, μ_B is the Bohr magneton, and N_A is Avogadro's constant. The obtained μ_{eff} is 3.15 μ_B, which is slightly larger than the V^{3+} spin-only value (S = 1) of 2.83 μ_B. Plots of the isothermal magnetization with magnetic field applied at various magnitudes in the c axis, which are presented in Fig. 5.1(d), show that the magnetization increases linearly

without achieving saturation, indicating strong antiferromagnetic interactions such that 7 T is not large enough to ferromagnetically polarize VCl_3 completely.

Both the AntiFM transition and structural phase transition are also reflected in specific heat and thermal conductivity measurements. Fig. 5.2(a) presents the temperature dependence of specific heat measured at 0 and 9 T magnetic fields. Two sharp features are clearly seen around 104 K and 21.7 K, with the former feature remains intact at all applied fields while the latter one shifts to slightly lower temperature at 9 T, corresponding to the crystallographic and magnetic transitions, respectively. For magnetic system, the heat capacity can be written as

$$C = C_{el} + C_{ph} + C_{mag} \tag{5.3}$$

where the three terms on the right hand of the equation represent the contribution of conduction electrons, phonons, and magnons. Here the first term C_{el} can be neglected because VCl_3 is a large gap semiconductor, thus the equation can be simplified to

$$C = C_{ph} + C_{mag} \tag{5.4}$$

Because VCl_3 has a layered structure, we can extract C_{mag} by subtracting the contribution of C_{ph}, which is found by fitting the heat capacity data to the 2D Debye model

$$C_{ph} = \alpha N k_B \left(\frac{T}{\theta_D}\right)^2 \int_0^{\frac{T}{\theta_D}} \frac{x^2\, dx}{e^x - 1} \tag{5.5}$$

where $a\alpha$ is a proportionality constant, N is the number of atoms per unit volume, and θ_D is the Debye temperature. [226] The selected fitting range is from 47 K to 75 K to avoid the contribution from both spin fluctuation and structural transition. The best fit for C_{ph} is plotted as the red curve shown in Fig. 5.2(a), and θ_D is found to be 217 K. The extracted C_{mag} at zero field is depicted in Fig. 5.2(b). The saturated value of the integrated magnetic entropy S_{mag} is about 6.8 $J{\cdot}K^{-1}mol^{-1}$, which is smaller than the theoretical value for $S = 1$. An applied magnetic field of 9 T reduces C_{mag} due to the suppression of magnetic excitations, as is clearly seen in the inset of Fig. 5.2(b).

Fig. 5.2(c) shows the temperature dependence of longitudinal thermal conductivity κ_{xx} measured at 0 T and 9 T. Just as in the specific heat data, two features are observed at T_N and

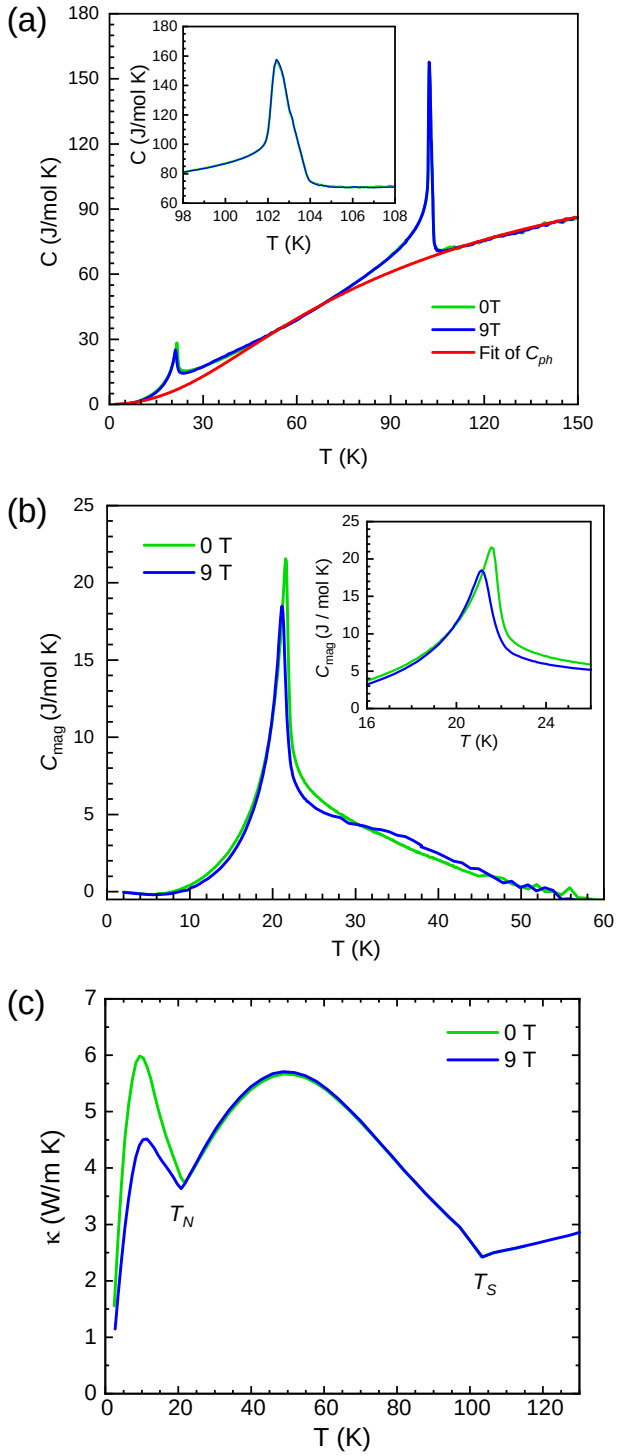

Figure 5.2 (a) Temperature-dependent heat capacity C measured at 0 and 9 T. The inset shows an expanded view near the structural phase transition. (b) The temperature dependence of C_{mag}. The inset shows an expanded view near the magnetic phase transition. (c) Longitudinal thermal conductivity κ_{xx} as a function of temperature measured at 0 and 9 T.

T_S, corresponding to magnetic and structural phase transitions, respectively. Above T_N, κ_{xx} is dominated by the phonon contribution. The competition between Umklapp and phonon-impurity scattering, which dominate in different temperature regions, leads to a broad maximum near 50 K. Below T_N, magnons can also contribute to heat conduction so κ_{xx} increases significantly. Applying a strong magnetic field largely reduces the magnon population suppressing κ_{xx} below T_N. This feature is in sharp contrast to what was reported on ferromagnetic VI_3 which shows an increase of κ_{xx} in the presence of large magnetic field due to the suppression of phonon scattering by magnons, implying much weaker magnon-phonon coupling in VCl_3 compared to VI_3. [74]

To probe the crystal structure above and below T_S as well as the magnetic structure below T_N, we have performed NPD measurements on VCl_3 powder obtained by grinding pieces of single crystals. Figs. 5.3(a) and (b) show the NPD data measured at 200 and 7 K on the POWGEN beamline at SNS, and the inset in Fig. 5.3(b) shows an expanded view of the comparison of these two diffraction patterns. Extra Bragg reflections due to peak splitting are clearly observed at 7 K, which originates from the structural phase transition to a crystal structure with reduced symmetry at lower temperatures. This is supported by the Q-T contour map shown in Figs. 5.3(d) and (e) where peak splitting at multiple Q values occurs below T_S.

Crystal structures of VCl_3 above and below T_S are solved by refining the NPD data shown in Figs. 5.3(a) and (b), respectively. The 200 K data can be fitted to the previously reported BiI_3-type structure belonging to space group $R\bar{3}$ (No. 148). As shown in Fig. 5.4(a) and (b), the edge-sharing VCl_6 octahedra drawn individually in Figs. 5.4(c) and (d) form undistorted honeycomb layers in the *ab*-plane separated by vdW gaps along the *c*-axis, with ABC stacking of the vanadium ions. To determine the low-temperature crystallographic structure, we employed the program ISODISTORT to generate the possible low-symmetry structures and attempted to fit the data with each of them. [227, 228] The best fit was achieved with a structure belonging to space group $P\bar{1}$ (no. 2). This low-temperature structure preserves the honeycomb lattice of V atoms without any buckling, albeit with slight distortions in the hexagons as shown in Figs. 5.4(e) and (f), and a small increase in interlayer separation. Detailed crystallographic information, including lattice parameters and

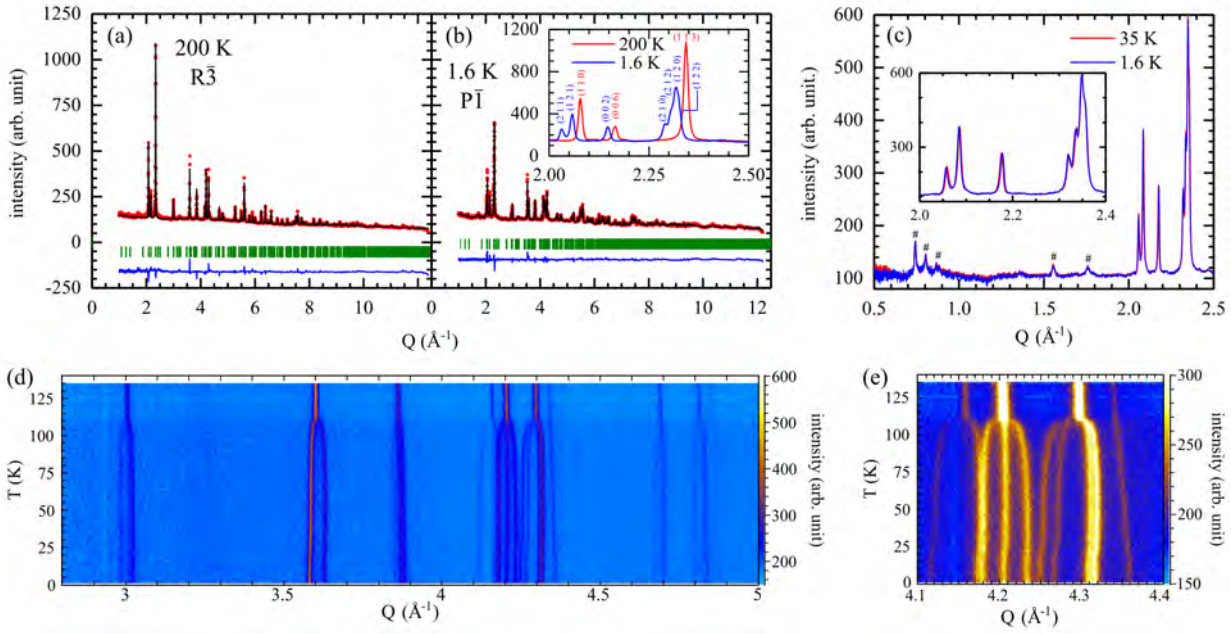

Figure 5.3 (a,b) Neutron diffraction patterns measured at 200 K and 7 K, respectively. The red dots represent the experimental data, while the black solid curves show the Rietveld fitting. The vertical bars display the Bragg peak positions of the crystal structure, and the continuous blue curves at the bottom of the figures show the difference between the experimental and calculated intensity. The sample can was loaded inside a helium displex. (c) Comparison of the diffraction patterns at low Q measured at T = 35 K and 1.6 K, showing no discernable magnetic peaks below T_{N}. The peaks denoted by # are background peaks appearing at both temperatures. The inset shows an expanded view. The sample can was loaded inside an orange cryostat. (d) T–Q contour plot of neutron diffraction data showing a structural phase transition occurring at T_{s}. Note that the nominal value (110 K) of T_{s} here is slightly larger than T_{s} obtained from specific heat and thermal conductivity measurements, mainly due to the relatively slow thermal equilibrium in neutron measurements during the warm-up process by sweeping the temperature. (e) An expanded view of the T–Q contour plot near Q = 4 Å^{-1}.

atomic positions, for both high- and low-temperature crystal structures is summarized in Tables 5.1 and 5.2. In the low-temperature $P\bar{1}$ structure, one pair of V-V bonds are appreciably shorter (≈1.3%) than the other two pairs, as illustrated in Fig. 5.4(f), forming a dimer-like structure. Such a feature is similar to what was reported in VI_3 below T_S whose V-V bond length varies by ≈ 0.76%. [229, 230]

We also attempted to determine the magnetic structure from the neutron diffraction measurements. However, as shown in Fig. 5.3(c), the NPD data show no discernible magnetic Bragg peaks measured at 1.6 K compared to the data measured at 35 K (above T_N). Within the instrumental

Table 5.1 Comparison of high- and low-temperature crystal structures and lattice parameters.

	200 K	1.6 K
Space group	$R\bar{3}$	$P\bar{1}$
a (Å)	6.049	10.6749(6)
b (Å)	6.049	6.111(1)
c (Å)	17.417	6.8296(5)
α	90°	90.316(12)°
β	90°	59.036(8)°
γ	120°	90.86(1)°
V–V interlayer separation (Å)	5.8057(2)	5.8565(7)

resolution, there is no noticeable change in intensity of the nuclear Bragg peaks and no appearance of new Bragg peaks at low Q. This suggests that VCl_3 possesses a magnetic ordered state with a small moment size (< 0.3 μ_B per V, which is limited by the instrumental resolution) despite the $S = 1$ configuration of V^{3+}. We also performed neutron diffraction measurements on a VCl_3 single crystal using the four-circle neutron diffractometer (HB3A) equipped with an area detector. Again, no sign of magnetic Bragg reflections was observed below T_N within the instrumental resolution.

Table 5.2 Atomic positions of the high- and low-temperature crystal structures.

Atom	Wyckoff pos.	x	y	z
		T = 200 K		
V	6c	0	0	0.3333
Cl	18f	-0.0137(6)	0.3190(5)	0.0780(7)
		T = 1.6 K		
V	2i	0.6667	0.6667	0
Cl1	2i	0.5696(16)	0.2621(10)	0.2665(14)
Cl2	2i	0.9204(13)	0.5652(11)	0.2538(11)
Cl3	2i	0.248(2)	0.9083(17)	0.2739(14)

Several scenarios could account for the indiscernibly small ordered moment in VCl_3. First, it is likely that VCl_3 ($S = 1$, $L = 1$ for V^{3+}) possesses a large orbital moment antiparallel to the spin moment and strong SOC, a feature similar to VI_3 which shows a magnetic moment of 1.3 μ_B instead of 2 μ_B per V^{3+}. [229, 231, 232] In this case, one would expect even larger orbital moment canceling the spin moment in VCl_3 than in VI_3, considering that the former compound has a much smaller magnetic moment and weaker SOC compared to the latter. Second, since V^{3+} ions occupy

the honeycomb lattice and the dominant exchange interactions are antiferromagnetic as implied by the negative Curie-Weiss temperature, the potential magnetic exchange frustration can suppress the ordered moment. Third, the dimer-like structure of V-V bonds shown in Fig. 5.4(f) may yield a spin-singlet state, while the weaker interdimer interactions leads to the long-range magnetic ordered state with a smaller ordered moment. Future studies, such as measurements of Muon spin rotation and inelastic neutron scattering as well as first-principles density functional theory calculations, are warranted to understand the magnetic ordering of VCl_3 and its underlying mechanisms.

5.1.3 Conclusion

In conclusion, we have studied crystal structure, and magnetic and thermal transport properties of a magnetic vdW material VCl_3. We show that VCl_3 undergoes a structural phase transition from a space group of $R\bar{3}$ to $P\bar{1}$ at $T_S = 104$ K followed by an antiferromagnetic transition at $T_N = 21.7$ K. Despite the long-range order, no magnetic Bragg reflections are revealed in neutron diffraction measurements, suggesting a small ordered magnetic moment in VCl_3 which may be associated with large orbital moment of V^{3+}, geometrical magnetic frustration, or potential spin-dimer structure induced by structural distortion.

5.2 Transport Study of $V_xCr_{1-x}I_3$ Compounds

5.2.1 Growth of $V_xCr_{1-x}I_3$ for $x = \frac{1}{2}, \frac{1}{3}, \frac{1}{4}$

VI_3 and CrI_3 single crystals were grown by CVT. Vanadium granules and iodine powder were mixed in a molar ratio of 1:3 with a slight excess of iodine, and sealed in an evacuated quartz tube which was loaded into a two-zone furnace heated to 650°C at the hot end and 550°C at the cold end. VI_3 crystals were collected after four days of growth. Similarly, chromium granules and iodine powder were mixed in a molar ratio of 1:3 with a slight excess of iodine, and sealed in an evacuated quartz tube which was loaded into a two-zone furnace heated to 650°C at the hot end and 350°C at the cold end. CrI_3 crystals were collected after four days of growth.

$V_{1/2}Cr_{1/2}I_3$, $V_{1/3}Cr_{2/3}I_3$, and $V_{1/4}Cr_{3/4}I_3$ single crystals were grown by mixing VI_3 and CrI_3 crystals in a 1:1, 1:2, and 1:3 molar ratio, respectively, sealed in an ampule, and loaded into a two-zone furnace heated to 650°C at the hot end and 450°C at the cold end. Crystals of were

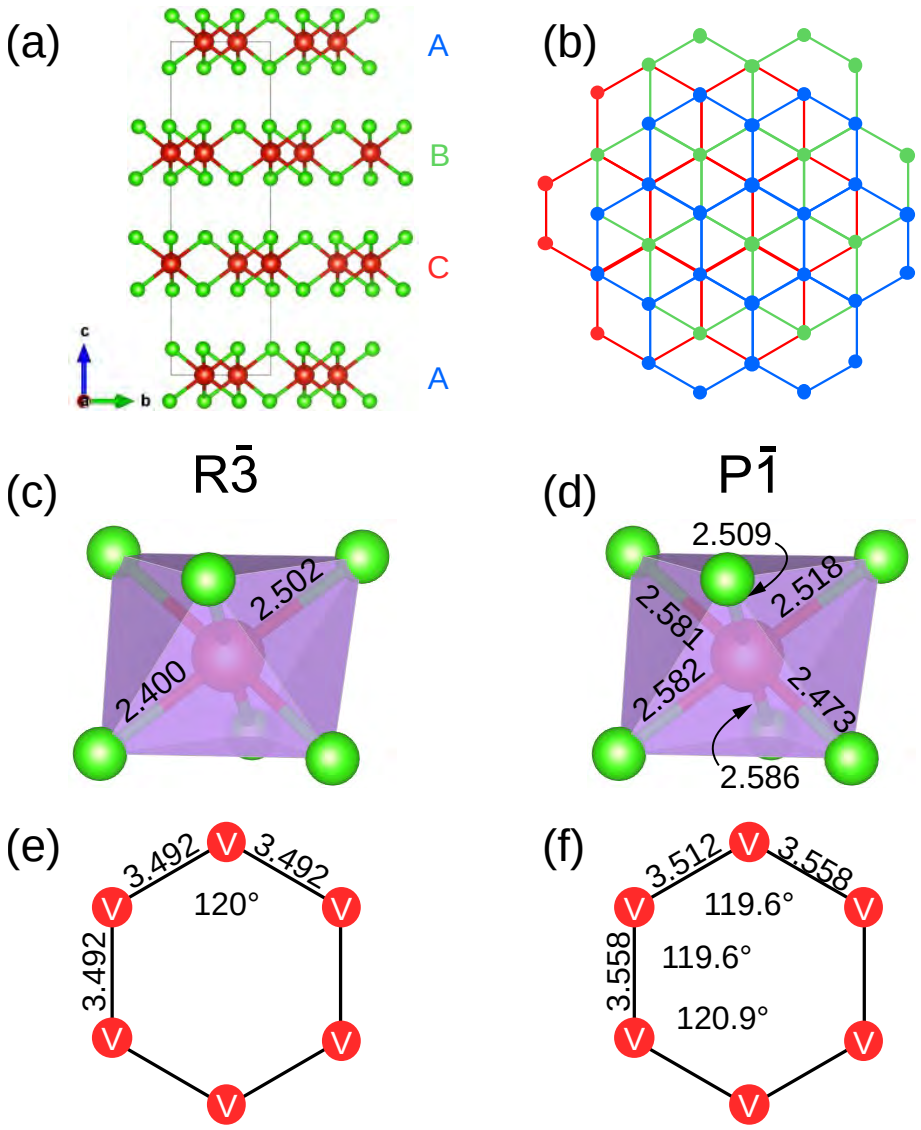

Figure 5.4 (a,b) Side view and top view of the crystal structure of VCl_3, respectively. The vanadium atoms form ABC-stacked honeycomb layers separated by van der Waals (vdW) gaps. (c,d) and (e,f) show schematics of VCl_6 octahedra and the vanadium honeycomb lattice for the high-temperature $R\bar{3}$ phase and the low-temperature $P\bar{1}$ phase, respectively. Bond angle and V–V bond length are denoted.

collected after seven days.

5.2.2 Measurements

Fig. 5.5 shows the susceptibility and magnetization of a single crystal of $V_{1/2}Cr_{1/2}I_3$. Both FC and ZFC susceptibilities measured perpendicular and parallel to the hexagonal plane reveal a magnetic transition around 50 K and another small feature at 79 K which is likely due to a structural transition. The magnetization also shows a transition to magnetic order below 60 K with a saturated moment of $1.6\mu_B$/f.u. and a coercive field of about 1.5 T. The longitudinal conductivity κ_{xx} as a function of field and temperature is shown in Fig. 5.5. The field dependence shows an increased conductivity under applied magnetic field indicating strong magnon-phonon coupling for reasons explained in Section 1.3.7. The temperature-dependent plot also possesses a higher-temperature feature that is likely due to a structural transition. Fig. 5.6 show the transverse thermal conductivity of this material κ_{yx} which mirrors the magnetization in its hysteresis and transition temperature. However, the maximum value of κ_{yx}, which is plotted in Fig. 5.7, is temperature dependent reflecting the change in number of thermal carriers and scattering frequency.

Because crystals of this group of compounds are thin and flat, we checked the reproducibility of our measurements by selecting a very small specimen that was convincingly a single crystal to minimize the risk of accidentally measuring multiple crystallites. The out-of-plane susceptibility is shown in Fig. 5.9 and it appears to show two distinct magnetic transitions at $\sim$ 50K and $\sim$ 60 K which are indicated by arrows. These temperatures are close to the transition temperatures of VI_3 and CrI_3 and they imply that the sample reflects the combined properties of VI_3 and CrI_3 independently rather than novel properties.

Fig. 5.10 shows the susceptibility and magnetization of a single crystal of $V_{1/3}Cr_{2/3}I_3$. FC and ZFC susceptibilities show a magnetic transition at 58 K, with no additional transition visible below 100 K. The out-of-plane magnetization shows a saturated moment of $3\mu_B$/f.u. and a coercive field of about 0.6 T. The longitudinal thermal conductivity is shown in Fig. 5.11 and it increases when a magnetic field is applied suggesting strong magnon-phonon coupling. The transverse thermal conductivity, shown in Fig. 5.12, displays very unusual behavior in that shape of the hysteresis

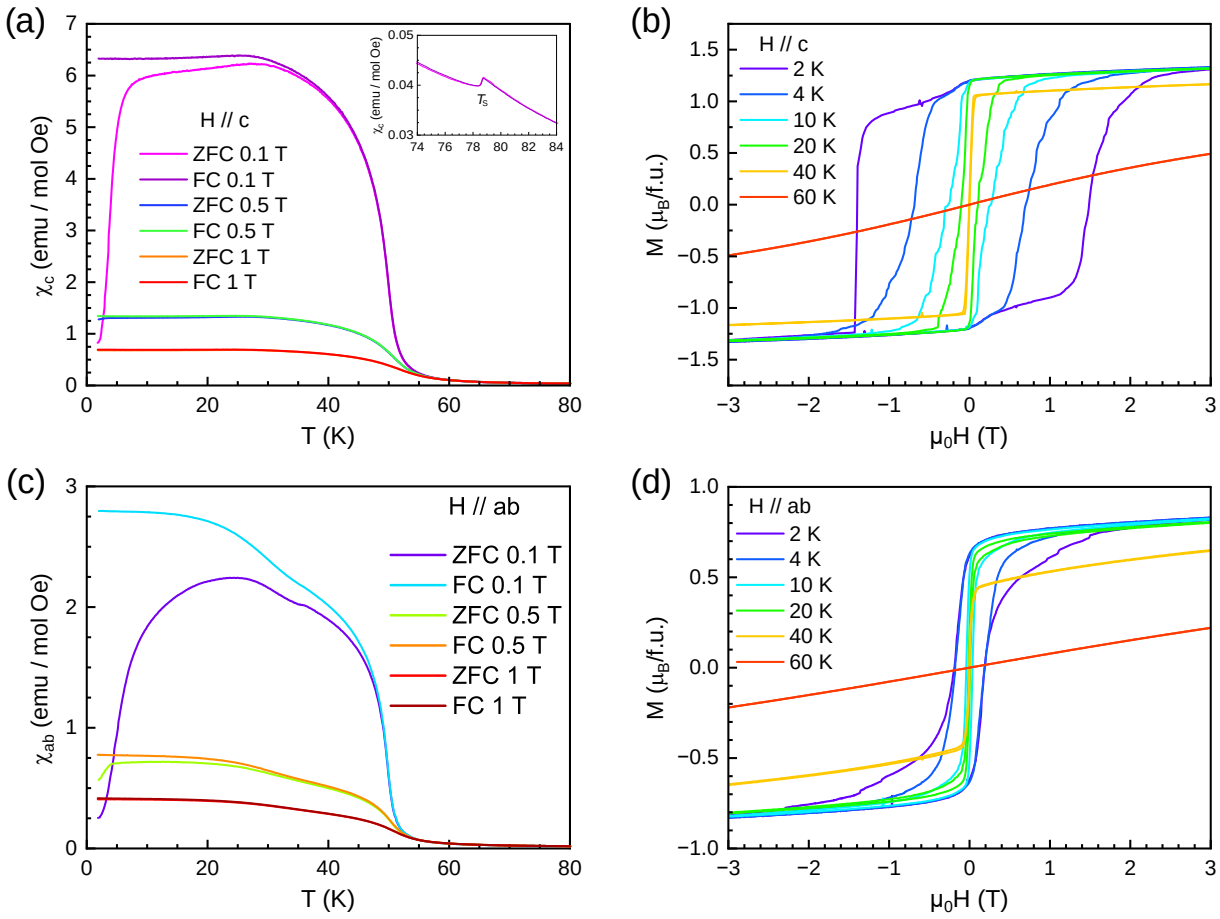

Figure 5.5 Magnetic properties of $V_{1/2}Cr_{1/2}I_3$ (a) Temperature dependent magnetic susceptibility along the *c* axis. (b) Field dependent magnetic moment in the *c* axis at various temperatures. (c) Temperature dependent magnetic susceptibility in the *ab* plane. (d) Field dependent magnetic moment in the *ab* plane at various temperatures.

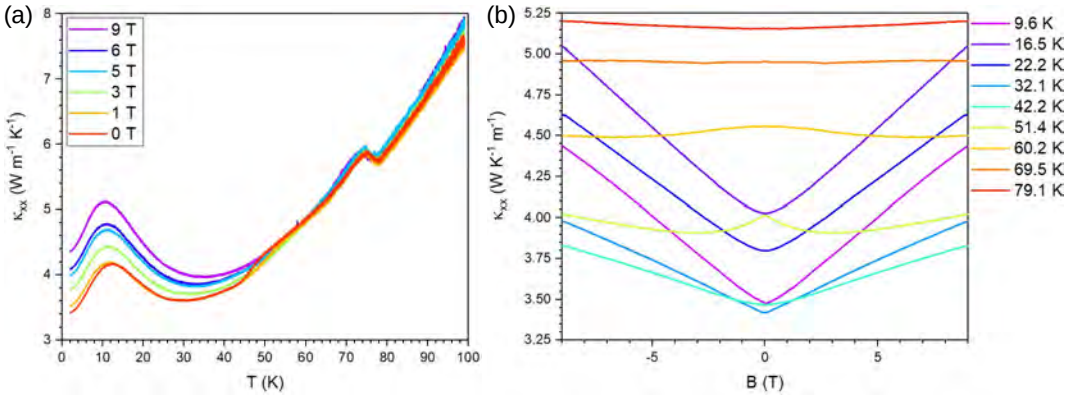

Figure 5.6 Longitudinal thermal conductivity κ_{xx} of $V_{1/2}Cr_{1/2}I_3$ under (a) varied temperature and (b) varied field.

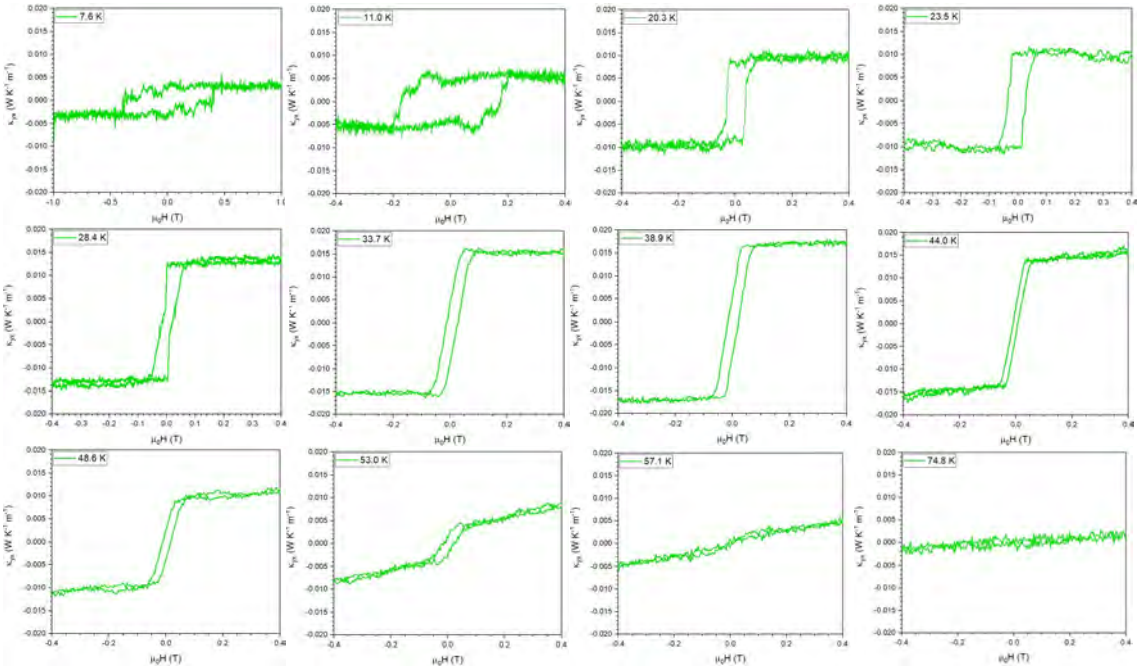

Figure 5.7 Transverse thermal conductivity κ_{yx} of $V_{1/2}Cr_{1/2}I_3$ under varied magnetic field, plotted at several temperatures.

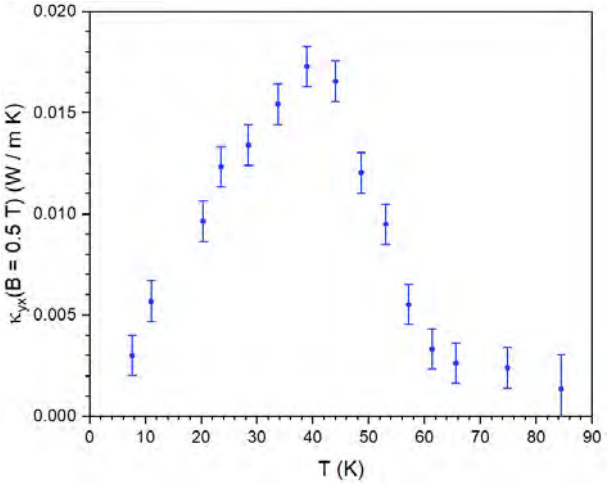

Figure 5.8 Saturation value of κ_{yx} for $V_{1/2}Cr_{1/2}I_3$.

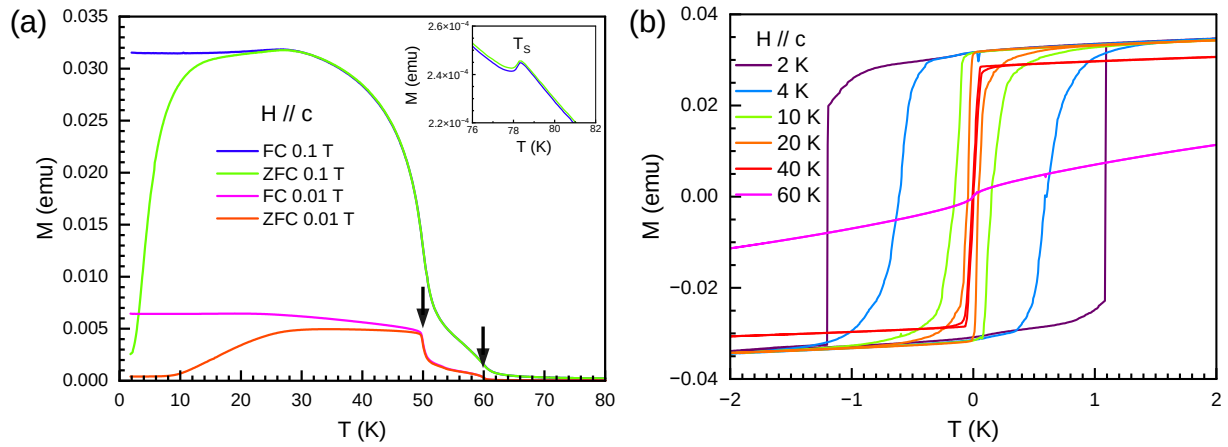

Figure 5.9 Magnetic properties of a second sample of $V_{1/2}Cr_{1/2}I_3$ of unknown mass. (a) Temperature dependent magnetic moment (unnormalized) along the c axis. This curve may show two transitions that reflect the properties of VI_3 and CrI_3 individually, indicated by arrows. (b) Field dependent magnetic moment (unnormalized) in the c axis at various temperatures.

becomes inverted near 25 K. The saturation value of κ_{yx} is plotted in Fig. 5.13.

Fig. 5.14 shows the susceptibility and magnetization of a single crystal of $V_{1/4}Cr_{3/4}I_3$. FC and ZFC susceptibilities show a magnetic transition at 58 K, with no additional transition visible below 100 K. The out-of-plane magnetization shows a saturated moment of $2.2\mu_B$/f.u. and a coercive field of about 0.8 T. Thermal conductivity was not measured for this material.

5.2.3 Discussion

Some similarities can be identified for the three $V_xCr_{1-x}I_3$ materials studied here. The M(H) curves all show hysteresis perpendicular and parallel to the honeycomb plane, but the width of the hysteresis is much larger out of the plane. This indicates that the magnetic structures of these materials have a large FM component out of the plane and a significancy smaller FM component within the plane. This is in contrast to both VI_3 and CrI_3 whose magnetic structures are FM only out of the plane. Therefore, mixing V and Cr atoms results in modified exchange interactions and a more complex magnetic structure. Furthermore, the M(H) curves show that saturation is reached in the out-of-plane direction at much lower fields than for the in-plane direction suggesting an easy axis anisotropy. This anisotropy appears to be weakest in the $V_{1/2}Cr_{1/2}I_3$ where the in-plane moment reached the highest saturation value for equal field strength.

Only samples of $V_{1/2}Cr_{1/2}I_3$ showed a clear structural transition below 300 K and it brings

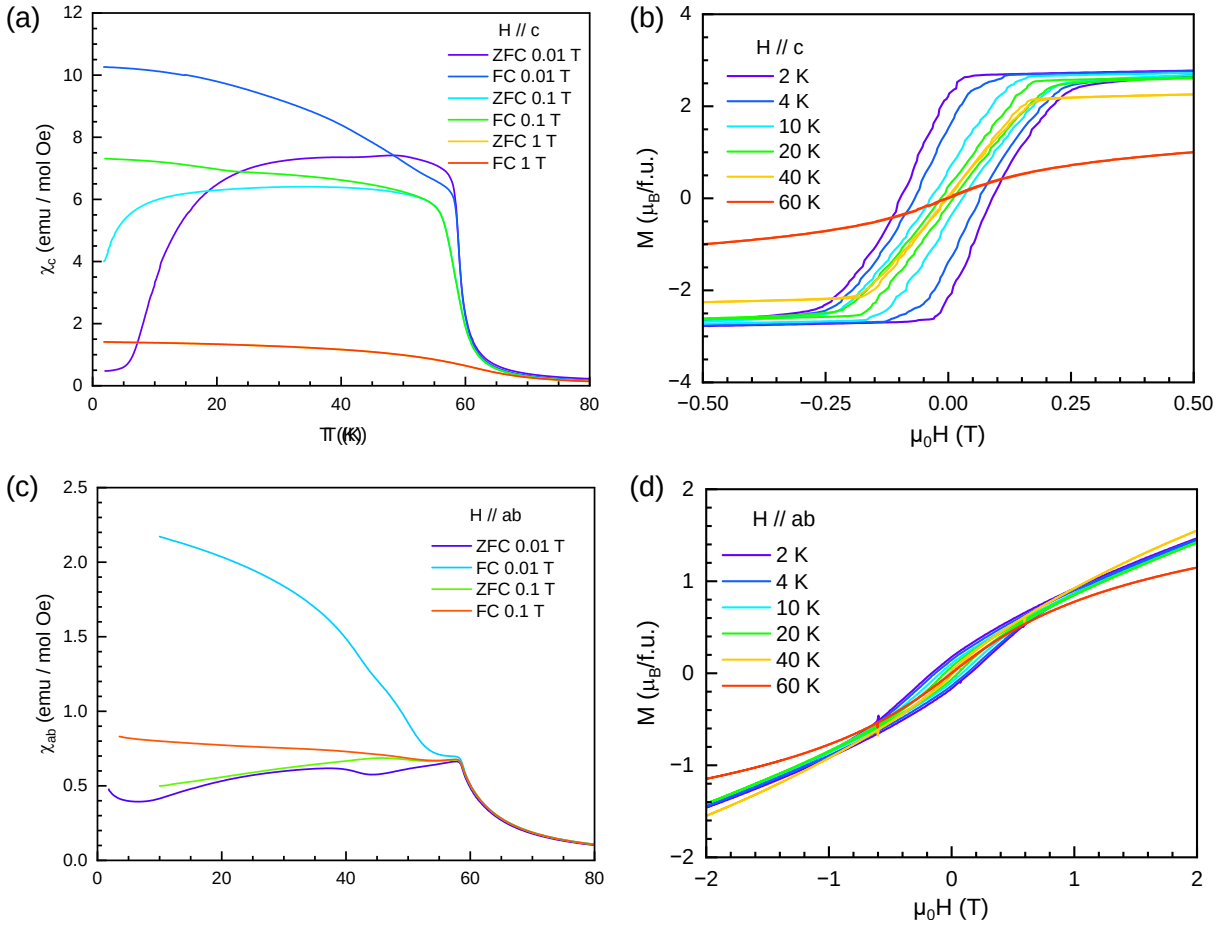

Figure 5.10 Magnetic properties of $V_{1/3}Cr_{2/3}I_3$ (a) Temperature-dependent magnetic susceptibility along the *c* axis. (b) Field-dependent magnetic moment in the *c* axis at various temperatures. (c) temperature dependent magnetic susceptibility in the *ab* plane. (d) Field dependent magnetic moment in the *ab* plane at various temperatures.

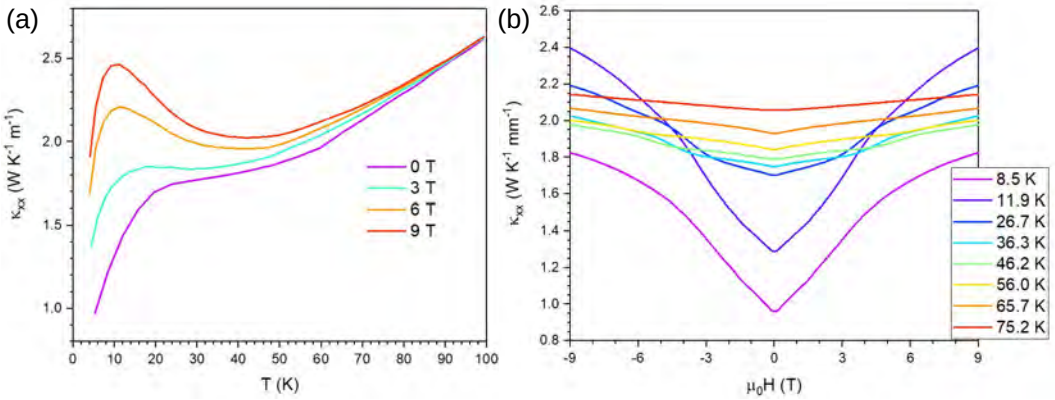

Figure 5.11 Longitudinal thermal conductivity κ_{xx} of $V_{1/3}Cr_{2/3}I_3$ under (a) varied temperature and (b) varied field.

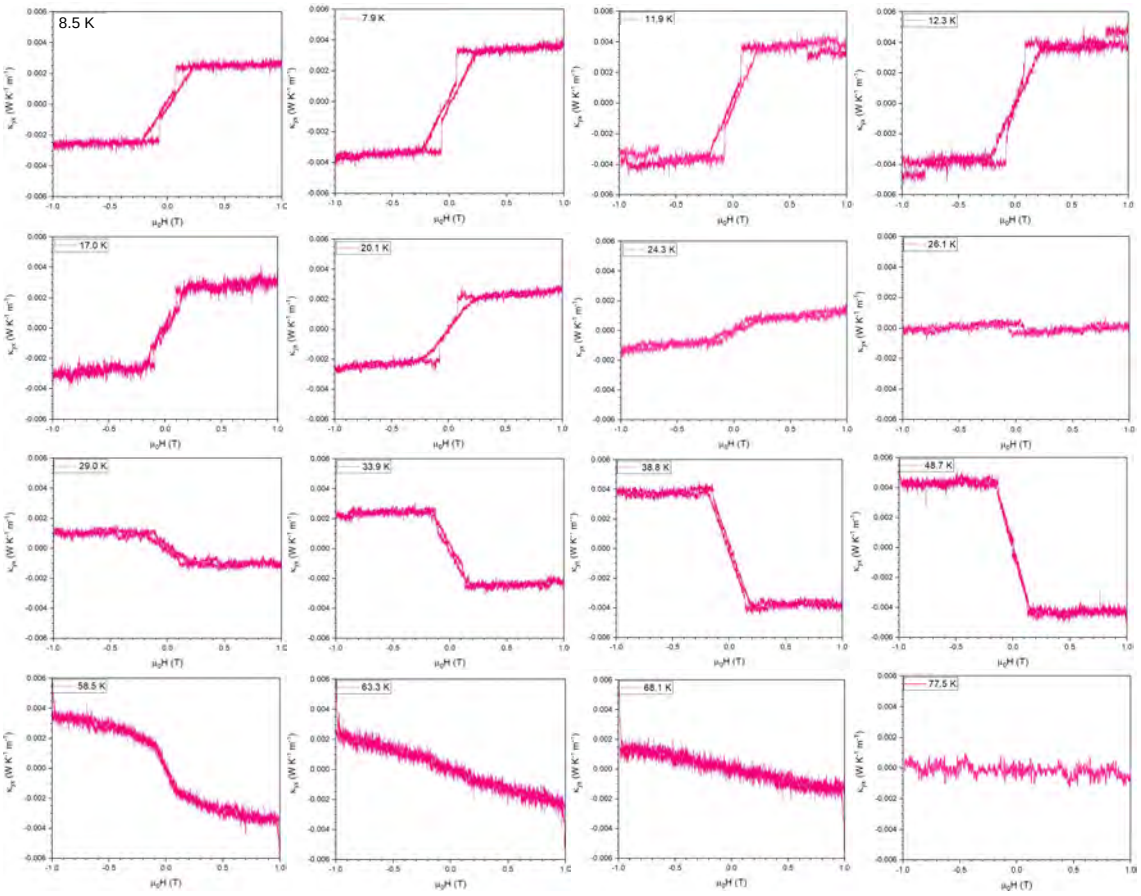

Figure 5.12 Transverse thermal conductivity κ_{yx} of $V_{1/3}Cr_{2/3}I_3$ under varied magnetic field, plotted at several temperatures. The shape of the hysteresis loop becomes inverted near 25 K.

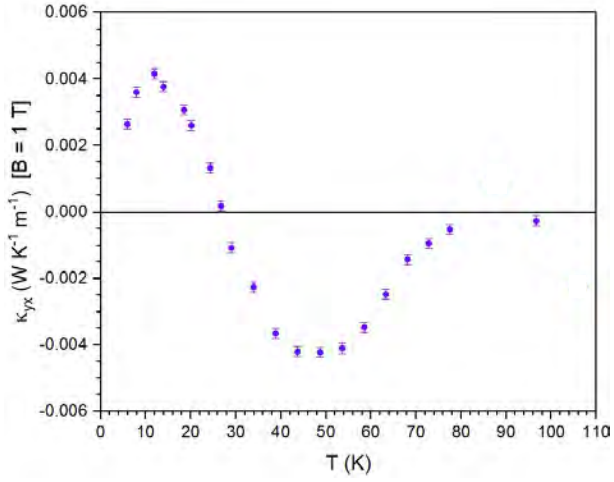

Figure 5.13 Saturation value of κ_{yx} for $V_{1/3}Cr_{2/3}I_3$.

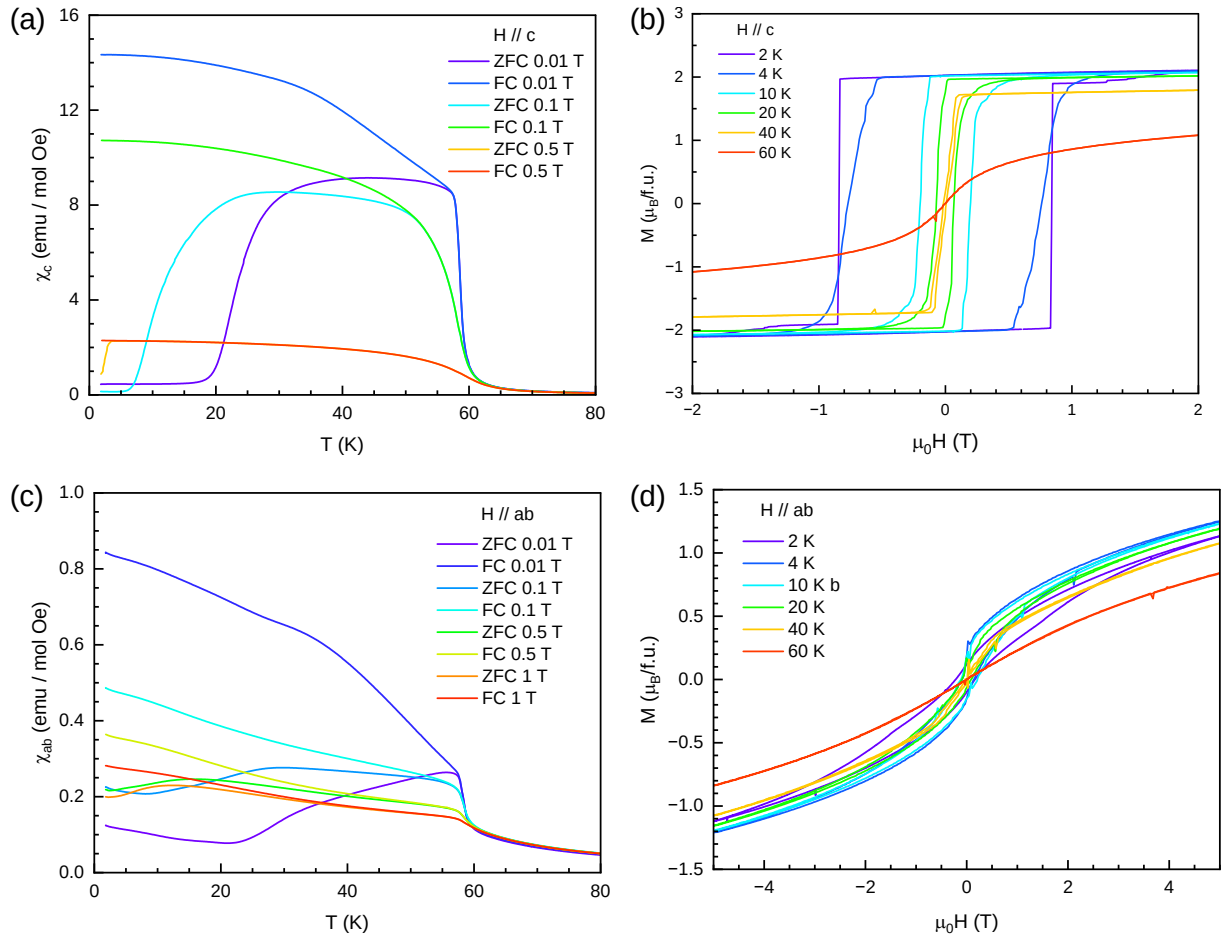

Figure 5.14 Magnetic properties of $V_{1/4}Cr_{3/4}I_3$ (a) Temperature dependent magnetic susceptibility along the *c* axis. (b) Field dependent magnetic moment in the *c* axis at various temperatures. (c) temperature dependent magnetic susceptibility in the *ab* plane. (d) Field dependent magnetic moment in the *ab* plane at various temperatures.

into question how V and Cr atoms are distributed within a single crystal. Samples of $V_{1/2}Cr_{1/2}I_3$ suggested that VI_3 and CrI_3 could be present as separate phases that act independently. However, this is not certain since we would expect to see the magnetic properties of VI_3 and CrI_3 also appear individually in the M(H) curves, which is not the case.

Thermal transport measurements of the two measured samples both showed magnon-phonon coupling and the thermal Hall effect, which is also expected of the parent compounds. For $V_{1/2}Cr_{1/2}I_3$, the THE mirrors the behavior of the magnetization, but for $V_{1/3}Cr_{2/3}I_3$ the THE undergoes a sign inversion at $\sim$ 25 K which is not seen in the magnetization. This phenomenon may be the sign of a topological phase transition, as was predicted for certain Kagome lattice

ferromagnets with the DM interaction. [233] Honeycomb lattices can support the DM interaction on next-nearest-neighbor bonds so the nature of the THE sign inversion may reflect similar underpinnings. However, the parent compounds have opposite signs of the THE and if the samples studied here were composed of non-interacting phases of VI_3 and CrI_3, it may be the case that THE observed here only reflects the sum of the two components. At present, neither XRD nor neutron scattering has been conducted for these samples, which could illuminate how V and Cr atoms are mixed.

5.2.4 Conclusion

In conclusion, we have studied the magnetic and thermal transport properties of three members of the family $V_xCr_{1-x}I_3$. Early results suggest that a new magnetic structure evolves from the mixture of V and Cr atoms, unique from the parent compounds and these materials may potentially host a novel kind of topological phase transition. However, before a solid conclusion can be reached, the nature of V and Cr mixing must be determined by additional measurements.

CHAPTER 6

PREPARATION OF DIAMOND SAMPLES FOR HALL EFFECT MEASUREMENTS

6.1 Introduction

Though electrical transport measurements on doped diamond have been reported in the literature (Section 1.7.7 has many examples), the steps for preparing a sample are not readily available and depend on the tools available to the diamond grower. The steps developed in this chapter are outlined in Fig. 6.1. The major hurtles were in patterning the photoresist, which required eliminating the large edge bead (discussed in Section 6.3), and growing diamond in the pattern, which required a hard mask that could withstand the reactor environment (Section 6.4). The uniqueness of DS5 also adds to the unknowns, since it cannot directly be compared to any other diamond reactor.

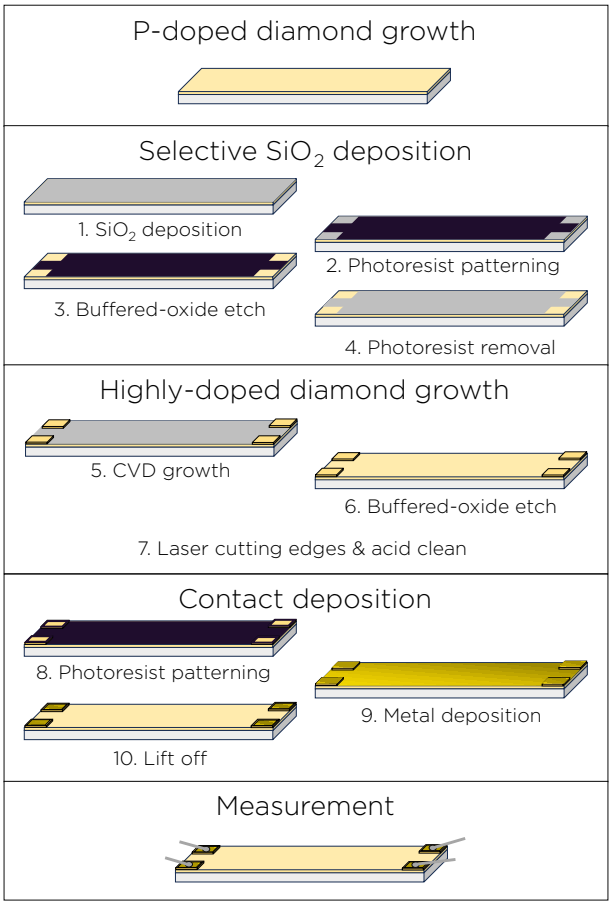

Figure 6.1 The steps required to prepare a PDD sample for electrical transport measurements.

6.2 Reactor Study

Temperature is an important parameter for diamond growth, however DS5 does not have the means to set the temperature of a diamond during growth directly. Temperature is determined by several factors including pressure, MW power, sample holder height, gas flow rate, and the balance of input gases. Of these, only MW power can be easily adjusted during growth. Therefore, for the diamond substrate to reach the desired temperature quickly during growth, a good guess of the required MW power is needed before the growth begins so that only fine tuning is necessary in the early phase of growth.

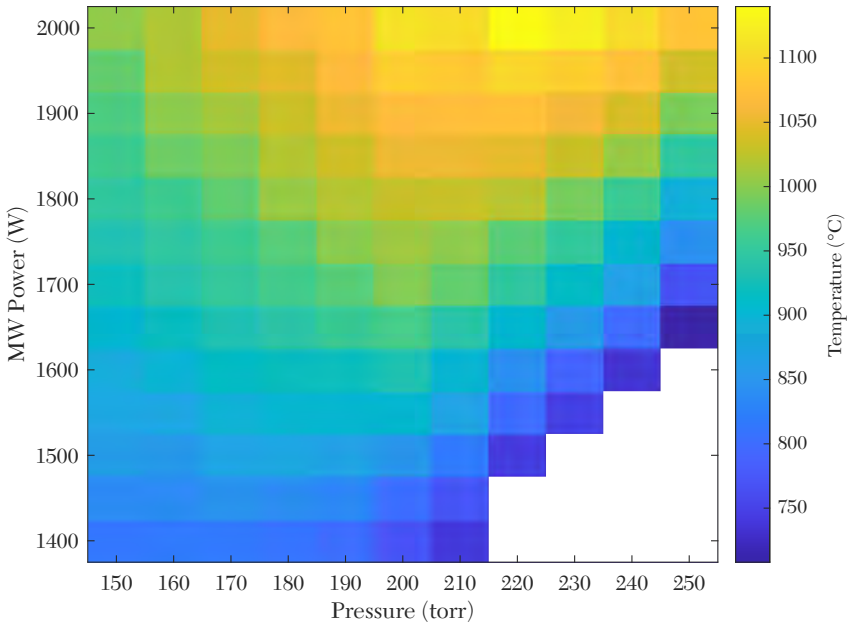

Figure 6.2 Diamond temperature under varied pressure and power in DS5.

To observe the relationship between pressure, MW power, and temperature, we varied the pressure and power and observed the temperature of a $\sim 300\mu$m thick diamond substrate placed on the flat pocket holder with a gas flow of 348 sccm H_2. This flow rate was chosen because it is equal to the total gas flow rate of Fraunhofer's n^+ recipe which is provided in Table 2.1. Methane and phosphine were substituted with hydrogen to avoid growing graphite-containing diamond. Graphite has a different emissivity coefficient and could skew the temperature reported by the optical pyrometer. The temperatures measured over the range of 150 to 250 torr and 1400 to

2000 W is shown in Fig. 6.2. Blank regions represent temperatures below the detection limit of the pyrometer, which is 700°C.

6.3 Spin-Coating Small Samples

Preparing a diamond for a Hall effect measurement requires formation of ohmic contacts in the van der Pauw configuration as described in Section 2.1.2. Photolithography is the standard method of doing that and the first step of photolithography is spin-coating. The diamond substrates used in this work had a square top surface of dimensions 3 mm × 3 mm and an approximate thickness of 300 µm. The problem encountered with spin-coating small samples is the formation of an edge bead, a thicker ring of photoresist that forms along the sample's outer edge during spin coating due to surface tension and centrifugal forces. While this is not unique to small samples, it becomes a problem for small samples when the the edge bead significantly reduces the area that can be patterned. This is especially inconvenient when the desired pattern is the van der Pauw pattern which places electrical contacts in the corners, where the edge bead is most pronounced. An example of a diamond substrate with large edge beading is shown in Fig. XXX. To develop a method of patterning our substrates, we conducted a series of tests to understand how the photoresist behaves under different applications.

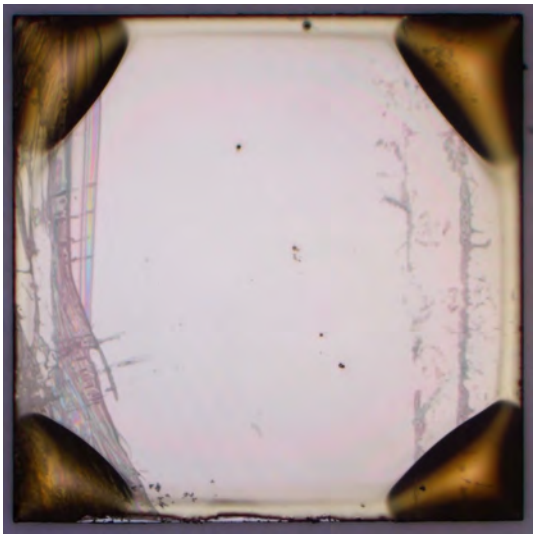

Figure 6.3 Diamond substrate with a large edge bead. Streaks on the opposite surface are visible because the diamond is transparent.

6.3.1 Masks

Fig. 6.4 shows the design used for the van der Pauw pattern on diamond substrates. The photolithography masks were produced using commercially available transparent plastic sheets printed with black ink at a local office supply store. [234] These masks are not considered high-quality lithographic masks. A close-up view in Fig. 6.5 illustrates that the printed edges are not perfectly straight, and small amounts of stray ink are present in areas intended to remain transparent. However, because the van der Pauw geometry does not require precise edge definition, these imperfections did not interfere with the Hall effect measurements. Moreover, the stray ink deposits were sufficiently transparent to UV light during exposure, and no adverse effects were observed in the final patterned samples. The main advantage of this source of mask is its low cost and rapid turnaround, since new mask designs can be generated and printed within the same day. Nonetheless, future work would benefit from the use of higher-quality masks.

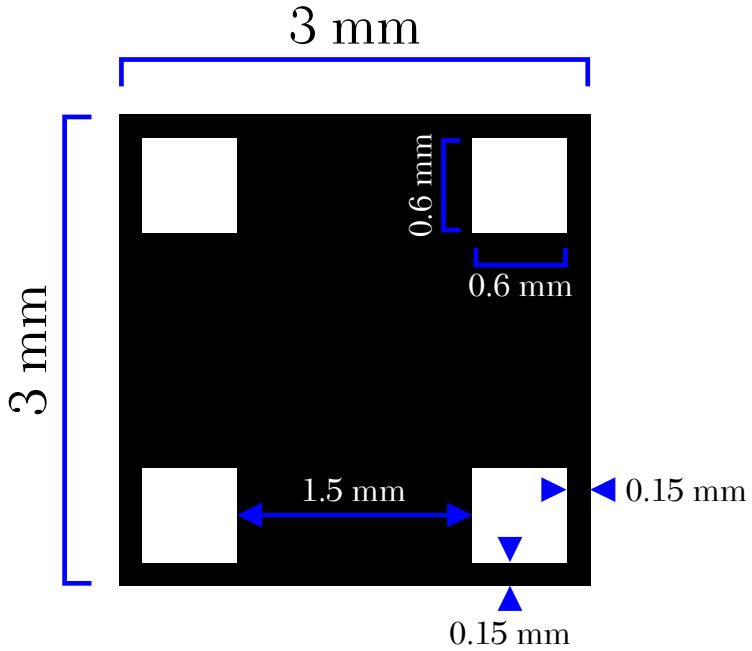

Figure 6.4 Schematic of the van der Pauw mask used for 3 mm × 3 mm diamond substrates.

6.3.2 Tests on Si Wafers

Microposit S1813 photoresist was used for all tests described in this chapter. Tests were done on Si wafers of dimension 1 cm × 1 cm with the goal of observing how the photoresist behaves

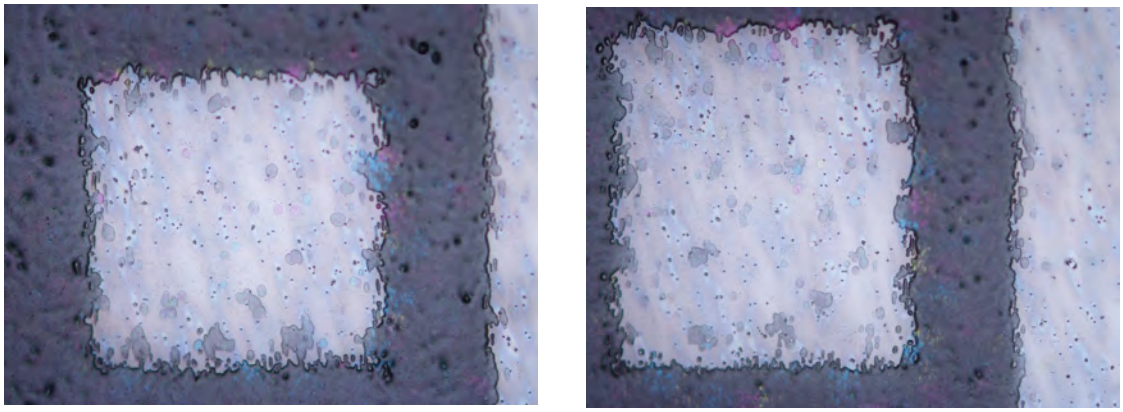

Figure 6.5 Photos of masks purchased from Staples under 10x magnification.

under varied conditions. The wafers were subjected to an RCA clean before each test. Photoresist is refrigerated at all times when not in use, and brought to room temperature only when needed for spin-coating.

6.3.2.1 Diluting Photoresist

The first considered method of reducing the edge beading was to dilute the photoresist in order to reduce the viscosity. Photoresist solutions were prepared by diluting the base resist with PGMEA at dilution ratios of 0% (undiluted), 50%, 100%, 200%, and 500%. Three drops of photoresist was applied to the wafers while stationary then spin-coated at 6000 rpm for 60 seconds. After this the wafers were soft-baked at 115°C for 60 seconds and subsequently exposed to UV light for 180 seconds. The photomask used for exposure contained both curved and sharp-cornered features as shown in Fig. 6.6(g) to observe the patterned sharpness of the film. After exposure, the wafers were developed for 60 seconds in Microposit MF-319 developing solution, rinsed with deionized water, and baked again at 115°C for 60 seconds. Fig. 6.6 presents the resulting photoresist thickness as a function of dilution ratio, along with images of the wafer surfaces.

The photoresist layer thickness decreased significantly at 50% and 100% dilution levels and then remained relatively constant at higher dilution ratios. The pattern quality also deteriorated progressively with increasing dilution. At 200% and 500% dilution, the resulting patterns have fragmented features and delaminated edges. This suggests that higher dilution reduces the adhe-

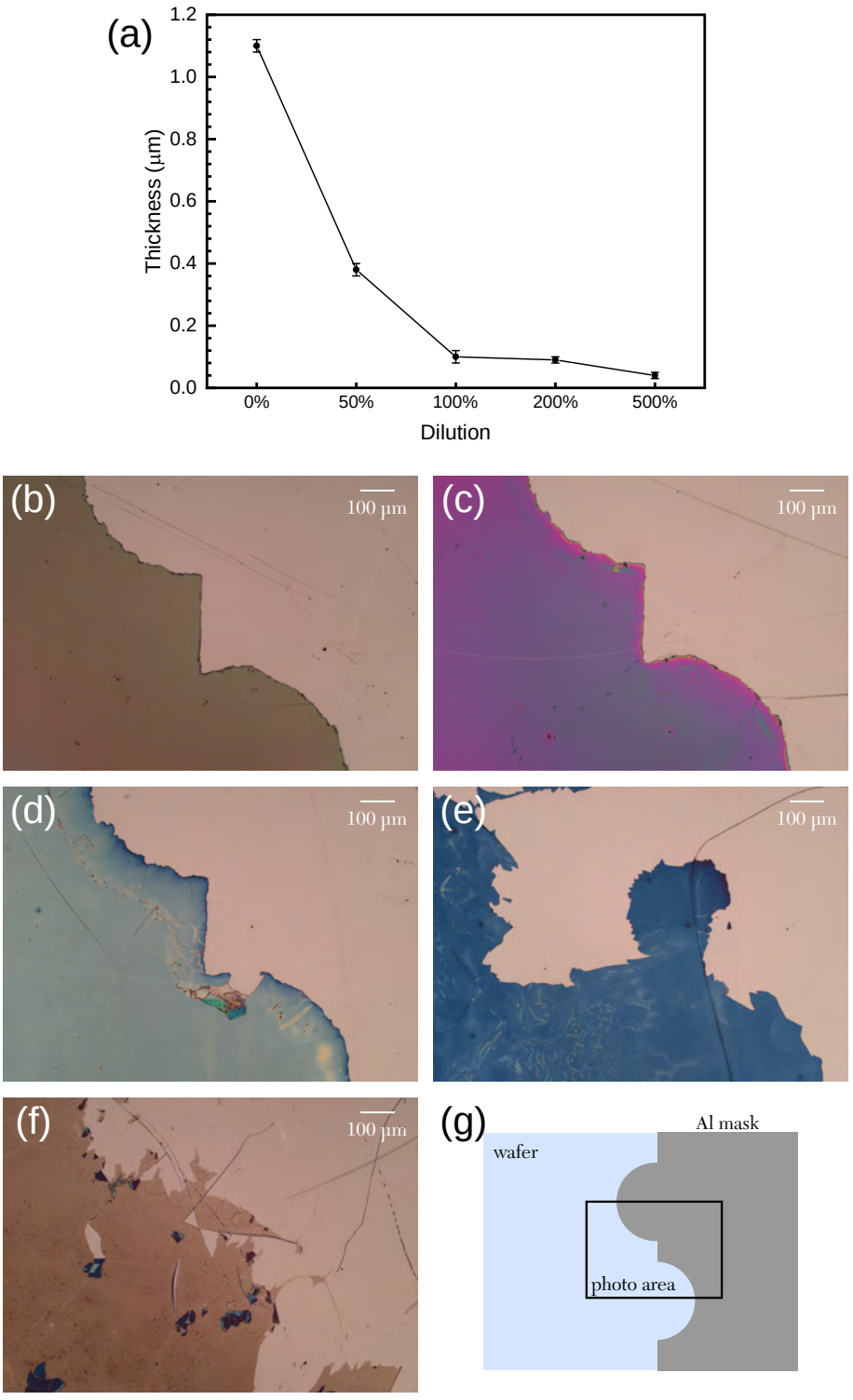

Figure 6.6 Photoresist film thickness and quality under increasing dilution with PGMEA. (a) Thickness as a function of dilution. (b-f) Microscope photos of the films revels that strong dilution results in poor films that delaminate from the wafer. The color change is the result of different thicknesses. (b) No dilution. (c) 50% dilution. (d) 100% dilution. (e) 200% dilution. (f) 500% dilution. (g) Diagram of the mask used for these tests and the region captured in the photos.

sion of the photoresist to the Si surface, even when the overall film thickness does not decrease substantially.

6.3.2.2 Varying Rotation Speed

Another potential method of reducing the edge bead was to vary the rotation rate. Fast rotation rates, for example, could fling the photoresist off the sample and reduce the amount of excess material. Or perhaps a fast rate would push more photoresist to the edges. To clarify this, the photoresist was spin-coated with varied rotation rates.

Photoresist was applied to 10 mm × 10 mm Si wafers and spin-coated at 1000, 2000, 4000, or 6000 rpm for 60 seconds. Then the wafers were soft-baked at 115°C for 60 seconds and subsequently exposed to UV light for 180 seconds. After exposure, the wafers were developed for 60 seconds, rinsed with deionized water, and baked again at 115°C for an additional 60 seconds. Fig. 6.7(a) presents the resulting photoresist thickness as a function of rotation speed. These values are in very good agreement with the manufacturer's specifications.

Similar tests were done on diamond substrates. Photoresist was applied to a 7 mm × 7 mm diamond substrate and spin-coated at 2000, 3000, 4000, or 6000 rpm for 60 seconds. Photoresist was also applied to a 3 mm × 3 mm diamond substrate and spin-coated at 4000 or 6000 rpm for 60 seconds. The rest of the procedure was the same as described for Si wafers above. Fig. 6.8(a) shows how the film thickness varied with rotation speed for two diamond sizes. We see that photoresist behaves differently on a diamond surface compared to Si surface. There was essentially no variation in photoresist thickness between 2000 and 4000 rpm on the 7 mm × 7 mm diamond substrate. However, when the substrate was rotated at 6000 rpm, the resist was pushed away from the center of rotation leaving an uncoated area and a nonuniform layer of resist on the rest of the surface. Photos and thickness profiles of this diamond are shown in Figs. 6.8(b-d). The 3 mm × 3 mm diamond substrate did not develop an uncoated area when spun at 6000 rpm. This figure also reveals that large a large edge bead remained even at this high spin rate.

We see from these tests that photoresist behaves differently on Si and diamond surfaces, and that wafer size has an influence on the photoresist film across the whole wafer surface. The photo

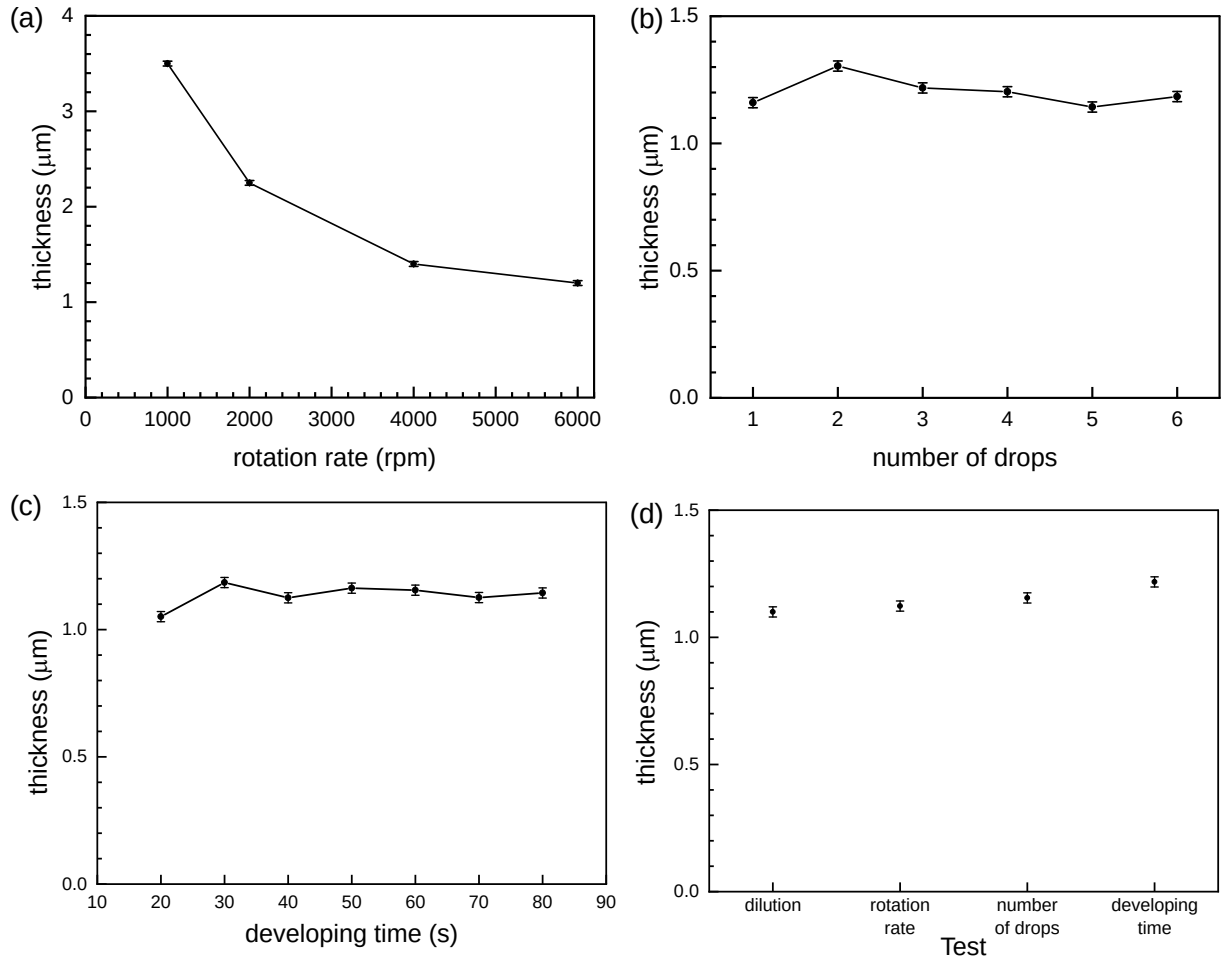

Figure 6.7 Photoresist film thickness on Si wafers observed over a series of trials. (a) Film thickness following varied rotation rate. (b) Film thickness following different number of drops of photoresist before cpin coating. (c) Film thickness following varied developing time. (d) Film thickness of equivalent spin coating procedures performed on different days.

in Fig. 6.8(e) also provides a hint as to why exposing the edge bead fails to remove it. When the layer has a uniform thickness, as shown in Fig. 6.8(f), the UV light can penetrate through and completely degrade the photoresist. But nonuniformity of the film as illustrated in Fig. 6.8(g) and (h) can result in the light being refracted or reflected such that the photoresist is only partly degraded or almost completely intact. If the exposed edge beads in the lower part of Fig. 6.8(e) are the remnants of incomplete exposure due to reflection of the light, longer exposure could not result full degradation of the photoresist in those areas. It is therefore necessary to develop a different method of sample patterning that avoids significant edge bead formation.

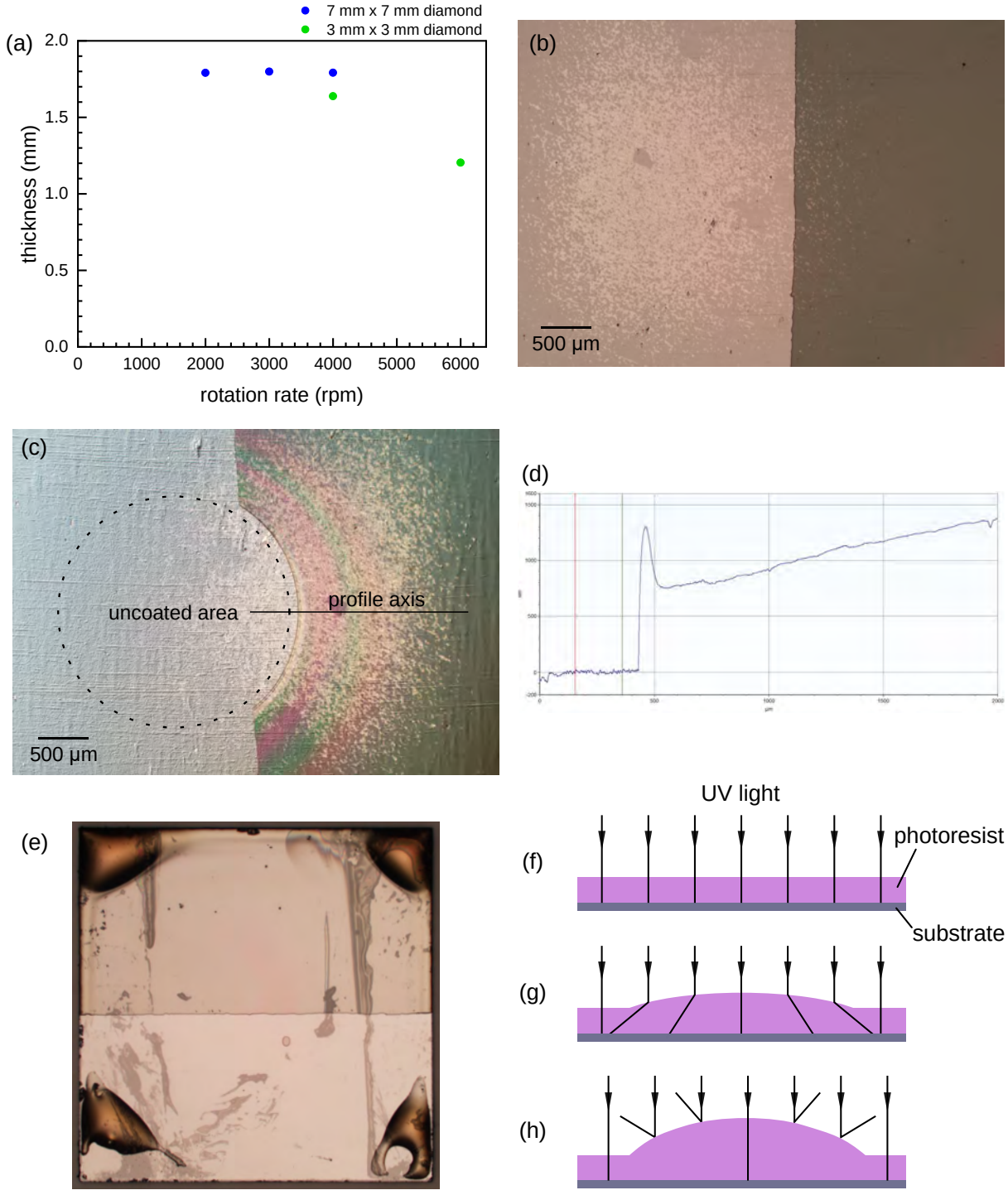

Figure 6.8 Observations of photoresist patterning on diamond substrates. (a) Film thickness under varied rotation speed for different diamond sizes. (b) When the 7 mm × 7 mm diamond substrate is rotated up to 4000 rpm, the film is uniform over the center. (c) When the 7 mm × 7 mm diamond substrate is rotated at 6000 rpm, the center region becomes uncoated and the surrounding film is not uniform. (d) Layer profile of the 7 mm × 7 mm diamond substrate rotated at 6000 rpm. (e) Photo of the 3 mm × 3 mm diamond substrate rotated at 6000 rpm and exposed over half the surface. The edge beads in the lower half remain poorly degraded. (f-h) Interaction of the UV light with the photoresist film showing possible ways that edge beading results in poor patterns.

6.3.2.3 Varying drop number

One possible way to reduce the edge bead could be to add less photoresist to the sample. Yet this could lead to incomplete coverage of the surface so it is always necessary to add more photoresist than is absolutely required. In order to gauge the effect of excess photoresist, it was applied to 10 mm × 10 mm Si wafers by dropping between one and six drops of resist onto each wafer, followed by spin-coating at 6000 rpm for 60 seconds. Then the wafers were soft-baked at 115°C for 60 seconds and subsequently exposed to UV light for 180 seconds. After exposure, the wafers were developed for 60 seconds, rinsed with deionized water, and baked again at 115°C for an additional 60 seconds. Fig. 6.7(b) shows that film thickness had no significant dependence on the number of drops. This suggests that the excess photoresist is flung off the sample.

6.3.2.4 Varying exposure time

To establish the time needed to fully expose a layer of photoresist with a given thickness, the exposure time was tested. Photoresist was applied to 10 mm × 10 mm Si wafers and spin-coated at 6000 rpm for 60 seconds. Then the wafers were soft-baked at 115°C for 60 seconds and exposed to UV light in two phases. In the first phase, half of each wafer was exposed for durations ranging from 10 to 120 seconds. The wafers were then rotated by 90°, and the other half of each wafer was exposed for 300 seconds, a duration determined to be sufficient for complete degradation of the photoresist layer. Following exposure, the wafers were developed for 60 seconds, rinsed with deionized water, and baked at 115 °C for an additional 60 seconds. Fig. 6.9 presents the measured photoresist thickness as a function of exposure time. A linear fit to the data yields a reduction rate of approximately 40 nm/s. The plot also indicates that an exposure time of 90 seconds is sufficient to fully remove even the thickest photoresist films produced in this study.

6.3.2.5 Varying Developing Time

Photoresist was applied to 10 mm × 10 mm Si wafers and spin-coated at 6000 rpm for 60 seconds. Then the wafers were soft-baked at 115°C for 60 seconds and subsequently exposed to UV light for 180 seconds. Following exposure, the wafers were developed for time periods between 20 and 80 seconds, rinsed with deionized water, and baked at 115 °C for an additional 60

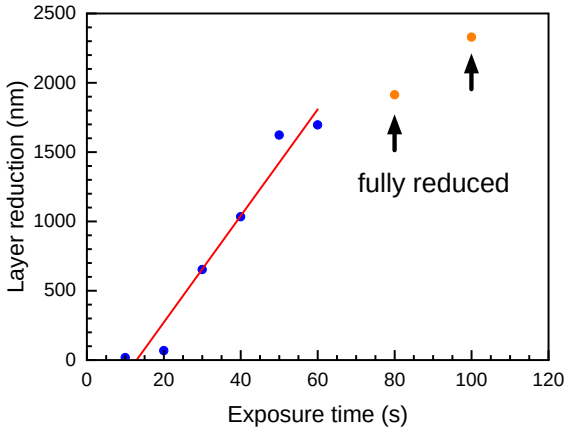

Figure 6.9 Reduction of the layer thickness over varied exposure periods. The orange points represent layers that were completely removed by the exposure. The line of best fit to the remaining points indicates that the layer reduction rate is 40 nm/s and that 90 s is enough to remove any layer observed in this series of tests.

seconds. This range of developing times was chosen because it brackets the time recommended by the manufacturer. Fig. 6.7(c) presents the measured photoresist thickness as a function of developing time. There is no significant effect on layer thickness from varying the developing time and no visible difference could be seen in film quality under 10x magnification. This tells is that the S1813 photoresist is not very sensitive to developing time.

6.3.2.6 Observing Consistency

Because several of the experiments described above employed a common procedure, these results can be used to assess the consistency of the photoresist film thickness across different days. In this procedure, photoresist was applied to 10 mm × 10 mm Si wafers and spin-coated at 6000 rpm for 60 seconds. The wafers were then soft-baked at 115°C for 60 seconds, exposed to UV light for 180 seconds, developed for 60 seconds, rinsed with deionized water, and baked at 115°C for an additional 60 seconds. Fig. 6.7(d) presents the resulting film thicknesses obtained on separate days. Although some variation is observed, the results indicate that the films are generally consistent in thickness across multiple sessions.

6.3.2.7 Summary of Observations

From these tests we can draw a few valuable conclusions. First, diluting the photoresist has a very drastic effect on film thickness. A 100% dilution reduces the film thickness by a factor

of roughly 10. Therefore, dilution is likely most useful up to 100%. Higher dilution also risks resulting in film delamination. Also, we have verified that the quality of our photoresist is good and refrigerating it keeps it from degrading quickly. Additionally, we have calculated the rate of photoresist degradation under UV light and determined that 90 seconds of exposure is enough to pattern any layer of typical thickness. However, our tests on Si wafers have not been able to shed light on preventing the formation of an edge bead. We also see that photolithography on a diamond surface may produce different results and the conclusions drawn here using Si wafers may be of limited relevance.

6.3.3 Tests on Diamonds

With the information gathered form the previous tests it was easier to narrow down which aspects of the photolithography process to focus on when attempting to pattern diamond substrates with a small edge bead.

6.3.3.1 Mounting Techniques

The smaller size of the diamond substrates requires that a different method is used for mounting the sample for spin coating compared to the larger silicon substrates. The first two methods that we investigated were mounting the diamond on a chuck and mounting it on a Si wafer. In the first method, the diamond was mounted directly onto the chuck and secured by a vacuum pump. In the second method, the diamond was attached to a Si wafer using adhesive tape, and the wafer was then mounted onto the spin coater with a larger chuck. Figs. 6.10(a,b) show photographs of both configurations. The direct mounting method is generally preferred due to the ease of mounting and removing the sample. In contrast, the wafer-mounting method requires a strong adhesive to ensure that the diamond remains fixed during the spin-coating process. This makes dismounting more difficult and increases the risk of scratching the photoresist layer when removing the diamond with tweezers. Additionally, adhesive residue may remain on the bottom surface, potentially causing problems with the remaining patterning process.

Despite these drawbacks, the wafer-mounting method generally results in improved photoresist film quality. As shown in Figs. 6.10(c-f), when both mounting methods are compared under

(a) Diamond on chuck

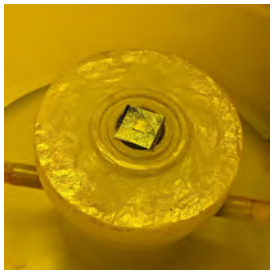

(b) Diamond on wafer

Diamond mounted on chuck

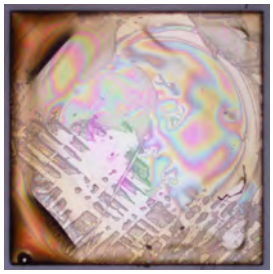

(c) 100% dilution

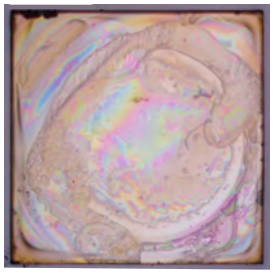

(d) 200% dilution

Diamond mounted on wafer

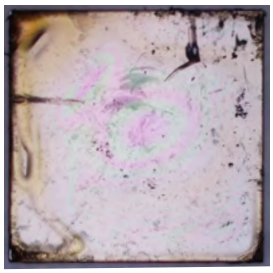

(e) 100% dilution

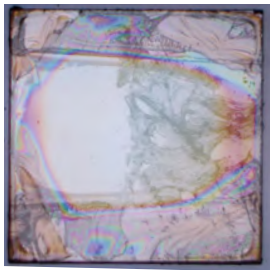

(f) 200% dilution

Figure 6.10 Comparison of two methods for mounting 3 mm × 3 mm diamond substrates for spin coating. (a) A diamond mounted on a chuck for small samples. (b) A diamond mounted on a Si wafer held down by a chuck for larger samples. (c,d) Two dilution tests done using the chuck-mounting method. The film is not very uniform. (e,f) Two dilution tests done using the wafer-mounting method. The films are more uniform compared to (c,d) because the photoresist can spread out more.

identical spin-coating conditions, the wafer-mounting method produces a more uniform film and significantly reduces edge beading because the excess photoresist can spread out over a larger area. Some edge beading still occurs, but it is less pronounced than when the chuck is used.

6.3.3.2 Repeated Application

To improve the uniformity of the photoresist film, a procedure involving multiple sequential applications of diluted photoresist was studied. Each diamond substrate was first mounted onto a Si wafer, after which a layer of diluted photoresist was spin-coated at 6000 rpm for 60 seconds and subsequently baked at 115°C for 60 seconds. The spin-coating and baking steps were then repeated a specified number of times to incrementally build up the film. Fig. 6.11 presents three trials of this procedure performed with different dilution ratios.

Ultimately, this approach did not yield a sufficiently uniform film. As shown in Fig. 6.11, the photoresist continued to exhibit significant edge beading, and in some cases ripples and bare areas formed. Moreover, repeated application did not produce a film substantially thicker than that obtained from a single coating. The resulting layers were extremely thin and not adequate for patterning.

6.3.3.3 Consistency Observations

Through a variety of similar trials, it was possible to compare samples prepared using identical procedures. Fig. 6.12 presents photographs of diamonds processed in the same manner, showing that some variation persists in the distribution of photoresist across the surface. This variability indicates that the film quality is highly sensitive to minor differences in the spin-coating process. The most challenging aspect to reproduce consistently is the application of an identical volume of photoresist, primarily due to the small surface area of the diamond.

Our method of applying the photoresist was to brush a pipette tip loaded with photoresist across the diamond surface, aiming to deposit the smallest feasible amount needed to cover the entire surface. This step inherently introduces variability in the deposited volume, which directly affects the resulting film. Samples that receive more photoresist tend to exhibit more pronounced edge beading. Therefore, it is critical to apply the smallest possible amount of photoresist while ensuring

200% dilution, mounted on wafer

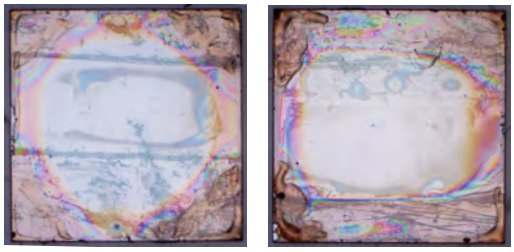

(a) 1 application (b) 2 applications

500% dilution, mounted on chuck

(c) 1 application (d) 2 applications (e) 3 applications (f) 4 applications (g) 5 applications

500% dilution, mounted on wafer

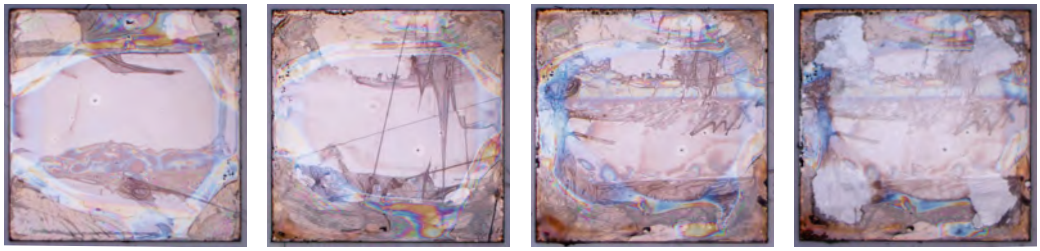

(h) 1 application (i) 2 applications (j) 3 applications (k) vdP pattern

1000% dilution, mounted on chuck

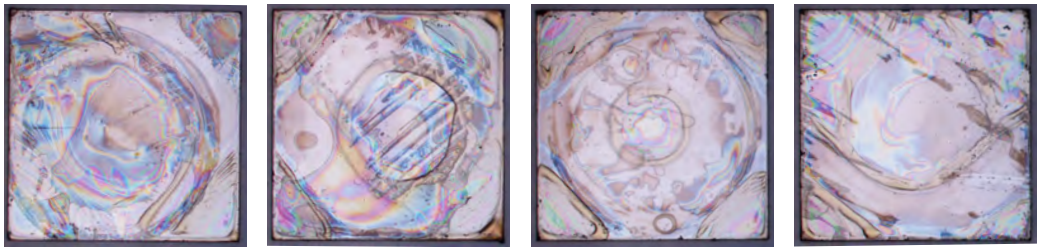

(l) 1 application (m) 5 applications (n) 10 applications (o) 15 applications

Figure 6.11 Tests of repeated applications of diluted photoresist. (a,b) With a 200% dilution and wafer-mounting method, large edge beads formed in the corners after only two applications. (c-g) With a 500% dilution and chuck-mounting method, large edge beads and surface ripples formed and grew with an increasing number of applications. (h-k) With a 500% dilution and wafer-mounting method, the film uniformity was improved but the patterning shows incomplete degradation of the exposed areas and a very thin layer overall. (l-o) With a 1000% dilution and chuck-mounting method, there is little improvement compared to (c-g) and the film is much thinner.

200% dilution, 1 application, mounted on chuck.

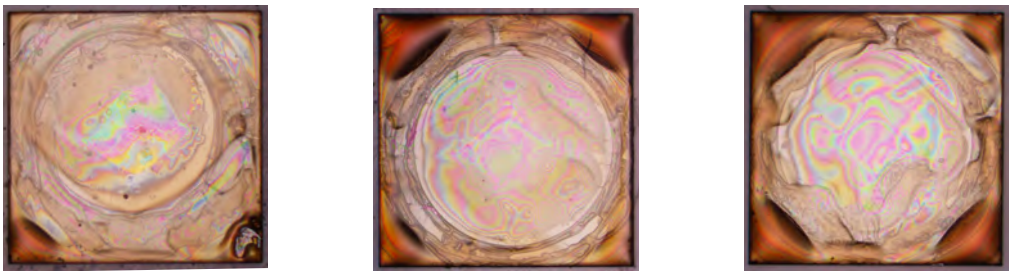

(a) (b) (c)

200% dilution, 1 application, mounted on wafer.

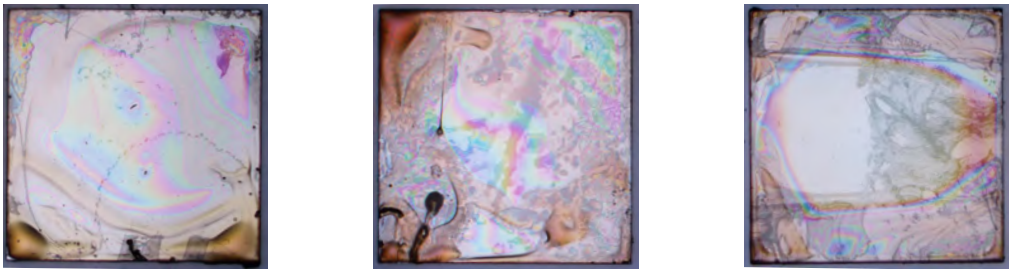

(d) (e) (f)

Figure 6.12 Comparison of repeated spin-coating techniques shows unintentional differences in film quality. (a-c) One application of 200% diluted photoresist with the chuck-mounting method. (d-f) One application of 200% diluted photoresist with the wafer-mounting method. The differences across each set of samples comes from minute differences in the quantity of photoresist applied to the diamond surface.

complete surface coverage.

6.3.3.4 Selective Exposure

Because the edge bead forms around the periphery of the diamond, we explored strategies to reduce it by selectively exposing those regions before the final patterning. In the first attempt, the diamond was prepared by spin-coating a 200% diluted photoresist solution at 6000 rpm for 60 seconds, followed by baking at 115°C for 60 seconds. The edges were then exposed for 90 seconds using a square-inset mask, after which the diamond was developed for 60 seconds, rinsed with deionized water, and baked again at 115°C for 60 seconds. A second photoresist layer was then applied by spin-coating a 500% diluted solution at 6000 rpm for 60 seconds, baking at 115 °C for 60 seconds, exposing for 90 seconds under the van der Pauw mask, developing for 60 seconds, rinsing,

and finally baking again at 115 °C for 60 seconds. Figs. 6.13(a-d) show photographs of the sample at various stages of this process. Although the final photoresist layer exhibited a slightly reduced edge bead, remnants of photoresist remained within the exposed van der Pauw pattern areas. These residual regions correspond to locations where the first photoresist layer had thickened due to edge beading, preventing proper exposure through the second mask.

In a second attempt, the same procedure was repeated using an octagonal mask. However, the initial edge exposure again failed to sufficiently remove the excess photoresist, and the subsequent patterning step did not produce a clean van der Pauw pattern as shown in Figs. 6.13(e-h).

Finally, a circular mask was crudely fabricated from aluminum foil using a hole punch. The diamond was spin-coated with a 50% diluted photoresist solution at 6000 rpm for 60 seconds, baked at 115°C for 600 seconds, and the edges were exposed for 600 seconds using the circular mask. The sample was then developed for 60 seconds, rinsed, and baked at 115°C for 60 seconds. Figs. 6.13(i,j) show the resulting pattern. Even with this extended exposure time, the photoresist at the bead region remained intact. This result suggests that the problem is not only due to increased photoresist thickness at the edges. The curvature of the bead alters the local incident angle of the UV light, leading to incomplete exposure in certain regions. This result supports our hypothesis from Section 6.3.2.2 and underscores the importance of achieving a uniform film through spin-coating.

6.3.3.5 Light Leakage

In some patterned samples, a grid-like pattern appeared unexpectedly in regions that should have been protected by the mask. Fig. 6.14 shows photographs of patterned samples with the grid-like pattern. This effect was likely due to light leakage through the printed ink of the mask. To mitigate this issue in later patterns, at least two layers of the mask were used during exposure to minimize light transmission through the opaque areas.

Notably, unintentional exposure caused by light leakage was observed only in samples with very thin photoresist films, on the order of 100 nm or less in thickness. Our target film thickness was at least 500 nm, and no evidence of light leakage was detected in films of this thickness. Therefore, the imperfect opacity of the masks did not have a significant impact on the patterning quality of

Edge bead exposure using square mask

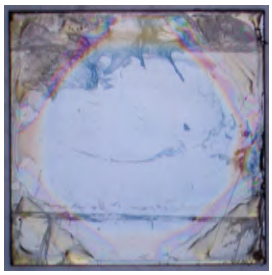

(a) 200% dilution, 1 application

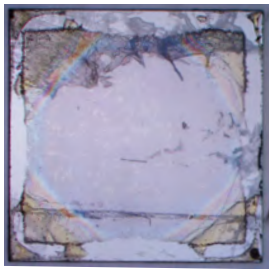

(b) Edge bead exposure, 90 sec

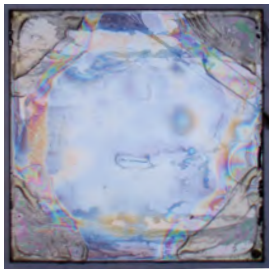

(c) 500% dilution, 1 application

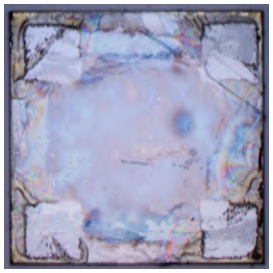

(d) vdP pattern, 90 sec

Edge bead exposure using octagonal mask

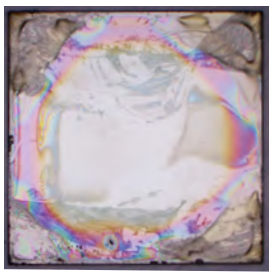

(e) 100% dilution, 1 application

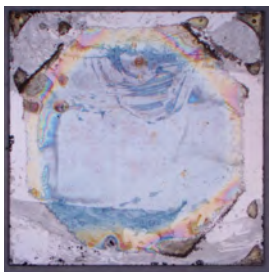

(f) Edge bead exposure, 90 sec

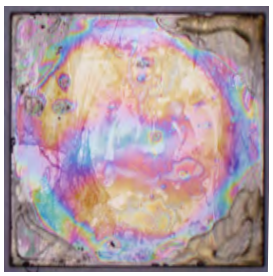

(g) 100% dilution, 1 application

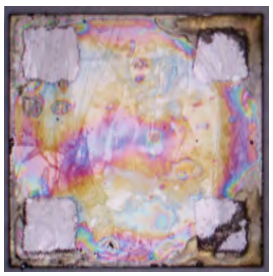

(h) vdP pattern, 90 sec

Edge bead exposure using Al circle mask

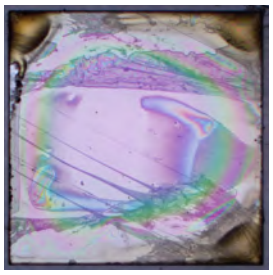

(i) 50% dilution, 1 application

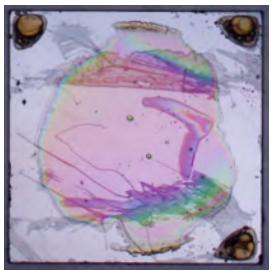

(j) Circle pattern, 600 sec

Figure 6.13 Some attempts at selectively exposing the edge bead to form a more uniform film by a second photoresist application. (a-d) A square mask that exposed the edges was not successful in producing a clean pattern since the photoresist collects in large quantities in the corners. (e-h) An octagonal mask showed some improvement compared to the square mask, but edge beading could not be completely avoided. (i,j) A circle mask and very long exposure could also not completely eliminate excess photoresist in the corners, supporting the hypothesis that the curvature of the film results in low penetration of UV light to those regions.

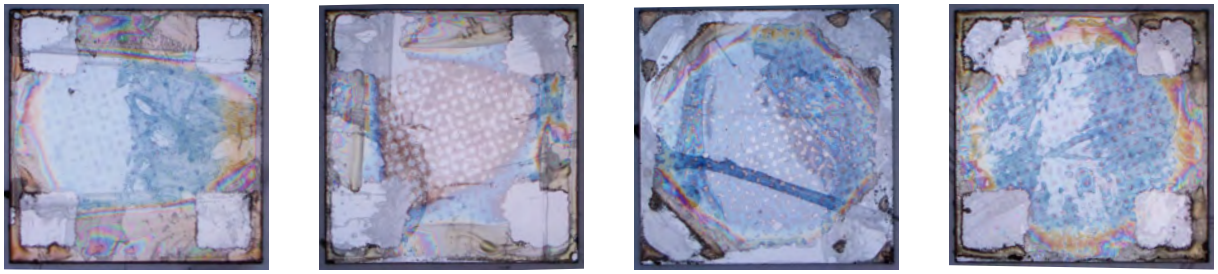

(a) (b) (c) (d)

Figure 6.14 Films spin-coated and exposed under various conditions. The grid pattern and thin film thickness in these photos result from light UV leakage through the mask. By layering at least two masks, the leakage is significantly reduced.

sufficiently thick photoresist layers.

6.3.3.6 Displacement from Center

Of all the trials discussed in this section, the only method that successfully reduced edge beading was mounting the diamond substrate onto a Si wafer during spin coating. The wafer provided a larger surface area for the photoresist to spread across, which reduced the accumulation of photoresist along the edges of the diamond.

To enhance this effect, we tiled the area surrounding the diamond with additional substrates and Si wafer fragments of comparable thickness. The hypothesis was that by providing a continuous surface at the same height as the diamond in the center, the photoresist could spread more evenly and potentially eliminate edge beading altogether. In practice, however, it was not possible to tile the substrates without leaving small gaps between them. Fig. 6.15 shows the resulting film morphologies for the central diamond substrate and the adjacent substrates. Curiously, while the central diamond still exhibited noticeable edge beading, the neighboring substrates showed only minimal beading.

This observation suggested that centrifugal effects associated with radial position on the spin coater might also influence film uniformity. To test this hypothesis, a diamond substrate was mounted near the edge of a 2-inch Petri dish and flanked by two Si wafers during spin coating. Under these conditions, the edge bead was substantially smaller than in any previous trial. As shown in Fig. 6.16, the off-center spinning method followed by patterning produced a film approximately 600 nm thick, with a sharply defined step in the thickness profile between the exposed and unexposed

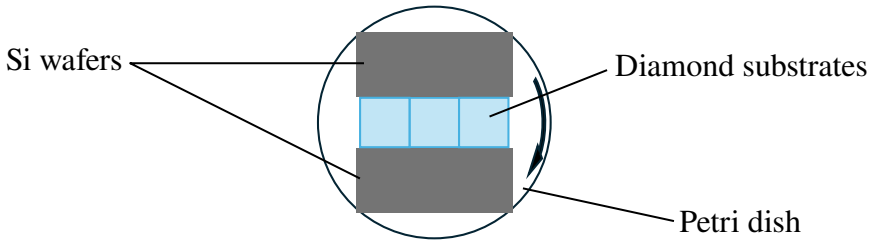

(a) Spin configuration

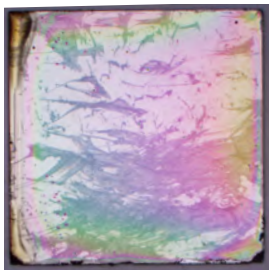

(b) Left substrate, before patterning

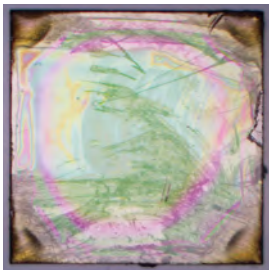

(c) Center substrate, before patterning

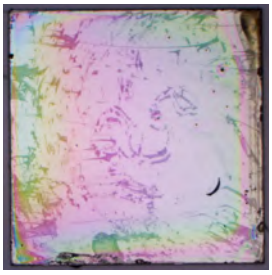

(d) Right substrate, before patterning

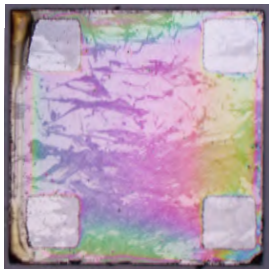

(e) Left substrate, patterned

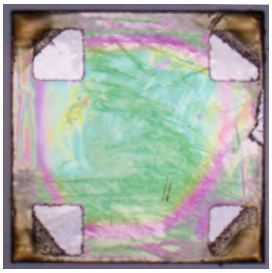

(f) Center substrate, patterned

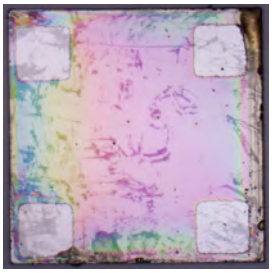

(g) Right substrate, patterned

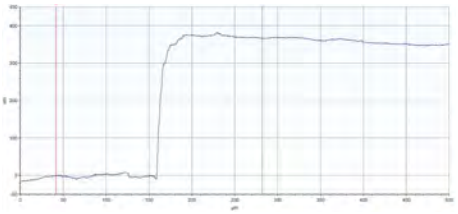

(h) Left pattern profile

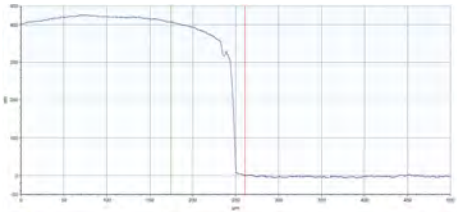

(i) Right pattern profile

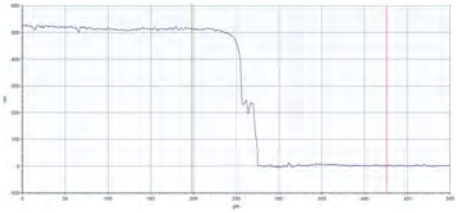

(j) Center pattern profile

Figure 6.15 (a) This tiling of diamonds and wafers unintentionally resulted in thick films (~ 400 nm) with low edge beading in the left (b,e,h) and right (d,g,i) diamond substrates. The center diamond (c,f,j) had the worst film quality.

regions and only a very small edge bead. This patterning technique yielded the best results, and the remaining processing steps such as etching and metal deposition can be carried out following this procedure. The detailed procedure is provided in Section 2.1.2.

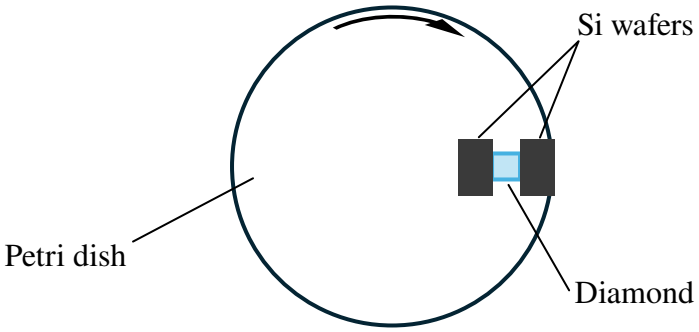

(a) Spin-coat configuration

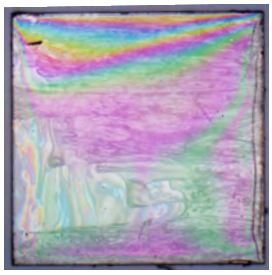

(b) Undiluted photoresist

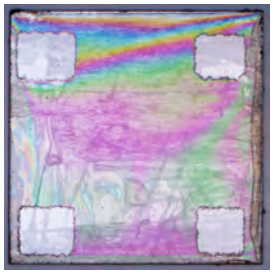

(c) vdP pattern

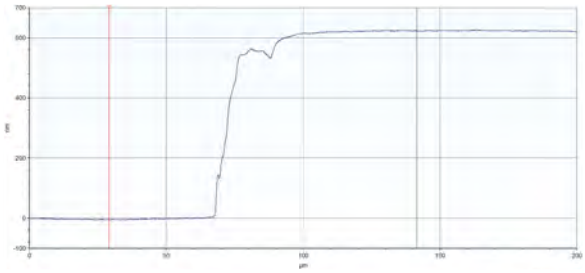

(d) Pattern profile

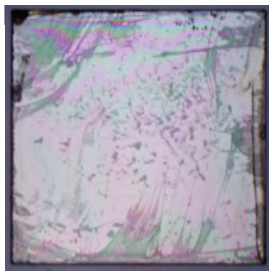

(e) Undiluted photoresist

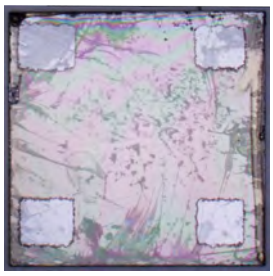

(f) vdP pattern

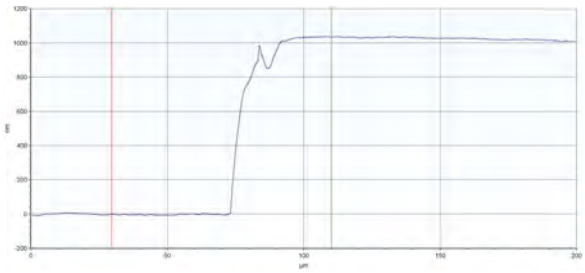

(g) Pattern profile

Figure 6.16 By attaching a diamond to the edge of a petri dish with two Si wafers on opposite sides, the photoresist can form a thick and very uniform layer with sharp relief when patterned. Two successfully patterned samples are shown here.

6.4 Selective Growth of Diamond

6.4.1 Patterning SiO_2

The SiO_2 mask was fabricated by depositing a film of SiO_2 onto the sample, patterning a photoresist layer, etching the exposed SiO_2 through the developed pattern, and finally removing the photoresist. The SiO_2 film was deposited by plasma-enhanced chemical vapor deposition (PECVD) under the conditions listed in Table 6.1.

Pressure	1 torr
Power	30 W
Temperature	300°C
N_2O	710 sccm
5% SiH_4 in N_2	170 sccm

Table 6.1 Deposition conditions used for SiO_2 films. [235]

Initially, the SiO_2 film growth rate and its etch rate in buffered oxide etchant (BOE) were unknown. These parameters were determined experimentally by depositing SiO_2 layers on diamond substrates for varying deposition durations, patterning the films using photolithography, and then etching them in BOE. The etch progress was monitored at timed intervals until the diamond surface became visible. From these measurements, the SiO_2 growth rate was found to be approximately 80 nm/min, while the BOE etch rate at room temperature was in the range of 400 to 500 nm/min.

The etch time does not need to be tuned very precisely as long as the SiO_2 layer is completely removed in the exposed regions without excessive overetching leading to undercutting of the photoresist. No issues of photoresist peeling were observed for etch times up to one hour. The SiO_2 is patterned before being annealed because the etch rate of the annealed film is much slower, about 100 nm/min.

6.4.2 Using SiO_2 in DS5

The as-deposited SiO_2 film is highly susceptible to plasma etching during the ramp-up and deposition steps. To improve the film's resistance to plasma etching, the SiO_2 layer is annealed in a vacuum furnace at 900°C for 2 hours. [236]

The durability of SiO_2 is aided by modifying the plasma ramp-up procedure so that the MW

power is set to the lowest value capable of sustaining a plasma. Table 6.2 lists the minimum MW powers required to maintain plasma at various chamber pressures. Because the plasma may be extinguished at an intermediate pressure before reaching the final pressure, the MW power at the target pressure must be slightly increased. For ramp-up to 160 torr, a MW power of 550 W is sufficient. For ramp-up to 240 torr, a power of 800 W is sufficient. Under these modified ramp-up conditions, no etching of the SiO_2 film occurs.

Even after annealing, however, the SiO_2 film gets etched by the plasma, though at a much slower rate compared to the as-grown film. Therefore, it was necessary to quantify the etch rate in order to determine the minimum SiO_2 thickness required. To measure the etch rate at 160 Torr, a layer of SiO_2 was deposited and exposed to the diamond growth plasma under the conditions listed in Table 6.3 at 160 torr for 15-minute intervals, and the film thickness measured after each interval. Under these conditions, the annealed SiO_2 exhibited an etch rate of approximately 150 nm/min. The same procedure was repeated at 240 torr using 5-minute exposure intervals, revealing a significantly higher etch rate of approximately 400 nm/min.

Pressure (torr)	Power (W)
100	425
160	500
200	650
240	700

Table 6.2 Minimum MW power needed to sustain a plasma at several pressures.

For the SiO_2 mask to remain intact throughout the diamond growth process, it must withstand the plasma for the time required to deposit 500 nm of diamond. Using a (1 1 1)-oriented substrate and the growth conditions listed in Table 6.3, this corresponds to a deposition time of 15 minutes. Therefore, a SiO_2 layer at least 6 μm thick is required to produce the desired selective growth.

Because the SiO_2 gets etched in all directions, it gradually recedes from the edges of the diamond during growth, exposing portions of the underlying diamond surface. This allows diamond to grow along the edges, as in Fig. 6.17(g), and some diamond may grow on the sides of the original substrate as well. To prevent these unintended growth regions from contributing ring currents that

Pressure	240 torr
MW Power	1550 W
Temperature	950°C
$[H_2]$	280 sccm
$[CH_4]$	12 sccm
$[PH_3]$	56 sccm

Table 6.3 Growth conditions used for selective growth. The phosphine is diluted to 0.1% in hydrogen.

could interfere with Hall effect measurements, approximately 50 μm of material is removed from the edges of the diamond using a laser.

During selective growth, a thin diamond layer forms over the SiO_2 in the center of the sample. An example of this is shown in Fig. 6.17(b). This overgrowth can be beneficial because it provides some protection of the underlying SiO_2 from plasma etching. However, this diamond layer also prevents removal of the SiO_2 in BOE. The thin diamond film can be removed by gently scraping surface against a polishing wheel. Then the sample can be immersed in BOE until the SiO_2 layer is completely dissolved.

6.5 Conclusion

This chapter describes how the process of patterning a diamond with selectively grown diamond regions overtopped by metal contacts was developed. The method of spin-coating small substrates away from the center of rotation will allow us to patten photoresist using photolithography without the issue of a large edge bead. Then the process of depositing, etching, and annealing SiO_2 that is described here will allow us to grow diamond in the patterned regions, albeit with a small amount of excess growth along the edges that can be removed with a laser. We have also observed the relationship between pressure, power, and temperature in DS5 that will facilitate diamond growth.

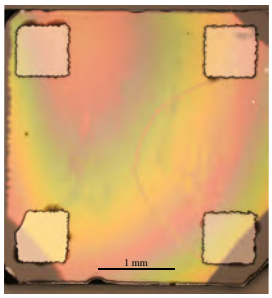

(a) Patterned and annealed SiO_2

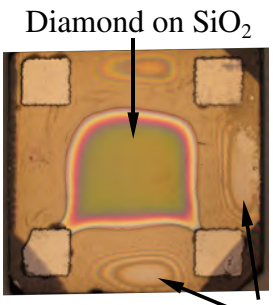

(b) After growth

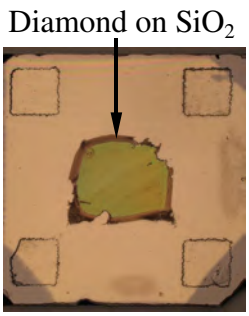

(c) After first etch

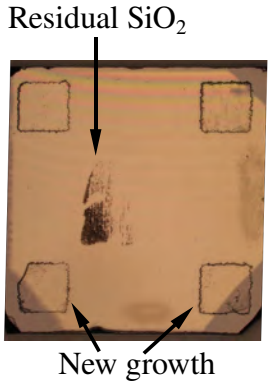

(d) After second etch

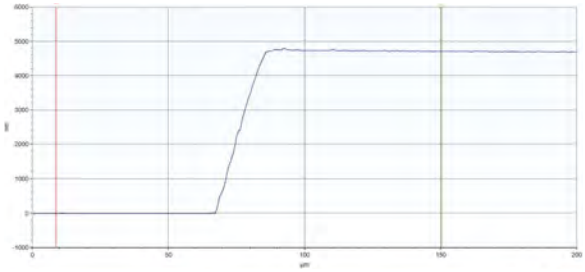

(e) Initial SiO_2 profile

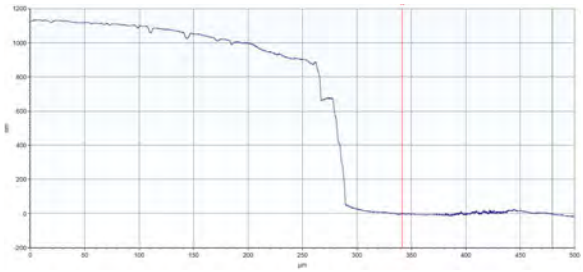

(f) Grown area profile

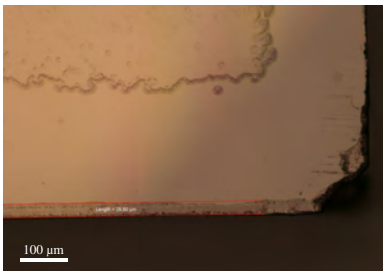

(g) Edge growth

Figure 6.17 Test of selective growth in the van der Pauw configuration on a (1 0 0)-oriented 3.5 mm × 3.5 mm diamond. (a) The annealed SiO_2 in the van der Pauw pattern. (b) After growth some areas of the SiO_2 have been etched though. (c) Most of the SiO_2 has been dissolved except for material protected by the diamond layer that formed during the growth. (d) When the undesired diamond layer is removed, the SiO_2 can be completely dissolved, although a slight amount remained on this sample. The new growth is in the van der Pauw pattern. (e) The initial layer of 4.8 µm SiO_2 is able to withstand close to 15 minutes of growth before it becomes etched all the way through in some areas. (f) The amount grown on this diamond was more than 1 µm. (g) The selective growth is not perfectly selective. This photo shows that about 30 µm of diamond grew along the edges. This can be removed with a laser.

CHAPTER 7

HALL EFFECT MEASUREMENTS OF P-DOPED DIAMOND

7.1 Diamond Growth

To find a set of growth conditions that produce a heavily P-doped diamond with low defect density, a series of single-crystal diamond samples was grown on (111)-oriented substrates with dimensions of 3 mm × 3 mm × 0.3 mm purchased from the provider Flawless Technical Diamonds, and characterized by electrical transport measurements from 300 K to 700 K. Table 7.1 describes the growth conditions used for each sample as well as some surface characteristics.

Sample	Offcut angle	Pressure (torr)	Power (W)	Temp. (°C)	$[H_2]$ (sccm)	$[CH_4]$ (sccm)	$[PH_3]$ (sccm)	Time	Grown thickness (μm)	Growth rate (μm/hr)	Surface roughness (nm)
#1	1.05°	240	1550	950	280	12	56	4 hr	6.65	1.66	70
#2	1.04°	200	1540	950	280	12	56	4 hr	12.5	3.13	
#3	1.32°	200	2370	960	240	6	128	3 hr	3.92	1.31	128
#4	0.40°	240	2250	950	280	5	56	4 hr	66.4	16.6	146
#5	0.95°	240	1760	950	224	5	112	2 hr	23.9	11.9	102
#6	0.96°	240	1870	950	112	5	224	2 hr	26.2	13.1	89

Table 7.1 Growth conditions and surface characteristics of SCD samples. Phosphine is diluted in hydrogen to 0.1% concentration.

7.2 Characterization Measurements

Microscope images of Sample #1 are shown in Fig. 7.1. The diamond appears very dark, though not completely opaque, and exhibits a bumpy, rough surface morphology that is not indicative of step-flow growth. Over a 10 μm × 10 μm area, the average surface roughness was measured to be approximately 70 nm. The combination of dark coloration and high roughness was consistently observed across all SCD samples grown in this study. The origin of these features remains unclear, though they may be signs of a high density of structural defects and impurity incorporation that results in significant visible light absorption. The rough surface morphology suggests a growth mechanism prone to defect formation.

Before proceeding with transport measurements on this sample, the contacts were checked for ohmic behavior. Fig. 7.2 shows the IV curves of each contact permutation at several temperatures.

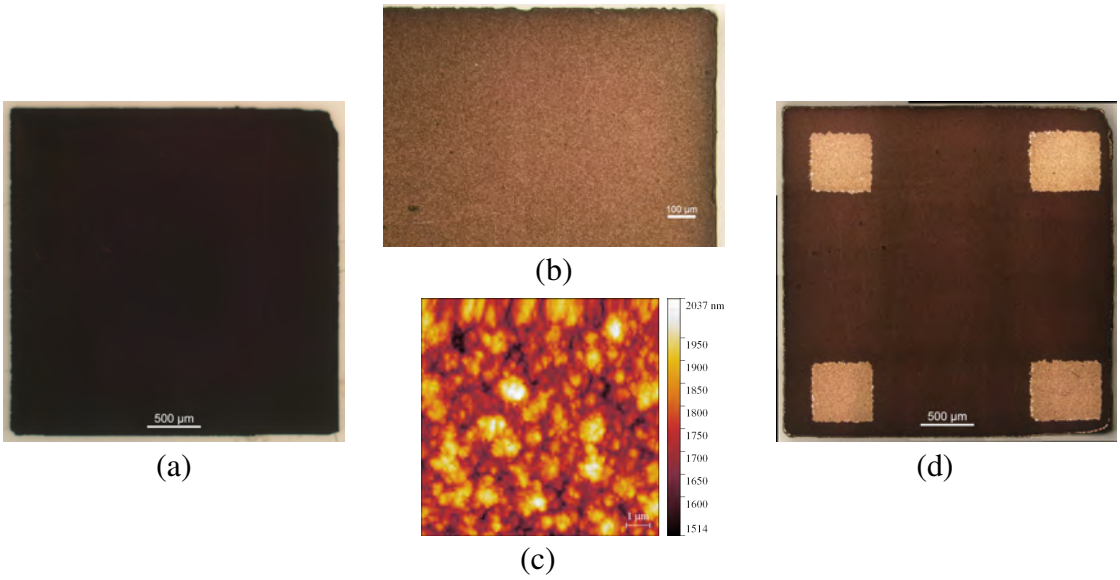

Figure 7.1 (a,b) Microscope images of Sample #1 at 2.5x and 10x magnification, respectively. (c) AFM image of the surface. (d) Patterned sample with Ti/Au contacts. (Composite photograph.)

The curves are very linear which is a sign that transport measurements will accurately capture the carrier properties of this sample. Comparison of Figs. 7.2(a) and (b) shows that the contact quality improves after annealing, which occurs after heating up to 700 K. The curves in Fig. 7.2(b) are slightly more linear than the curves in Fig. 7.2(a), and the resistivity is lower after annealing due to the formation of a TiC layer at the diamond-contact interface that promotes electron transport. [175, 237, 238]

Electrical transport measurements for Sample #1 are presented in Fig. 7.3. The Hall coefficient exhibits significant noise up to approximately 500 K, above which it first decreases and then returns close to zero. The coefficient remains negative throughout this temperature range, indicating that electrons are the dominant charge carriers. The Hall mobility and carrier concentration display a similar temperature dependence of high noise at lower temperatures and a non-monotonic trend above 500 K. The pronounced noise in the measurements may be attributed to the high resistivity of the sample as can be seen in Fig. 7.3(d). However, the origin of the non-monotonic behavior in the Hall coefficient and carrier concentration remains uncertain but it may reflect the influence of compensating defects that become electrically activated at different temperatures.

The transport measurements make it difficult to asses the effectiveness of P doping in this

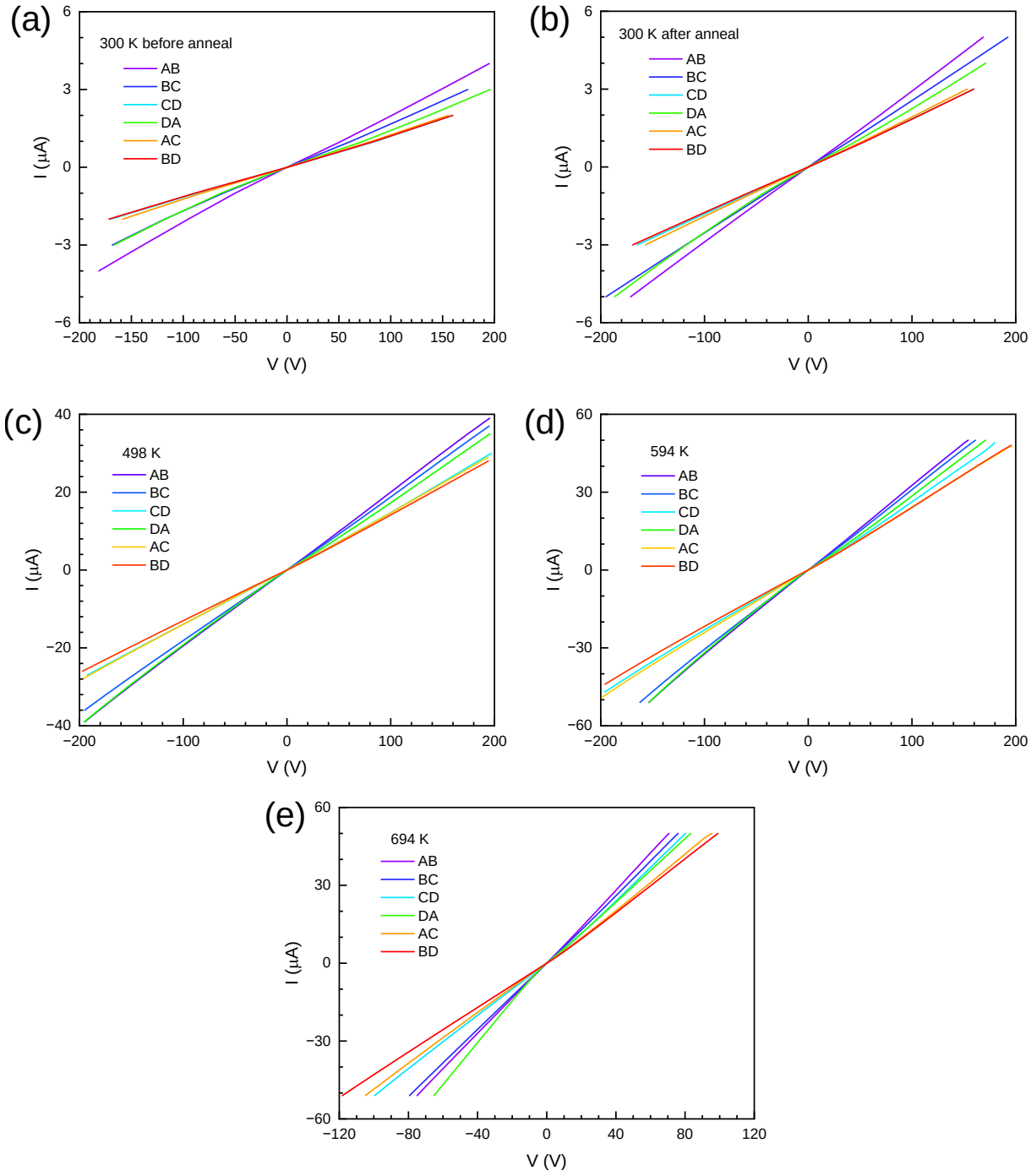

Figure 7.2 IV curves of Sample #1 at selected temperatures.

sample. The non-monotonic shape of the carrier concentration curve does not allow for a good fit to Eq. 1.77, which would allow us to determine the number of donors and acceptors. However, the carrier concentration reaches a maximum of roughly 10^{14} cm^{-3} which implies a total donor number of 10^{18} to 10^{19} cm^{-3} if electrons are the only carrier. This can be approximated using the equation

$$[P] = n\, e^{\frac{E_a}{k_B T}} \tag{7.1}$$

where the activation energy E_a is the P donor level equal to 0.6 eV. [39] This sample may have a P concentration close to the heavy doping level needed to form ohmic contacts. Yet the unusual electrical transport behavior and the very dark and rough physical qualities of this sample suggest that the growth conditions used for Sample #1 did not yield a high-quality diamond.

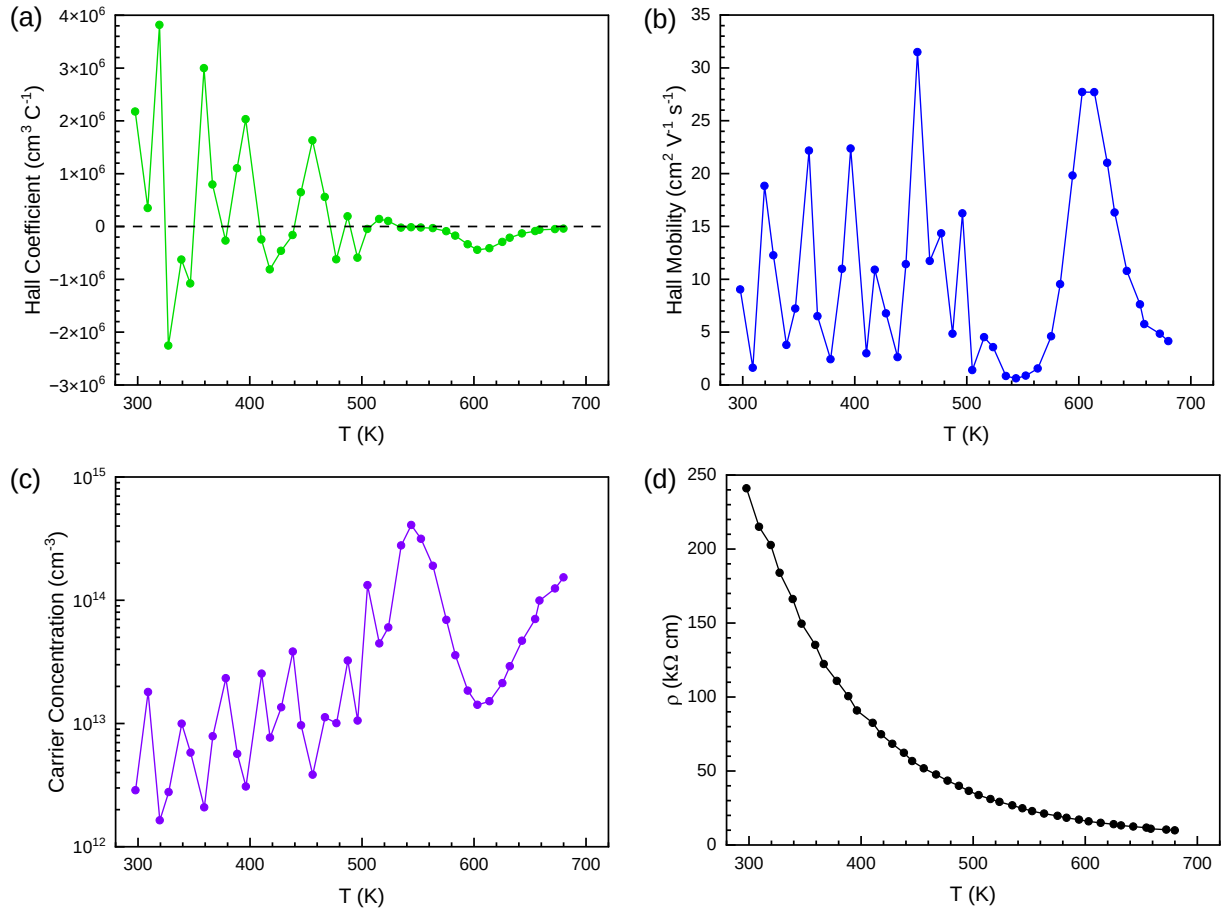

Figure 7.3 Electrical transport measurements of Sample #1: (a) Hall coefficient. (b) Hall mobility. (c) Carrier concentration. (d) Resistivity.

Microscope images of Sample #2 are shown in Fig. 7.4(a). This diamond is also very dark and the surface morphology is very rough. This diamond was patterned in the van der Pauw configuration with selectively grown regions overtopped by Ti/Au contact pads as described in Section 2.1.2. Fig. 7.4(b) shows an enlarged view of on of the contact pads, demonstrating the success of selective growth followed by metal deposition. The ring pattern in the contact area is a result of nonuniform thickness of the diamond in the selectively grown regions, which is a drawback of the growth conditions rather than the process of sample preparation. The profile in Fig. 7.4(c) shows that the desired thickness of 0.4 µm was met, though not uniformly.

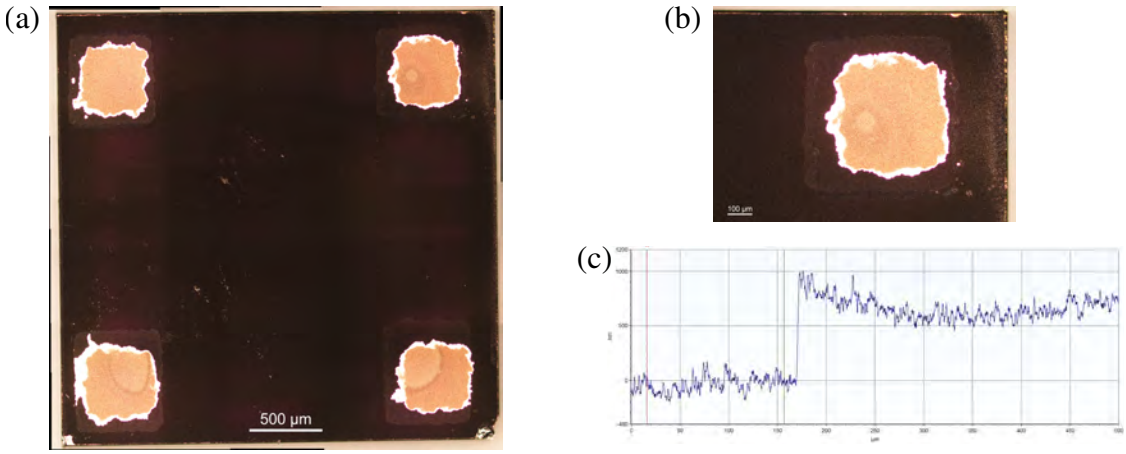

Figure 7.4 Sample #2 was prepared for Hall effect measurements with selective growth regions and metal deposition in the van der Pauw configuration. (a) Whole sample photo. (b) Enlarged photo of one contact pad. (c) Profile measurement of on of the selective growth regions.

The IV curves of each contact pair is shown in Fig. 7.5. Three curves are very linear, although the change in slope towards higher temperature implies an increase in the contact resistance, which is not expected of good ohmic contacts. The remaining three show nonlinear behavior at low temperate but become much more linear approaching 700 K due to thermionic emission of carriers. The three nonlinear curves all have contact D in common, which indicates that this contact was different from all the others. At this time, we cannot determine which contact was labeled D, and cannot conclude what caused the nonlinear behavior. Additional measurements could clarify the cause of the issue.

Electrical transport measurements for Sample #2 are presented in Fig. 7.6. The plots of

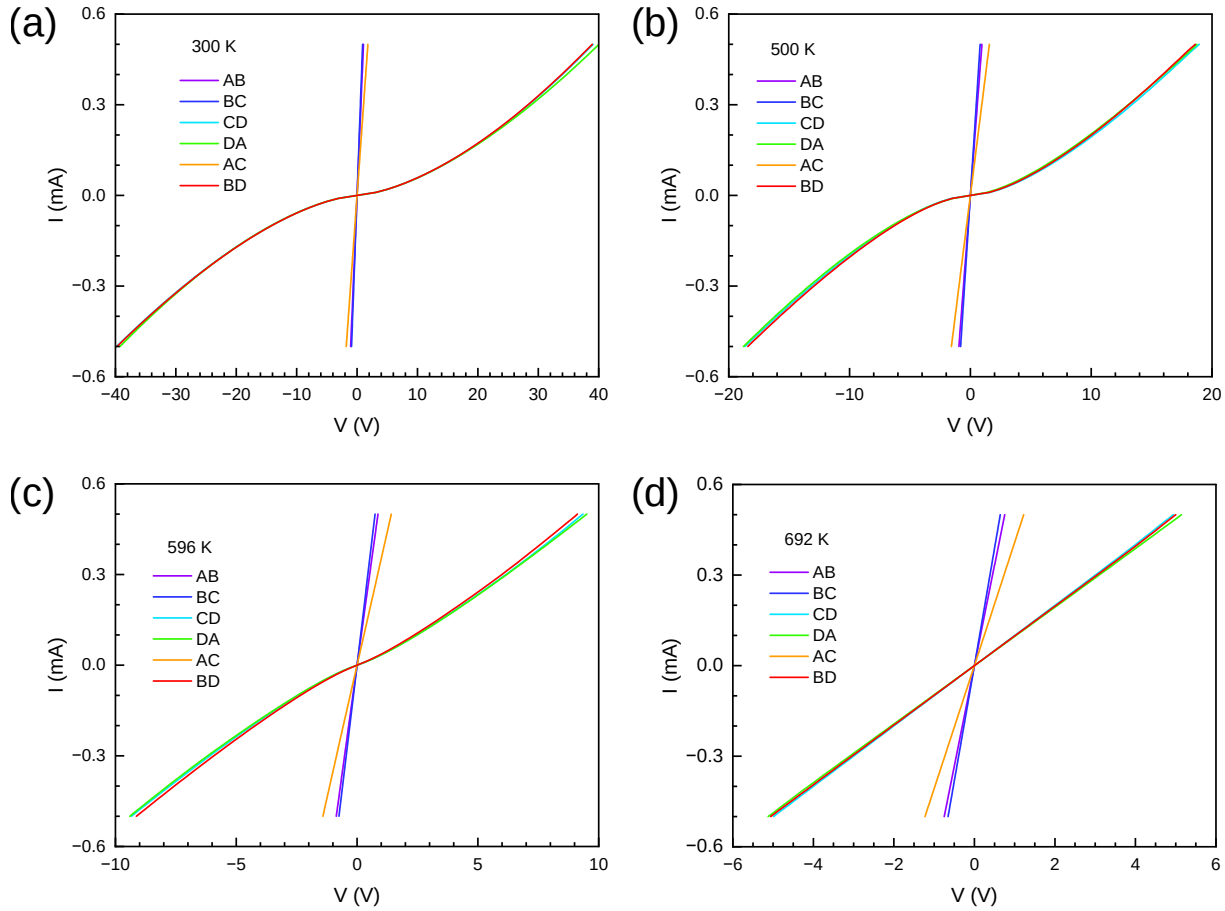

Figure 7.5 IV curves of Sample #2 at selected temperatures. (a) 300 K. (b) 500 K. (c) 596 K. (d) 692 K.

Figs. 7.6(a), (b), and (c) are predominantly noisy with no discernible trend. The resistivity rises starting at 300 K before falling above 380 K. These properties are due to the poor contact quality that makes the measurements unreliable.

Microscope images of Sample #3 are shown in Fig. 7.7. Like the previous samples, it is dark and rough. This diamond shows unique hexagonal features that were not formed by the growth conditions listed in Table 7.1. Rather they are present because the substrate had been used in previous growth attempts that etched these shapes into the original surface. Electrical transport measurements of Sample #3 are shown in Fig. 7.8. Similar to Sample #1, the Hall coefficient shows noisy behavior up to higher temperature. Above 600 K, the Hall coefficient becomes consistently negative. The carrier concentration reaching 10^{20} cm^3 suggests a very high donor concentration of only electrons from phosphorus are assumed to contribute. In fact, it would

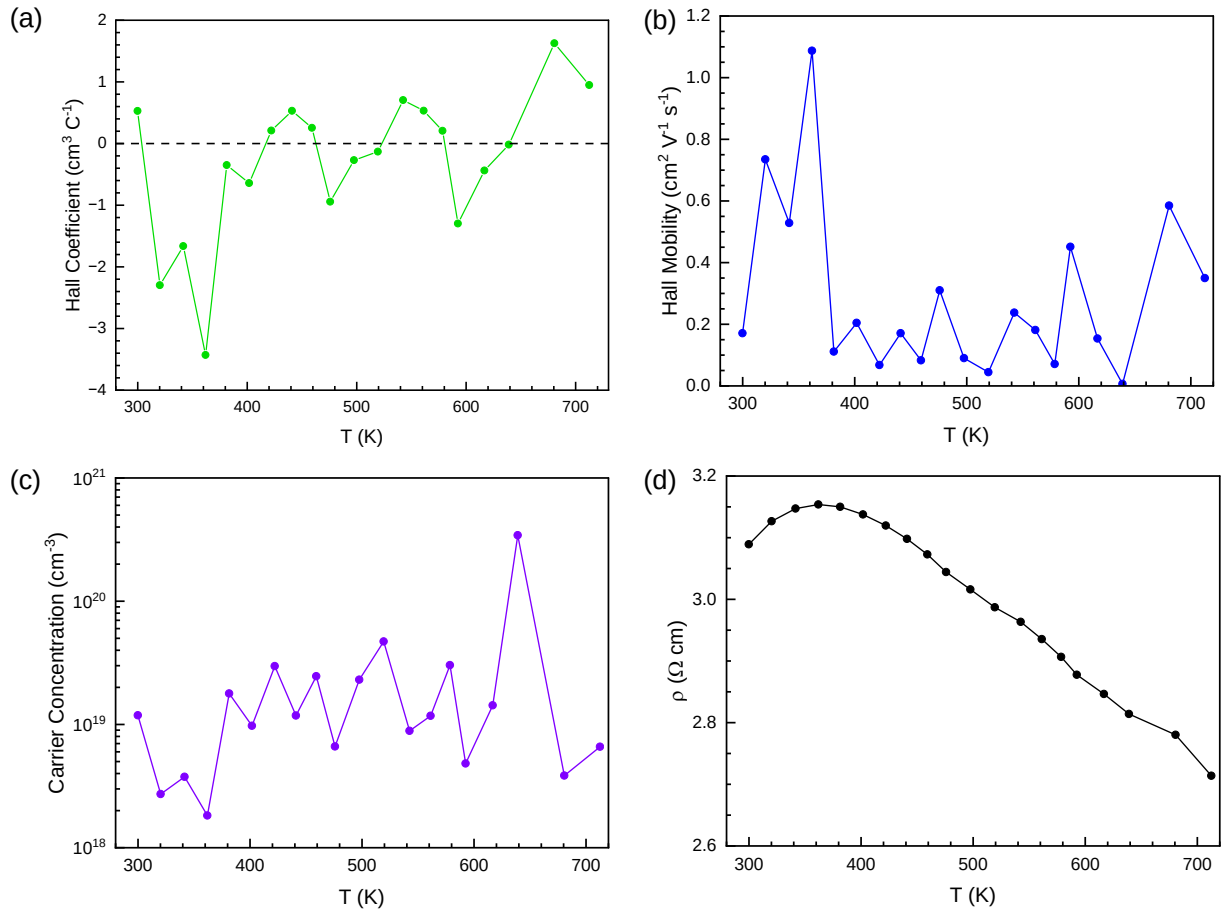

Figure 7.6 Electrical transport measurements of Sample #2. (a) Hall coefficient. (b) Hall mobility. (c) Carrier concentration. (d) Resistivity.

suggest a P concentration that is unrealistically high. It is more likely that carriers are introduced from defects or impurities. Fitting the carrier concentration to an Arrhenius relation, as shown in the inset of Fig. 7.8, gives an activation energy of 0.183 eV.

Microscope images of Sample #4 are shown in Fig. 7.9. This sample has a rough surface morphology like the others but the AFM scan in Fig. 7.9(c) shows that the textural features are micron-sized, which is much larger than the features seen on the other samples. The features have distinct facets which are angled off the horizontal plane by approximately 24° to 35° as labeled in the plot.

Electrical transport measurements of Sample #4 are shown in Fig. 7.10. The Hall coefficient for Sample #4 is predominantly positive in the high temperature range, although it becomes negative at the highest measured temperature. The Hall mobility is low, similar to the previous samples.

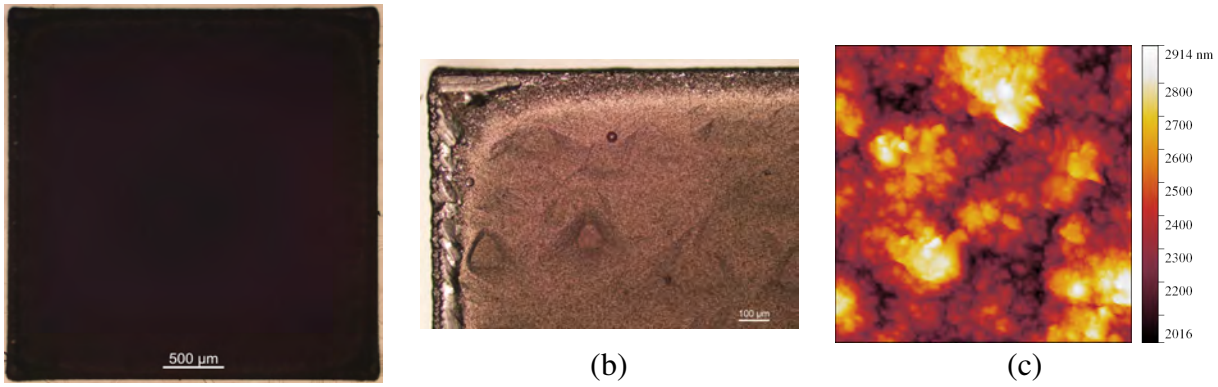

(a) (b) (c)

Figure 7.7 (a,b) Microscope images of Sample #3 at 2.5x and 10x, respectively. (c) AFM image of the surface.

Fitting the carrier concentration to an Arrhenius function gives an activation energy of 0.273 eV, as shown in the inset of Fig. 7.10(c).

To verify the accuracy of these transport measurements, we look to the IV curves plotted in Fig. 7.11. These contacts are not very ohmic at any temperature as seen from the nonlinearity, but they they are not rectifying. This implies that the transport measurements are not completely accurate at low temperatures, but become more accurate at higher temperatures.

Samples #5 and #6 were grown using similar growth conditions as Sample #4, but with the flow of phosphine gas doubled for each subsequent growth, and the hydrogen reduced appropriately to maintain the same total gas flow. Like each of the previous samples, Samples #5 and #6 had have a rough surface morphology and very dark color (not shown). Electrical transport measurements of Sample #5 are shown in Fig. 7.12. The carrier properties show that the carrier concentration is nearly temperature independent on the order of 10^{18} cm^{-3} and the Hall coefficient remains close to zero throughout the range suggesting a similar number of electrons and holes acting as carriers. The consistently low mobility suggests a high amount of scattering, possibly due to defects.

The electrical transport properties of Sample #6 are shown in Fig. 7.13. The carrier concentration generally declines at high temperatures suggesting increasing compensation. This may be due to defects. The Hall coefficient goes from negative to positive values suggesting multiple contributing acceptor and donor states that become activated at different temperatures.

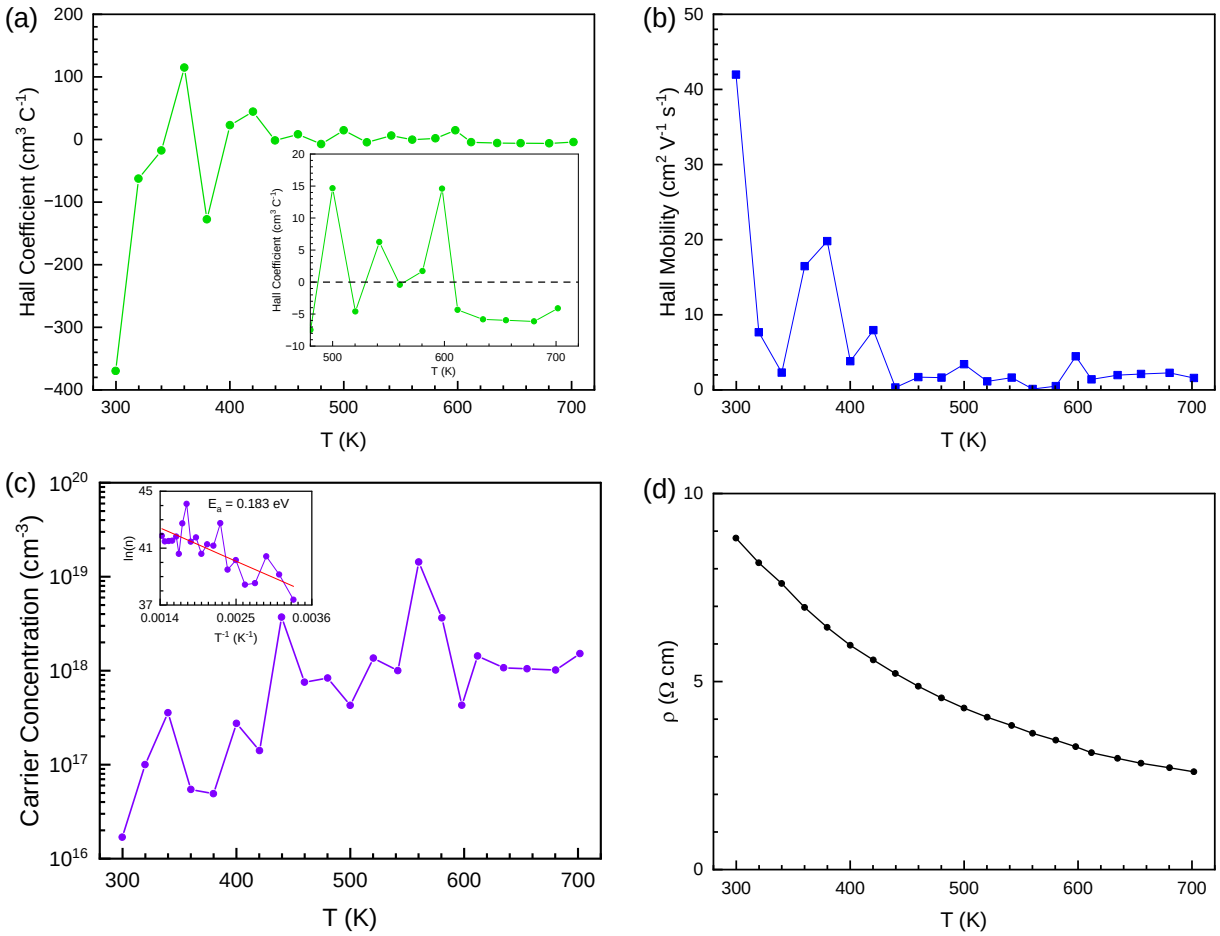

Figure 7.8 Electrical transport measurements of Sample #3. (a) Hall coefficient. (b) Hall mobility. (c) Carrier concentration. (d) Resistivity.

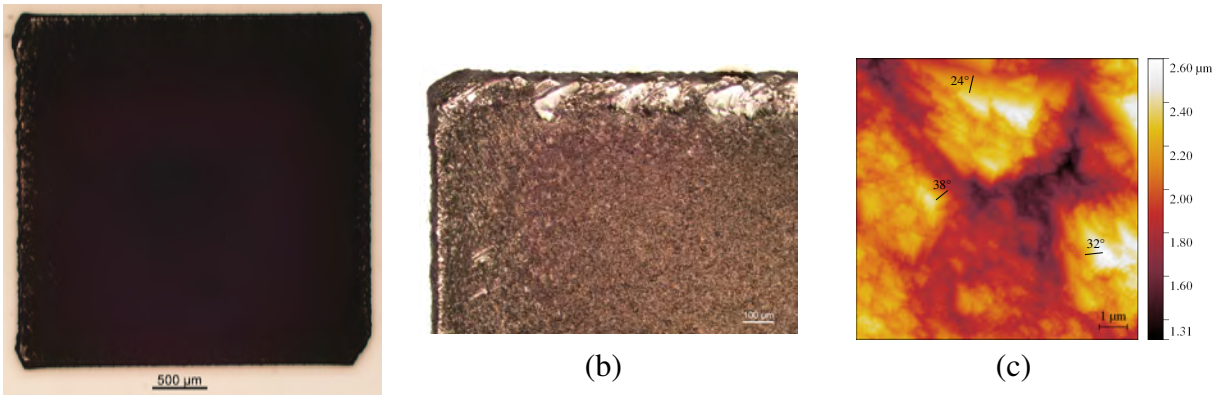

(a) (b) (c)

Figure 7.9 (a,b) Microscope images of Sample #4 at 2.5x and 10x, respectively. (c) AFM image of the surface.

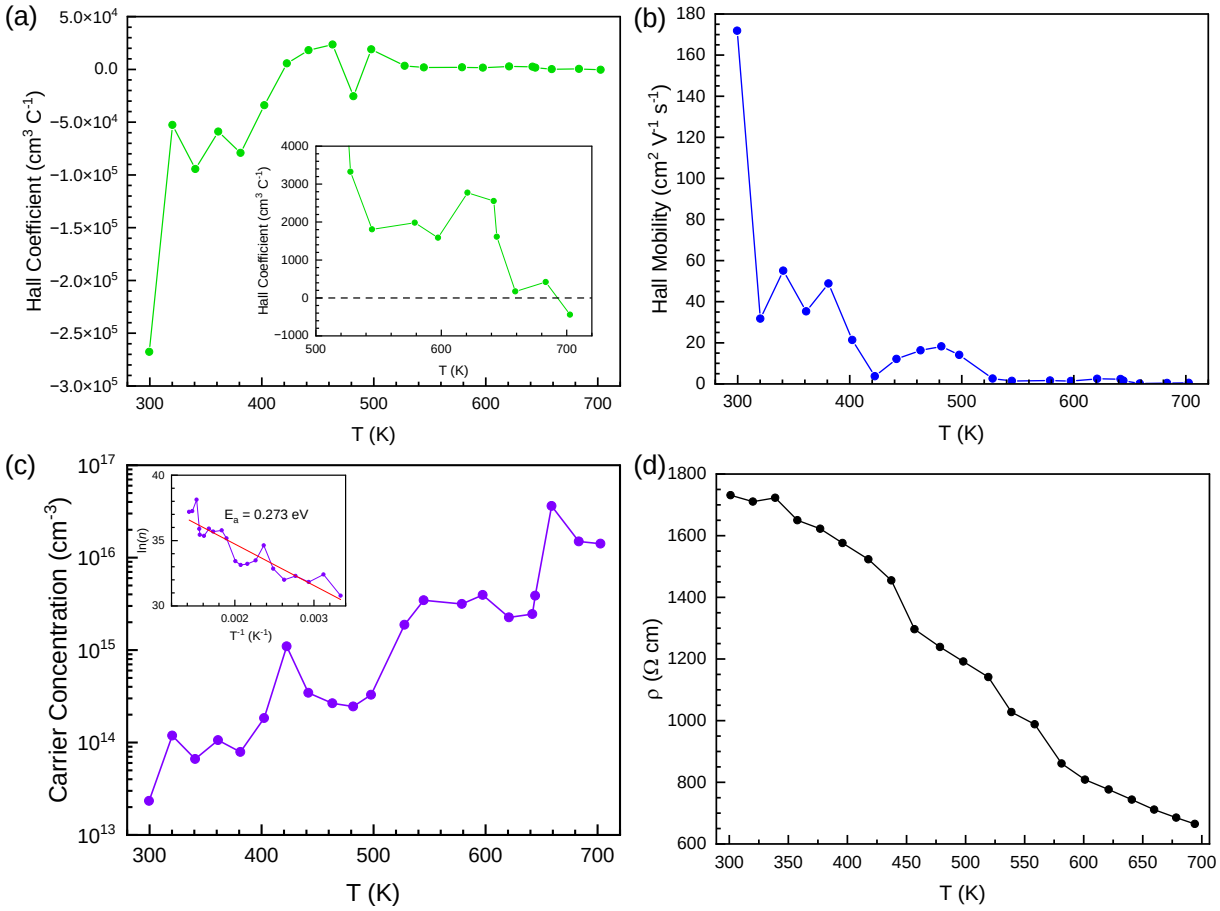

Figure 7.10 Electrical transport measurements of Sample #4. (a) Hall coefficient. (b) Hall mobility. (c) Carrier concentration. (d) Resistivity.

7.3 Discussion

The samples grown in this series do not show characteristics of high-quality heavily P-doped diamond. The electrical transport properties of certain samples suggests that they are heavily phosphorus doped, yet inconsistencies are present. Samples #1 and #3 have shown carrier concentrations up to 700 K that imply P incorporation of close to 10^{20} cm^3 or exceeding that amount. 10^{20} cm^3 is the limit of P incorporation that is expected to result in ohmic contacts. Indeed, when the growth conditions for Sample #1 were used in the fabrication of electrical contacts on Sample #2, most contacts did appear ohmic. However, the overall transport properties of Sample #1, including the non-monotonic carrier concentration and very low mobility, do not suggest a high quality diamond. Sample #2 does show that the procedure developed in Chapter 6 is capable of selective growth with metal contact pads. However, the growth conditions used for the selectively grown regions are

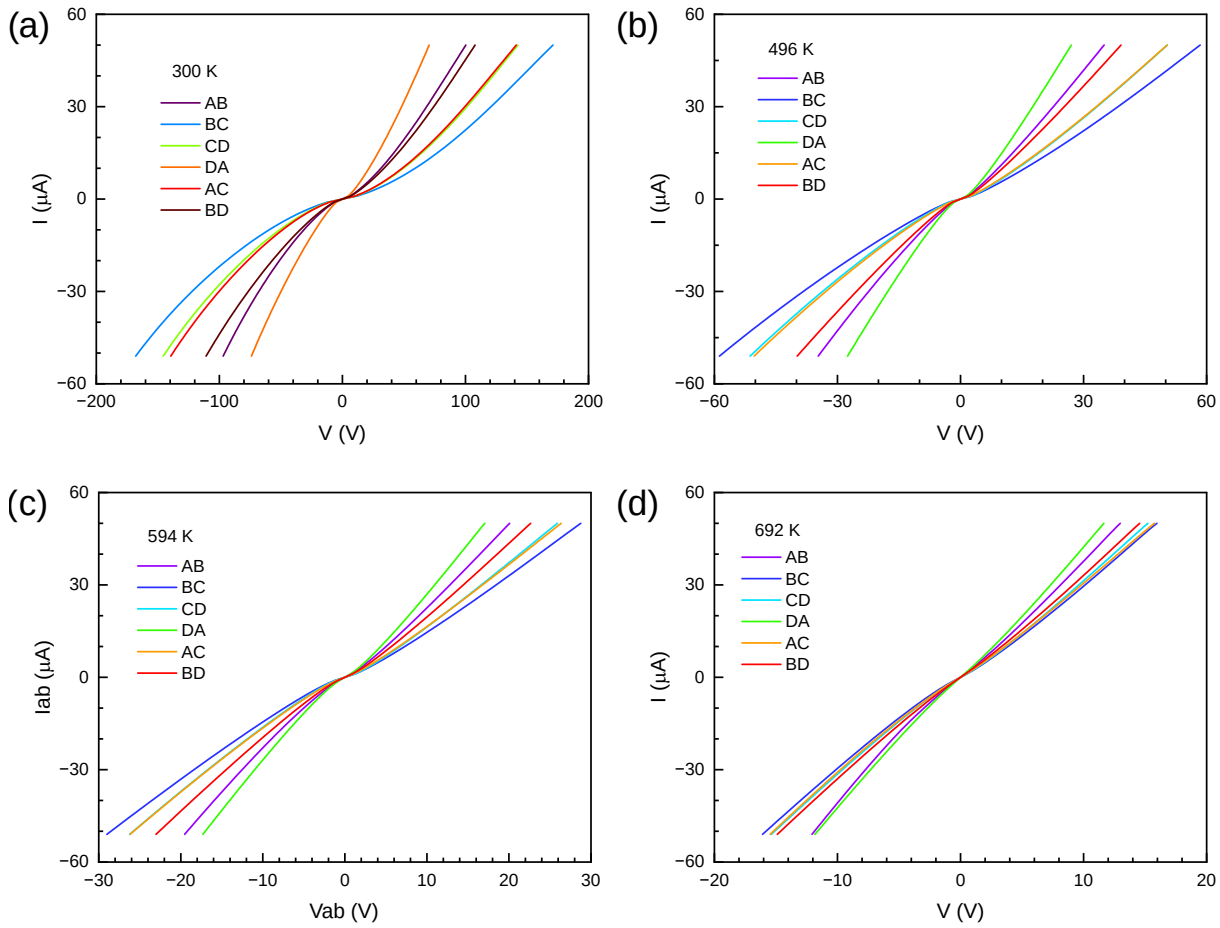

Figure 7.11 IV curves of Sample #4 at selected temperatures.

not suitable for this purpose, either due to insufficient P concentration, an excess of compensating defects, or thickness non-uniformity. The remaining samples in this sequence attempted to find growth conditions that would produce diamond of sufficient quality.

Though Sample #3 also has a high carrier concentration that suggests this sample is heavily doped, the IV curves are not sufficiently ohmic to support this. The activation energy of 0.183 eV also does not suggest that the carriers come from phosphorus. Sample #4 exhibited the highest growth rate and conclusions of *ab intio* studies would predict that fast growth rate results in higher P incorporation. [142] Yet this sample was predominantly *p*-type with a carrier activation energy of 0.273 eV. Perhaps the high growth rate was more conducive to defect formation as was seen by other researchers. [151, 152, 155] The activation energies seen for both Samples #3 and #4 are far too low for phosphorus. Boron's acceptor level is 0.37 eV, but heavy doping can lower the

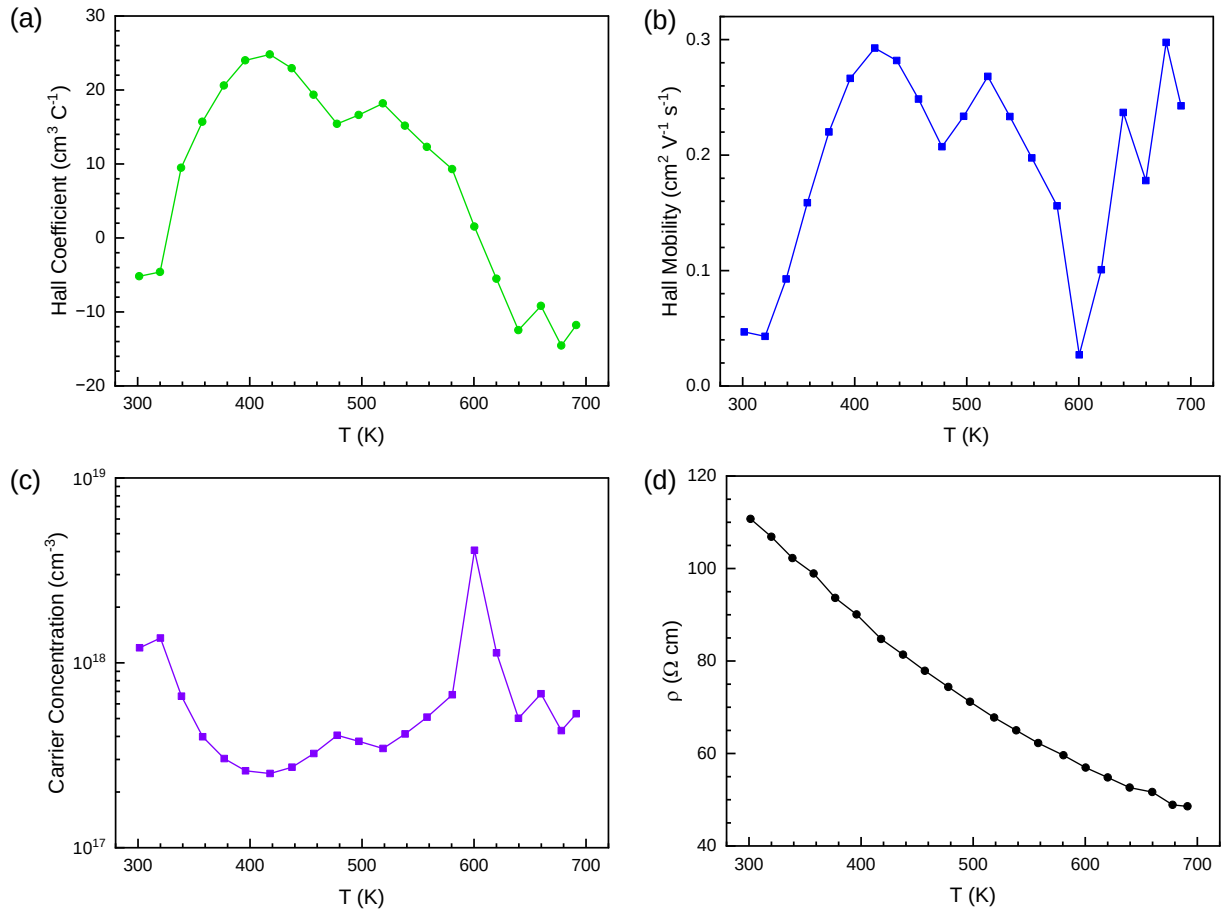

Figure 7.12 Electrical transport measurements of Sample #5. (a) Hall coefficient. (b) Hall mobility. (c) Carrier concentration. (d) Resistivity.

activation energy down to 0.18 eV. [239, 240] This would suggest extreme contamination of our diamond reactor, which is unlikely. However, these values should be considered estimates since the contact quality is not perfectly ohmic in the full temperature ranges.

If some fraction of carriers observed in these samples is a result of electrically active defects, it is unclear if they result from phosphorus incorporation. The PV center may be present in high densities, but it is not expected to be electrically active. [241] The dark color of these samples prevents us from characterizing them with spectroscopic methods since ionizing absorption dominates and obscures potentially informative signals.

The surface morphologies of these samples is not characteristic of step-flow growth and suggests a more disordered growth that could be the reason for a highly defective structure. The presence of crystal facets that are highly angled relative to the (111) plane seen for Sample #4 suggests that

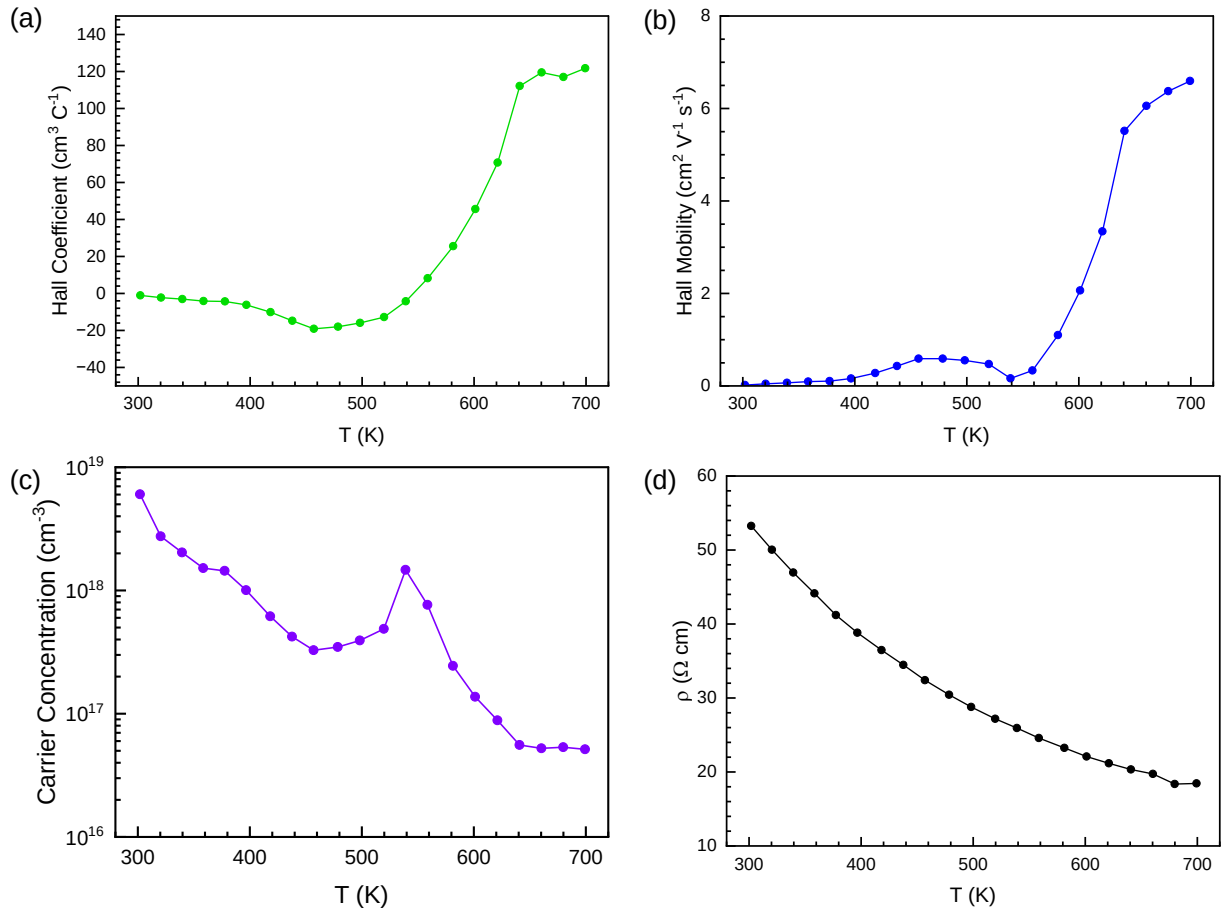

Figure 7.13 Electrical transport measurements of Sample #6. (a) Hall coefficient. (b) Hall mobility. (c) Carrier concentration. (d) Resistivity.

the lattice is preferentially growing along a different plane. The (113) plane is 29.5° away from the (111) plane, and this value is between the angles measured on the facets in Fig. 7.9(c). Perhaps the growth conditions used in Table 7.1 do not favor growth on the (111) plane. Highly defective growth may be the result of competition between growth on the exposed (111) surface and growth on more favorable planes.

Samples #5 and #6 had the most unusual transport properties. A carrier concentration that is nearly independent of temperature or that falls at high temperature implies that these samples are not of good quality.

7.4 Conclusion

We have grown a series of samples under varied growth conditions in order to find optimal conditions to grow high-quality, heavily phosphorus-doped diamond. The six samples measured

here do not show transport properties that are expected for heavily P-doped diamond with low defect density. The growth conditions tested result in diamond that is likely rich in defects that passivate donor P atoms. The cause of measured *p*-type conductivity is not clear, either resulting from defects or contaminants. The formation of electrical contacts in the van der Pauw pattern has been successfully demonstrated, though ohmic properties rely on finding better growth conditions. Future progress will likely benefit from beginning with growth conditions for Sample #1 and varying the proportions of process gasses, for example, by raising the flow of PH_3 or reducing the flow of CH_4. This may lead to higher P surface adsorption and faster growth rate which would both result in heavy doping, though high defect content may persist. Additional techniques such as secondary-ion mass spectrometry may be necessary to determine P incorporation and identify contaminants.

CHAPTER 8

CONCLUSION

In this work, we have characterized several classes of single-crystal materials primarily using transport measurements. These materials range from 2D magnets, including large band-gap van der Waals materials and R166 topological kagome metals, as well as semiconducting phosphorus-doped diamond.

Observations of van der Waals magnets which posses layered honeycomb structures with very weak interlayer interactions demonstrate the complex interactions of phonons and magnons, which manifest macroscopically though field-dependent thermal transport. We have also refined the previous unknown crystal structure of an antiferromagnetic material with an extremely weak magnetic moment, which may be the result of unusual spin-orbit coupling.

The family of R166 topological kagome metals has served as a sandbox where we have systematically modified the exchange interactions and observed changes in the magnetic structure. The phase diagram of Tb and Y end members reveals novel structures and clarifies conflicts among the preexisting literature. Anomalous transport coefficients stem from the topological underpinnings described by previous studies of the end members.

A procedure for preparing single-crystal diamond for Hall effect measurements was developed, involving a unique method of spin-coating small samples with low edge-beading and the precise conditions to prepare patterned SiO_2 films to withstand etching from the plasma within the diamond reactor. This procedure was successfully used to grow diamond in selective areas topped by metal contact pads in the van der Pauw configuration.

A series of P-doped diamond samples were grown using varied reactor conditions with the intention of identifying conditions that produce heavily P-doped diamond with low defect density. The samples grown here have not yet met that goal, either due to low phosphorus concentration, high quantities of compensating defects, or contaminants. We have not been able to precisely determine the identities of electrically active donors. In order to study the effects of growth conditions on P incorporation and defect density, the conditions to grow heavily P-doped diamond are a necessary

prerequisite for ohmic contact formation. Future endeavors to study P-doped diamond at MSU must try to identify these conditions. Some suggestions are made to future diamond growers on how this might be achieved, based on the results of this work.

This work takes an important step forward in the development of P-doped diamond at MSU. The procedure laid out here to measure electrical transport of doped diamond will be necessary to study the effects of growth conditions on P incorporation and defect density with the goal of achieving fine control over the doping levels and electrical properties of PDD samples. This would bring the progress of *n*-type diamond up to the level that is currently achieved for *p*-type diamond through boron doping.

APPENDIX A

P-DOPED DIAMOND SAMPLE LABELS

The diamond samples grown in Chapter 7 were labeled in the order that they were grown and measured. Table A.1 matches those labels to our research group's substrate labeling system.

Sample #1	24_09
Sample #2	24_10
Sample #3	24_07
Sample #4	24_01
Sample #5	24_03
Sample #6	24_04

Table A.1 Labels used in this work matched with our research group's labeling system.

Sample #1 has been lost.

BIBLIOGRAPHY

[1] Shunji Matsuura et al. “Protected boundary states in gapless topological phases”. In: *New Journal of Physics* 15.6 (2013), p. 065001.

[2] M Zahid Hasan and Charles L Kane. “Colloquium: topological insulators”. In: *Reviews of modern physics* 82.4 (2010), pp. 3045–3067.

[3] Mingrui Ao et al. “A RISC-V 32-bit microprocessor based on two-dimensional semiconductors”. In: *Nature* (2025), pp. 1–8.

[4] Andrii V Chumak et al. “Magnon spintronics”. In: *Nature physics* 11.6 (2015), pp. 453–461.

[5] AV Chumak and H Schultheiss. “Magnonics: Spin waves connecting charges, spins and photons”. In: *arXiv preprint arXiv:1901.07021* (2019).

[6] Gerrit EW Bauer, Eiji Saitoh, and Bart J Van Wees. “Spin caloritronics”. In: *Nature materials* 11.5 (2012), pp. 391–399.

[7] Gerrit EW Bauer, Eiji Saitoh, and Bart J Van Wees. “Spin caloritronics”. In: *Nature materials* 11.5 (2012), pp. 391–399.

[8] Qing Lin He et al. “Topological spintronics and magnetoelectronics”. In: *Nature materials* 21.1 (2022), pp. 15–23.

[9] Mengyun He, Huimin Sun, and Qing Lin He. “Topological insulator: Spintronics and quantum computations”. In: *Frontiers of Physics* 14 (2019), pp. 1–16.

[10] Dmytro Pesin and Allan H MacDonald. “Spintronics and pseudospintronics in graphene and topological insulators”. In: *Nature materials* 11.5 (2012), pp. 409–416.

[11] Daniel Azses et al. “Identification of symmetry-protected topological states on noisy quantum computers”. In: *Physical Review Letters* 125.12 (2020), p. 120502.

[12] Sergey Gladchenko et al. “Superconducting nanocircuits for topologically protected qubits”. In: *Nature Physics* 5.1 (2009), pp. 48–53.

[13] Emanuel Knill. “Quantum computing with realistically noisy devices”. In: *Nature* 434.7029 (2005), pp. 39–44.

[14] Meng Cheng, Roman M Lutchyn, and S Das Sarma. “Topological protection of Majorana qubits”. In: *Physical Review B—Condensed Matter and Materials Physics* 85.16 (2012), p. 165124.

[15] Constantin Schrade and Liang Fu. “Majorana superconducting qubit”. In: *Physical Review Letters* 121.26 (2018), p. 267002.

[16] Y Kajiwara et al. “Transmission of electrical signals by spin-wave interconversion in a magnetic insulator”. In: *Nature* 464.7286 (2010), pp. 262–266.

[17] Y Shiomi, R Takashima, and E Saitoh. “Experimental evidence consistent with a magnon Nernst effect in the antiferromagnetic insulator MnPS 3”. In: *Physical Review B* 96.13 (2017), p. 134425.

[18] Motoi Kimata et al. “Magnetic and magnetic inverse spin Hall effects in a non-collinear antiferromagnet”. In: *Nature* 565.7741 (2019), pp. 627–630.

[19] Nabeel Aslam et al. “Photo-induced ionization dynamics of the nitrogen vacancy defect in diamond investigated by single-shot charge state detection”. In: *New Journal of Physics* 15.1 (2013), p. 013064.

[20] Jianpei Geng et al. “Dopant-assisted stabilization of negatively charged single nitrogen-vacancy centers in phosphorus-doped diamond at low temperatures”. In: *npj Quantum Information* 9.1 (2023), p. 110.

[21] Lucio Robledo et al. “Control and Coherence of the Optical Transition of Single Nitrogen Vacancy Centers in Diamond”. In: *Physical review letters* 105.17 (2010), p. 177403.

[22] A Watanabe et al. “Shallow NV centers augmented by exploiting n-type diamond”. In: *Carbon* 178 (2021), pp. 294–300.

[23] Yuki Doi et al. “Pure negatively charged state of the NV center in n-type diamond”. In: *Physical Review B* 93.8 (2016), p. 081203.

[24] T Murai et al. “Engineering of Fermi level by nin diamond junction for control of charge states of NV centers”. In: *Applied Physics Letters* 112.11 (2018).

[25] Toshiharu Makino et al. “High-efficiency excitonic emission with deep-ultraviolet light from (001)-oriented diamond p–i–n junction”. In: *Japanese journal of applied physics* 45.10L (2006), p. L1042.

[26] Chris JH Wort and Richard S Balmer. “Diamond as an electronic material”. In: *Materials today* 11.1-2 (2008), pp. 22–28.

[27] Henri Schneider, J-L Sanchez, and Jocelyn Achard. “The diamond for power electronic devices”. In: *2005 European Conference on Power Electronics and Applications*. IEEE. 2005, 9–pp.

[28] Xiang Zhang et al. “Diamond: Recent Progress in Synthesis and Its Potential in Electron-

ics". In: *Chemistry of Materials* 37.8 (2025), pp. 2679–2698.

[29] Cui Yu et al. "Hydrogen-terminated diamond MOSFETs on (0 0 1) single crystal diamond with state of the art high RF power density". In: *Functional Diamond* 2.1 (2022), pp. 64–70.

[30] Feiyang Zhao et al. "A review of diamond materials and applications in power semiconductor devices". In: *Materials* 17.14 (2024), p. 3437.

[31] Hiromitsu Kato et al. "N-type control of single-crystal diamond films by ultra-lightly phosphorus doping". In: *Applied Physics Letters* 109.14 (2016).

[32] Taisuke Kageura et al. "Superconductivity in nano-and micro-patterned high quality single crystalline boron-doped diamond films". In: *Diamond and Related Materials* 90 (2018), pp. 181–187.

[33] Thonke Klaus et al. "The boron acceptor in diamond". In: (2003).

[34] Thierry Klein et al. "Metal-insulator transition and superconductivity in boron-doped diamond". In: *Physical Review B—Condensed Matter and Materials Physics* 75.16 (2007), p. 165313.

[35] EA Ekimov et al. "Superconductivity in diamond". In: *nature* 428.6982 (2004), pp. 542–545.

[36] William D. Nesse. *Introduction to Mineralogy*. 3rd. Oxford University Press, 2017.

[37] C. G. Shull, W. A. Strauser, and E. O. Wollan. "Neutron Diffraction by Paramagnetic and Antiferromagnetic Substances". In: *Phys. Rev.* 83 (2 July 1951), pp. 333–345. DOI: 10.1103/PhysRev.83.333. URL: https://link.aps.org/doi/10.1103/PhysRev.83.333.

[38] Ralph Skomski. *Simple models of magnetism*. Oxford university press, 2008.

[39] Neil W Ashcroft and N David Mermin. *Solid state physics*. Cengage Learning, 2022.

[40] Sam Mugiraneza and Alannah M Hallas. "Tutorial: a beginner's guide to interpreting magnetic susceptibility data with the Curie-Weiss law". In: *Communications Physics* 5.1 (2022), p. 95.

[41] Eva Pavarini et al. *Correlated Electrons: From Models to Materials*. Verlag des Forschungszentrums Jülich, 2012.

[42] John B. Goodenough. "Theory of the Role of Covalence in the Perovskite-Type Manganites $[\mathrm{La}, M(\mathrm{II})]\mathrm{MnO}_3$". In: *Phys. Rev.* 100 (2 Oct. 1955), pp. 564–573. DOI: 10.

1103/PhysRev.100.564. URL: https://link.aps.org/doi/10.1103/PhysRev.100.564.

[43] John B. Goodenough. "An interpretation of the magnetic properties of the perovskite-type mixed crystals La1xSrxCoO3". In: *Journal of Physics and Chemistry of Solids* 6.2 (1958), pp. 287–297. ISSN: 0022-3697. DOI: https://doi.org/10.1016/0022-3697(58)90107-0. URL: https://www.sciencedirect.com/science/article/pii/0022369758901070.

[44] Junjiro Kanamori. "Superexchange interaction and symmetry properties of electron orbitals". In: *Journal of Physics and Chemistry of Solids* 10.2 (1959), pp. 87–98. ISSN: 0022-3697. DOI: https://doi.org/10.1016/0022-3697(59)90061-7. URL: https://www.sciencedirect.com/science/article/pii/0022369759900617.

[45] P. W. Anderson. "Antiferromagnetism. Theory of Superexchange Interaction". In: *Phys. Rev.* 79 (2 July 1950), pp. 350–356. DOI: 10.1103/PhysRev.79.350. URL: https://link.aps.org/doi/10.1103/PhysRev.79.350.

[46] Charles Kittel and Paul McEuen. *Introduction to solid state physics*. John Wiley & Sons, 2018.

[47] Edwin H Hall et al. "On a new action of the magnet on electric currents". In: *American Journal of Mathematics* 2.3 (1879), pp. 287–292.

[48] Leo J van der Pauw. "A method of measuring the resistivity and Hall coefficient on lamellae of arbitrary shape". In: *Philips technical review* 20 (1958), pp. 220–224.

[49] Xiaokai Hu et al. "Electrostatic derivation for the van der Pauw formula and simulation using arbitrarily shaped resistive materials". In: *AIP Advances* 12.7 (2022).

[50] Alexander Altland and Ben D Simons. *Condensed matter field theory*. Cambridge university press, 2010.

[51] John R Hook and Henry Edgar Hall. *Solid state physics*. John Wiley & Sons, 2013.

[52] Robert Karplus and J. M. Luttinger. "Hall Effect in Ferromagnetics". In: *Phys. Rev.* 95 (5 Sept. 1954), pp. 1154–1160. DOI: 10.1103/PhysRev.95.1154. URL: https://link.aps.org/doi/10.1103/PhysRev.95.1154.

[53] Robert E Camley and Karen L Livesey. "Consequences of the Dzyaloshinskii-Moriya interaction". In: *Surface Science Reports* 78.3 (2023), p. 100605.

[54] Xing Guo et al. "Spin chirality driven by the Dzyaloshinskii–Moriya interaction in one-dimensional antiferromagnetic chain". In: *AIP Advances* 13.4 (2023).

[55] Honghui Wang et al. "Magnetic frustration driven high thermoelectric performance in the

kagome antiferromagnet YMn 6 Sn 6". In: *Physical Review B* 108.15 (2023), p. 155135.

[56] Qi Wang et al. "Field-induced topological Hall effect and double-fan spin structure with ac-axis component in the metallic kagome antiferromagnetic compound Y Mn 6 Sn 6". In: *Physical Review B* 103.1 (2021), p. 014416.

[57] B Chafik El Idrissi et al. "Magnetic structures of TbMn6Sn6 and HoMn6Sn6 compounds from neutron diffraction study". In: *Journal of the Less Common Metals* 175.1 (1991), pp. 143–154.

[58] Simon XM Riberolles et al. "Low-temperature competing magnetic energy scales in the topological ferrimagnet TbMn 6 Sn 6". In: *Physical Review X* 12.2 (2022), p. 021043.

[59] Jia-Xin Yin et al. "Discovery of a quantum limit Chern magnet TbMn6Sn6". In: *arXiv preprint arXiv:2006.04881* (2020).

[60] Nirmal J Ghimire et al. "Competing magnetic phases and fluctuation-driven scalar spin chirality in the kagome metal YMn6Sn6". In: *Science Advances* 6.51 (2020), eabe2680.

[61] H Zhang et al. "Topological magnon bands in a room-temperature kagome magnet". In: *Physical Review B* 101.10 (2020), p. 100405.

[62] Christopher Muratore, Andrey A Voevodin, and Nicholas R Glavin. "Physical vapor deposition of 2D Van der Waals materials: a review". In: *Thin Solid Films* 688 (2019), p. 137500.

[63] Samuel Mañas-Valero et al. "Fundamentals and applications of van der Waals magnets in magnon spintronics". In: *Newton* 1.1 (2025).

[64] Renji Bian et al. "Recent progress in the synthesis of novel two-dimensional van der Waals materials". In: *National Science Review* 9.5 (2022), nwab164.

[65] B hsHuang et al. "Layer-dependent ferromagnetism in a van der Waals crystal down to the monolayer limit". In: *Nature* (2017).

[66] Lebing Chen et al. "Topological spin excitations in honeycomb ferromagnet CrI 3". In: *Physical Review X* 8.4 (2018), p. 041028.

[67] Lebing Chen et al. "Magnetic field effect on topological spin excitations in CrI 3". In: *Physical Review X* 11.3 (2021), p. 031047.

[68] Verena Brehm et al. "Topological magnon gap engineering in van der Waals CrI 3 ferromagnets". In: *Physical Review B* 109.17 (2024), p. 174425.

[69] Esteban Aguilera et al. "Topological magnonics in the two-dimensional van der Waals

magnet CrI 3". In: *Physical Review B* 102.2 (2020), p. 024409.

[70] Zhengwei Cai et al. "Topological magnon insulator spin excitations in the two-dimensional ferromagnet CrBr 3". In: *Physical Review B* 104.2 (2021), p. L020402.

[71] Saikat Banerjee and Stephan Humeniuk. "Interacting Dirac magnons in honeycomb ferromagnets CrBr _3". In: *arXiv preprint arXiv:2506.07650* (2025).

[72] Suhan Son et al. "Bulk properties of the van der Waals hard ferromagnet VI 3". In: *Physical Review B* 99.4 (2019), p. 041402.

[73] Shangjie Tian et al. "Ferromagnetic van der Waals crystal VI3". In: *Journal of the American Chemical Society* 141.13 (2019), pp. 5326–5333.

[74] Heda Zhang et al. "Anomalous thermal Hall effect in an insulating van der Waals magnet". In: *Physical Review Letters* 127.24 (2021), p. 247202.

[75] Christoph E Nebel. "General properties of diamond". In: *Nanodiamonds*. Elsevier, 2017, pp. 1–24.

[76] MW Geis, NN Efremow, and JA Von Windheim. "High-conductance, low-leakage diamond Schottky diodes". In: *Applied physics letters* 63.7 (1993), pp. 952–954.

[77] Y Yamamoto et al. "The measurement of thermal properties of diamond". In: *Diamond and Related Materials* 6.8 (1997), pp. 1057–1061.

[78] Jörg Wrachtrup and Fedor Jelezko. "Processing quantum information in diamond". In: *Journal of Physics: Condensed Matter* 18.21 (2006), S807.

[79] Wikipedia contributors. *Carbon — Wikipedia, The Free Encyclopedia*. Accessed: 2024-06-30. 2024. URL: https://en.wikipedia.org/wiki/Carbon.

[80] Alexander M Zaitsev. *Optical properties of diamond: a data handbook*. Springer Science & Business Media, 2013.

[81] Wang Lin et al. "Effect of growth rate on the incorporation of silicon impurity in single crystal diamond". In: *Materials Science in Semiconductor Processing* 180 (2024), p. 108554.

[82] Isao Sakaguchi et al. "Silicon incorporation into chemical vapor deposition diamond: A role of oxygen". In: *Applied physics letters* 71.5 (1997), pp. 629–631.

[83] Isao Sakaguchi et al. "Homoepitaxial growth and hydrogen incorporation on the chemical vapor deposited (111) diamond". In: *Journal of applied physics* 86.3 (1999), pp. 1306–1310.

[84] Satoshi Koizumi, Christoph Nebel, and Milos Nesladek. *Physics and applications of CVD diamond*. John Wiley & Sons, 2008.

[85] AM Fischer et al. "The effect of step-flow growth on the surface morphology and optical properties of thick diamond films". In: *Diamond and Related Materials* 140 (2023), p. 110507.

[86] James E Butler and Richard L Woodin. "Thin film diamond growth mechanisms". In: *Philosophical Transactions of the Royal Society of London. Series A: Physical and Engineering Sciences* 342.1664 (1993), pp. 209–224.

[87] Hiroyuki Tamura et al. "First-principle study on reactions of diamond (100) surfaces with hydrogen and methyl radicals". In: *Physical Review B* 62.24 (2000), p. 16995.

[88] James E Butler and Ivan Oleynik. "A mechanism for crystal twinning in the growth of diamond by chemical vapour deposition". In: *Philosophical Transactions of the Royal Society A: Mathematical, Physical and Engineering Sciences* 366.1863 (2008), pp. 295–311.

[89] Ben L Green, Alan T Collins, and Christopher M Breeding. "Diamond spectroscopy, defect centers, color, and treatments". In: *Reviews in Mineralogy and Geochemistry* 88.1 (2022), pp. 637–688.

[90] Melvin Lax and Elias Burstein. "Infrared lattice absorption in ionic and homopolar crystals". In: *Physical Review* 97.1 (1955), p. 39.

[91] CD Clark and ST Davey. "One-phonon infrared absorption in diamond". In: *Journal of Physics C: Solid State Physics* 17.6 (1984), p. 1127.

[92] Claude A Klein, Thomas M Hartnett, and Clifford J Robinson. "Critical-point phonon frequencies of diamond". In: *Physical Review B* 45.22 (1992), p. 12854.

[93] Simon M Sze, Yiming Li, and Kwok K Ng. *Physics of semiconductor devices*. John wiley & sons, 2021.

[94] Karlheinz Seeger. *Semiconductor physics*. Springer Science & Business Media, 2013.

[95] S Yamanaka et al. "Low-compensated boron-doped homoepitaxial diamond films". In: *Diamond and Related Materials* 9.3-6 (2000), pp. 956–959.

[96] V Mortet et al. "Effect of substrate crystalline orientation on boron-doped homoepitaxial diamond growth". In: *Diamond and Related Materials* 122 (2022), p. 108887.

[97] CM Yap et al. "Properties of near-colourless lightly boron doped CVD diamond". In: *Diamond and Related Materials* 88 (2018), pp. 118–122.

[98] S Yamanaka et al. “Low-compensated boron-doped homoepitaxial diamond films using trimethylboron”. In: *physica status solidi (a)* 174.1 (1999), pp. 59–64.

[99] Karin Larsson. “Substitutional n-type doping of diamond”. In: *Computational materials science* 27.1-2 (2003), pp. 23–29.

[100] A.T. Collins and E.C. Lightowlers. “The Properties of Diamond”. In: *The Properties of Diamond*. Ed. by J.E. Field. London: Academic Press, 1979. Chap. 3, pp. 79–105.

[101] RP Messmer and GD Watkins. “Molecular-orbital treatment for deep levels in semiconductors: substitutional nitrogen and the lattice vacancy in diamond”. In: *Physical Review B* 7.6 (1973), p. 2568.

[102] EB Lombardi et al. “Computational models of the single substitutional nitrogen atom in diamond”. In: *Journal of Physics: Condensed Matter* 15.19 (2003), p. 3135.

[103] Y Fang et al. “Manipulation of magnetic field on dielectric constant and electric polarization in Cr2WO6”. In: *Applied Physics Letters* 104.13 (2014).

[104] S Koizumi et al. “Growth and characterization of phosphorus doped n-type diamond thin films”. In: *Diamond and related materials* 7.2-5 (1998), pp. 540–544.

[105] Nozomi Orita, Takeshi Nishimatsu, and Hiroshi Katayama-Yoshida. “Ab initio study for site symmetry of phosphorus-doped diamond”. In: *Japanese journal of applied physics* 46.1R (2007), p. 315.

[106] RJ Eyre et al. “Theory of Jahn–Teller distortions of the P donor in diamond”. In: *Journal of Physics: Condensed Matter* 17.37 (2005), p. 5831.

[107] Takeshi Nishimatsu, Hiroshi Katayama-Yoshida, and Nozomi Orita. “Theoretical study of hydrogen-related complexes in diamond for low-resistive n-type diamond semiconductor”. In: *Physica B: Condensed Matter* 302 (2001), pp. 149–154.

[108] Takeshi Nishimatsu, Hiroshi Katayama-Yoshida, and Nozomi Orita. “Ab initio study of donor–hydrogen complexes for low-resistivity n-type diamond semiconductor”. In: *Japanese journal of applied physics* 41.4R (2002), p. 1952.

[109] LG Wang and Alex Zunger. “Phosphorus and sulphur doping of diamond”. In: *Physical Review B* 66.16 (2002), p. 161202.

[110] SJ Sque et al. “Shallow donors in diamond: chalcogens, pnictogens, and their hydrogen complexes”. In: *Physical review letters* 92.1 (2004), p. 017402.

[111] T Graf et al. “Electron Spin Resonance of Phosphorus in n-Type Diamond”. In: *physica status solidi (a)* 193.3 (2002), pp. 434–441.

[112] J Isoya et al. “Pulsed EPR studies of Phosphorus shallow donors in diamond and SiC”. in: *Physica B: Condensed Matter* 376 (2006), pp. 358–361.

[113] Ken Haenen et al. “The phosphorous level fine structure in homoepitaxial and polycrystalline n-type CVD diamond”. In: *Diamond and related materials* 13.11-12 (2004), pp. 2041–2045.

[114] E Gheeraert et al. “Electronic states of phosphorus in diamond”. In: *Diamond and Related Materials* 9.3-6 (2000), pp. 948–951.

[115] E Gheeraert et al. “Low temperature excitation spectrum of phosphorus in diamond”. In: *Diamond and related materials* 10.3-7 (2001), pp. 444–448.

[116] Ken Okano et al. “Synthesis of n-type semiconducting diamond film using diphosphorus pentaoxide as the doping source”. In: *Applied Physics A* 51 (1990), pp. 344–346.

[117] Rajat Roychoudhury et al. “Growth and characterization of phosphorus doped diamond films using trimethyl phosphite as the doping source”. In: *Journal of applied physics* 81.8 (1997), pp. 3644–3646.

[118] SN Schauer et al. “Phosphorus incorporation in plasma deposited diamond films”. In: *Applied physics letters* 64.9 (1994), pp. 1094–1096.

[119] S Koizumi et al. “Growth and characterization of phosphorous doped {111} homoepitaxial diamond thin films”. In: *Applied Physics Letters* 71.8 (1997), pp. 1065–1067.

[120] Satoshi Koizumi, Tokuyuki Teraji, and Hisao Kanda. “Phosphorus-doped chemical vapor deposition of diamond”. In: *Diamond and Related Materials* 9.3-6 (2000), pp. 935–940.

[121] SA Kajihara et al. “Nitrogen and potential n-type dopants in diamond”. In: *Physical review letters* 66.15 (1991), p. 2010.

[122] Koblar Jackson, Mark R Pederson, and Joseph G Harrison. “Donor levels and impurity-atom relaxation in nitrogen-and phosphorus-doped diamond”. In: *Physical Review B* 41.18 (1990), p. 12641.

[123] I Stenger et al. “Impurity-to-band activation energy in phosphorus doped diamond”. In: *Journal of Applied Physics* 114.7 (2013).

[124] TA Grotjohn et al. “Heavy phosphorus doping by epitaxial growth on the (111) diamond surface”. In: *Diamond and related materials* 44 (2014), pp. 129–133.

[125] Yūki Katamune et al. “Heavy phosphorus doping of diamond by hot-filament chemical vapor deposition”. In: *Diamond and Related Materials* 134 (2023), p. 109789.

[126] Nephi Temahuki et al. “New Process for Electrical Contacts on (100) N-type Diamond”. In: *physica status solidi (a)* 214.11 (2017), p. 1700466.

[127] Thomas Schuelke and Timothy A Grotjohn. “Diamond polishing”. In: *Diamond and Related Materials* 32 (2013), pp. 17–26.

[128] Hiromitsu Kato et al. “n-type diamond growth by phosphorus doping on (0 0 1)-oriented surface”. In: *Journal of Physics D: Applied Physics* 40.20 (2007), p. 6189.

[129] Hiromitsu Kato, Satoshi Yamasaki, and Hideyo Okushi. “n-type doping of (001)-oriented single-crystalline diamond by phosphorus”. In: *Applied Physics Letters* 86.22 (2005).

[130] Hiromitsu Kato, Satoshi Yamasaki, and Hideyo Okushi. “Carrier compensation in (001) n-type diamond by phosphorus doping”. In: *Diamond and related materials* 16.4-7 (2007), pp. 796–799.

[131] Hiroyuki Kawashima et al. “Desorption time of phosphorus during MPCVD growth of n-type (001) diamond”. In: *Diamond and Related Materials* 64 (2016), pp. 208–212.

[132] I Stenger et al. “Electron mobility in (100) homoepitaxial layers of phosphorus-doped diamond”. In: *Journal of Applied Physics* 129.10 (2021).

[133] Masayuki Katagiri et al. “Lightly phosphorus-doped homoepitaxial diamond films grown by chemical vapor deposition”. In: *Applied physics letters* 85.26 (2004), pp. 6365–6367.

[134] Hiromitsu Kato et al. “Growth of phosphorus-doped diamond using tertiarybutylphosphine and trimethylphosphine as dopant gases”. In: *Diamond and related materials* 14.3-7 (2005), pp. 340–343.

[135] T Kociniewski et al. “n-type CVD diamond doped with phosphorus using the MOCVD technology for dopant incorporation”. In: *physica status solidi (a)* 203.12 (2006), pp. 3136–3141.

[136] Yaso Balasubramaniam et al. “Thick homoepitaxial (110)-oriented phosphorus-doped n-type diamond”. In: *Applied Physics Letters* 109.6 (2016).

[137] Marie-Amandine Pinault-Thaury et al. “Phosphorus-doped (113) CVD diamond: A breakthrough towards bipolar diamond devices”. In: *Applied Physics Letters* 114.11 (2019).

[138] Marie-Amandine Pinault-Thaury et al. “Attractive electron mobility in (113) n-type phosphorus-doped homoepitaxial diamond”. In: *Carbon* 175 (2021), pp. 254–258.

[139] Ryota Ohtani et al. “Large improvement of phosphorus incorporation efficiency in n-type chemical vapor deposition of diamond”. In: *Applied Physics Letters* 105.23 (2014).

[140] Marie-Amandine Pinault-Thaury et al. “Electrical activity of (100) n-type diamond with full donor site incorporation of phosphorus”. In: *physica status solidi (a)* 212.11 (2015), pp. 2454–2459.

[141] Takashi Yamamoto et al. “Toward highly conductive n-type diamond: Incremental phosphorus-donor concentrations assisted by surface migration of admolecules”. In: *Applied Physics Letters* 109.18 (2016).

[142] Takehide Miyazaki et al. “Energetics of dopant atoms in subsurface positions of diamond semiconductor”. In: *Superlattices and Microstructures* 40.4-6 (2006), pp. 574–579.

[143] Yasuo Koide. “Analysis of electron statistics involving compensation and deep-dopant effects for phosphorus-doped n-type diamond”. In: *Japanese journal of applied physics* 43.6R (2004), p. 3307.

[144] JP Goss et al. “Theory of hydrogen in diamond”. In: *Physical Review B* 65.11 (2002), p. 115207.

[145] M Kasu et al. “Formation of stacking faults containing microtwins in (111) chemical-vapor-deposited diamond homoepitaxial layers”. In: *Applied physics letters* 83.17 (2003), pp. 3465–3467.

[146] Hiromitsu Kato et al. “N-type doping on (001)-oriented diamond”. In: *Diamond and related materials* 15.4-8 (2006), pp. 548–553.

[147] Norio Tokuda et al. “Hillock-free heavily boron-doped homoepitaxial diamond films on misoriented (001) substrates”. In: *Japanese journal of applied physics* 46.4R (2007), p. 1469.

[148] R Jones, JE Lowther, and J Goss. “Limitations to n-type doping in diamond: The phosphorus-vacancy complex”. In: *Applied physics letters* 69.17 (1996), pp. 2489–2491.

[149] Hiroyuki Okazaki et al. “Multiple phosphorus chemical sites in heavily phosphorus-doped diamond”. In: *Applied Physics Letters* 98.8 (2011).

[150] Masataka Hasegawa, Tokuyuki Teraji, and Satoshi Koizumi. “Lattice location of phosphorus in n-type homoepitaxial diamond films grown by chemical-vapor deposition”. In: *Applied Physics Letters* 79.19 (2001), pp. 3068–3070.

[151] M-A Pinault-Thaury et al. “n-Type CVD diamond: Epitaxy and doping”. In: *Materials Science and Engineering: B* 176.17 (2011), pp. 1401–1408.

[152] M-A Pinault-Thaury et al. “Phosphorus donor incorporation in (1 0 0) homoepitaxial diamond: Role of the lateral growth”. In: *Journal of Crystal Growth* 335.1 (2011), pp. 31–36.

[153] MP Everson and MA Tamor. "Investigation of growth rates and morphology for diamond growth by chemical vapor deposition". In: *Journal of materials research* 7.6 (1992), pp. 1438–1444.

[154] Philip Martineau et al. "Effect of steps on dislocations in CVD diamond grown on {001} substrates". In: *physica status solidi c* 6.8 (2009), pp. 1953–1957.

[155] M-A Pinault-Thaury et al. "High fraction of substitutional phosphorus in a (100) diamond epilayer with low surface roughness". In: *Applied Physics Letters* 100.19 (2012).

[156] N Casanova et al. "Epitaxial growth of phosphorus doped diamond on {111} substrate". In: *Diamond and related materials* 11.3-6 (2002), pp. 328–331.

[157] F Lloret et al. "High phosphorous incorporation in (100)-oriented MP CVD diamond growth". In: *Diamond and Related Materials* 133 (2023), p. 109746.

[158] Hiromitsu Kato et al. "n-Type diamond growth by phosphorus doping". In: *MRS Online Proceedings Library (OPL)* 1039 (2007), 1039–P05.

[159] Hiromitsu Kato et al. "Electrical activity of doped phosphorus atoms in (001) n-type diamond". In: *physica status solidi (a)* 205.9 (2008), pp. 2195–2199.

[160] Hiromitsu Kato et al. "Energy level of compensator states in (001) phosphorus-doped diamond". In: *Diamond and related materials* 20.7 (2011), pp. 1016–1019.

[161] Takehide Miyazaki and Satoshi Yamasaki. "Ab initio energetics of phosphorus related complex defects in synthetic diamond". In: *Physica B: Condensed Matter* 376 (2006), pp. 304–306.

[162] Stephen J Harris. "Mechanism for diamond growth from methyl radicals". In: *Applied Physics Letters* 56.23 (1990), pp. 2298–2300.

[163] David G Goodwin. "Scaling laws for diamond chemical-vapor deposition. I. Diamond surface chemistry". In: *Journal of Applied Physics* 74.11 (1993), pp. 6888–6894.

[164] Stephen J Harris and DG Goodwin. "Growth on the reconstructed diamond (100) surface". In: *The Journal of Physical Chemistry* 97.1 (1993), pp. 23–28.

[165] F Silva et al. "High quality, large surface area, homoepitaxial MPACVD diamond growth". In: *Diamond and Related Materials* 18.5-8 (2009), pp. 683–697.

[166] M Muehle et al. "Extending microwave plasma assisted CVD SCD growth to pressures of 400 Torr". In: *Diamond and Related Materials* 79 (2017), pp. 150–163.

[167] KW Hemawan et al. "Improved microwave plasma cavity reactor for diamond synthesis at

high-pressure and high power density". In: *Diamond and Related Materials* 19.12 (2010), pp. 1446–1452.

[168] Yuri A Mankelevich, Michael NR Ashfold, and Jie Ma. "Plasma-chemical processes in microwave plasma-enhanced chemical vapor deposition reactors operating with C/H/Ar gas mixtures". In: *Journal of applied physics* 104.11 (2008).

[169] Yu A Mankelevich and PW May. "New insights into the mechanism of CVD diamond growth: Single crystal diamond in MW PECVD reactors". In: *Diamond and Related Materials* 17.7-10 (2008), pp. 1021–1028.

[170] EV Bushuev et al. "Synthesis of single crystal diamond by microwave plasma assisted chemical vapor deposition with in situ low-coherence interferometric control of growth rate". In: *Diamond and Related Materials* 66 (2016), pp. 83–89.

[171] J Achard et al. "High quality MPACVD diamond single crystal growth: high microwave power density regime". In: *Journal of Physics D: Applied Physics* 40.20 (2007), p. 6175.

[172] A Tallaire et al. "Homoepitaxial deposition of high-quality thick diamond films: effect of growth parameters". In: *Diamond and related materials* 14.3-7 (2005), pp. 249–254.

[173] T Kociniewski et al. "MOCVD doping technology for phosphorus incorporation in diamond: Influence of the growth temperature on the electrical properties". In: *Diamond and related materials* 16.4-7 (2007), pp. 815–818.

[174] Hiromitsu Kato et al. "Low specific contact resistance of heavily phosphorus-doped diamond film". In: *Applied Physics Letters* 93.20 (2008).

[175] Tokuyuki Teraji et al. "Electrical contacts for n-type diamond". In: *Japanese journal of applied physics* 38.10A (1999), p. L1096.

[176] T Teraji, S Koizumi, and H Kanda. "Ga Ohmic contact for n-type diamond by ion implantation". In: *Applied Physics Letters* 76.10 (2000), pp. 1303–1305.

[177] Tokuyuki Teraji et al. "Ohmic contact formation for N-type diamond by selective doping". In: *Japanese journal of applied physics* 42.8A (2003), p. L882.

[178] Heda Zhang. *Neutron Scattering and Transport Studies of Quantum Materials*. Michigan State University, 2022.

[179] *Silicon Dioxide (SiO_2) Etchants*. `https://transene.com/sio2/`. Accessed: 2025-08-29.

[180] Isil Berkun. *High temperature hall effect measurement system design, measurement and analysis*. Michigan State University, 2015.

[181] Jens Als-Nielsen and Des McMorrow. *Elements of modern X-ray physics*. 2nd. Wiley, 2011.

[182] D.S. Sivia. *Elementary Scattering Theory: For X-ray and Neutron Users*. Oxford University Press, Jan. 2011. ISBN: 9780199228676. DOI: 10.1093/acprof:oso/9780199228676.001.0001. eprint: https://academic.oup.com/book/7397/book-pdf/50580908/9780191004773_web.pdf. URL: https://doi.org/10.1093/acprof:oso/9780199228676.001.0001.

[183] Albert Furrer, Joël. F. Mesot, and Thierry Strässle. *Neutron Scattering In Condensed Matter Physics*. Series On Neutron Techniques And Applications. World Scientific Publishing Company, 2009. ISBN: 9789813102507. URL: https://books.google.com/books?id=SPQ7DQAAQBAJ.

[184] Vasile O Garlea et al. "The high-resolution powder diffractometer at the high flux isotope reactor". In: *Applied Physics A* 99 (2010), pp. 531–535.

[185] Ashfia Huq et al. "POWGEN: rebuild of a third-generation powder diffractometer at the Spallation Neutron Source". In: *Journal of Applied Crystallography* 52.5 (Oct. 2019), pp. 1189–1201. DOI: 10.1107/S160057671901121X.

[186] A. Huq et al. "Powgen: A third-generation highresolution high-throughput powder diffraction instrument at the Spallation Neutron Source". In: *European Powder Diffraction Conference; August 2010, Darmstadt, Germany*. München: Oldenbourg Wissenschaftsverlag, 2011, pp. 127–136. ISBN: 9783486991321. DOI: doi:10.1524/9783486991321-024. URL: https://doi.org/10.1524/9783486991321-024.

[187] Juan Rodríguez-Carvajal. "Recent advances in magnetic structure determination by neutron powder diffraction". In: *Physica B: Condensed Matter* 192.1 (1993), pp. 55–69. ISSN: 0921-4526. DOI: https://doi.org/10.1016/0921-4526(93)90108-I. URL: https://www.sciencedirect.com/science/article/pii/092145269390108I.

[188] A.S Wills. "A new protocol for the determination of magnetic structures using simulated annealing and representational analysis (SARAh)". In: *Physica B: Condensed Matter* 276-278 (2000), pp. 680–681. ISSN: 0921-4526. DOI: https://doi.org/10.1016/S0921-4526(99)01722-6. URL: https://www.sciencedirect.com/science/article/pii/S0921452699017226.

[189] Matjaz Valant, Anna-Karin Axelsson, and Neil Alford. "Peculiarities of a solid-state synthesis of multiferroic polycrystalline BiFeO3". In: *Chemistry of Materials* 19.22 (2007), pp. 5431–5436.

[190] Christopher S Knee, Marianne AL Field, and Mark T Weller. "Neutron diffraction study of the antiferromagnetic oxyhalides Sr3Fe2O5Cl2, Sr3Fe2O5Br2 and Sr3FeCoO5Cl2". In: *Solid state sciences* 6.5 (2004), pp. 443–450.

[191] Brian C Sales et al. “Electronic, magnetic, and thermodynamic properties of the kagome layer compound FeSn”. In: *Physical Review Materials* 3.11 (2019), p. 114203.

[192] ZW Riedel et al. “Magnetic order and physical properties of the kagome metal UNb 6 Sn 6”. In: *Physical Review Materials* 9.8 (2025), p. 084401.

[193] Tai Kong et al. “Crystal structure and magnetic properties of the layered van der Waals compound VB r 3”. In: *Physical Review Materials* 3.8 (2019), p. 084419.

[194] Xiaoyun Yu et al. “Large magnetocaloric effect in van der Waals crystal CrBr3”. In: *Frontiers of Physics* 14.4 (2019), p. 43501.

[195] Xufan Li et al. “Van der Waals epitaxial growth of two-dimensional single-crystalline GaSe domains on graphene”. In: *ACS nano* 9.8 (2015), pp. 8078–8088.

[196] Yu D Kozmanov. “Investigation of the High Temperature Oxidation of Some Iron Tungten Alloys”. In: *Zh. Fiz. Khim* 31 (1957), p. 1861.

[197] J Walczak, I Rychiowska-Himmel, and P Tabero. “Iron (III) tungstate and its modifications”. In: *Journal of materials science* 27 (1992), pp. 3680–3684.

[198] Jean Senegas and Jean Galy. “L’oxyde double Fe2WO6. I. Structure cristalline et filiation structurale”. In: *Journal of Solid State Chemistry* 10.1 (1974), pp. 5–11.

[199] Raphael Schuler, Truls Norby, and Helmer Fjellvåg. “Defects and polaronic electron transport in Fe 2 WO 6”. In: *Physical Chemistry Chemical Physics* 22.27 (2020), pp. 15541–15548.

[200] H Pinto, M Melamud, and H Shaked. “Magnetic structure of Fe2WO6, a neutron diffraction study”. In: *Acta Crystallographica Section A: Crystal Physics, Diffraction, Theoretical and General Crystallography* 33.4 (1977), pp. 663–667.

[201] N Guskos et al. “Magnetic and EPR Studies of α-, β-, and γ-Fe2WO6 Phases at Low Temperatures”. In: *Journal of solid state chemistry* 120.2 (1995), pp. 216–222.

[202] N Guskos et al. “Electrical Transport and EPR Properties of the α, β, and γ Phases of Fe 2 WO 6”. In: *Physical Review B* 60.11 (1999), p. 7687.

[203] H Leiva, K Dwight, and Aaron Wold. “Preparation and characterization of conducting iron tungstates”. In: *Journal of Solid State Chemistry* 42.1 (1982), pp. 41–46.

[204] H Leiva et al. “Preparation and properties of the systems Fe2- xCrxWO6, Fe2- xRhxWO6, and Cr2- xRhxWO6”. In: *Journal of Solid State Chemistry* 47.3 (1983), pp. 293–300.

[205] Soumendra Nath Panja et al. “γ-Fe2WO6–A magnetodielectric with disordered magnetic

and electronic ground states". In: *Journal of Magnetism and Magnetic Materials* 466 (2018), pp. 354–358.

[206] H. Weitzel. "Magnetische Strukturen von $NiNb_2O_6$ und Fe_2WO_6". In: *Acta Crystallographica Section A* 32.4 (July 1976), pp. 592–597. DOI: 10.1107/S0567739476001265. URL: https://doi.org/10.1107/S0567739476001265.

[207] G. Kresse and J. Furthmüller. "Efficient iterative schemes for ab initio total-energy calculations using a plane-wave basis set". In: *Phys. Rev. B* 54 (16 Oct. 1996), pp. 11169–11186. DOI: 10.1103/PhysRevB.54.11169. URL: https://link.aps.org/doi/10.1103/PhysRevB.54.11169.

[208] G. Kresse and D. Joubert. "From ultrasoft pseudopotentials to the projector augmented-wave method". In: *Phys. Rev. B* 59 (3 Jan. 1999), pp. 1758–1775. DOI: 10.1103/PhysRevB.59.1758. URL: https://link.aps.org/doi/10.1103/PhysRevB.59.1758.

[209] John P. Perdew, Kieron Burke, and Matthias Ernzerhof. "Generalized Gradient Approximation Made Simple". In: *Phys. Rev. Lett.* 77 (18 Oct. 1996), pp. 3865–3868. DOI: 10.1103/PhysRevLett.77.3865. URL: https://link.aps.org/doi/10.1103/PhysRevLett.77.3865.

[210] S. L. Dudarev et al. "Electron-energy-loss spectra and the structural stability of nickel oxide: An LSDA+U study". In: *Phys. Rev. B* 57 (3 Jan. 1998), pp. 1505–1509. DOI: 10.1103/PhysRevB.57.1505. URL: https://link.aps.org/doi/10.1103/PhysRevB.57.1505.

[211] Yu Meng et al. "When density functional approximations meet iron oxides". In: *Journal of chemical theory and computation* 12.10 (2016), pp. 5132–5144.

[212] M.J. Rutter. "C2x: A tool for visualisation and input preparation for Castep and other electronic structure codes". In: *Computer Physics Communications* 225 (2018), pp. 174–179. ISSN: 0010-4655. DOI: https://doi.org/10.1016/j.cpc.2017.12.008. URL: https://www.sciencedirect.com/science/article/pii/S0010465517304137.

[213] AH Hill et al. "Neutron diffraction study of mesoporous and bulk hematite, α-Fe2O3". In: *Chemistry of Materials* 20.15 (2008), pp. 4891–4899.

[214] J. A. Van Allen and S. F. Singer. "On the Primary Cosmic-Ray Spectrum". In: *Phys. Rev.* 78 (6 June 1950), pp. 819–819. DOI: 10.1103/PhysRev.78.819. URL: https://link.aps.org/doi/10.1103/PhysRev.78.819.

[215] Thomas Birchall et al. "A study of iron–tungsten oxides and iron–chromium–tungsten oxides". In: *Canadian Journal of Chemistry* 66.4 (1988), pp. 698–702. DOI: 10.1139/v88-121.

[216] Oleg Vladimirovich Kovalev et al. “Representations of the Crystallographic Space Groups: Irreducible Representations, Induced Representations, and Corepresentations”. In: *(No Title)* (1993).

[217] Fatwa F. Abdi et al. “Assessing the Suitability of Iron Tungstate (Fe2WO6) as a Photoelectrode Material for Water Oxidation”. In: *The Journal of Physical Chemistry C* 121.1 (2017), pp. 153–160. DOI: 10.1021/acs.jpcc.6b10695. eprint: https://doi.org/10.1021/acs.jpcc.6b10695. URL: https://doi.org/10.1021/acs.jpcc.6b10695.

[218] Mahmoud M Khader, Mahmoud M Saleh, and Emad M El-Naggar. “Photoelectrochemical characteristics of ferric tungstate”. In: *Journal of Solid State Electrochemistry* 2 (1998), pp. 170–175.

[219] R Bharati and RA Singh. “The electrical properties of Fe 2 WO 6”. In: *Journal of Materials Science* 16 (1981), pp. 511–514.

[220] AA Bykov et al. “Magnetic phase diagram of Y1- xTbxMn6Sn6 compounds”. In: *Journal of Magnetism and Magnetic Materials* 424 (2017), pp. 347–351.

[221] NK Zajkov et al. “Magnetic properties of Tb1- xYxMn6Sn6 compounds”. In: *Journal of alloys and compounds* 363.1-2 (2004), pp. 40–45.

[222] NV Mushnikov et al. “Magnetic phase transitions in Y1- xTbxMn6Sn6, La1- xSmxMn2Si2, Lu2 (Fe1- Mnx) 17, and La (Fe0. 88SixAl0. 12- x) 13 intermetallic compounds”. In: *Journal of Magnetism and Magnetic Materials* 383 (2015), pp. 196–202.

[223] D Connor Jones et al. “Origin of spin reorientation and intrinsic anomalous Hall effect in the kagome ferrimagnet TbMn 6 Sn 6”. In: *Physical Review B* 110.11 (2024), p. 115134.

[224] Yi Zhou et al. “Giant Anomalous Hall Effect in the Kagome Ferrimagnet Tb1–x Y x Mn6Sn6 Single Crystals”. In: *Crystal Growth & Design* (2025).

[225] Zhentao Huang et al. “Microscopic origin of the spin-reorientation transition in the kagome topological magnet TbMn 6 Sn 6”. In: *Physical Review B* 109.1 (2024), p. 014434.

[226] Huibo B Cao et al. “Low-temperature crystal and magnetic structure of α-RuCl 3”. In: *Physical Review B* 93.13 (2016), p. 134423.

[227] Branton J Campbell et al. “ISODISPLACE: a web-based tool for exploring structural distortions”. In: *Applied Crystallography* 39.4 (2006), pp. 607–614.

[228] H. T. Stokes, D. M. Hatch, and B. J. Campbell. *ISODISTORT, ISOTROPY Software Suite*. Software suite. Available at https://iso.byu.edu.

[229] Yiqing Hao et al. “Magnetic order and its interplay with structure phase transition in van

der Waals ferromagnet VI3". In: *Chinese Physics Letters* 38.9 (2021), p. 096101.

[230] Thomas Marchandier et al. "Crystallographic and magnetic structures of the VI 3 and LiV I 3 van der Waals compounds". In: *Physical Review B* 104.1 (2021), p. 014105.

[231] Ke Yang et al. "VI 3: A two-dimensional Ising ferromagnet". In: *Physical Review B* 101.10 (2020), p. 100402.

[232] LM Sandratskii and K Carva. "Interplay of spin magnetism, orbital magnetism, and atomic structure in layered van der Waals ferromagnet VI 3". In: *Physical Review B* 103.21 (2021), p. 214451.

[233] Fengjun Zhuo, Hang Li, and Aurélien Manchon. "Topological phase transition and thermal Hall effect in kagome ferromagnets". In: *Physical Review B* 104.14 (2021), p. 144422.

[234] Staples. Retail location. 3003 E Michigan Ave, Lansing, MI 48912.

[235] DK Reinhard et al. "SiO2 antireflection layers for single-crystal diamond". In: *Diamond and related materials* 25 (2012), pp. 84–86.

[236] Cristian Javier Herrera-Rodriguez. *Diamond Power Electronics Design and Fabrication Including All Diamond and Diamond Heterostructure Devices*. Michigan State University, 2024.

[237] PE Viljoen, ES Lambers, and PH Holloway. "Reaction between diamond and titanium for ohmic contact and metallization adhesion layers". In: *Journal of Vacuum Science & Technology B: Microelectronics and Nanometer Structures Processing, Measurement, and Phenomena* 12.5 (1994), pp. 2997–3005.

[238] Jiro Nakanishi et al. "Formation of ohmic contacts to p-type diamond using carbide forming metals". In: *Journal of Applied Physics* 76.4 (1994), pp. 2293–2298.

[239] Eric P Visser et al. "Electrical conduction in homoepitaxial, boron-doped diamond films". In: *Journal of Physics: Condensed Matter* 4.36 (1992), p. 7365.

[240] TH Borst and O Weis. "Boron-Doped Homoepitaxial Diamond Layers: Fabrication, Characterization, and Electronic Applications". In: *physica status solidi (a)* 154.1 (1996), pp. 423–444.

[241] JP Goss et al. "Vacancy-impurity complexes and limitations for implantation doping of diamond". In: *Physical Review B—Condensed Matter and Materials Physics* 72.3 (2005), p. 035214.